Methanation of CO_2: Insight into deactivation mechanisms and catalyst stability under dynamic reaction conditions

zur Erlangung des akademischen Grades eines

DOKTORS DER NATURWISSENSCHAFTEN

(Dr. rer. nat)

von der KIT-Fakultät für Chemie und Biowissenschaften

des Karlsruher Instituts für Technologie (KIT)

genehmigte

DISSERTATION

von

Dipl.-Chem. Benjamin Mutz

aus

Horb am Neckar

KIT-Dekan:	Prof. Dr. Willem M. Klopper
Referent:	Prof. Dr. Jan-Dierk Grunwaldt
Korreferent:	Prof. Dr. Felix Studt
Tag der mündlichen Prüfung:	24.07.2017

Abstract

In a future power supply system mainly based on renewable sources, long-term energy storage systems are crucial to replace the depleting fossil fuel reserves gradually and to balance seasonal fluctuations of energy generated by wind and sunlight. The strategy of choice comprises chemical energy carriers of high energy density, which can be generated within the "power-to-chemicals" concept using renewable H_2 from water electrolysis and the greenhouse gas CO_2. Such reactions and processes are well studied during steady state operation. However, for the utilization of power from fluctuating renewable sources, the processes and especially the catalyst systems must tolerate the dynamic supply of energy and, thus, H_2. Therefore, new challenges in process control and catalyst design arise keeping in mind that the catalyst itself is also a dynamic system. In this thesis, the methanation of CO_2 was studied as an exemplary reaction to produce a chemical energy carrier with a fluctuating H_2 supply to gain first insights into the dynamics of the process and its impact on the catalyst structure and performance.

For this purpose, various Ni-based catalysts were studied under reaction conditions during the dynamically operated methanation of CO_2 using *operando* spectroscopy. First experiments with a commercial methanation catalyst and utilizing *operando* X-ray absorption spectroscopy (XAS) revealed a fast bulk oxidation of Ni in a less reducing atmosphere after a H_2 dropout of 50 min during the methanation of technical CO_2 (O_2 background) as an extreme scenario. Catalyst deactivation occurred in the subsequent methanation step due to residual NiO, which could not be reduced fully under methanation conditions.

For a more detailed insight into the structural behavior of the Ni particles under dynamic reaction conditions a 10 wt.% Ni/Al_2O_3 model catalyst was prepared and optimized to obtain small and uniformly sized Ni nanoparticles. Characterization of the catalyst using X-ray diffraction (XRD), temperature-programmed reduction with H_2 (H_2-TPR), scanning transmission electron microscopy (STEM) and XAS revealed Ni particles of 4 nm in size and a high metal dispersion of 21 %. The catalyst showed competitive performance in the methanation of CO_2, which was intensively studied by parameter

screening experiments in a continuous flow laboratory setup equipped with a stainless steel fixed-bed reactor and online analytics that was planned and built-up within this thesis. Proceeding the previous spectroscopic study of the process with fluctuating H_2 supply, an extended *operando* XAS experiment using the model catalyst showed continuous deactivation over cycles. However, the initial state and performance of the catalyst could be fully recovered within an efficient reactivation step with H_2 at elevated temperatures.

In the next step, quick-scanning extended X-ray absorption fine structure (QEXAFS) spectroscopy was applied to investigate short-term H_2 interruptions of 30 s, which revealed surface oxidation/reduction processes, whereas the core of the Ni particles remained reduced. The most reactive, *i.e.* low coordinated, metallic Ni sites were oxidized in less reducing atmospheres and could not be fully re-reduced during the subsequent methanation cycle, thus, causing deactivation. Coordination numbers estimated from EXAFS fitting suggest shape changes of the Ni particles under dynamic reaction conditions. These results clearly show the importance and opportunities arising from investigating the structural dynamics of catalysts, especially in power-to-chemicals processes relying on renewable H_2. Since even short-term interruptions of H_2 could not be tolerated by the catalyst, operational adjustments of the methanation process were developed to prevent catalyst oxidation and deactivation, also in the presence of O_2. This was realized either by a small continuous H_2 background flow through the reactor or the utilization of a CO_2/CH_4 mixture for the methanation reaction.

As coking represents another path frequently causing deactivation of Ni-based catalysts, *operando* Raman spectroscopy was applied to study the possible formation and nature of carbon deposits during dynamic methanation of CO_2/CH_4 mixtures as *e.g.* provided by biogas plants. It was discovered that the catalysts were resistant to carbon formation under various feed compositions, unless pure CH_4 was fed to the reactor. In the latter case, intensive graphite-like carbon deposits were observed by *operando* Raman spectroscopy at the surface of the working catalysts. Consequently, significant deactivation of the catalyst was observed after coking. However, the catalytic activity could be fully recovered after reactivation in H_2 at elevated temperatures, uncovering the surface of the metal particles. These results demonstrate that *operando* Raman

spectroscopy is a suitable tool to study the formation and nature of carbon deposits under realistic reaction conditions and in real-time.

The Ni-based model catalyst system was further developed to a promising 17 wt.% Ni_3Fe/Al_2O_3 catalyst with uniform Ni_3Fe alloy particles (4 nm), a narrow size distribution and a high metal dispersion of 24 % as determined by in-depth characterization by XRD, H_2-TPR, STEM combined with energy dispersive X-ray spectroscopy (EDX) as well as high resolution (HR)TEM and Raman spectroscopy. Outstanding catalytic performance and stability was achieved compared to a commercial Ni-based methanation catalyst under industrially relevant reaction conditions for 45 h time on stream. Consequently, this bimetallic Ni_3Fe catalyst emerged as a promising alternative for mid-temperature methanation of CO_2 in industrial applications.

In conclusion, this thesis comprises the planning and construction of a continuous flow laboratory setup specifically designed for catalyst screening in the methanation of CO_2 and for fast gas modulations to simulate dynamic reaction conditions. Catalysts with high dispersion and uniform particle size distribution featuring high performance and long-term stability were developed for structural investigations and, moreover, as promising alternatives for industrial methanation applications. Complex *operando* spectroscopic studies were performed to gain detailed insight into the behavior of the catalyst and the deactivation mechanisms under dynamic reaction conditions. It was found that fast load changes during the methanation of CO_2 influenced the catalyst and, thus, arouse interest to investigate also other power-to-chemicals processes using renewable H_2 under dynamic reaction conditions. Moreover, dynamic reaction conditions allow additional insights into the reaction mechanism.

Kurzfassung

Für eine zukünftige, auf erneuerbare Ressourcen basierende Energieversorgung sind Langzeitspeichersysteme unabdingbar, um fossile Rohstoffe schrittweise zu ersetzen und saisonale Schwankungen in der Energieproduktion aus Wind und Sonnenlicht auszugleichen. Vielversprechende Speichersysteme sind z.B. chemische Energieträger mit hoher Energiedichte, die im Rahmen des "Power-to-Chemicals"-Konzepts aus erneuerbarem H_2 (aus Wasserelektrolyse) und dem Treibhausgas CO_2 erzeugt werden können. Unter stationärer Betriebsweise wurden diese Prozesse und Reaktionen bereits eingehend untersucht und verstanden. Zur Nutzung von Strom aus fluktuierend anfallenden erneuerbaren Quellen müssen jedoch Schwankungen der H_2-Konzentration und deren Einfluss auf den Prozess und insbesondere auf das Katalysatorsystem in Betracht gezogen werden. Daraus ergeben sich neue Herausforderungen sowohl für die Prozessführung als auch für die Katalysatorentwicklung, da auch der Katalysator an sich ein dynamisches System darstellt. In dieser Arbeit wurde die Methanisierung von CO_2, als Prozessbeispiel zur Erzeugung eines chemischen Energieträgers, mit fluktuierender H_2-Zufuhr untersucht, um erste Einblicke in die Dynamik des Prozesses und die Auswirkungen auf die Katalysatorstruktur und –aktivität zu gewinnen.

Hierfür wurden verschiedene Ni-basierte Katalysatoren unter realitätsnahen Reaktionsbedingungen in der dynamisch geführten CO_2-Methanisierung mittels *Operando*-Spektroskopie untersucht. Eine erste Studie unter Verwendung eines kommerziellen Methanisierungskatalysators und *Operando*-Röntgenabsorptions-spektroskopie (XAS) zeigte eine schnelle Oxidation des Katalysators während eines ca. 50-minütigen H_2-Ausfalls bei der Methanisierung von technischem CO_2 (inklusive O_2-Spuren), was einen Extremfall der dynamischen Reaktionsbedingungen darstellt. Im darauffolgenden Methanisierungsschritt wurde eine Deaktivierung des Katalysators aufgrund verbleibender, inaktiver NiO-Spezies beobachtet, welche unter diesen Bedingungen nicht wieder reduziert werden konnten.

Um detailliertere Einblicke in das strukturelle Verhalten des Katalysators unter dynamischen Bedingungen zu gewinnen, wurde die Synthese eines 10 Gew.-% Ni/Al_2O_3

Modellkatalysators optimiert, um Ni-Nanopartikel mit einheitlicher Partikelgröße und hoher Metalldispersion zu erhalten. Eingehende strukturelle Untersuchungen des Katalysators mittels Röntgenbeugung (XRD), temperaturprogrammierter Reduktion mit H_2 (H_2-TPR), Rastertransmissionselektronen-mikroskopie (STEM) und XAS bestätigten Ni-Partikel einheitlicher Größe (4 nm) und einer Metalldispersion von 21 %. Der Katalysator wies damit optimale Voraussetzungen für strukturelle Untersuchungen unter Reaktionsbedingungen mittels *Operando*-Spektroskopie auf. Die katalytische Aktivität wurde in einem kontinuierlich betriebenen Katalysatorteststand bestehend aus einem Edelstahl-Festbettreaktor und Online-Analytik untersucht, welcher ebenfalls im Rahmen dieser Arbeit geplant, aufgebaut und ausgelegt wurde. Unter Variation verschiedener Reaktionsparameter erwies sich der Katalysator als sehr aktiv. Basierend auf den ersten spektroskopischen Studien der Methanisierung mit schwankender H_2-Zufuhr, wurde ein erweitertes *Operando*-XAS-Experiment am Modellkatalysator durchgeführt. Dies zeigte eine fortschreitende Deaktivierung des Katalysators bei mehreren aufeinanderfolgenden Störungen der H_2-Zufuhr. Allerdings gelang die vollständige Reduktion des Katalysators, und damit die Wiederherstellung der ursprünglichen Aktivität, durch einen Reaktivierungsschritt in H_2 bei erhöhter Temperatur.

Zur Untersuchung des Einflusses kurzzeitiger Störungen der H_2-Zufuhr von 30 s wurden XAS-Experimente mit hoher Zeitauflösung (QEXAFS) durchgeführt. Diese Untersuchungen zeigten Oxidations-/Reduktionsprozesse an der Oberfläche der Ni-Partikel, während der Kern der Partikel reduziert blieb. Dabei wurden die reaktivsten Ni-Zentren geringer Koordination zuerst oxidiert, welche unter den folgenden Methanisierungsbedingungen nicht wieder vollständig reduziert werden konnten. Dies ahtte eine Verringerung der katalytischen Aktivität zur Folge. Die aus der Feinstruktur der XAS-Spektren erhaltenen Ni-Koordinationszahlen könnten auf Veränderungen der Partikelgeometrie unter dynamischen Reaktionsbedingungen hindeuten. Diese Ergebnisse zeigen klar die Wichtigkeit solcher Studien im Hinblick auf die Katalysatorstruktur, besonders für “Power-to-Chemicals“-Prozesse unter Verwendung von erneuerbarem H_2. Auf Basis der bisherigen Ergebnisse wurde die prozessseitige Verhinderung der Katalysatoroxidation und -deaktivierung in Methanisierungsanlagen untersucht. Diese Studien zeigten, dass ein kleiner, kontinuierlicher H_2-Strom im Reaktor

oder die Methanisierung eines CO_2/CH_4-Gemisches der Oxidation des Katalysators durch Schwankungen der H_2-Zufuhr vorbeugen kann.

Neben der Oxidation stellt die Verkokung eine weitere, häufige Ursache der Deaktivierung von Ni-Katalysatoren dar. Um die Bildung und Eigenschaften möglicher Kohlenstoffablagerungen während der Methanisierung von CO_2/CH_4-Gemischen (z.B. aus Biogasanlagen) unter dynamischen Bedingungen zu untersuchen, wurde auf *Operando*-Raman-Spektroskopie zurückgegriffen. Mit Hilfe dieser Methode konnte gezeigt werden, dass in den verschiedenen Gasatmosphären, die während der dynamischen CO_2-Methanisierung auftreten könnten, keine Kohlenstoffablagerungen gebildet werden. Einzig in reinem CH_4 wurden intensive Raman-Banden beobachtet, die graphitischem Kohlenstoff zugeordnet werden konnten. Die Kohlenstoff-ablagerungen hatten eine erhebliche Katalysatordeaktivierung zur Folge. Allerdings konnte die ursprüngliche Aktivität des Katalysators durch Reaktivierung in H_2 bei erhöhter Temperatur zurückgewonnen werden, wobei die Oberfläche der Metallpartikel von den Kohlenstoffablagerungen befreit wurde. Wie diese Studie zeigte, ist *Operando*-Raman-Spektroskopie eine vielversprechende Methode, um die Bildung und Eigenschaften von Kohlenstoffablagerungen auf einem Katalysator unter realen Reaktionsbedingungen und in Echtzeit zu beobachten.

Im weiteren Verlauf wurde der Ni-Modellkatalysator zu einem bimetallischen 17 Gew.-% Ni_3Fe/Al_2O_3-System weiterentwickelt. Eingehende Charakterisierung mittels XRD, H_2-TPR, STEM gekoppelt mit energiedispersiver Röntgenspektroskopie (EDX), hochauflösender Transmissionselektronenmikroskopie (HRTEM) und Raman-Spektroskopie zeigten einheitliche Partikel der gewünschten Ni_3Fe-Legierung (4 nm) mit enger Partikelgrößenverteilung und hoher Metalldispersion von 24 %. In einem Langzeitversuch unter industrierelevanten Reaktionsbedingungen mit hoher Katalysatorbelastung zeigte der Katalysator eine hervorragende Aktivität und Stabilität für 45 h im Vergleich zu einem kommerziellen Ni-basierten Methanisierungskatalysator. Diese Ergebnisse belegen, dass der Ni_3Fe-Katalysator ein vielversprechendes Katalysatorsystem für die industrielle CO_2-Methanisierung im moderaten Temperaturbereich darstellt.

Diese Arbeit umfasst die Planung und den Aufbau eines kontinuierlich betriebenen Katalysatorteststands, welcher speziell zur Untersuchung der katalytischen Aktivität verschiedener Katalysatorproben und auch für die Methanisierung von CO_2 unter dynamischen Bedingungen mit schnellen Gaswechseln ausgelegt wurde. Katalysatorsysteme wurden entwickelt und optimiert, um spezielle Voraussetzungen und Anforderungen, wie z.B. einheitliche Partikelgröße für Strukturuntersuchungen, aber auch hohe katalytische Aktivität und Langzeitstabilität für industrielle Anwendung, zu vereinen. Komplexe spektroskopische Experimente wurden entwickelt und durchgeführt, um die Struktur und das Verhalten des Katalysators unter dynamischen Reaktionsbedingungen zu untersuchen und entsprechende Rückschlüsse auf Deaktivierungsmechanismen ziehen zu können. So wurde herausgefunden, dass schnelle Lastwechsel während der Methanisierung von CO_2, als Beispielreaktion zur Erzeugung chemischer Energieträger, den Katalysator beeinflussen. Diese Ergebnisse veranschaulichen die Wichtigkeit, auch andere Prozesse im Rahmen des Power-to-Chemicals-Konzepts, bei dem H_2 aus erneuerbaren Quellen genutzt wird, unter dynamischen Bedingungen zu betrachten. Weiterhin besteht die Möglichkeit anhand dynamischer Reaktionsbedingungen ergänzende Einblicke in den Reaktions-mechanismus zu gewinnen.

Table of contents

1 Introduction

1.1 Energiewende and renewable energy

The supply of energy in the near future poses major challenges due to the increasing population and the depleting fossil resources. Germany has agreed on realizing the "Energiewende" (energy revolution / transition) with the aim to shut down nuclear power plants and focus on renewable energy (RE) systems. The main advantage of this approach is the environmental protection and reduced emission of greenhouse gases.[1] RE generation can be realized *e.g.* by photovoltaics or solar thermal power plants, wind power technologies, geothermal energy, hydropower or by biomass either by thermal or biological conversion.[2-5]

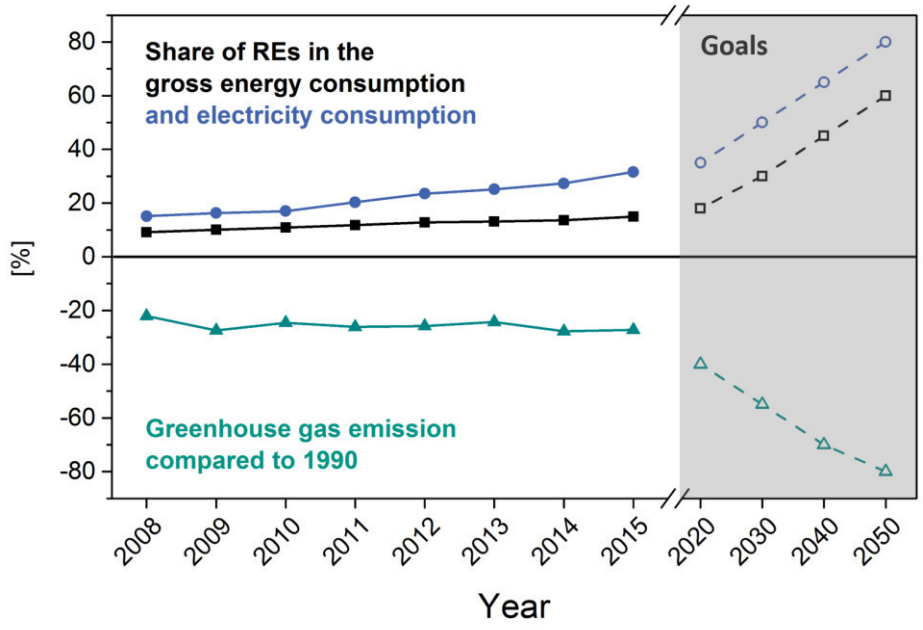

Figure 1: Share of renewable energies in the gross energy consumption (squares, black) as well as in the electricity consumption (circles, blue) and the CO_2 emission compared to that of 1990 according to the energy transition in Germany (data taken from "Fünfter Monitoring-Bericht zur Energiewende" by the Federal Ministry for Economic Affairs and Energy[6]). The dashed lines represent the goals by the German government.

The integration of REs into the energy sector in Germany is driven forth and increased steadily over the past years (Figure 1). In 2015 the share of RE in the gross electricity consumption was 31.6 %, which was mainly based on the huge growth of wind power. The share of RE in the sectors of heat and transport is less pronounced. Efforts need to be stepped up to achieve the reduction of greenhouse gas emissions, especially CO_2. The goals in the electricity sector for 2020 (35 %) will be reached ahead, but the share of RE need to be increased significantly until the year 2050 to replace conventional power plants suffering from high CO_2 emissions. Greenhouse gas emissions need to be reduced in this time frame by about 80 – 95 % compared to 1990. In this scenario, a fraction of 60 % of the gross energy consumption and 80 % of the electricity consumption will need to rely on renewable energies.[6]

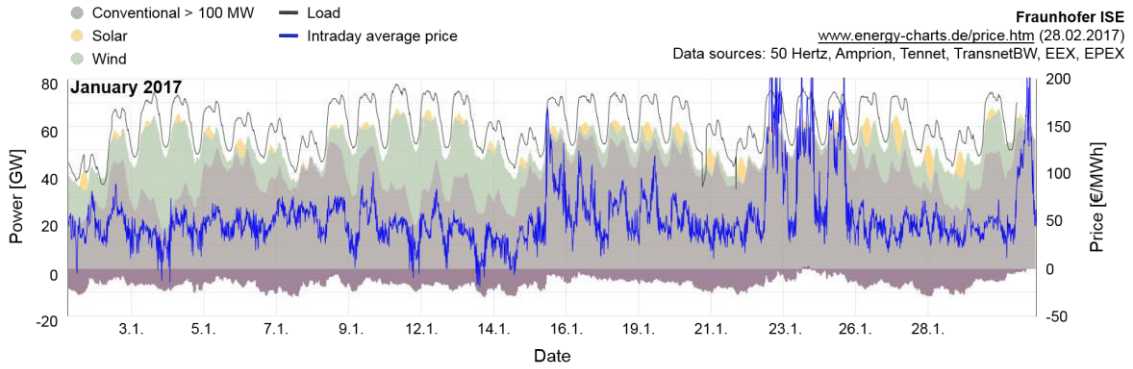

Figure 2: Energy production in Germany in January 2017 including wind (green), solar (yellow) and conventional (grey) power generation. Figure taken from "Energy Charts"[7], Copyright © by Fraunhofer-Gesellschaft, reproduced with permission.

The main challenge of an energy system that is mostly based on renewables is the fluctuating nature of wind and solar energy, not only on time scales of months and seasons but also of minutes. At the beginning of January 2017 exemplary shown in Figure 2, wind provided a high amount of energy whereas in the second half of the month much less energy was produced from wind. This phenomenon will be even more pronounced with a higher share of RE in future energy systems causing balancing issues in the electricity grid *e.g.* during wind calms. On the other hand wind turbines produce excess electricity during strong wind periods, which cannot be fed into the power grid entirely. Thus, the

supply with RE needs to be matched with the energy demand in temporal and spatial dimensions. Electricity produced in periods with high RE generation and low power demand needs to be shifted to periods with high power demand and low RE generation to guarantee grid stability. At the moment, the electricity grid is balanced by conventional power plants but in the future, grid stability need to be warranted by RE.[8-10]

1.2 Energy storage

The key strategy to manage the energy supply based mainly on renewable sources could be energy storage.[11-13] There are a couple of well-developed methods for the storage of energy.[9,11] Batteries for example can be utilized for short-term storage of small amounts of energy. Battery systems used for grid applications are for example sodium-sulfur batteries, redox-flow batteries or lithium-ion batteries.[14-16] However, batteries suffer from high cost and limited storage capacity. Pumped hydro energy storage exhibits a high storage capacity and reaction times for grid stabilization but is geographically limited. Compressed air energy storage suffers from range limitations of the caverns and low efficiency.[11] To bridge several weeks of wind calms and for the seasonal balancing of REs, long-term storage systems, such as chemical energy carriers are necessary.[1,11,12,17]

H_2 *e.g.* produced by water splitting using renewable electricity can serve as chemical energy carrier, offering an impressive gravimetric energy content (120 MJ kg^{-1}) due its low mass. However, the volumetric energy density (0.011 MJ L^{-1} (gas), 8.5 MJ L^{-1} (liquid, -253 °C)), crucial for energy storage, is very low compared to hydrocarbons (35 MJ L^{-1}).[12,17-19] State of the art H_2 storage technology requires pressures of 350 - 700 bar (4.5 MJ L^{-1})[12,18,19] in spherical or cylindrical vessels which requires huge mechanical energy by the compressor. Up to now, none of the investigated storage strategies of H_2 is suitable *e.g.* for passenger cars.[12,17-19] Further H_2 storage technologies such as H_2 adsorption on high-surface area materials or reversible chemical storage of H_2 in hydrides are investigated currently.[19-22]

Methane as energy carrier shows a higher volumetric energy density (0.036 MJ L^{-1} (gas)) and is usually stored as compressed natural gas at 200 bar (6.9 MJ L^{-1}) or as liquefied natural gas (21 MJ L^{-1} at -160 °C).[12,18] Beside the higher volumetric energy density, the main advantage of SNG is the infrastructure, which is already present on a large scale. SNG can be stored and distributed in the existing long-range natural gas pipeline network and storage facilities.[8,12,23,24] H_2 storage in the natural gas grid is also possible, but limited to a small amount.

Further promising chemical energy carriers with high energy density are hydrocarbons (35 MJ L^{-1}) from Fischer Tropsch synthesis (crucial as fuel *e.g.* for aviation) or methanol (16 MJ L^{-1}).[11,12,17,25-35] In this thesis, the focus was on the methanation of CO_2 to produce synthetic (or substitute) natural gas (SNG) as exemplary reaction to produce a versatile chemical energy carrier.

1.2.1 Power-to-gas

SNG can be produced within the power-to-gas (PtG) process (Figure 3), which links the power grid with the gas grid.[8,24,36,37] Surplus electrical power from wind and solar energies can be applied in water electrolysis to produce green H_2, which is then directly used to hydrogenate CO_2 in a heterogeneously catalyzed reaction to produce SNG with an efficiency of 75 – 80 %.[8,12,37] The direct utilization of H_2 for CO_2 hydrogenation is optimal for local flexible plants (*e.g.* in northern Germany near the wind parks) and avoids the acquisition of cost-intensive H_2 storage facilities, which would lower the overall efficiency of the PtG process.[12,38] CO_2 as feedstock could for example be acquired by CO_2 capture and storage (CCS) from industrial processes[39,40] or from biogas plants[8,9,24,41] using directly the delivered CO_2/CH_4 mixtures or the CO_2 after separation. CO_2 is recycled and used as feedstock, contributing to the decrease of the greenhouse gas and producing a CO_2 neutral fuel.[23,25-29,36,42,43]

SNG can be used directly as a fuel for passenger cars with combustion engines (see Audi e-gas-project in Werlte, Germany[44-46]), exhibiting higher efficiency and less emission of particulate matter and NO_x compared to conventional lean burn engines.[47,48]

Furthermore, reconversion to electricity for electrical grid stabilization is possible using gas turbines.[8,9] Additionally, lower dependency on natural gas imports is managed through SNG production. Attention needs to be payed regarding the emission of CH_4, since it shows a 25-times higher greenhouse gas potential compared to CO_2.[12,47]

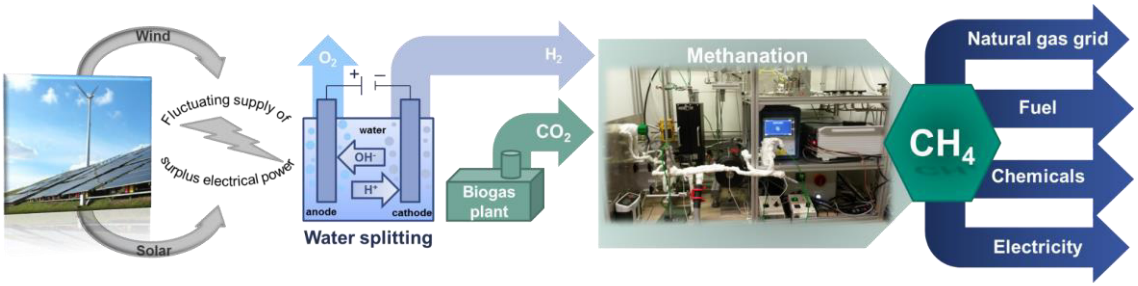

Figure 3: Schematic illustration of the power-to-gas concept using renewable energies from wind and solar power.

Challenges for the PtG process arise from the fluctuating and randomly supplied energy from wind and solar power. These fluctuations directly influence electro catalysis for H_2 generation and may progress further towards the methanation reactor as fluctuating H_2 feed.[24,38,49,50] The impact of such fluctuating reaction conditions on the process require in-depth investigation, especially in case of the catalytic reactions producing chemical energy carriers.[38]

Other chemical energy carriers such as hydrocarbons or methanol can be produced in a similar way (power-to-chemicals). Applied in the context of renewable energies all the processes for the production of chemical energy carriers have to face the issue of the fluctuating supply of wind and solar energies. In general, power-to-chemicals processes in small and local plants require a shift from steady state operation to operation under dynamic reaction conditions.[38] Note that a future scenario including an energy system mainly based on renewables is considered here. As long as electricity is generated by fossil fuels, it is not worthwhile to use hydrogen for the synthesis of hydrocarbons instead of direct electricity generation.[11,12]

1.3 Methanation of carbon dioxide

The so-called Sabatier Reaction (1)) that describes the methanation of CO_2 is a well-developed process under steady state conditions.[28,51,52] The reaction is highly exothermic ($\Delta H_{298\,K}$ = -165 kJ mol^{-1}) due to the formed water, which is the main product beside methane. Increased pressure shifts the equilibrium to the product side because of the reduction in volume of the product molecules compared to the starting materials. Taking these aspects into account, the methanation of CO_2 is most favorable at low temperatures (< 400 °C) and elevated pressures. At temperatures above 450 °C the formation of CO as additional by-product increases due to the endothermic reverse water gas shift reaction (RWGS, (2)). In addition, the amount of unreacted CO_2 and H_2 increases at higher temperatures.[53] In literature catalyst testing for the methanation of CO_2 in lab-scale reactors is performed between 200 - 400 °C (in some cases 160 °C (Ru/TiO_2[54])) and at 1 – 30 bar.[51]

$$CO_2 + 4H_2 \rightleftharpoons CH_4 + 2H_2O \qquad \Delta H_{298\,K} = -165 \text{ kJ mol}^{-1} \qquad (1)$$

$$CO_2 + H_2 \rightleftharpoons CO + H_2O \qquad \Delta H_{298\,K} = -41 \text{ kJ mol}^{-1} \qquad (2)$$

$$CO + 3H_2 \rightleftharpoons CH_4 + H_2O \qquad \Delta H_{298\,K} = -206 \text{ kJ mol}^{-1} \qquad (3)$$

The methanation of CO_2 proceeds more selectively than the methanation of CO (3)[55,56] and the formation of CH_4 reached a higher rate in CO_2 methanation,[57,58] indicating different reaction routes. For the full reduction of CO_2 to CH_4, a transfer of eight electrons is necessary, which inhibits the reaction kinetically and highly active catalysts are required.[28,51]

1.3.1 Catalyst systems

To date, most active catalysts for the hydrogenation of CO_2 to CH_4 are supported Ni,[59-71] Ru,[54,68,72-77] Rh,[58,78-80] Co[81] or Pd[82,83] nanoparticles. Ru catalysts were

reported as the most active ones especially in the low-temperature regime.[28,51,52,84] A 0.8 wt.% Ru/TiO_2 catalyst containing highly dispersed Ru nanoparticles prepared by a barrel-sputtering method achieved near 100 % yield of CH_4 at only 160 °C. The turnover frequency (TOF) was calculated as $4.6 \cdot 10^{-3}$ s^{-1}. However, the gas flow of 70 mL g^{-1} h^{-1} was very low.[54] Due to low costs and good performance in the high-temperature regime, Ni-based catalysts are most commonly used. Surface defect-promoted Ni catalysts with low coordinated Ni sites and high dispersion enhance the performance at low temperatures between 220 - 300 °C, achieving a TOF of $2.4 \cdot 10^{-3}$ s^{-1} at 220 °C and excellent stability for 260 h at 290 °C.[62]

Apart from the common support materials such as Al_2O_3,[60,62,68-70,85-87] SiO_2[88] and TiO_2[54,63] also redox-active materials such as ZrO_2,[71,89-91] CeO_2[66,92] or CeO_2/ZrO_2 mixed oxides[64,65,93-96] were reported as promising supports, which promote the CO_2 activation by mild basic sites and, thus, increase the low temperature activity of Ni catalysts. A 10 wt.% Ni/CeO_2 catalyst prepared by a wet impregnation method achieved high activity ($X(CO_2$ = ca. 90 %) around 300 °C and a selectivity near 100 %, which was superior compared to Ni catalysts supported on MgO, TiO_2 and α-Al_2O_3.[66] Doping the Al_2O_3 support, which exhibits high thermal stability and specific surface area, with ZrO_2 or CeO_2 to combine the advantages of both materials resulted in an enhanced activity of Ni-based catalysts, especially at low temperatures between 250 - 300 °C.[61,70,97] Other promotors are for example MgO, which (similar to ZrO_2 and CeO_2) enhances the reducibility as well as the catalytic performance, increases the Ni dispersion and suppresses sintering of the metal particles.[88,98] MgO as a promotor to a Ni/SiO_2 catalyst resulted in an improved performance and stability at for 50 h 350 °C.[88] Ni-Zr-Sm catalysts show enhanced activity due to the stabilization of the active tetragonal zirconia phase by Sm, which also increases the number of surface Ni atoms.[89,99] Enormous TOFs were reported for 14 wt.% Ni/ZrO_2 catalysts doped with Ce or Sm and prepared by an ultrasound-assisted method as well as for a 5 wt.% Ni catalyst supported on mesostructured silica nanoparticles with a high concentration of basic sites. At 300 °C reaction rates in terms of TOF values around 1.5 and 1.6 s^{-1} were achieved, respectively.[59,71]

Complementing a Ni catalyst system with an additional active metal to further enhance the catalytic performance and life time has recently been investigated. NiFe alloy catalysts have been reported to achieve a significantly higher catalytic performance due to an improved CO dissociation (details on the reaction mechanism see section 1.3.2) as predicted by computational studies.[100,101] Experimental results revealed that the addition of Fe enhanced the methanation of CO compared to the monometallic Ni catalysts and excellent catalytic performances were reported.[102,103] Furthermore, compared to monometallic Ni catalysts bimetallic NiFe catalysts achieved higher performances in the methanation of CO_2[104] as well as in the combined methanation of CO and CO_2[104,105]. In contrast, a monometallic Fe catalyst was significantly less active than the Ni catalyst.[104,106]

The influence of dopants such as Fe, Co, Cu, Zr, Y and Mg on Ni catalysts in the methanation of CO_2 was experimentally investigated by Hwang *et al.*[87] and Ren *et al.*[91]. The superior performance of the Fe-doped Ni catalyst compared to the other dopants was ascribed to the weak metal-support interaction and an optimal CO dissociation energy at the surface of the alloy.[87,91] NiFe catalysts show the lowest peak temperature in temperature-programmed surface reactions compared to monometallic catalysts or other bimetallic systems, which experimentally supports the assumption of an optimal CO dissociation energy in the methanation of CO_2.[87] The optimum Ni/Fe ratio in the desired alloy was found to be around 3 as reported by various studies.[103-106] Noble metal addition of Ru or Rh in small amounts was reported to enhance the activity of a Ni-based catalyst significantly. Moreover, the noble metals lower the reduction temperature of the bimetallic Ni catalyst, provide sulfur resistance and long-term stability.[93,107-110]

The catalytic activity for each study reported in the literature is hard to compare with each other, since variegated reaction conditions in terms of gas flow per catalyst mass, degree of dilution, temperature and pressure were applied.

1.3.2 Mechanism

This short literature review of mechanisms proposed for the methanation of CO_2 shows that the reaction routes are not resolved adequately and are still under discussion.

The reaction routes including CO as intermediate and the direct hydrogenation of CO_2 are both accepted in the literature. Moreover, metals, supports, dopants and their interaction with each other might play a crucial role resulting in alternative reaction routes, which has to be analyzed in each specific case.

On unsupported Ni catalysts, the hydrogenation of CO_2 includes first the fast RWGS reaction (2) followed by the conventional methanation of CO: CO is dissociated to surface C and O, which is then hydrogenated gradually to CH_4 and H_2O.[57,111-113] This route was also proposed on a Rh/Al_2O_3 catalyst during low temperature methanation of CO_2, including the oxidation of Rh caused by the dissociation of CO_2 and followed by the mechanism of CO methanation.[78] Using noble metals supported on ceria, CO_2 is activated on surface Ce^{3+} sites leading to the formation of CO and the oxidation of the support.[92] In the mechanism according to Marwood *et al.*[114] (Figure 4) CO_2 is adsorbed on the support of a Ru/TiO_2 catalyst forming hydrogen carbonate (step 1) and formate species (step 2). The latter species located at the metal-support interface are the precursors for CO (step 3), which is then hydrogenated to CH_4 on the Rh surface (step 4).

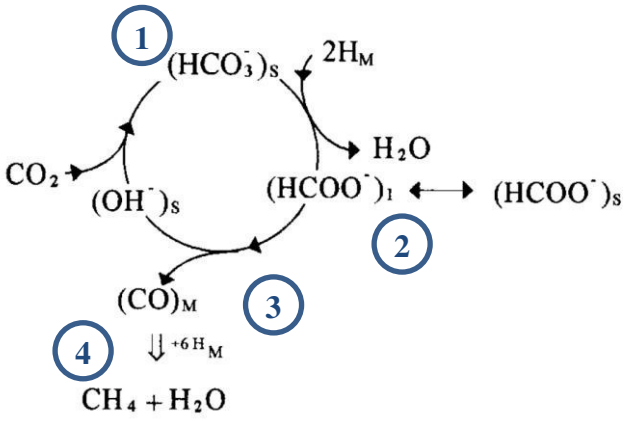

Figure 4: Reaction mechanism of the methanation of CO_2 on a Ru/TiO_2 catalyst. Reprinted from Marwood *et al.*[114] Copyright © 1997, with permission from Elsevier.

Formate species as surface intermediate were also reported in other studies,[115-117] however, according to Westermann *et al.*[116] they are located at Ni sites when using a Ni/zeolite (USY type) catalyst. According to Fisher *et al.*[58] using a Rh/SiO_2 catalyst the

common dissociation of CO_2 to CO is followed by the hydrogenation of adsorbed CO over H_2CO species as intermediate without the formation of surface C.

A direct hydrogenation of CO_2 without the formation of CO as intermediate was proposed for a Pd-Mg/SiO_2 catalyst in a bifunctional mechanism. The reaction is initiated by MgO, which adsorbs CO_2 and forms magnesium carbonate species. The carbonate is then hydrogenated stepwise to CH_4 with H atoms provided by Pd.[82,83] A similar reaction route was reported for a Ni catalyst supported on CeO_2/ZrO_2 mixed oxides, as shown in Figure 5 a). When CO_2 is adsorbed by the mild basic sites present on the $Ce_{0.5}Zr_{0.5}O_2$ support monodentate carbonate and monodentate formate species are formed (see lower path of Figure 5 a)), which are then hydrogenated quickly by H atoms provided by the Ni particles.[95,96,118,119]

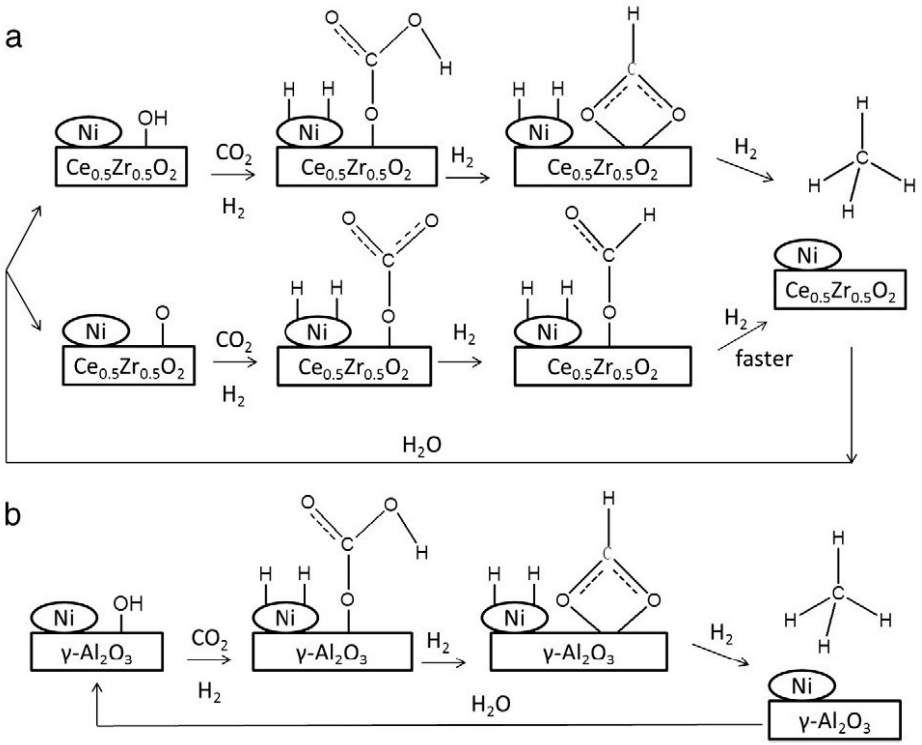

Figure 5: Mechanism for the methanation of CO_2 taking place on a) a Ni/$Ce_{0.5}Zr_{0.5}O_2$ and b) a Ni/Al_2O_3 catalyst according to Aldana *et al.*[95] and Pan *et al.*,[96] respectively. Reprinted from Pan *et al.*[96] Copyright © 2014, with permission from Elsevier.

Weak basic sites result in the formation of hydrogen carbonates and bidentate formats, which are hydrogenated with a lower rate (see upper path of Figure 5 a)).[96] This reaction route might also be taken on the Ni/Al_2O_3 catalyst (Figure 5 b)) exhibiting weak and strong basic sites as investigated by CO_2 temperature-programmed desorption (TPD).[96] CO is not formed within this mechanism, however, it probably occurs from a parallel reaction pathway as by-product.[95]

1.3.3 Methanation reactors and industrial applications

Typically, the methanation of CO_2 in lab-scale is performed in tubular packed bed reactors, which are easy to handle. Problems may occur concerning the removal of heat produced by the exothermic reaction. Therefore, high dilution of the catalyst bed with inert material such as SiC is used in order to guarantee good heat dispersion. Moreover, various zones with optimized dilution grades of the catalyst were applied in structured fixed-bed reactors to prevent the formation of hot sports.[120] Methanation in fixed-bed reactors was simulated during dynamic operation to gain kinetic data and insight into overheating phenomena during the transient reaction conditions.[121-123] Adiabatic fixed-bed reactors are also most commonly used reactor types in industrial applications. Series of fixed-bed reactors with gas recirculation, intermediate gas cooling or the utilization of heat exchangers were applied for syngas methanation in the 1970s and 1980s. The synthesis gas was produced mainly by coal gasification. Recently, a focus is on the methanation of syngas derived from biomass gasification at the same location to overcome the logistic issue of biomass distribution.[84,124,125]

Due to hot spot formation and overheating of the reactor caused by the exothermic reaction, alternative reactor types were tested to obtain isothermal conditions. For better temperature control, micro channel reactors equipped with altering cooling channels were developed exhibiting enhanced heat transfer.[72,126,127] High heat and mass transfer were successfully realized using fluidized-bed reactors in methanation reactions.[128,129] Fluidized-bed reactors with multiple feed inlets and catalyst regeneration cycles were also applied in industrial methanation applications.[84,124,125] Another reactor type facilitating

nearly isothermal operation is a the three-phase reactor in which the heat transfer is enhanced by an oil with high heat capacity. Furthermore, temperature variations can be smoothened during dynamic operation.[130,131]

Figure 6: Methanation unit of the Audi e-gas PtG plant in Werlte. Figure taken from Audi MediaCenter[132], Copyright © Audi AG, reproduced with permission.

Power-to-gas plants in Germany realizing the methanation of CO_2 are for example the Audi e-gas-project[44-46] (Audi, ETOGAS, ZSW, Fraunhofer IWES, EWE Biogas) which is in operation since 2013 and produces 1000 t SNG per year, depending on the availability of wind energy. Renewable electricity is converted to SNG with an efficiency of 54 %, additional heat management between the methanation reactor and the biogas plant would increase the efficiency to 60 % and higher. The methanation unit (Figure 6) consists of a fixed-bed multi-tubular reactor equipped with molten salt cooling. CO_2 is provided by a biogas plant using organic waste.[44-46] Earlier demonstration plants were developed by ETOGAS, ZWS and Fraunhofer IWES in 2009 and 2012 located in Stuttgart. Current developments aim at commercial PtG plants producing 13000 m^3 CH_4 per day.[133,134] Another PtG plant is *e.g.* the EXYTRON demonstration plant in

Rostock.[135] The HELMETH project coordinated by the Karlsruhe Institute of Technology (KIT) aims at demonstrating the economic feasibility of the PtG concept, improving the efficiency to about 85 % by thermal interlinkage of high temperature electrolysis and methanation of CO_2. The latter will be performed in a series of fixed-bed reactors operated at 30 bar and around 300 °C with intermediate water removal.[136,137] An overview of operating PtG plants in Europe was published recently by Bailera *et al.*.[138]

1.3.4 Catalyst deactivation

The long-term stability of catalysts is of capital importance especially for industrial applications. This section addresses typical causes of deactivation of Ni-based catalysts, which may arise during methanation reactions.

1.3.4.1 Formation of volatile compounds

Ni is prone to form volatile and toxic carbonyl species (4) in CO atmosphere at 50 - 100 °C and decomposing at around 180 °C, which is known from the Mond process for the purification of Ni.

$$Ni + 4CO \rightleftharpoons Ni(CO)_4 \qquad \Delta H_{298\,K} = -158\ kJ\ mol^{-1} \qquad (4)$$

The formation of $Ni(CO)_4$ may lead to loss of the active materials and/or Ni particle growth *via* Ostwald ripening.[139,140] Therefore, methanation reactions containing CO and utilizing Ni-based catalysts need to be operated at temperatures above 200 °C.[51]

1.3.4.2 Poisoning and oxidation

Catalyst poisoning occurs by strong chemisorption of one poisonous substance on the active sites of the catalyst and, thus, blocking these adsorption sites for the

reactants.[139,141,142] A common catalyst poison in methanation reactions is H_2S, which appears as impurity from coal or biomass gasification. H_2S adsorbs dissociatively on metallic Ni blocking the active sites through strong chemisorption and degrading the catalytic long-term performance. Furthermore, it has been reported, that sulphur poisoning promotes sintering[108,143] as well as oxidation[108] of the Ni particles. Small NiRu particles supported on SiO_2 showed enhanced sulphur tolerance.[108] In industrial applications H_2S is removed by applying a gas purification step, *e.g.* by Rectisol® scrubbing or by a ZnO bed, but sulphur compounds may still be present on ppb levels.[84,144]

Similarly to sulphur even low concentrations of oxygen may also act as catalyst poison on Ni sites.[139] In extreme cases full oxidation of the metal particles can occur in O_2. Since reduced Ni is the active species in the methanation of CO_2, oxidation of the active sites has to be prevented. Catalyst oxidation which caused catalyst deactivation during performance tests was reported in literature.[88,108]

1.3.4.3 Sintering

Growth of metal particles during the methanation of CO_2 performed in lab-scale reactors was reported frequently.[69,88,93,145] Metal particle growth originates from crystallite migration and coalescence (Smoluchowski ripening, Figure 7 a)) or atomic migration *via* hopping mechanism, diffusion on the surface of the support or through volatile species (Ostwald ripening, Figure 7 b)). During atomic migration, the size of smaller particles diminishes and larger particles grow since the latter are more stable. As a result of metal particle sintering the active surface diminishes reducing the catalytic performance. The tendency towards particle sintering is highly dependent on the temperature but also on the reaction atmosphere, metal species, promotors, support and its pore size.[139,141,142,146]

The temperature at which Ni atoms on defect sites become mobile (Hütting temperature) is 518 °C.[141] Ni particle sintering accelerates with increasing temperature between 550 °C – 750 °C, and an increasing steam content in the feed also contributes to

the sintering progress.[143,147] Ni particles grow fast in the first few hours on stream but only minor particle growth emerged during further operation.[143,148] The fast sintering in the beginning is induced by Ostwald ripening since very small particles are present.[146]

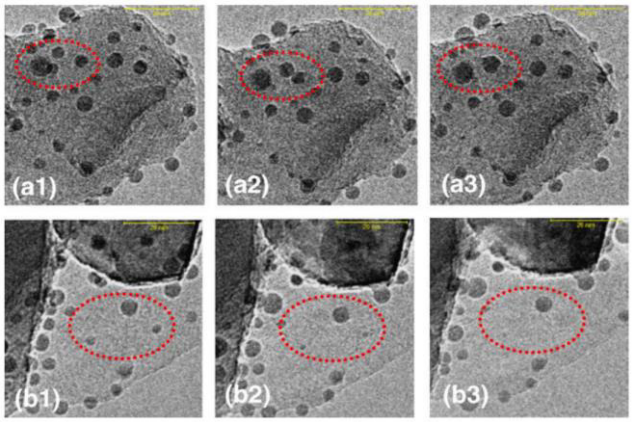

Figure 7: Electron microscopy images of a Ni/$MgAl_2O_4$ steam reforming catalyst. Images a1 – a3 show the particle migration and coalescence sintering mechanism, whereas the images b1 – b3 show the particle growth originated from Ostwald ripening. Reprinted from Sehested[144] Copyright © 2006, with permission from Elsevier.

High reaction temperatures may arise during calcination, due to formation of hot sports during the methanation of CO_2, which is an issue in adiabatic fixed bed reactors, or during regeneration steps such as coke burning or reduction of NiO.[125,141] Sintering caused by overheating effects becomes a major issue when the methanation process is operated dynamically.[122] Significant sintering of Ni particles was observed especially during high temperature methanation (≥ 600 °C) in industrial applications.[149,150] Sintering of metal particles may be prevented using promotors as discussed in section 1.3.1.

1.3.4.4 Coking

Coking (or fouling) describes the deposition of unwanted species covering the surface of the catalyst. Catalyst fouling by carbonaceous deposits is a major issue,

especially in methanation applications containing CO.[151,152] The formation of carbon deposits from CO is described by the Boudouard reaction (5).[53,139,142,153]

$$2CO \rightleftharpoons C + CO_2 \qquad \Delta H_{298\,K} = -172\ kJ\ mol^{-1} \qquad (5)$$

Another scenario leading to carbon formation is the decomposition of CH_4 (6) *e.g.* in CH_4 reforming applications.[53,144,153-156]

$$CH_4 \rightleftharpoons C + 2H_2 \qquad \Delta H_{298\,K} = 75\ kJ\ mol^{-1} \qquad (6)$$

The carbonaceous deposits cover the catalyst surface and, thus, block active sites as well as the pores of the catalysts.[139,153] In extreme cases, carbon whiskers or nanotubes may form (Figure 8 d)), thus, detaching Ni particles from the support.[141,156,157] In case of a methanation pathway with CO as intermediate followed by its dissociation, monoatomic surface carbon species are formed as reaction intermediates (Figure 8 c)) which can easily be hydrogenated to CH_4.[152] When atomic carbon species agglomerate to large and inert carbonaceous species, catalyst deactivation through fouling occurs (Figure 8 d)).[139,153,156]

A higher coking resistance in dry reforming application was reported for a NiFe catalyst, due to the oxidation of carbon deposits by lattice oxygen from FeO_X.[158,159] Ni catalysts promoted with small amounts of Rh also exhibit a higher coke resistance in dry reforming applications.[160,161] Detailed studies on the formation of carbon deposits in different atmospheres were conducted to investigate the nature and the removal of the formed carbon thoroughly.[162,163]

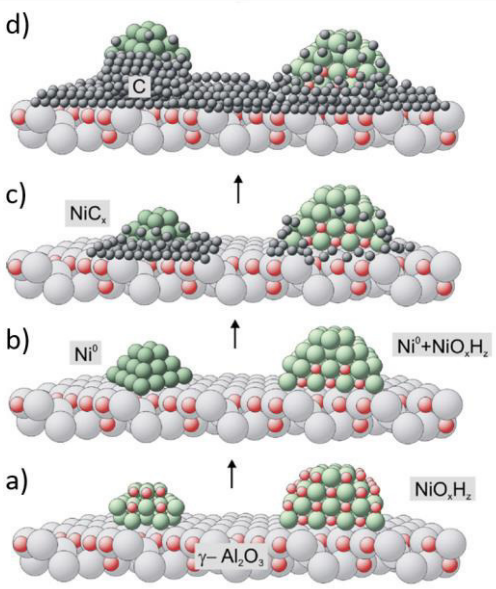

Figure 8: Illustration of carbon deposition during methanation of CO on a Ni/Al_2O_3. a) fresh catalyst in oxidized state, b) reduced catalyst, c) working catalyst with carbon decoration, d) working catalyst with carbon deposits and carbon whisker formation after long methanation runs. Reprinted from Czekaj *et al.*[156] Copyright © 2007, with permission from Elsevier.

In general, the amount of carbon formation during steady state methanation of CO_2 with model gas compositions is negligible.[53,93] As discussed in section 1.3.2, the methanation of CO_2 can be described by initial RWGS reaction (2), followed by the methanation of CO (3) containing water. H_2O suppresses the deposition of carbon according to reactions (7) and (8).[53] In industrial applications, steam is added to the feed to prevent carbon deposits during methanation of syngas.[84]

$$C + H_2O \rightleftharpoons CO + H_2 \qquad \Delta H_{298\,K} = 131\ kJ\ mol^{-1} \qquad (7)$$

$$C + 2H_2O \rightleftharpoons CO_2 + 2H_2 \qquad \Delta H_{298\,K} = 90\ kJ\ mol^{-1} \qquad (8)$$

However, catalyst deactivation from carbon deposition may occur under dynamic reaction conditions comprising *e.g.* a fluctuating H_2 feed. Furthermore, feed gas for methanation of CO_2 contains significant amounts of CH_4 when using biogas (CO_2/CH_4)

or product gas recycling for isothermal reactor conditions.[8,24,84,124,125,138,149] Such more realistic feed gas compositions may also cause carbon deposition.

1.4 Dynamics in catalysis

It is well-known that the structure of catalysts is very dynamic, responding to the current reaction conditions in the reactor (Figure 9).[38,164-167] As discussed in section 1.3.4, supported metal particles may increase in size through sintering, but also re-dispersion may occur as reported for reduction-oxidation-reduction treatments for Ni/SiO_2 catalysts.[168] Dissolution of the active material may occur *e.g.* volatile $Ni(CO_4)$ as discussed above. Metal particles may oxidize/reduce or undergo phase transformations, *e.g.* $Ba(NO_3)_2$ formation in in NO_X storage catalysts.[169,170] Variations in the redox potential of the gas atmosphere may lead to different metal-support interactions, which may further cause morphological changes of the metal particles *i.e.* wetting of the support, decoration effects, surface alloying or composite formation.[171-173] Surface segregation was observed for Pd_2Ga catalysts in the hydrogenation of acetylene forming Pd-like patches and Ga_2O_3 as active phase.[174] More examples and detailed insights into the structural changes of catalysts are given in the following sections.

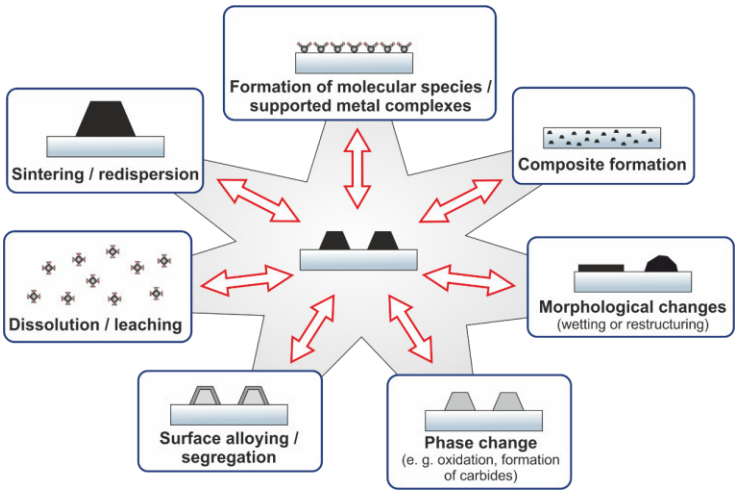

Figure 9: Illustration of structural changes of supported catalysts. Adapted from Kalz *et al.*[38] available under the terms and conditions of the Creative Commons Attribution-NonCommercial 4.0 International license (https://creativecommons.org/licenses/by-nc/4.0/); the Figure was rearranged, Copyright © 2017.

This few examples show that the structure of the catalyst is dynamic and may undergo changes under different reaction atmospheres. Furthermore, those structural changes may lead to different properties and, thus, reactivity of the catalyst. Dynamic reaction conditions are expected for the methanation of CO_2 in combination with surplus electricity from wind and solar energies. Systems, which are already studied under transient reaction conditions are *e.g.* the Fischer-Tropsch reaction, where the influence of unsteady state conditions on the process itself was investigated.[49,50,175] Changing feed compositions in the methanation of CO were simulated to study the response of the reactor, which shows a self-stabilizing effect for high cycling frequencies.[123] Forced periodic operation of chemical reactors was applied, with the aim to improve conversion rates *e.g.* for liquid flow interruptions in trickle-bed reactors.[176-178] Variations in temperature and composition of the feed composition are common problems in the field of exhaust gas aftertreatment, which influences structure and activity of the catalyst.[179,180] Catalysts in fuel cells operating under dynamic conditions suffer from degradation implying dynamic driving cycles or start/stop cycles.[181,182]

Characterization techniques under realistic reaction conditions while monitoring the catalytic performance (*operando*) are required to investigate the behavior the catalyst and to connect structural properties and the changes in the activity.[183-186] Various spectroscopy, diffraction and microscopy techniques have been applied under reaction conditions to reveal detailed insight into different structural changes of catalysts used in processes operated under changing reaction atmospheres.[38,164,165,187]

1.4.1 *In situ* and *operando* characterization studies in catalysis

In situ transmission electron microscopy (TEM) was applied to monitor the sintering of metal particles[188] or the growth of carbon nanofiber[157] on supported catalysts, which may cause catalyst deactivation as discussed in section 1.3.4. Identical location (IL) TEM delivered detailed insight into the behavior of Pt-based fuel cell catalysts during transient operation. Various degradation effects such as agglomeration,

carbon corrosion, dissolution and detachment of the Pt particles were caused by 3600 start-stop cycles.[182]

Another powerful tool to explore the structure of the catalyst under reaction conditions is X-ray absorption spectroscopy (XAS).[171,189-195] Changing the redox potential of the gas atmospheres may lead to structural changes of the active material, as observed for Cu/ZnO catalysts in using *operando* XAS combined with X-ray diffraction (XRD)[171] (Figure 10 a)) or *in situ* TEM[172] Figure 10 b)). Switching between wet and dry syngas during methanol synthesis the Cu coordination numbers received from the evaluation of the extended X-ray absorption fine structure (EXAFS) indicated reversible morphology changes of the Cu species from spherical particles (Figure 10 a) A) to flat Cu particles decorated with reduced Zn (Figure 10 a) D), respectively.[171] Further studies of the commercial Cu/ZnO/Al_2O_3 system showed a complete overlayer of metastable graphite-like ZnO on the Cu particles after reductive treatment. The combined results from TEM and DFT studies indicated that ZnO_x species may act as co-catalyst and stabilizing promotor, enhancing the activity of the Cu catalyst in the methanol synthesis.[173,196-198]

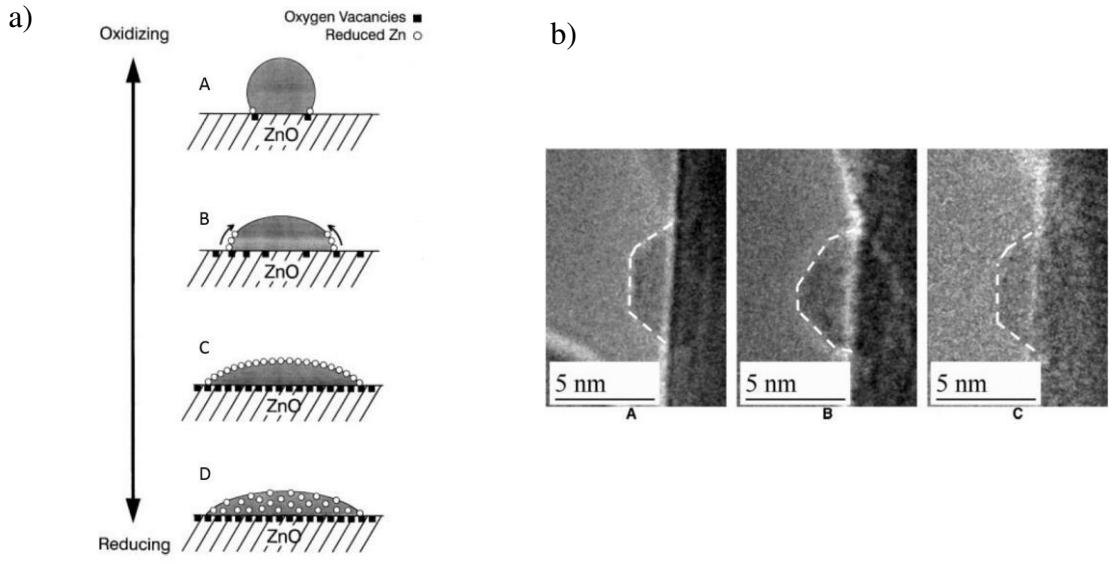

Figure 10: a) Illustration of a Cu/ZnO catalyst and its morphological changes in more reducing and more oxidizing atmosphere. from (A) spherical shaped particle to (D) Cu particles which are more flat with strong wetting of the support and decorated by reduced Zn species. Reprinted from Grunwaldt *et al.*[171] Copyright © 2000, with permission from Elsevier. b) TEM images of the reversible morphological changes of the Cu particle under (A), (C) reducing and (B) oxidizing conditions. Figure taken from Hansen *et al.*[172] Copyright © 2002, reprinted with permission from AAAS.

Further structural dynamics investigated by *operando* XAS were reported for a Cs promoted Ru/C Fisher-Tropsch catalyst. Switching between H_2 and CO atmospheres resulted in reversible Ru-Cs particle reconstruction emphasizing a strong interaction with CO.[199] The ignition in the partial oxidation of methane with a $RhPt/Al_2O_3$ catalyst was studied using *operando* XAS and a high speed X-ray camera. It was found, that in the beginning of the reaction reduction of the catalyst occurs at the end of the catalyst bed and the reduction front propagates towards the reactor inlet. Thus, the method gave remarkable insight into the reaction mechanism along the catalyst bed and into the phase transformations of catalyst particles.[193] The oscillatory behavior of a Pd/Al_2O_3 system during the partial oxidation of methane was explored by *operando* XAS, revealing dynamic structural changes between PdO, Pd and PdC_x along the catalyst bed.[194] Similar dynamics in the catalyst structure were observed during oscillatory CO oxidation.[191]

The formation and nature of carbon deposits on Pt/Al_2O_3 catalysts during the dehydrogenation of propane in various gas atmospheres was studied by Sattler *et al.*[200] applying *operando* Raman spectroscopy, which is a suitable tool to monitor the carbon formation under reaction conditions due to the characteristic bands in the region of 1200 – 1600 cm^{-1}. It was found that the addition of H_2 decreased the size of the carbon crystallites during the reaction.

1.4.2 *In situ* and *operando* characterization studies in methanation reactions

Some of these spectroscopic techniques were also applied in connection to the methanation reaction. Mechanistic studies discussed in section 1.3.2 were performed using *in situ* and *operando* diffuse reflectance infrared spectroscopy (DRIFTS) or infrared spectroscopy (IR).[58,78,95,96,114,116-119] For this purpose, Aldana *et al.*[95] studied the methanation of CO_2 during with varying feed gas mixtures monitoring the catalyst's response with *operando* IR and mass spectrometry (MS) and gained important conclusions about the mechanism. Similar feed gas modulation experiments were performed by other groups.[117,119] DRIFTS coupled with MS in combination with modulation of the feed gas composition and phase sensitive detection was used by Zarfl

et al.[201] to gather more detailed information on the reaction steps involved in the methanation of CO on a Ni/Al_2O_3 catalyst. The modulation excitation approach improved the sensitivity towards variations in the IR signals and revealed that CO dissociation occurs on isolated low coordinated Ni sites, whereas CO adsorbed on crystalline sites is less reactive.

XAS is a powerful tool to investigate the catalytic structure of methanation catalysts and to correlate it to the activity.[67,202-205] *In situ* X-ray absorption near-edge structure (XANES) spectroscopy showed that Pt doping of Co catalysts enhances the reducibility of the catalyst significantly, suggesting a long-distance H atom spillover from Pt to Co. This effect is also expected to occur under methanation conditions leading to an increase in the formation rate of CH_4.[202] *In situ* EXAFS revealed that a higher Ru dispersion arising from different calcination treatments led to an enhanced selectivity in CO methanation.[203] Investigations on a Rh/zeolite (Y type) catalyst using *in situ* EXAFS spectroscopy revealed structural changes of the Rh particles during the methanation of CO_2. The peak intensity of the Rh-Rh scattering as well as the catalytic activity increased during steady state operation, indicating the formation of an optimal structure during the reaction, thus, leading to a higher performance of the catalyst.[205,206]

To date, detailed investigations of the catalyst structure, especially the catalyst behavior in changing feed composition using spectroscopic techniques combined with mass spectrometry has rarely been done.

2 Scope of the thesis

Powering the planet using renewable energy, storage systems are necessary due to the fluctuating supply of wind and solar energy. Among other strategies, energy can be stored in chemical energy carriers such as methane, hydrocarbons, methanol or higher alcohols. One of the main steps to generate promising chemical energy carriers is the hydrogenation of CO_2 using renewable H_2. This process needs to withstand fluctuations in electricity supply from wind and solar power plants, which occur temporarily and fluctuate on a time scale of seconds to days. When using a small or even no H_2 reservoir, these fluctuations are transferred to the catalytic reactor and impose a varying H_2 feed that is needed to hydrogenate CO_2. This is crucial especially for local plants, which directly consume the produced H_2 for the hydrogenation of CO_2.

Inspired by spectroscopic and mechanistic studies in the literature investigating adsorbed and reactive species under changing reaction atmospheres in methanation reactions, the aim of this thesis was to focus on the structure and the dynamics of the catalyst under such conditions. Considering the fluctuating supply of renewable H_2, investigations under fast load changes with focus on the catalyst structure and its behavior are required to gain information about morphology changes of the active material and deactivation processes due to stress and strain of the catalyst. The methanation of CO_2 was chosen as an exemplary reaction to produce a chemical energy carrier and to demonstrate the importance of such studies when catalysts undergo start/stop procedures or dynamic reaction atmospheres in the reactor.

Essential for catalytic performance tests in such processes is a continuous flow laboratory setup, which has been planned and constructed in this thesis. Parameters such as temperature and pressure as well as reaction conditions and catalyst load should be adjustable to establish the optimum catalytic performance. Furthermore, the dosage of different gas mixtures, additional gases and fast load changes need to be possible to simulate dynamic reaction conditions. The configuration of the laboratory setup is described in chapter 4.

A first approach addressing the general response of a commercial Ni-based methanation catalyst is outlined during a H_2 dropout in the methanation of CO_2 to demonstrate the applicability of the concept (chapter 5). *Operando* X-ray absorption spectroscopy (XAS) has been applied to monitor structural changes of the catalyst under reaction conditions.

For in-depth studies of the structural behavior, a Ni-based model catalyst specifically designed for *operando* XAS studies has been prepared (chapter 6). This requires Ni particles of uniform size to determine changes in size, structure and morphology. Likewise, a catalyst support, which does not affect the XAS measurements at the Ni K-edge in transmission mode is required. The catalyst preparation and its composition has been optimized to that effect.

Based on the first results with the commercial catalyst, further *operando* XAS studies with fluctuating H_2 flow has been planned and executed using the novel Ni-based catalyst to assess the structural behavior of the catalyst and the influence on the stability and deactivation under such conditions (chapter 6). The time period of the H_2 dropouts has been varied and extended experiments with numerous cycles are realized to study the influence on the catalyst stability and to simulate fluctuating reaction conditions to an extreme grade (chapter 7). For this purpose, advanced XAS techniques with high time resolution have been applied.

Since the formation of carbon deposits is a well-known deactivation phenomenon for Ni catalysts, in-depth investigations during fluctuating H_2 supply related to the *operando* XAS experiments have been carried out. Questions such as “In which reaction atmospheres reflecting realistic gas mixtures and dynamic reaction conditions do carbon deposits form?”, “What is the nature of those carbon species and how do they behave in different atmospheres?”, “How do carbon deposits influence the catalytic performance and how can they be removed?” could be answered. To monitor carbon deposition in real-time and under realistic reaction conditions, *operando* Raman spectroscopy has been established and applied (chapter 8).

Finally, promising bimetallic systems, which exhibit enhanced catalytic performance and stability and at the same time fulfill the requirements for further

structural investigations by *operando* XAS, have been prepared, optimized, characterized regarding the interplay of both metals and tested for their catalytic performance (chapter 8 and 9). The most promising catalyst has been exposed to industrially relevant, harsh reaction conditions to verify its limitations and compared with commercial Ni-based methanation catalysts as benchmark (chapter 9).

An overview of this thesis within its specific aims is summed up in the following scheme:

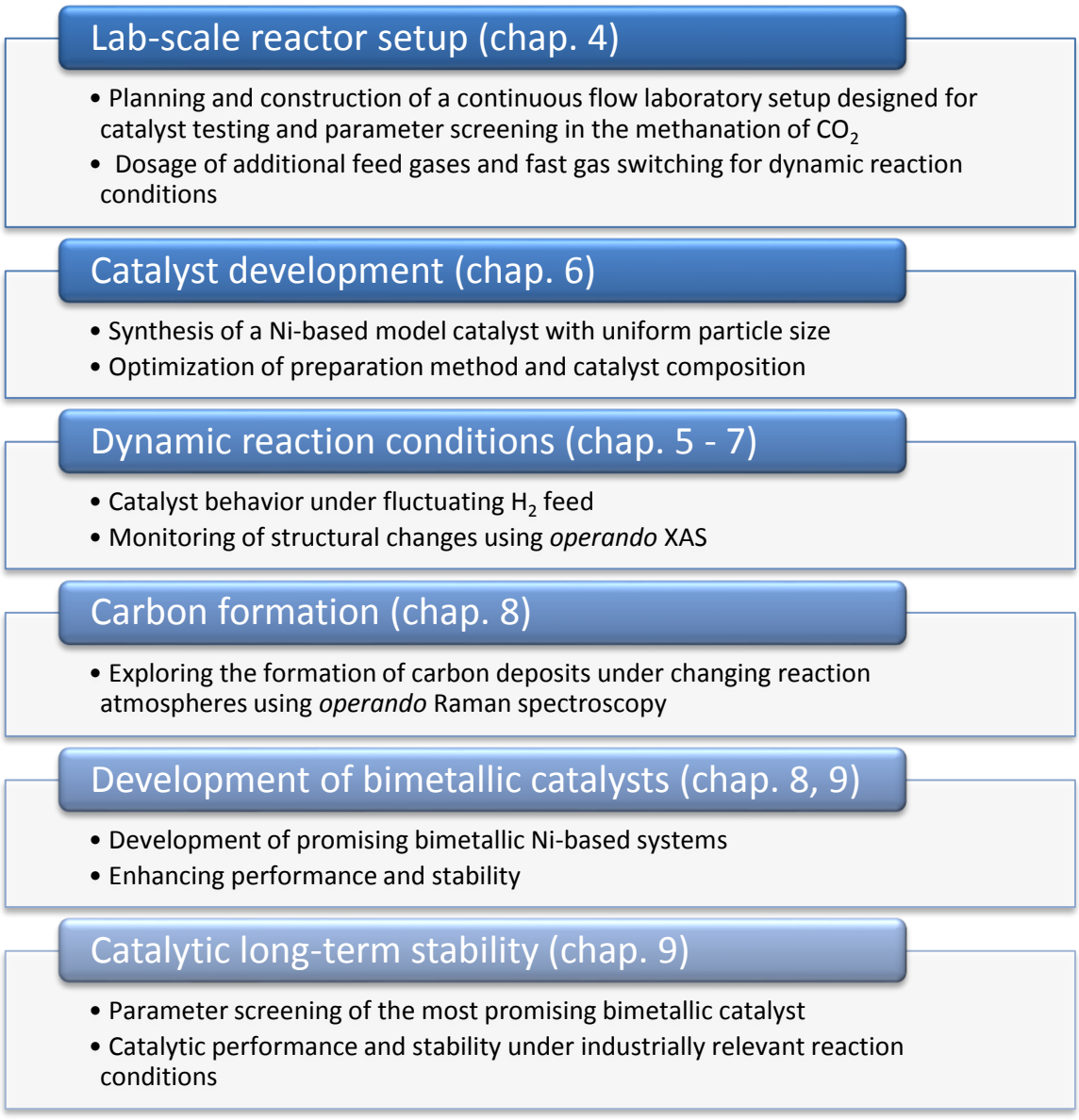

3 Experimental details

3.1 Catalyst materials and preparation

The experiments in chapter 5 were carried out using a commercial Ni/Al_2O_3 methanation catalyst. The received catalyst pellets were crushed and calcined in a separate oven under static air at 500 °C (5 K min^{-1}) for 4 h.

The prepared catalysts utilized in chapters 6 to 9 were prepared by homogeneous deposition-precipitation with urea as precipitating agent.[207-209] Typically, 2 - 4 g of the catalyst sample were prepared in one batch. The synthesis mixture consisted of a 0.3 mol L^{-1} solution of the metal precursors in deionized water ($Ni(NO_3)_2 \cdot 6\,H_2O$, $Fe(NO_3)_3 \cdot 9\,H_2O$ both Merck, ≥ 99 % and $Rh(NO_3)_3 \cdot x\,H_2O$ by Sigma Aldrich, 36 % Rh content) and 5-8 equivalents of urea (Carl Roth, crystalline, ≥ 99.6 %). The precursors of the bimetallic catalysts were dissolved and precipitated simultaneously. The intended metal loadings and the utilized masses of the chemicals are shown in Table 1.

Table 1: Materials and amounts used for the preparation of the catalysts.

Cat.	**Load. [wt.%]**	**Ni-nitrate [g]**	**Fe-nitrate [g]**	**Rh-nitrate [g]**	**Urea [g]**	**Al_2O_3 [g]**	**V_{H_2O} [mL]**
Chapter 3							
Ni	10	1.001	-	-	1.038	1.800	115
Chapter 7							
Ni	5	1.001	-	-	1.245	3.800	115
Ni_3Fe	5	0.751	0.347	-	1.401	3.800	115
$NiRh_{0.1}$	3.4	0.567	-	0.055	1.227	3.800	115
Chapter 8							
Ni	20	2.002	-	-	2.906	1.600	230
Ni_3Fe	20	1.502	0.695	-	3.270	1.600	230

The desired molar ratio for the bimetallic catalysts were Ni/Fe = 3 and Ni/Rh = 10. Commercial γ-Al_2O_3 support (Alfa Aesar, 1/8" pellets, crushed and calcined at 600 °C (5 K min^{-1}) for 4 h) was added to the solution and the suspension was stirred for 1 h at room temperature at a pH value of 5. The suspension was then heated to 90 °C to hydrolyze urea and stirred under reflux for 18 h (36 h in case of the 17 wt.% Ni_3Fe catalyst) at constant temperature. Afterwards, the suspension was cooled to room temperature and stirred for another hour, resulting in a pH value of 7 - 8. The solid was filtered off, washed with 500 mL deionized water, dried at 110 °C over night and calcined at 500 °C (5 K min^{-1}) for 4 h in static air. To characterize the catalysts in their reduced state, the samples were treated in 50 % H_2/N_2 at 500 °C (5 K min^{-1}) for 2 h and stored under N_2 for the *ex situ* measurements, which were then performed in air.

3.2 Characterization methods

The chemical composition of the catalysts was determined *via* **optical emission spectroscopy with an inductively coupled plasma (ICP-OES)** using an Agilent 720/725 emission spectrometer. For the elemental analysis of the Ni and Ni_3Fe catalysts in chapter 9 the samples were first digested in HCl + H_2SO_4 + H_2O_2 (2:2:1) at 240 °C for 12 h using a Berghof pressure digestion system DAB-2 and then the solution was analyzed using a Perkin Elmer Optima 4300 DV System.

The specific surface area of the catalyst was determined by **N_2 physisorption** at -196°C according to the Brunauer-Emmet-Teller **(BET)** method *via* multi point measurements using a BELSORP-mini II (Rubotherm).

X-ray diffraction (XRD) patterns of the calcined and reduced catalyst powders were recorded *ex situ* on a rotating sample holder using a PANalytical X'Pert PRO diffractometer with Ni-filtered Cu Kα radiation (1.54060 Å) in a range of 2θ = 20 - 80° and a step size of 0.017° (0.51 s per scan step) and. The crystallite size was calculated using the Scherrer equation and LaB_6 was used as standard to correct the experimental signal broadening of the equipment.

Electron microscopy investigations were carried out using the reduced and spent catalyst samples. The powders were directly dispersed on copper grids covered with holey carbon film. The morphology and structure of the catalysts was characterized by high resolution transmission electron microscopy (HRTEM) and high angle annular dark-field (HAADF) scanning transmission electron microscopy (STEM) in a FEI Titan 80-300 microscope operated at 300 kV for the reduced fresh samples and 80 kV for the spent samples, when carbon deposits were investigated (chapter 8). Information about the average composition of the catalysts in large areas or the local composition of the nanoparticles was acquired by STEM coupled with energy-dispersive X-ray spectroscopy (EDX) using a S-UTW EDX detector (EDAX) and electron energy loss spectroscopy (EELS) using a GIF 863 Tridiem energy-filtering spectrometer (Gatan). Quantification analysis of the EDX/EELS spectra, STEM-EDX and STEM-EELS spectrum imaging was carried out by using TEM Image & Analysis (TIA 4.7 SP3 version) software and Gatan DigitalMicrograph (DM, version 1.71). The size of the supported metal nanoparticles was determined using ImageJ software fitting the particles with ellipsoid shapes. The metal dispersion was calculated using the approximation of spherical particles, their mean diameter and element specific data such as the area occupied by surface metal atoms and the volume occupied by metal atoms in the bulk material according to literature.[210]

Temperature-programmed reduction with H_2 (H_2-TPR) was carried out using a Micromeritics AutoChem II 2920 chemisorption analyzer equipped with a thermal conductivity detector (TCD). 100 mg of the catalyst sample (100 – 200 µm sieved fraction) was placed in a U-shaped quartz tube and pretreated at 500 °C (10 K min^{-1}) in 50 mL min^{-1} of 10 % O_2/He followed by the TPR between 40 – 900 °C (10 K min^{-1}) using 50 mL min^{-1} of 10 % H_2/Ar.

Temperature programmed oxidation (TPO) coupled with thermogravimetric analysis and mass spectrometry (TG-MS) was conducted on the spent catalyst samples using a NETZSCH STA 449 F3 *Jupiter* ASC connected to a QMS 403 D *Aëolos*. 20 mg of the samples were heated from 40 to 700 °C (5 K min^{-1}) in 10 % O_2/He (50 mL min^{-1}).

3.3 Catalytic tests

3.3.1 *In situ* cell microreactor

The catalytic performance of the commercial catalyst (chapter 5) was tested in a stainless steel fixed-bed microreactor. The gases were doses by individual mass flow controllers (Bronkhorst) placed on a mobile setup used for *in situ* studies. The microreactor was packed with 50 mg of the calcined catalyst (250 - 500 µm sieved fraction). Before the catalytic tests, the catalyst was reduced *in situ* in the reactor at 450 °C (5 K min^{-1}) for 2 h in 50 % H_2/N_2 and a flow rate of 50 mL min^{-1}. Afterwards it was cooled to 200 °C in N_2 (50 mL min^{-1}). The methanation of CO_2 was carried out in the range between 200 and 500 °C with 50 °C steps. Each temperature was kept for ca. 30 min. All measurements were performed at atmospheric pressure. The ratio of the reaction gases was fixed to $H_2/CO_2 = 4$ diluted in 40 % N_2. A total flow of 40 mL min^{-1} was used resulting in a gas hourly space velocity (GHSV) of 15000 h^{-1} and a weight hourly space velocity (WHSV) of 6000 mL_{CO2} g_{cat}^{-1} h^{-1} calculated as follows:

$$\mathrm{GHSV} = \frac{\dot{\mathrm{V}}(\mathrm{total})}{\mathrm{V}(\mathrm{cat})} \tag{9}$$

$$\mathrm{WHSV} = \frac{\dot{\mathrm{V}}(\mathrm{CO_2})}{\mathrm{m}(\mathrm{cat})} \tag{10}$$

The composition of the feed and the product gas stream was analyzed by a Thermo Scientific C2V-200 micro gas chromatograph (µGC) equipped with a molecular sieve (5 Å) and a QS-BOND column, He as carrier gas and a thermal conductivity detector (TCD).

3.3.2 Tubular fixed-bed reactor

The performance tests and parameter screening of the prepared catalysts (chapter 7 to 9) were performed in the new continuous flow laboratory setup using a stainless steel tubular fixed-bed reactor. The planning and construction of the laboratory setup is described in chapter 4. The catalyst samples (300 – 450 µm sieved fraction) were diluted in SiC (210 µm) and packed into the reactor (exact masses see Table 2). Details and specifications of the laboratory setup and the packing of the reactor are described in chapter 4.

First, the catalyst was reduced *in situ* at 500 °C (10 K min^{-1}) for 2 h in 50 % H_2/N_2. Then the reactor was cooled to 200 °C and the gas atmosphere was switched to $H_2/CO_2 = 4$ in 50 - 75 % N_2. The methanation reaction was performed between 200 and 450 °C in 50 °C steps to determine the optimum reaction conditions. Each temperature was kept for ca. 30 min to obtain stable values in the product analysis.

Table 2: Masses of the catalysts, gas mixtures and total gas flow as well as WHSV and GHSV used for the catalyst tests in the chapters 6 – 8.

Catalytic tests	**m_{cat} [mg]**	**Total flow [mL min^{-1}]**	**Gas mixture**	**WHSV [mL_{CO2} g_{cat}^{-1} h^{-1}]**	**GHSV [h^{-1}]**
Chapter 6	150	600	$H_2/CO_2 = 4$ in 75 % N_2	12000	26700
Chapter 7	300	300	$H_2/CO_2 = 4$ in 50 % N_2	6000	13400
Chapter 8	300	300	$H_2/CO_2 = 4$ in 50 % N_2	6000	13400

Reactant and product gas compositions were analyzed either by a Thermo Scientific C2V-200 micro gas chromatograph (chapter 5 and 6) equipped with a molecular sieve (5 Å) and a QS-BOND column, He as carrier gas and a thermal conductivity detector (TCD) or an INFICON micro gas chromatograph Fusion (chapter 7 to 9) equipped with molecular sieve (5 Å) and Q-BOND columns with Ar or He as carrier gas, respectively, and a TCD. For pressure screening experiments (chapter 9), this procedure was applied

between 1 and 20 bar in 5 bar steps, respectively. Details of the reaction conditions applied in each study are specified in Table 2.

3.3.3 Catalytic tests with methane containing feed

The experiments with CH_4 as additional feed component (chapter 8) were performed with 75 % N_2 to match the reaction conditions applied in the *operando* Raman experiments (section 3.4.3). The resulting GHSV was 26800 h^{-1}, whereas the amount of CO_2 and H_2 and, thus, the WHSV remained the same compared to the screening experiments (6000 $mL_{CO2}\ g_{cat}^{-1}\ h^{-1}$). Further gas mixtures contained 20 % H_2 + 5 % CO_2 + 4 % CH_4 in N_2, 4 % CH_4 in N_2 or 50 % H_2 in N_2 (for reactivation). All applied gas compositions declared as "Phase A-E *lab-scale reactor*" are listed in Table 3. The Thermo Scientific C2V-200 µGC was used for gas analysis.

Table 3: Composition of the gas mixtures applied during experiments in a lab-scale reactor. (reaction conditions: 400 °C, 1 bar, time on stream (TOS) 30 min each phase, except Phase D: 500 °C, 60 min). Reproduced from Mutz *et al.*[211] Copyright © 2018 Published by Elsevier B.V.

Lab-scale reactor	Feed gas composition
Phase A	20 % H_2 + 5 % CO_2 / N_2
Phase B	4 % CH_4 / N_2
Phase C	20 % H_2 + 5 % CO_2 / N_2
Phase D	50 % H_2 / N_2
Phase E	20 % H_2 + 5 % CO_2 / N_2

3.3.4 Long-term stability tests[1]

The kinetic measurements and long-term stability tests described in chapter 9 were carried out in cooperation with Michael Belimov at the Institute for Micro Process

[1] Description taken from Mutz *et al.*:[212] B. Mutz, M. Belimov, W. Wang, P. Sprenger, M.-A. Serrer, D. Wang, P. Pfeifer, W. Kleist, J.-D. Grunwaldt, "Potential of an Alumina-Supported Ni_3Fe Catalyst in the Methanation of CO_2: Impact of Alloy Formation on Activity and Stability", *ACS Catal.* **2017**, *7*, 6802-6814. Copyright © 2017, American Chemical Society.

Engineering (IMVT) at KIT. A microchannel packed bed reactor[213] concept with integrated temperature setting possibility was utilized for long-term stability tests and kinetic measurements. Slit dimensions are 60 x 8 x 1.5 mm^3 (length x width x depth). Compressed air in the range of 100 L min^{-1}, pre-heated to the reaction temperature with an external device, was used as heat transfer medium in 72 x 36 cross-flow microchannels, each 500 µm wide and 230 µm deep. Four axially distributed thermocouples of K-type in the metal housing, close to the packed bed, allowed temperature measurement. The reaction zone was packed with 150 mg (mesh 200 - 300 µm) of catalyst diluted with SiC (mesh 300 - 400 µm). The reactants were dosed *via* MKS mass flow controllers. WHSV values of 80500 $mL_{CO2}\, g_{cat}^{-1}\, h^{-1}$ were adjusted using the gas composition with the initial amount of 9.1 % CO_2, H_2/CO_2 = 4 and the reaction was operated at 6 bar. An industrial catalyst sample with nominal 20 wt.% Ni/Al_2O_3 was used as standard for comparison in the tests under industrially relevant conditions. As it was supplied in tablets, it was crushed and sieved to the desired particle size of 200 - 300 µm. The gas compositions were analyzed using an Agilent online gas chromatograph 7890 including a Pora-Plot Q capillary column and a HP-Plot 5 Å molecular sieve. For detection, thermal conductivity and flame ionization detectors were used.

The mass transport limitations were estimated according to the following criteria. The used values are listed in Table 4. The results and evaluation are further discussed in section 9.4.

Carberry number- External mass transport limitation (according to Ref[214])

$$Ca = \frac{R_{V,CO2}^{obs}}{k_g a_V C_{CO2,b}} < \frac{0.05}{n} \tag{11}$$

Mears criterion- External heat transport limitation (according to Ref[214])

$$\Delta T_{film} = \frac{R_{V,CO2}^{obs}\, |\Delta_R H|\, d_p}{6 a_p} < \frac{0.05 RT}{E_a} \tag{12}$$

Weisz-Prater criterion[215]

$$\Psi = \left(\frac{n+1}{2}\right) \frac{R_{V,CO2}^{obs} \left(\frac{d_p}{6}\right)^2}{D_{CO2,eff} C_{CO2,s}} \tag{13}$$

Effectiveness factor was estimated (according to Ref[216])

$$\eta = \frac{1}{\emptyset} \left(\frac{1}{\tanh(3\emptyset)} - \frac{1}{3\emptyset}\right) \tag{14}$$

Table 4: List of experimental data for estimating the mass transport limitations and effectiveness factor. Reproduced from Mutz *et al.*[212] Copyright © 2017, American Chemical Society.

Variable	Description	Value	SI unit
Ca	Carberry number		
Ψ	Weisz-Prater number		
ΔT_{film}	Temperature difference over film thickness on the catalyst pellet		
T	Temperature	360	°C
p	Pressure	6	bar
x_{CO2}	molar concentration of CO_2	0.09	
x_{H2}	molar concentration of H_2	0.36	
V_{tot}	Total volumetric flow (NTP)	2.2	L min^{-1}
m_{cat}	Catalyst mass	0.15	g
ρ_{cat}	Catalyst density	832	kg_{cat} m^{-3} cat^{-1}
n	Reaction order in CO_2	0.5	
$R_{V,CO2}$	Reaction rate of CO_2 acc. Ref[217]	569.5	mol m_{cat}^{-1} s^{-1}
$k_{g,CO2}$	Ext. mass transfer coeff. of CO_2	0.3738	m s^{-1}
a_V	Specific ext. surface area ($6/d_p$)	2400	m^{-1}
$C_{CO2,b}$	Molar bulk concentration of CO_2	10.36	mol m^{-3}
$\Delta_R H$	Reaction enthalpy	$-1.65 \cdot 10^5$	J mol^{-1}
d_p	Catalyst particle diameter	250	µm
α_p	Particle heat transfer coefficient	1488.8	W m^{-1} K^{-1}

R	Ideal gas constant	8.314	J mol^{-1} K^{-1}
E_a	Activation energy acc. to Ref[217]	82000	J mol^{-1}
$D_{CO2,eff}$	Intraparticle effective diffusion coeff.	$1.1 \cdot 10^{-6}$	m^2 s^{-1}
ε_p	Particle porosity	0.7	
τ_p	Tortuosity	3	
$C_{CO2,s}$	Molar concentration of CO_2 on the catalyst surface	10.36	mol m^{-3}

3.3.5 Calculations of conversion and turnover frequency

Conversion, yield and selectivity were calculated in the catalytic tests as follows:

Conversion: $$X(CO_2) = \left(1 - \frac{CO_{2,out}}{CO_{2,out} + CH_{4,out} + CO_{out}}\right) 100\ \% \quad (15)$$

or including N_2 as internal standard for volume correction:

Conversion: $$X'(CO_2) = \left(1 - \frac{CO_{2,out} \cdot N_{2,in}}{N_{2,out} \cdot CO_{2,in}}\right) \cdot 100\ \% \quad (16)$$

Yield: $$Y(CH_4 \text{ or } CO) = \frac{CH_{4,out} \text{ or } CO_{out}}{CO_{2,out} + CH_{4,out} + CO_{out}} \cdot 100\ \% \quad (17)$$

Selectivity: $$S(CH_4) = \frac{Y(CH_4)}{X(CO_2)} \cdot 100\ \% \quad (18)$$

The turnover frequency (TOF) was calculated as moles of CH_4 produced per moles of surface metal atoms per second using the inlet flow of CO_2, the molar gas volume V(m) and the catalyst mass:

Turnover frequency: $$\mathrm{TOF} = \frac{\dot{V}(CO_2, in) \cdot Y(CH_4)}{V(m) \cdot N(surf) \cdot m(cat)} \quad (19)$$

The number of surface metal atoms N(surf) was estimated using the dispersion from TEM analysis (section 3.2).[210] Hence, all surface metal atoms were assumed to be equally active.

3.4 Spectroscopic studies

The *operando* XAS and Raman spectroscopy studies were performed in a capillary fixed-bed reactor connected to the gas dosing system (similar as described in chapter 4) which was heated by a hot air blower (Oxford GSB-1300). The catalysts (100 – 200 µm sieved fraction) were packed in 1 – 1.5 mm quartz glass capillaries resulting in a catalyst bed of 10 mm in length which was fixed between two quartz wool plugs (Figure 11).[192,218] Gases were analyzed with a Pfeiffer Vacuum ThermoStar™ GSD 320 mass spectrometer equipped with a quartz capillary (or a stainless steel capillary in case of the *operando* Raman spectroscopy experiments) and a C-SEM/Faraday detector.

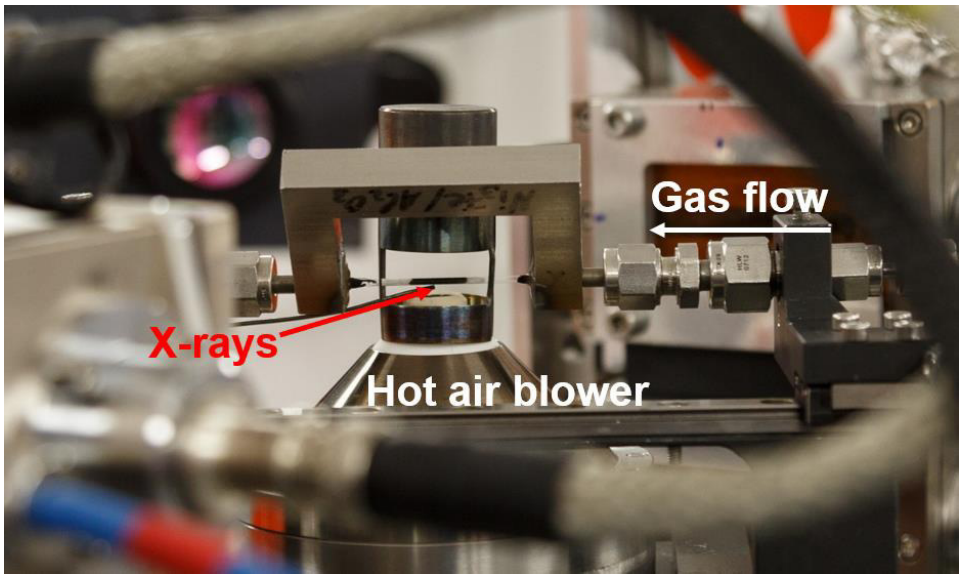

Figure 11: Exemplary image of the setup used for *operando* XAS experiments including a hot air blower and quartz glass capillary connected to the gas dosing system (photo taken by Paul Sprenger (ITCP, KIT)).

3.4.1 X-ray absorption spectroscopy[2]

X-ray absorption spectroscopy experiments (chapter 5 and 6) were performed at the XAS beamline at the ANKA synchrotron radiation source in Karlsruhe, Germany (2.5 GeV ring, 100 – 150 mA). All measurements were carried out in transmission mode at the Ni-K edge at 8333 eV. *Ex situ* XAS measurements (energy range 8200 eV to 9300 eV) were conducted on pressed pellets of the catalyst powder diluted in cellulose and fixed with Kapton tape using an X-ray beam of 1 mm in height and 7 mm in width. For the *in situ* XAS experiment the catalyst was diluted with γ-Al_2O_3 (catalyst/Al_2O_3 = 1:2 for the commercial catalyst and 1:1 for 10 wt.% Ni/Al_2O_3) and packed in a 1 mm quartz glass capillary with a wall thickness of 20 µm.[192] The measurements were carried out with an X-ray beam of 0.75 x 5 mm in size. Different gas mixtures such as 100 % He as inert atmosphere, 15 % H_2/He for activation, 15 % H_2, 3.8 % CO_2 / He (H_2/CO_2 = 4) for the methanation reaction and 3.8 % CO_2/He in the absence of H_2, were used. Details about the applied reaction conditions for the *operando* XAS experiments in chapter 5 and 6 are listed in Table 5.

Table 5: Net weight of the catalysts, gas mixtures and total gas flow as well as WHSV and GHSV used for the *operando* XAS studies in chapter 5 and 6.

Catalytic tests	**m_{cat} [mg]**	**Total flow [mL min^{-1}]**	**Gas mixture**	**WHSV [mL$_{CO2}$ g$_{cat}^{-1}$ h^{-1}]**	**GHSV [h^{-1}]**
Chapter 4	2	60	H_2/CO_2 = 4 in 81 % He	67500	480000
Chapter 5	3	50	H_2/CO_2 = 4 in 81 % He	37500	415000

The data was analyzed by Hudson W.P. Carvalho (ITCP, KIT), who used the Athena and Artemis software of the IFEFFIT package.[220] For the XAS analysis the spectra were energy calibrated using a reference Ni metal foil (Ni K = 8333 eV) and the

[2] Description taken from Mutz *et al.*:[219] B. Mutz, H. W. P. Carvalho, S. Mangold, W. Kleist, J.-D. Grunwaldt, "Methanation of CO_2: Structural response of a Ni-based catalyst under fluctuating reaction conditions unraveled by *operando* spectroscopy", *J. Catal.* **2015**, *327*, 48-53. Copyright © 2015, with permission from Elsevier.

data were normalized. The XANES spectra were fitted by linear combination analysis (LCA) using bulk NiO and the fully reduced Ni catalyst as references. Also references such as $NiCO_3$ and Ni carbide (NiC, Ni_3C) were considered in the data evaluation as possible intermediates during the reaction (see supporting information in the Appendix). The analysis was performed in the energy range from 20 eV in front of and 70 eV after the absorption edge.

Additionally, the EXAFS spectra were background subtracted using the AUTOBKG algorithm in Athena. The k^2-weighted EXAFS functions ($k^2\chi(k)$) were Fourier transformed in the k range of 3.0-12 $Å^{-1}$ (Hanning window sills $\Delta k = 1$ $Å^{-1}$). For EXAFS refinements, structural models were built using the crystal structure for metallic Ni (ICSD reference code 64989) and NiO (ICSD reference code 9866) and calculation of the corresponding backscattering amplitudes and phases by FEFF 6.0.[221] The theoretical data were adjusted to the experimental spectra by a least square method in R space from 1.0 - 3.3 Å for the oxide-like phases and from 1 - 4.5 Å for the metallic phases. The amplitude reduction factors (S_0^2) were determined using metallic Ni foil and NiO bulk reference compounds. Then the coordination numbers (N), bond distances (r), energy alignment between the theory and the experiment (ΔE_0) and mean square deviation of inter atomic distances (σ^2) were refined. The absolute misfit between theory and experiment was expressed by ρ.[222]

3.4.2 Quick EXAFS[3]

In cooperation with Andreas M. Gänzler (ITCP, KIT) quick scanning X-ray absorption spectroscopy (QEXAFS)[224,225] experiments (chapter 7) were performed. The QEXAFS experiments were conducted at the SuperXAS beamline at the Swiss Light Source (SLS) synchrotron facility (Paul Scherrer Institute (PSI), Villigen, Switzerland)

[3] The description is taken from Mutz *et al.*:[223] B. Mutz, A. M. Gänzler, M. Nachtegaal, O. Müller, R. Frahm, W. Kleist, J.-D. Grunwaldt, "Surface Oxidation of Supported Ni Particles and Its Impact on the Catalytic Performance during Dynamically Operated Methanation of CO_2", *Catalysts* **2017**, *7*, 279. Available under the terms and conditions of CC BY 4.0 license (http://creativecommons.org/licenses/by/4.0/), Copyright © 2017.

which operates in top-up mode at 400 mA and 2.4 GeV. The measurements were performed at the Ni K-edge (8333 eV) in transmission mode. The polychromatic X-ray beam was collimated using a Si-coated mirror at 2.5 mrad located in front of the monochromator. The monochromatized beam was focused to a beam size of 200 µm x 200 µm at the sample position using a Rh-coated mirror at 2.5 mrad. A channel-cut Si(111) monochromator oscillating at 22 Hz was used together with N_2-filled gridded ionization chambers both dedicated for fast data acquisition, where a Ni foil was measured simultaneously with the data for absolute energy calibration. In each oscillation of the monochromator, two spectra were recorded, one with increasing energy, another one with decreasing energy. With this system *operando* X-ray absorption spectroscopy data were recorded with 44 spectra s^{-1}.

For the *operando* XAS experiments 5 mg of the 10 wt.% Ni/Al_2O_3 catalyst was diluted with Al_2O_3 (1:1) and placed into a 1.5 mm quartz glass capillary (20 µm wall thickness).[192] Spectra were acquired at the middle of the catalyst bed. The total gas flow was adjusted to 20 mL min^{-1} using similar compositions as in the catalyst screening in the lab-reactor (reduction: 50 % H_2/He, methanation: 25 % reactants ($H_2/CO_2 = 4$) in He). The same WHSV of 12000 $mL_{CO2}\ g_{cat}^{-1}\ h^{-1}$ as during parameter screening was used resulting in a higher GHSV of 71700 h^{-1} due to the different dimensions of the reactor. Fast switches of the gas atmosphere were realized using a microelectric VICI Valco 4-way valve.

The data was analyzed by Andreras M. Gänzler (ITCP, KIT) who used Matlab® routines for merging QEXAFS data, for energy calibration to a metallic Ni foil, for normalization and for conducting LCA. The measurement of 44 spectra s^{-1} allowed detection of changes with a time resolution of 23 ms. However, it was found that a 1 s time resolution was sufficient to monitor the structural changes of the catalyst, and thus, the spectra could be averaged for 1 s each to improve data quality. For the LCA, a linear combination of reference spectra was fitted to the sample spectra in the XANES region (-30 eV to +50 eV). The spectrum of the reduced catalyst in 50 % H_2/He atmosphere and of the oxidized catalyst in 5 % O_2/Ar/He, both acquired at 400 °C, were used as reduced and oxidized reference, respectively (see Figure S 7 in the Appendix). EXAFS data analysis was performed using Athena and Artemis of the IFEFFIT software package[220]

on spectra collected during steady state conditions and on selected spectra during fluctuating operation. In this case 220 spectra were averaged. The theoretical data was adjusted to fit the experimental spectra by a least square method in R space (with k^1, k^2 and k^3-weighted EXAFS functions, R range see supporting information in the Appendix) considering metallic Ni (ICSD: 64989) and NiO (ICSD: 9866). Corresponding backscattering amplitudes and phases were calculated with Feff 6.0[221]. Amplitude reduction factors (S_0^2) were obtained on metallic and NiO bulk references. Coordination number (N), bond distance (R), and energy alignment between theoretical and experimental data (ΔE_0) were refined for each spectrum. The mean square deviation of interatomic distances (σ^2) was obtained by simultaneously refining spectra of the sample in similar conditions and at the same temperature (*cf.* Appendix).

3.4.3 *Ex situ* and *operando* Raman spectroscopy[4]

Microscopic Raman spectroscopy was performed using a Renishaw inVia Reflex Spectrometer System equipped with a frequency doubled Nd:YAG Laser with 100 mW at 532 nm. For all samples, a 20x objective and a grating with 2400 lines mm^{-1} was used and seven individual scans with three accumulations each were averaged. For metal-oxide-bands, the acquisition time for each accumulation was set to 60 s at 10 % laser power in a spectral range of 60 - 1320 cm^{-1}. For carbonaceous species, the acquisition time was set to 300 and 600 s at 0.5 % laser power in a range from 1000 - 2000 cm^{-1}. The data treatment was performed by Paul Sprenger (ITCP, KIT) who used WiRE 4.2 from Renishaw.

Operando Raman spectroscopy (chapter 8) was performed in cooperation with Paul Sprenger (ITCP, KIT). Typically, the data was collected in a spectral range from 960 to 2077 cm^{-1} with a grating of 2400 lines mm^{-1} resolution. For spectroscopic experiments under reaction conditions, 10 mg of the catalyst samples (100 – 200 µm sieved fraction)

[4] The description is adapted from Mutz *et al.*:[211] B. Mutz, P. Sprenger, W. Wang, D. Wang, W. Kleist, J.-D. Grunwaldt, "*Operando* Raman spectroscopy on CO_2 methanation over alumina-supported Ni, Ni_3Fe and $NiRh_{0.1}$ catalysts: Role of carbon formation as possible deactivation pathway", *Appl. Catal. A* **2018**, *556*, 160-171. Copyright © 2018 Published by Elsevier B.V.

were packed in quartz glass capillaries (1.5 mm outer diameter, 0.01 mm wall thickness).[192] The total gas flow was set to 20 mL min^{-1}, resulting in a GHSV = 69800 h^{-1}, which was higher compared to the experiments in the laboratory reactor in section 3.3.3 due to the different reactor geometry. The WHSV of 6000 mL_{CO2} g_{cat}^{-1} h^{-1} remained similar to the catalytic tests in the lab-scale reactor (section 3.3.3). The gas mixtures and the sequences of the *operando* Raman experiments are listed in Table 6. The denotation of the phases is in correlation with the experiments performed in the lab-scale reactor to construct the link between the experiments. A microelectric VICI Valco 4-way valve allowed fast switches of the gas atmospheres.

The laser beam for Raman spectroscopy was focused on the catalyst bed *via* Renishaw's video fibre optics probe (Figure 12) with a long distance objective with a focal length of 70 mm. The laser spot size on the catalyst bed was approximately 70 µm in diameter. Raman spectra were recorded continuously at an effective laser power of 2 mW with 60 s acquisition time per individual spectrum. The data treatment was performed with WiRE 4.2 from Renishaw.

Table 6: Composition of the gas mixtures applied during the *operando* Raman spectroscopy experiments. (reaction conditions: 370 °C, 1 bar, time on stream (TOS) 30 min each phase/modulation, except Phase D: 510 °C, 60 min). Reproduced from Mutz *et al.*[211] Copyright © 2018 Published by Elsevier B.V.

Spectroscopic microreactor	**Gas composition**
Phase A	20 % H_2 + 5 % CO_2 / He
Methanation of CO_2 containing CH_4	20 % H_2 + 5 % CO_2 4 % CH_4 / He
Phase B	4 % CH_4 / He
Modulation 1	5 % CO_2 / He ↔ 4 % CH_4 / He
Modulation 2	20 % H_2 / He ↔ 4 % CH_4 / He
Modulation 3	20 % H_2 + 5 % CO_2 / He ↔ 4 % CH_4 / He
Phase C	20 % H_2 + 5 % CO_2 / He
Phase D	50 % H_2 / He
Phase E	20 % H_2 + 5 % CO_2 / He

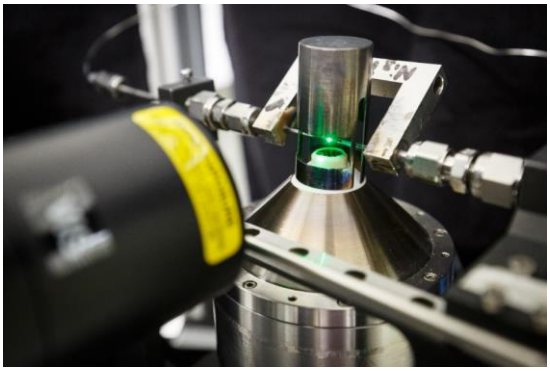

Figure 12: Image of the setup used for *operando* Raman spectroscopy experiments including a hot air blower and quartz glass capillary (*spectroscopic microreactor*) connected to the gas dosing system (photo taken by Paul Sprenger (ITCP, KIT)).

4 Design and construction of a laboratory setup

A continuous flow laboratory setup designed for catalyst screening and dynamic reaction conditions in the methanation of CO_2 was planned and built-up. Fast online analytics and a microelectric valve allowed the application and monitoring of the reaction under dynamic reaction conditions. The spent catalysts were easily recoverable from the reactor for characterization. This setup was applied for the catalytic tests described in the chapters 6 to 9 (except the long-term test). The piping and instrumentation diagram (P&ID) is shown in Figure 13 and a picture of the setup in operation is presented in Figure 14.

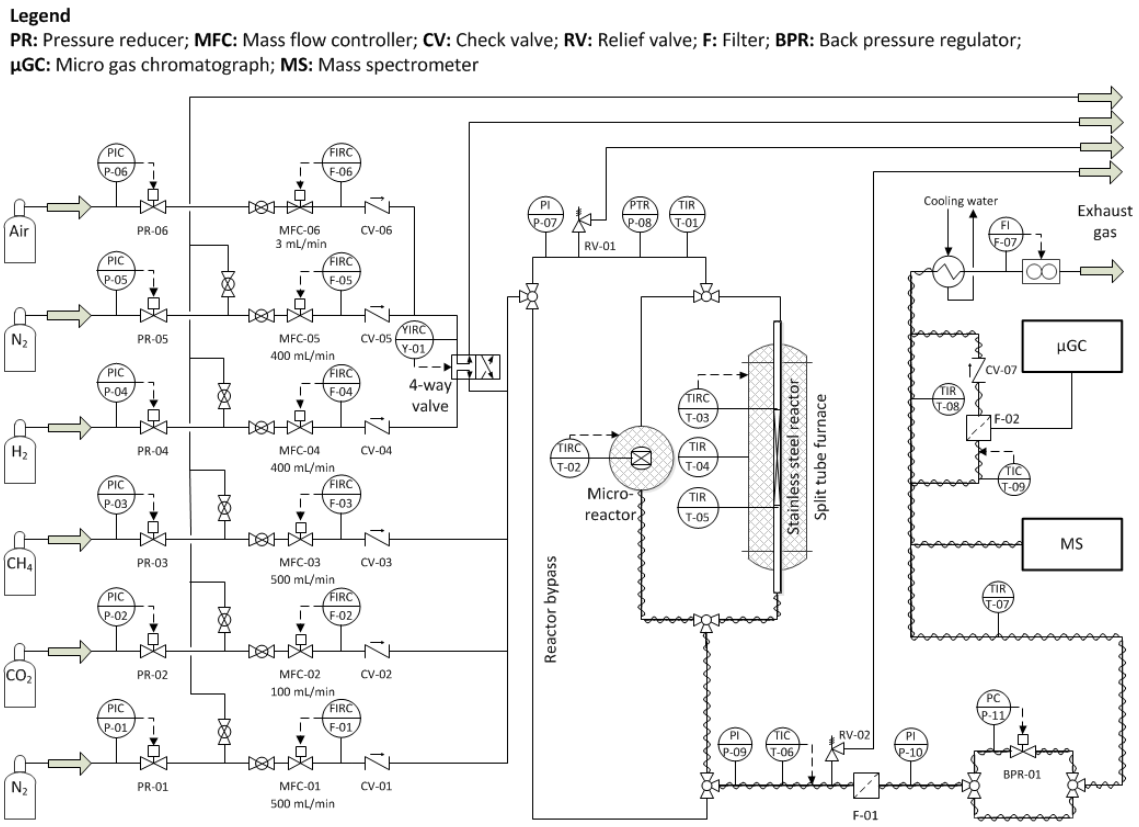

Figure 13: Piping and instrumentation diagram (P&ID) of the laboratory plant for the methanation of CO_2.

The gases N_2, H_2, CO_2 as well as CH_4 and air can be dosed and adjusted by six individual mass flow controllers (Bronkhorst, MFC F-01-06 in the P&ID). Expansion of the model gas composition in the methanation of CO_2 is possible. H_2 and N_2 are connected to a VICI Valco microelectric 4-port 2-position valve and, thus, can be substituted with each other to simulate fast H_2 dropouts during the reaction. An additional air pipe is connected to the valve to oxidize the catalyst. To avoid mixing of H_2 and O_2, air can only be fed to the reactor when H_2 is absent from the stream by using the exhaust position of the 4-way valve.

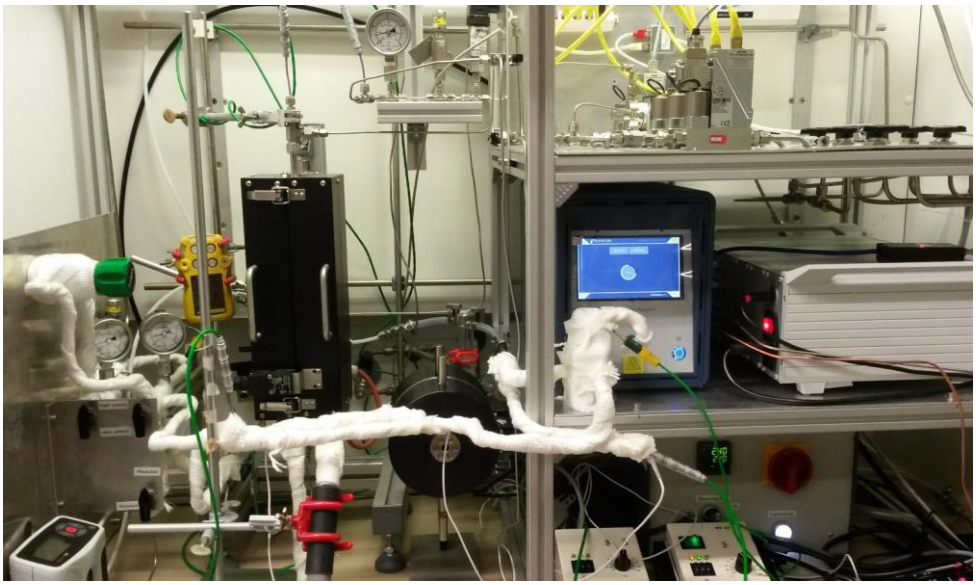

Figure 14: Picture of the laboratory setup for the methanation of CO_2.

The gases are mixed and can be either fed into the reactor in down-flow position or guided through the bypass to adjust the feed gas composition. The catalytic reaction is performed in a stainless steel tubular fixed-bed reactor (L_r = 410 mm; d_o = 3/8 “, d_i = 7 mm, Figure 15). The reactor is packed with catalyst particles with a grain size (d_p) of 300 – 450 µm which are diluted in SiC (Carborundum, VWR Chemicals) with a grain size of 210 µm as inert material to reduce local overheating effects from the exothermic reaction (in combination with the dilution of the reaction gases with inert gas). In general, the degree of catalyst dilution is 2 - 5 which should not result in an irregular distribution

or channeling effects.[226] Applying those conditions, a $5d_i$-sized catalyst bed is obtained (Figure 15). The bed length (L_b = 35 mm) is 80 – 120-fold larger than d_p, which fulfills the criteria $L_b/d_p > 50$ to avoid axial dispersion of the reaction gases along the catalyst bed.[227] Radial concentration gradients and wall effects can be excluded since the ratio of d_i/d_p is 16 – 23 and fulfills the criteria $d_i/d_p > 10$.[216,226,228]

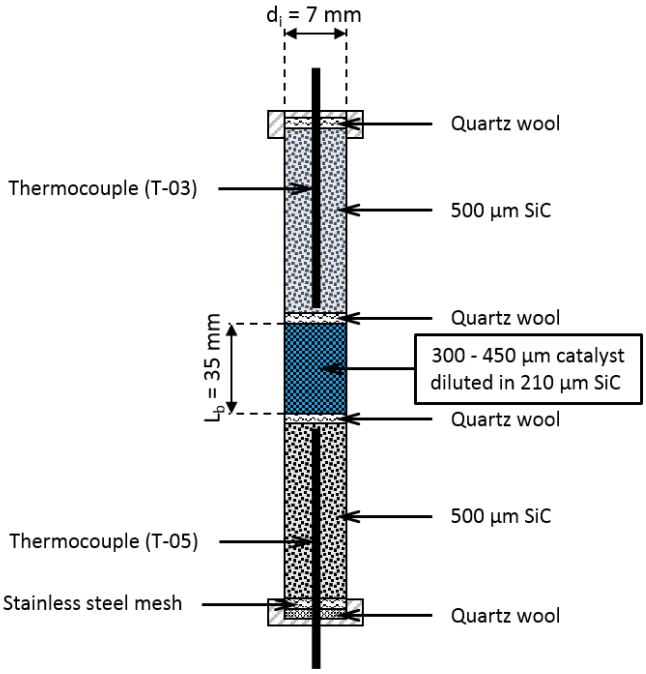

Figure 15: Scheme of the packed tubular reactor used for the methanation of CO_2.

The different grain sizes of the catalyst material and SiC enable an easy recovery of the catalyst by sieving for characterization of the used catalyst after the reaction. The spare void of the reactor is filled with SiC (Carborundum, VRW Chemicals, 500 µm) for optimal gas mixing and to minimize the dead volume. The various packing zones are separated with quartz wool. The temperature inside the reactor can be monitored with two K-type thermocouples (T-03 and T-05 in the P&ID) placed in front and behind the catalyst bed.

The reactor is heated by a custom-made split-tube oven (HTM Reetz, LK type oven). The inner diameter of the oven is fitted to the outer reactor diameter and features

a temperature constant zone of 50 mm within a heated length of 280 mm. The temperature can be regulated by an Eurotherm 2416 PID controller and the thermocouple in front of the catalyst bed inside the reactor (T-03). The oven temperature is monitored by an additional thermocouple (T-04) in the middle of the oven. In parallel to the tubular fixed-bed reactor, a stainless steel microreactor can be connected, which can be used for *operando* XAS studies at elevated pressures. It is heated by an appropriate split furnace regulated with a PMA – KS 20 temperature controller and a K-type thermocouple placed in the wall of the reactor.

The pressure in the reactors can be adjusted by a back-pressure regulator (Swagelok, KBP series). All pipes and instruments down-flow of the reactor outlet are heated to 120 – 150 °C with heating wires (Horst) controlled by Horst HT 30 and HT 31 temperature controllers and K-type thermocouples (T-06 and T-09 in the P&ID) to avoid water condensation.

Quantitative gas analysis can be performed using a micro gas chromatograph (µGC). The gas compositions in the experiments can be analyzed using either a Thermo Scientific C2V-200 µGC equipped with a molecular sieve (5 Å) and a QS-BOND column with He as carrier gas and a thermal conductivity detector (TCD) or an INFICON Fusion µGC equipped with molecular sieve (5 Å) and Q-BOND columns with Ar and He carrier gas, respectively, and a TCD. Fast gas analysis in only 130 s was possible using the INFICON µGC, which was crucial for experiments under dynamic reaction conditions. In addition to the quantitative gas analysis *via* µGC real-time monitoring of the gas composition is realized with a Pfeiffer Vacuum ThermoStar^{TM} GSD 320 mass spectrometer equipped with a quartz capillary and a C-SEM/Faraday detector.

Full remote control of the laboratory plant is possible. The position of the 4-way valve and the temperature of the reactor can be controlled and recorded by LabView programs. Temperature and pressure are recorded with an in-house built Data Logger and a separate LabView program. Specifications of the laboratory setup are listed in Table 7. Gas hourly space velocity (GHSV) concerning total gas flow and volume of the catalyst bed and weight hourly space velocity (WHSV) concerning gas flow of CO_2 and catalyst mass were calculated according to (9) and (10), see section 3.3.

Table 7: Specification of the laboratory setup designed for catalyst screening in the methanation of CO_2.

Temperature	Tested up to 550 °C ($T_{max, oven}$: 1000 °C)
Pressure	Up to 20 bar
Gas flow (N_2)	10 - 500 mL min^{-1}
Gas flow (H_2)	8 - 400 mL min^{-1}
Gas flow (CO_2)	2 - 100 mL min^{-1}
Gas flow (CH_4)	10 - 500 mL min^{-1}
Gas flow (Air)	0.06 - 3 mL min^{-1}
Catalyst mass	80 - 1000 mg
GHSV	1000 - 40000 h^{-1}
WHSV	120 - 75000 mL_{CO2} g_{cat}^{-1} h^{-1}

5 Hydrogen dropout during the methanation of carbon dioxide[1]

5.1 Introduction

One of the main challenges for the future electrical power supply from renewable resources like wind and sunlight concerns the long-term storage of renewable energy to balance its seasonal supply. However, considering the fluctuating supply of renewable H_2, investigations under fast load changes with focus on the catalyst structure and its behavior are required to get information about morphology changes of the Ni particles and deactivation processes due to stress and strain of the catalyst.

The study in this chapter aims at the understanding of structural changes occurring in the system when changing the hydrogen supply. Such studies need to be conducted under *operando* conditions[183-186] since Ni is known to be very prone to oxidation even at room temperature. Moreover, supported nanoparticles are known to be very dynamic (*e.g.* Refs[38,165-167]). In this chapter, we thus give a first insight into structural changes that occur when a commercial Ni-based catalyst is exposed to changing reaction atmospheres using *operando* XAS and to demonstrate the importance of such studies for catalysts under dynamic reaction atmospheres.

5.2 Catalyst characteristics

The commercial catalyst consisted of 23 wt.% Ni on Al_2O_3, promoted with 5 wt.% CaO and exhibited a specific surface area of 170 $m^2\ g^{-1}$. The XRD pattern (Figure 16) of the calcined sample showed reflections of NiO planes at 2Θ = 37.3° (111), 43.3° (200),

[1] The text and figures of this chapter are taken from Mutz *et al.*:[219] B. Mutz, H. W. P. Carvalho, S. Mangold, W. Kleist, J.-D. Grunwaldt, "Methanation of CO_2: Structural response of a Ni-based catalyst under fluctuating reaction conditions unraveled by *operando* spectroscopy", *J. Catal.* **2015**, *327*, 48-53. Copyright © 2015 Published by Elsevier Inc.

62.9° (220), and 75.4° (311). Using the Scherrer equation and the reflection of the (200) plane a crystallite size of 9 nm was estimated. Reduction tests at different temperatures revealed a full reduction of the catalyst at 450 °C (5 K min^{-1}) in 50 % H_2/N_2 for 2 h (afterwards cooled in N_2). New reflections of metallic Ni at 2Θ = 44.5° (111), 51.9° (200) and 76.4° (220) were observed. The isolated Ni reflection at 51.9° was used for estimation of the crystallite size resulting in a size of about 8 nm.

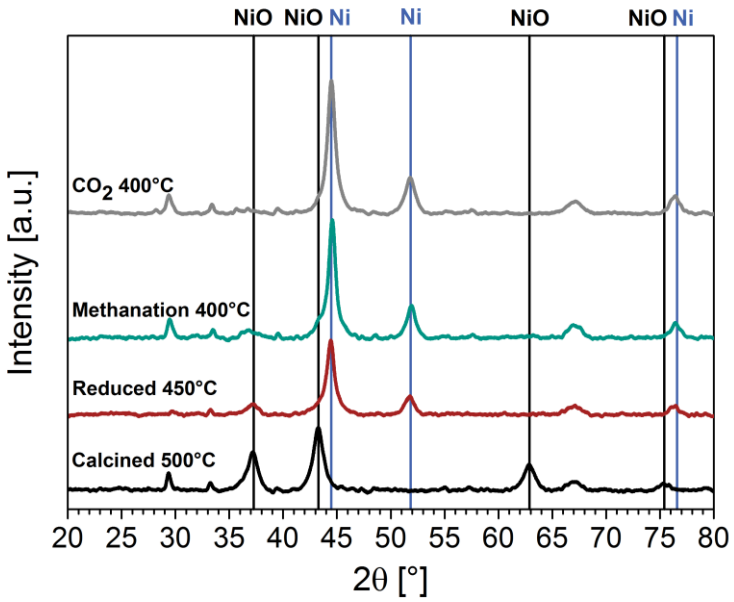

Figure 16: XRD pattern of the commercial 23 wt.% Ni/CaO-Al_2O_3 catalyst at different conditions: calcined (black, 500 °C, 5 K min^{-1}, 4 h in air), reduced (red, 450 °C, 5 K min^{-1}, 2 h in 50 % H_2/N_2), after the methanation of CO_2 (green, 400 °C, 1 h, H_2/CO_2 = 4, 40 % N_2) and treated in CO_2 (grey, 400 °C, 3 h, 17 % CO_2/N_2); the latter two experiments each after reduction. Unmarked reflexes belong to $CaCO_3$ (2Θ = 29.4° and 39.4°), CaO (2Θ = 37.4°) and Al_2O_3 (2Θ = 33.2° and 67.3°). Crystallite size was estimated using the Scherrer equation (reduced sample: Ni (111) at 2Θ = 44,5°) and Ni (200) at 2Θ = 51.9° result in 8 nm; sample after methanation: FWHM of Ni (200) results in 9 nm). Reproduced from Mutz *et al.*[219] Copyright © 2015, with permission from Elsevier.

The XRD pattern of a catalyst after the methanation reaction (400 °C, 1 h, cooled in N_2) revealed only a negligible increase of the crystallite size (9 nm, (200) plane) and a partial oxidation to NiO indicated by the shoulder in the NiO region at 43.3°. Also Du *et al.*[67] observed for a Ni/MCM-41 catalyst that the particle size remained rather similar even after harsh reaction conditions and that Ni was slightly oxidized. Moreover, Bando

et al.[205,206] showed that Rh particles were very dynamic during methanation. Furthermore, no reflections due to crystalline phases of NiC or Ni_3C were observed in the XRD patterns, which is in line with Ocampo *et al.*[93] and with the fact that the presence of CO_2 and the formed water prevent carbon/carbide formation. Also $NiCO_3$ was not observed by X-ray diffraction analysis. The other unmarked signals in Figure 16 can be assigned to $CaCO_3$ ($2\Theta = 29.4°$ and 39.4°), CaO ($2\Theta = 37.4°$) and Al_2O_3 ($2\Theta = 33.2°$ and 67.3°). $CaCO_3$ is present after calcination at 500 °C and is converted to CaO during H_2 treatment. After introducing CO_2, $CaCO_3$ is formed again. Especially after CO_2 treatment of the catalyst, CaO is converted completely to $CaCO_3$. The small signal around 37° after methanation could be either CaO or NiO. The Al_2O_3 support did not change at any conditions, so the reflexes at 33.2° and 67.3° are present in all diffractograms.

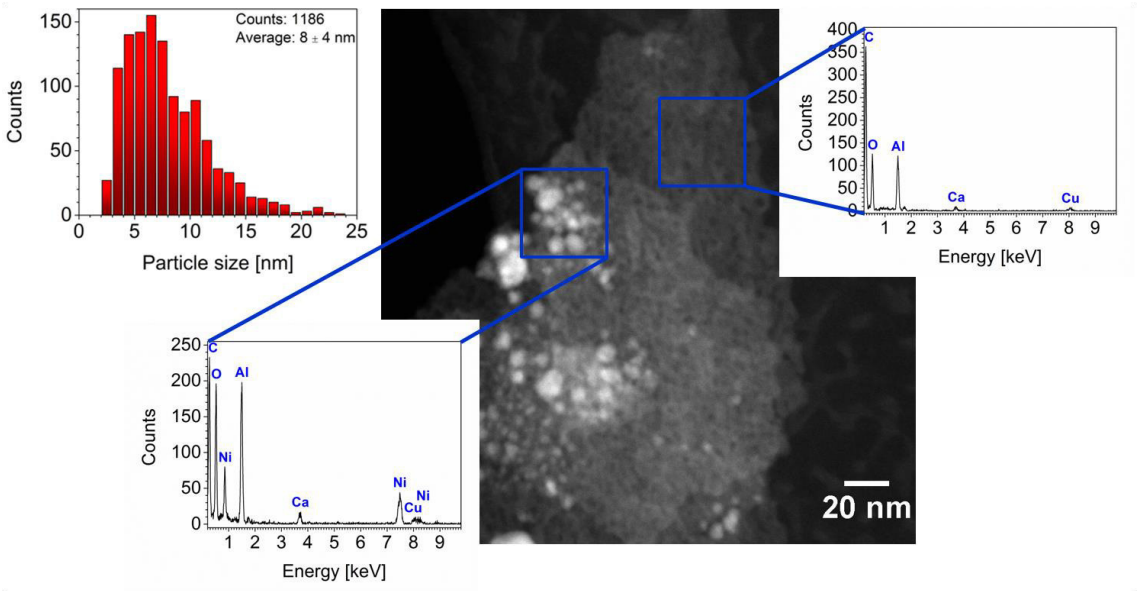

Figure 17: STEM-HAADF image of the reduced commercial 23 wt.% Ni/CaO-Al_2O_3 catalyst and Ni particle size distribution after fitting 1185 particles assuming an ellipsoidal shape of the particles. Bright regions are related to Ni particles, identified with EDX. C and Cu signals belong to the TEM grid. Reproduced from Mutz *et al.*[219] Copyright © 2015, with permission from Elsevier.

For further information on the Ni particle size and distribution STEM images in HAADF mode were recorded (Figure 17), which revealed a rather low and inhomogeneous dispersion of Ni on the support. The images were evaluated redrawing

and admeasuring 1185 Ni particles to get a representative statistical size distribution. The results showed a broad particle size distribution (2 – 20 nm) and an average particle size of 8 ± 4 nm. The dispersion of the Ni particles was calculated to ca. 9 % implying a high fraction of bulk nickel. Ca-species were homogeneously distributed over the support as unraveled by EDX.

5.3 Catalytic activity

The catalytic activity was tested in the temperature range 200 – 500 °C by analyzing the gas phase composition for 30 min at each temperature. The results are summarized in Figure 18.

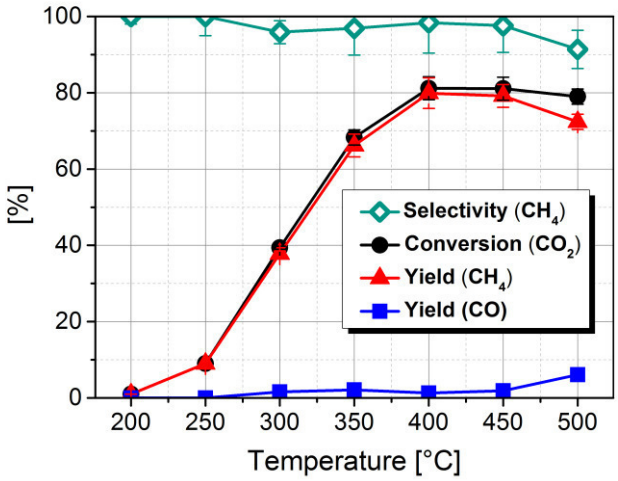

Figure 18: Methanation of CO_2 using a commercial 23 wt.% Ni/CaO-Al_2O_3 catalyst (50 mg) at T = 200 – 500 °C performed in a stainless steel microreactor (H_2/CO_2 = 4 in 40 % N_2, WHSV = 6000 $mL_{CO2}\ g_{cat}^{-1}\ h^{-1}$ GHSV = 15000 h^{-1}). Reproduced from Mutz *et al.*[219] Copyright © 2015, with permission from Elsevier.

High selectivity towards CH_4 was achieved and beside CO no other carbon containing byproducts, like ethane, butane or methanol, were detected. Since the equations (15) and (16) provided the same results we assume there was no carbon loss

during the reaction. The catalyst was already active at 200 °C converting 1 % CO_2 into CH_4. Conversion of CO_2 increased constantly with rising temperature to a maximum value of 81 % at 400 °C resulting in a CH_4 yield of 80 % and a selectivity of 99 %. Further increase of the temperature to 500 °C resulted in higher CO yields due to the endothermic reverse water gas shift reaction which is favored at these temperatures.[53] The TOF was calculated considering the surface Ni atoms estimated by the 9 % dispersion calculated from the STEM evaluation and amounted to 0.02 s^{-1} at 250 °C (9 % CO_2 conversion with > 99 % selectivity towards CH_4). This rate is comparable to the TOFs reported in literature,[61,229] even though lower temperatures have been applied in the present study.

5.4 *Ex situ* XAS evaluation

Catalysts in calcined and pre-reduced (fully reduced, exposed to air for about 3 days) state were studied *ex situ* by XAS for structural investigations of the Ni particles. The amplitude of Fourier transformed EXAFS was similar to the bulk NiO for the calcined catalyst (Figure 19). Likewise, distances and number of neighbors (see Table S 1 in the Appendix for the results of the EXAFS analysis) were equal to those obtained for bulk NiO. However, the larger refined σ^2 suggested that the mean square deviation of the bond lengths were slightly larger for the calcined catalyst than for the bulk NiO, which might be a result of the smaller particle size. Linear combination analysis of the XANES spectrum of the pre-reduced catalyst (Figure 20) showed that it was partially oxidized after air exposure (preparation of the pellets) resulting in a mixture of 35 % NiO and 65 % metallic Ni. The *ex situ* EXAFS data showed a lower coordination number for the first Ni coordination shell than reported for bulk materials (Table S 1). Nevertheless, the EXAFS signal is an average of all Ni absorbers and therefore the coordination number for the pre-reduced pellet must be corrected.

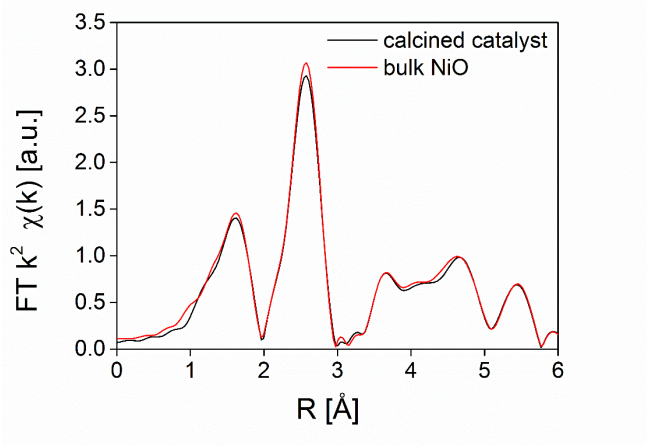

Figure 19: k^2-weigthed Fourier transformed EXAFS spectra of the calcined catalyst (black) measured *ex situ* as pressed pellets and a NiO reference sample (red). Reproduced from Mutz *et al.*[219] Copyright © 2015, with permission from Elsevier.

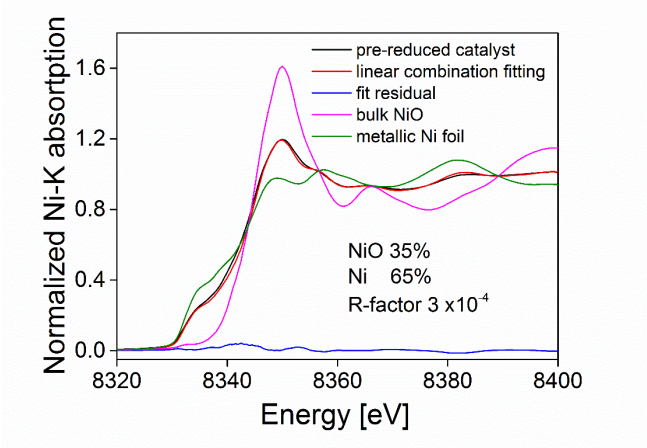

Figure 20: XANES spectra of the pre-reduced catalyst in black, metallic Ni (green) and NiO (purple) references. Additionally, the result of the linear combination analysis (red) and the fit residual (blue) is shown. Reproduced from Mutz *et al.*[219] Copyright © 2015, with permission from Elsevier.

In summary, XANES and EXAFS indicated a mixture of remaining metallic Ni and newly formed NiO phases after air exposure. Moreover, the spectra demonstrated that the catalyst can undergo changes when it is removed from the reactor. Hence, realistic information on the catalyst structure under dynamic working conditions can only be gained using *operando* spectroscopy.[183-186]

5.5 *Operando* XAS studies

Figure 21 presents the fraction of the reduced Ni determined by LCA of the XANES spectra (shown in Figure 22 a)) and the formation of CH_4, both recorded under *operando* conditions. The pre-reduced catalyst (65 % Ni, 35 % NiO) was activated by treatment in a 15 % H_2/He stream at 500 °C (10 K min^{-1}) for 30 min (step 1 in Figure 21). Reduced Ni was identified by decreasing white line and increasing pre-edge peak in Figure 22 a).[67,230] The EXAFS spectrum (Figure 22 b)) recorded in reducing atmosphere after cooling to room temperature showed that the oxide phase was completely reduced and the coordination number for Ni in the first shell increased to 8 ± 1 atoms (details in the Appendix, Table S 1).

After the activation (still at room temperature) the reaction atmosphere was switched to 15 % H_2, 3.8 % CO_2 / He ($H_2/CO_2 = 4$) and heated again to 400 °C (10 K min^{-1}; step 2 in Figure 21). At lower temperatures, a slight oxidation occurred on the Ni surface. Similar to the results in Figure 18, CH_4 formation started around 250 °C during the *operando* spectroscopic measurements. As the temperature increased the catalyst became again fully reduced and remained in this state while producing CH_4 at 400 °C (conditioned during ca. 50 min). During the first methanation cycle the coordination number was slightly decreased compared to the freshly reduced catalyst, probably due to adsorption or incorporation of oxygen. However, the contribution of oxygen in the EXAFS was too small to be analyzed. Although oxygen containing species might be adsorbed during the reaction, these processes might be too dynamic and too fast to monitor with XAS in this experiment. Considering further compounds such as $NiCO_3$ to the data treatment, no improvement of the fits were achieved and bulk carbonates can therefore be ruled out as possible component formed during the experiment (details see Appendix). This does not exclude the formation of surface carbonates. Carbon deposition and the formation of Ni carbides was not considered due to studies in literature[53,93] reporting that this is negligible for the methanation of CO_2. To finally rule out the formation of Ni carbides, we simulated corresponding spectra and performed linear combination fits and target transformations which did not give any indication of such a phase. Finally, principle component analysis indicated that mainly two components are present in the partly oxidized samples (details see Appendix).

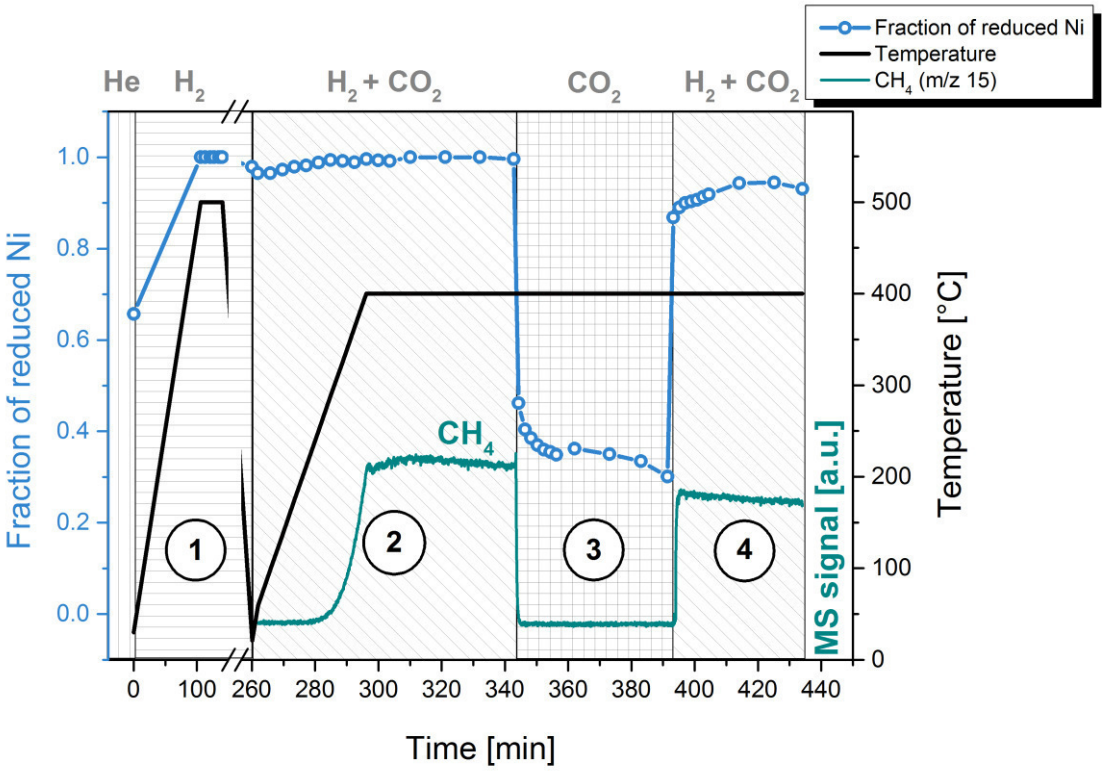

Figure 21: *Operando* XAS experiment during methanation of CO_2 over pre-reduced 23 wt.% Ni/CaO-Al_2O_3 catalyst (100 – 200 µm sieved fraction, diluted with 2x γ-Al_2O_3) conducted in a quartz glass capillary with on-line gas analysis under changing reaction conditions. The plot shows the fraction of metallic Ni from linear combination analysis of the XANES spectra, the temperature and the MS signal of the produced CH_4. The particular reaction atmospheres are shaded accordingly. Step 1 (H_2): complete reduction of the pre-reduced catalyst at 500 °C under 15 % H_2/He (60 mL min^{-1}, GHSV = 480000 h^{-1}) followed by cooling to room temperature. Step 2 (H_2 + CO_2): addition of CO_2, heating to 400 °C (10 K min^{-1}) and holding the temperature for ca. 50 min. Step 3 (CO_2): switching to 3.8 % CO_2/He and holding for ca. 50 min. Step 4 (H_2 + CO_2): adding again H_2 and holding for ca. 50 min. Reproduced from Mutz *et al.*[219] Copyright © 2015, with permission from Elsevier.

Removal of H_2 from the gas stream (step 3 in Figure 21) resulted in an immediate termination of the CH_4 formation, which was also reported by Aldana *et al.*[95], due to the poor H_2 storage capacity of the catalyst (full MS data is shown in Figure S 2 in the Appendix). Additionally, XANES data proved a fast oxidation (54 % oxidized fraction) in the less reducing atmosphere which might be caused by CO_2 or traces of oxygen or water in the system, respectively. Note that the used CO_2 had a background of O_2. In the following 50 min, the oxidation continued slowly reaching 70 % of NiO, probably due to diffusion of oxygen into the core of the particles. The EXAFS refined Ni-O coordination

number agreed with the fraction of oxidized Ni determined by XANES. Additionally, the bond length was close to that determined for the NiO reference, therefore hinting at the formation of a NiO-like phase. Obviously, oxidation of Ni occurred after removal of H_2 from the gas stream. The dynamic change of the gas composition under reaction conditions leads to a significantly higher fraction of oxidized Ni than the oxidation under ambient conditions (35 % oxidation, see section 5.4). The corrected coordination number for the metallic Ni phase decreased to 5 ± 2, whereas the Ni-Ni bond length increased by 0.05 Å compared to the freshly reduced catalyst. Further analysis and comparison is given in the Appendix (Figure S 3 b), Table S 1 and Figure S 4).

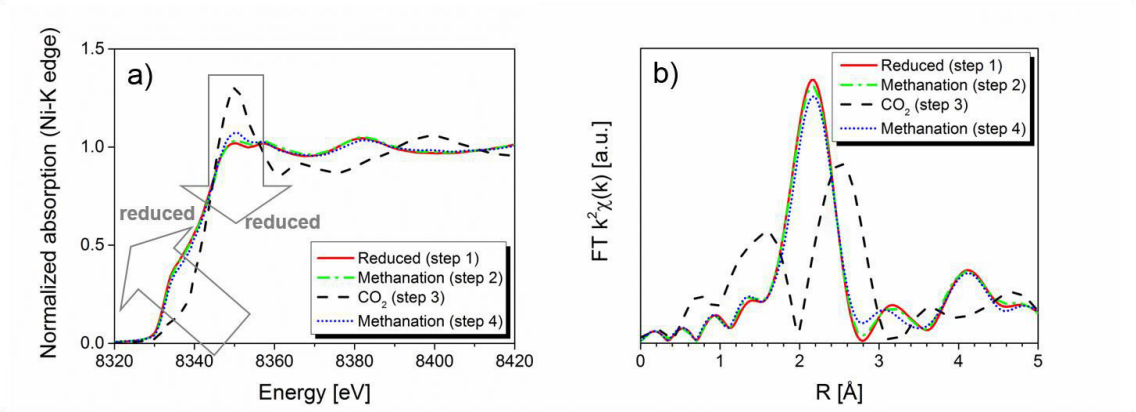

Figure 22: a) Evolution of the Ni K-absorption edge in the XANES spectra and b) corresponding Fourier transformed EXAFS spectra of Ni traced under dynamic atmospheric conditions. The XANES threshold intensity and position was used to evaluate the oxidation state of Ni. The main peak in the EXAFS around 2 Å corresponds to the Ni-Ni first coordination shell of metallic Ni phase, whereas the two mains peaks at 1.5 Å and 2.5 Å (in CO_2) are associated to the first (Ni-O) and second (Ni-Ni) coordination shell of a NiO-like phase, respectively. Reproduced from Mutz *et al.*[219] Copyright © 2015, with permission from Elsevier.

When H_2 was again added to the gas stream (step 4 in Figure 21), CH_4 formation resumed instantaneously and the reduced fraction increased abruptly, reaching 94 % of metallic Ni within 20 min after switching the reaction atmosphere. Although the gas analysis proved a high CH_4 yield in the second methanation cycle, the value did not reach the same level as in the first methanation step. Whereas the Fourier transformed EXAFS spectra looked similar (Figure 22 b)) (also EXAFS analysis, see Figure S 4), the XANES spectra remained different with a slightly higher whiteline (Figure 22 a)) in line with the

6 % fraction oxidized Ni found by LCA. Furthermore, the formation of CH_4 seems to decrease gradually as a function of time which is explained in literature by sintering.[93] However, no significant change in this regard was observed here (Figure S 4). Hence, dropout of H_2 in the methanation reaction seems to provoke catalyst oxidation under dynamic conditions, thus requiring an efficient reactivation step to reach the initial value of the CH_4 yield in the second cycle.

5.6 Conclusions

In this chapter, the methanation of CO_2 was studied under both steady state and dynamic reaction conditions using a commercial Ni-based catalyst for a fist attempt. At 400 °C the methanation reaction reached 81 % CO_2 conversion and a selectivity of 99 % towards CH_4, which is – as well as the obtained TOF of 0.02 s^{-1} at 250 °C – comparable to other Ni-based catalysts reported in literature. XRD analysis as well as EXAFS evaluation revealed only a negligible increase of the Ni particle size. However, strong structural changes were found for this standard catalyst under dynamic reaction conditions. *Operando* XAS showed that a fast bulk-like oxidation of the Ni particles occurred immediately after removal of H_2 from the gas stream. In the following methanation step a lower catalytic performance was observed due to residuals of partly oxidized Ni, indicating that an efficient reactivation step is necessary after a H_2 dropout to return to the initial activity. These results are important for methanation applications operated in industrially scale, where the fluctuating supply of renewable H_2 has to be considered. Consequently, oxidation of the catalyst has to be prevented or efficient reactivation procedures need to be developed. Further investigations of the bulk-

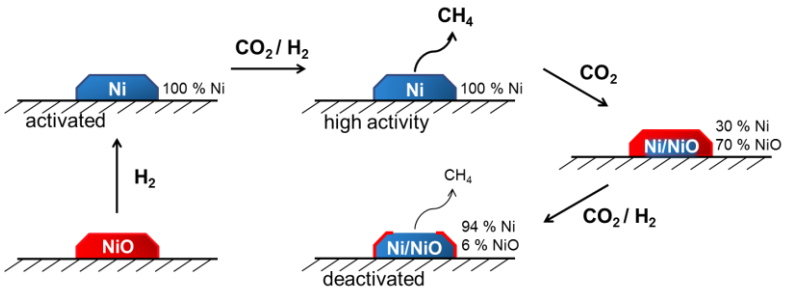

Scheme 1: Illustration of the oxidation/reduction effects of the Ni particles occurred under dynamic conditions. Reproduced from Mutz *et al.*[219] Copyright © 2015, with permission from Elsevier.

like oxidation are required with next generation catalysts and using highly time-resolved *operando* techniques to monitor the mechanistic steps of deactivation. These first results on Ni catalysts on methanation reactions under changing reaction atmosphere demonstrate that catalysts need to be studied under dynamic conditions in heterogeneous catalysis, that have received reasonable attention for the storage of electrical energy under fluctuating conditions.

6 Effect of repetitive hydrogen interruptions and reactivation[1]

6.1 Introduction

The methanation of CO_2 to produce a chemical energy carrier needs to withstand fluctuations in the H_2 feed, which is produced by water splitting using renewable energies from wind and sunlight. In the previous chapter *operando* XAS was used to investigate the catalyst's response during a H_2 dropout in the methanation of technical CO_2. It was observed that a fast bulk oxidation of the Ni particles occurred after removal of H_2 from the feed gas.[219] In this work we present an extended experiment on the basis of the results from chapter 5 revealing the effects of cycling and a reactivation step on the catalyst. For a more detailed insight into the structural changes of the catalyst, the preparation of a model catalyst was developed and optimized to obtain uniformly sized Ni particles. Inbound characterization using XRD, STEM, XAS and H_2-TPR as well as the test of the catalytic performance in a newly designed laboratory setup show the capability of the catalyst for the structural investigations under dynamic reaction conditions with *operando* XAS.

[1] The text and figures of the sections 6.2 and 6.3 are taken from Mutz *et al.*:[223] B. Mutz, A. M. Gänzler, M. Nachtegaal, O. Müller, R. Frahm, W. Kleist, J.-D. Grunwaldt, "Surface Oxidation of Supported Ni Particles and Its Impact on the Catalytic Performance during Dynamically Operated Methanation of CO_2", *Catalysts* **2017**, *7*, 279. Available under the terms and conditions of the Creative Commons Attribution 4.0 license (CC BY 4.0, http://creativecommons.org/licenses/by/4.0/), Copyright © 2017.

The text and figures of section 6.4 are taken from Mutz *et al.*:[231] B. Mutz, H. W. P. Carvalho, W. Kleist, J.-D. Grunwaldt, "Dynamic transformation of small Ni particles during methanation of CO_2 under fluctuating reaction conditions monitored by *operando* X-ray absorption spectroscopy", *J. Phys.: Conf. Ser.* **2016**, *712*, 012050. Available under the terms of the Creative Commons Attribution 3.0 license (CC BY 3.0, https://creativecommons.org/licenses/by/3.0/), Copyright © 2016.

6.2 Catalyst characterization

A catalyst featuring uniform and rather small Ni particles was essential to determine the structural changes of the Ni particles during dynamically operated methanation. Homogeneous deposition-precipitation[207-209] method was chosen to obtain a Ni/Al_2O_3 catalyst with these properties. Elemental analysis using ICP-OES confirmed a catalyst loading of 10 wt.% Ni/Al_2O_3. The specific surface area of the catalyst was 200 m^2 g^{-1} and the mean pore diameter was 11 nm. XRD was not suitable to analyze the catalyst, since the Ni and NiO reflections were either superimposed by the signals of the support, the particles were too small to create reflections or the phases were X-ray amorphous, respectively (Figure 23).

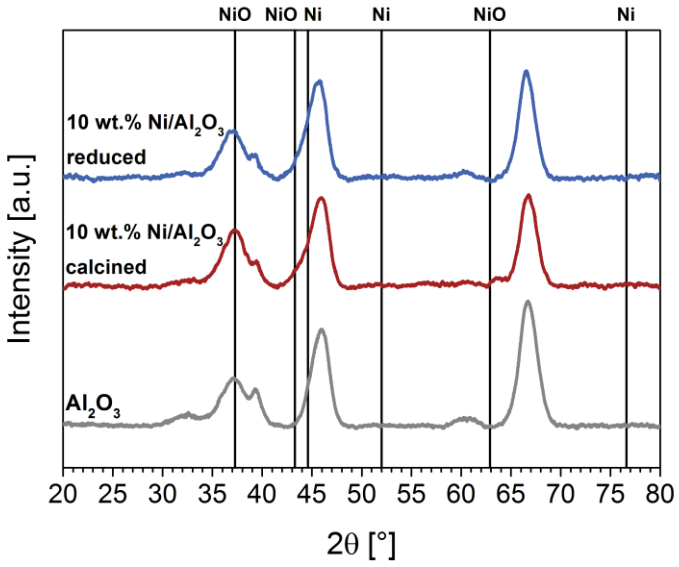

Figure 23: XRD patterns of the γ-Al_2O_3 support (grey) calcined at 600 °C (4 h, 5 K min^{-1}), the 10 wt. % Ni/Al_2O_3 catalyst (red) prepared by deposition-precipitation and calcined at 500 °C (4 h, 5 K min^{-1}) in static air and the catalyst in the reduced state (blue) after treatment in 50 % H_2/N_2 flow at 500 °C (2 h, 5 K min^{-1}) measured *ex situ* Reproduced from Mutz *et al.*[223] under the terms and conditions of CC BY 4.0 license (http://creativecommons.org/licenses/by/4.0/), Copyright © 2017.

As shown in Figure 24, electron microscopy revealed a homogeneous dispersion of the particles on the support resulting in small Ni particles with a diameter of 3.7 ± 1.2 nm, a narrow size distribution and a Ni dispersion of 21 %. These values are comparable with

those reported in literature for supported Ni catalysts that were prepared using the same preparation technique.[232,233]

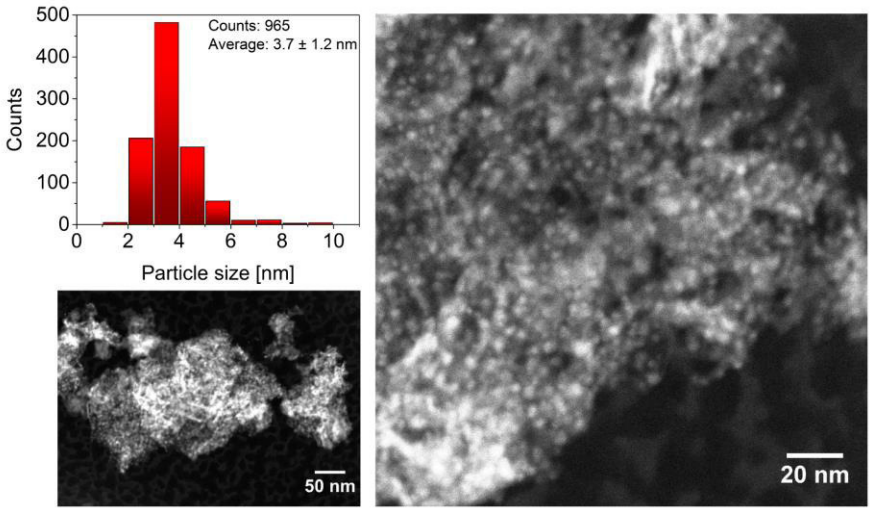

Figure 24: STEM-HAADF images and particle size distribution (top left) of the 10 wt.% Ni/Al_2O_3 catalyst prepared by homogeneous deposition-precipitation Reproduced from Mutz *et al.*[223] under the terms and conditions of CC BY 4.0 license (http://creativecommons.org/licenses/by/4.0/), Copyright © 2017.

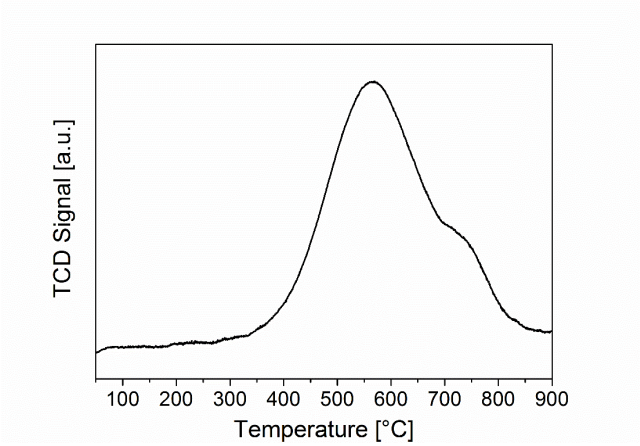

Figure 25: H_2-TPR profile of the 10 wt.% Ni/Al_2O_3 catalyst using 10 % H_2/Ar (50 mL min^{-1}, 100 mg sample), ramp rate 10 K min^{-1}. Reproduced from Mutz *et al.*[223] under the terms and conditions of CC BY 4.0 license (http://creativecommons.org/licenses/by/4.0/), Copyright © 2017.

Additionally, TPR experiments show H_2 consumption in a small temperature range (peak maximum at 565 °C, see Figure 25) confirming the uniform particle size and the

absence of agglomerates or larger particles. Furthermore, the Ni particles were reduced at lower temperature compared to other Ni/Al_2O_3 catalysts reported in literature (peak maxima between 680 – 800 °C[60,234,235]), which suggests a weaker metal-support interaction in the catalyst prepared in this study due to the synthesis method.

6.3 Catalytic performance

The catalyst was applied in the methanation of CO_2 and showed high conversion and selectivity with CO being the only by-product (Figure 26). The results of eq (15) and (16) from the experimental section obtained similar values for the conversion of $X(CO_2)$ and $X'(CO_2)$, which excludes the formation of other products in significant amounts. In Figure 26 the values obtained from eq (15) are shown. The formation of CH_4 started between 200 and 250 °C and the conversion of CO_2 increased with rising temperature reaching the highest value of 69 % at 400 °C at a maximum selectivity towards CH_4 of 95 %. The results are comparable with reports in the literature using Ni/Al_2O_3 catalysts treated under related reaction conditions.[68,145]

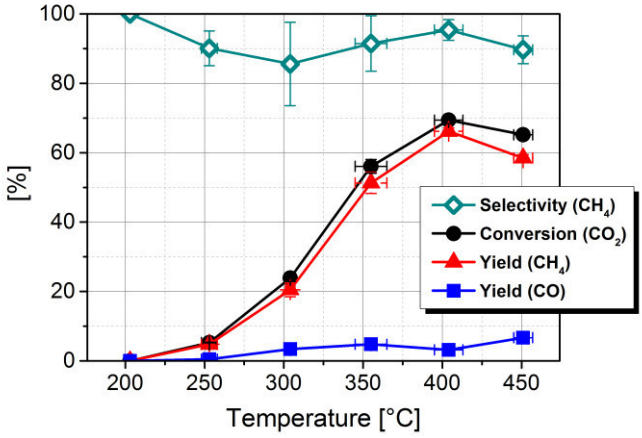

Figure 26: Conversion of CO_2 (black), yield of CH_4 (red) and yield of CO (blue) as well as selectivity of CH_4 (green) for the 10 wt.% Ni/Al_2O_3 catalyst; conditions: stainless steel tubular fixed-bed reactor, 150 mg catalyst, $H_2/CO_2 = 4$ diluted in 75 % N_2, p = 1 atm, T = 200 – 450 °C, GHSV = 26700 h^{-1} and WHSV = 12000 $mL_{CO2}\ g_{cat}^{-1}\ h^{-1}$). Reproduced from Mutz *et al.*[223] under the terms and conditions of CC BY 4.0 license (http://creativecommons.org/licenses/by/4.0/), Copyright © 2017.

The TOF at 250 °C was calculated as 0.02 s^{-1} or as 0.08 s^{-1} at 300 °C. The reported TOFs for Ni/Al_2O_3 methanation catalysts reported in literature cover a broad range between 0.69 s^{-1},[59] 0.10 s^{-1},[69] 0.041 - 0.097 s^{-1},[61] and $0.5 \cdot 10^{-3} – 2.4 \cdot 10^{-3}$ s^{-1}.[62] The achieved TOFs correspond to typical dimensions, however, it is difficult to compare the results due to the diverse reaction conditions applied in these studies. In conclusion, the catalyst used in this study can be regarded as a representative methanation catalyst, which is well suited for our experiments to evaluate the effects of fluctuating reaction conditions on the structure of the active component and their impact on the catalyst activity.

6.4 *Operando* XAS studies

Figure 27 visualizes the results of the *operando* XAS experiment which was performed based on the earlier studies in chapter 5.[219] The corresponding XANES spectra in each atmosphere at 400 °C can be seen in Figure 28. A pre-reduced catalyst was activated in 15 % H_2/He at an oven temperature of 500 °C (10 K min^{-1}, temperature 460-470 °C measured with a thermocouple at the location of the capillary) for about 40 min. Obviously, the catalyst was not fully reduced which might be due to the strong interaction of the small Ni particles with the Al_2O_3 support and the low H_2 concentration used for the activation. On the other hand, no $NiAl_2O_4$ spinel species could be identified in LCA. As reduced Ni reference the XANES spectrum of the reduced commercial catalyst from chapter 5 was used. The commercial catalyst exhibits larger Ni particles which makes the XANES spectrum look more like bulk Ni, whereas reduced Ni nanoparticles on an oxidic support do not differ from bulk Ni. The capillary was cooled to room temperature to receive a spectrum of the reduced catalyst in good quality as reference.

Afterwards the gas atmosphere was switched to methanation conditions ($H_2/CO_2 = 4$, diluted in 81 % He) and the reactor was heated to 400 °C (10 K min^{-1}, real temperature 350 - 360 °C). Even at room temperature the catalyst was oxidized to some extent but was reduced again when the production of CH_4 started at about 200 °C. 80 % of the Ni nanoparticles remained in the reduced state during the 40 min methanation period at 400 °C. After removing H_2 from the gas stream 75 % of the Ni fraction were immediately

oxidized in the less reducing atmosphere and the formation of CH_4 stopped as well in the absence of H_2.

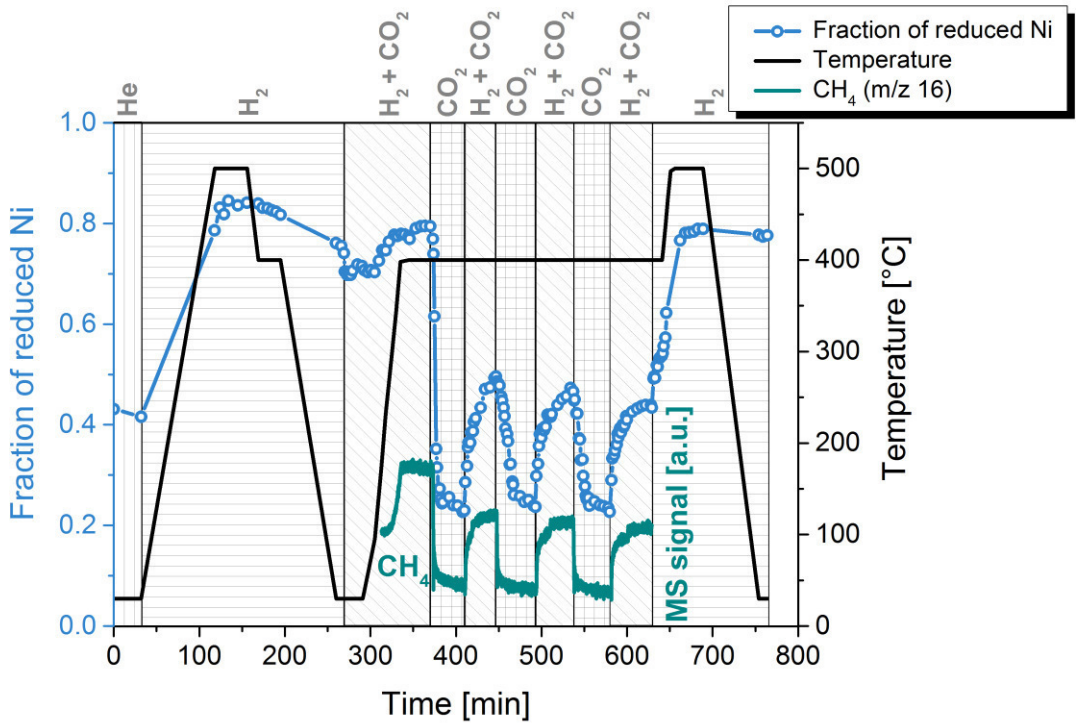

Figure 27: *Operando* XAS experiment for the methanation of CO_2 using the 10 wt.% Ni/Al_2O_3 catalyst at ANKA synchrotron Karlsruhe. The fraction of reduced Ni was calculated with linear combination analysis of the XANES spectra. Reproduced from Mutz *et al.*[231] under the terms and conditions of CC BY 3.0 license (https://creativecommons.org/licenses/by/3.0/), Copyright © 2016.

After another 40 min, H_2 was introduced again to restore the previous methanation conditions. In the first few minutes Ni was reduced fast and afterwards more slowly resulting in about 50 % metallic Ni. The oxidation of the catalyst during the next switch to the less reducing atmosphere took longer than during the first switch. In the third and fourth methanation cycle a behavior similar to the second cycle was observed which means that the fast reduction in the first few minutes was decelerating over time.

Overall, the maximum percentage of metallic Ni decreased with the number of cycles and also the produced amount of CH_4 decreased slightly. The first H_2 dropout caused a faster oxidation than the following cycles which might be due to oxygen contamination

in the system. Therefore, a deep bulk oxidation occurred which was not fully reversible under methanation atmosphere. In the following cycles dynamic oxidation and reduction of the Ni particles with a small but continuous deactivation was observed.

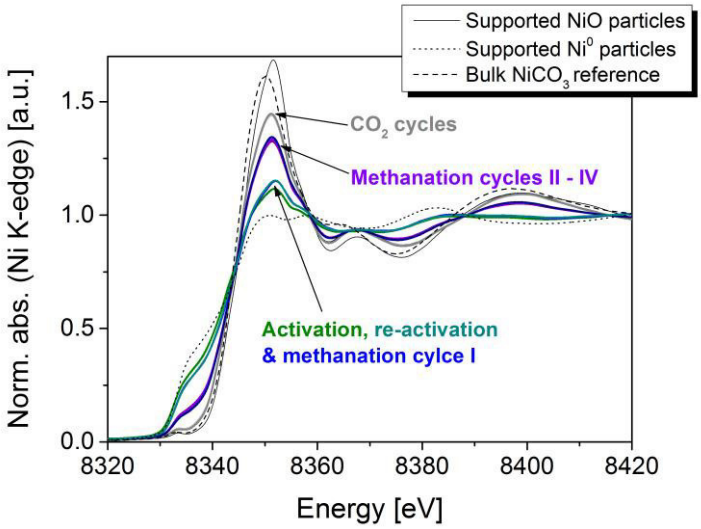

Figure 28: Normalized XANES spectra at 400 °C for each atmosphere according to Figure 27 as well as the reference spectra used for the LCA. Reproduced from Mutz *et al.*[231] under the terms and conditions of CC BY 3.0 license (https://creativecommons.org/licenses/by/3.0/), Copyright © 2016.

Figure 29 shows the development of each Ni phase (Ni, NiO and $NiCO_3$) during the experiment calculated from LCA. After exposure to air the pre-reduced catalyst showed a Ni and NiO phase as well as $NiCO_3$. During the reduction in H_2, NiO and $NiCO_3$ phases were reduced. During the methanation of CO_2, only traces of $NiCO_3$ were present in the catalyst. Removal of H_2 from the feed gas always led to the formation of NiO in the first step and its subsequent conversion into $NiCO_3$ (best seen in CO_2 cycle 2 and 3). In the following methanation atmosphere first a fast reduction of $NiCO_3$ occurred followed by a delayed slower reduction of NiO to metallic Ni. Roughly 30 % of each oxidized compound remained on the catalyst during the methanation sequences after the first H_2 dropout.

As a result of the Ni oxidation during H_2 dropout a reactivation step was performed at the end of the experiment recovering the same fraction of reduced Ni (78 % at room

temperature, see Figure 27) as after the activation in the beginning. As depicted in Figure 29 bulk NiO and $NiCO_3$ could only be reduced in a reactivation step flushing the reactor with H_2 at 500 °C. A reactivation step with higher H_2 concentrations might be even more effective.

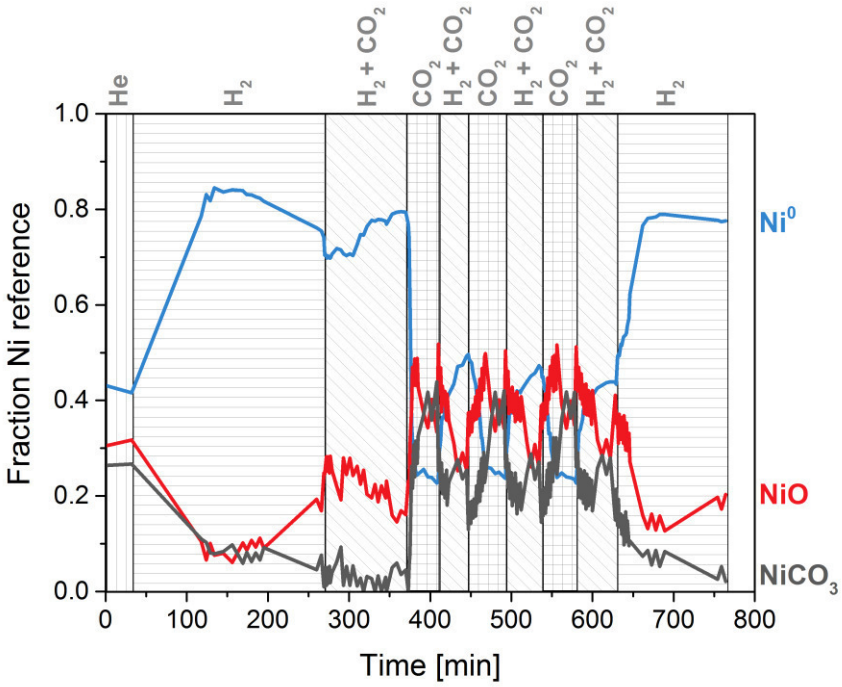

Figure 29. Fraction of Ni, NiO and $NiCO_3$ references derived from LCA evolving during the *operando* XAS experiment. Reproduced from Mutz *et al.*[231] under the terms and conditions of CC BY 3.0 license (https://creativecommons.org/licenses/by/3.0/), Copyright © 2016.

Comparing the EXAFS spectra of the activated catalyst and the catalyst after the reactivation step at room temperature (Figure 30), no significant changes could be observed. Therefore, it can be concluded that the size of the particles did not change during this short experiment. Performing the experiment four times in a row with the same catalyst sample, the Ni particle grew slightly to a mean diameter of 5.2 ± 1.2 nm (Figure 31) as determined from STEM images and the dispersion decreased to 14 %. Lovell *et al.*[168] reported a re-dispersion effect of Ni/SiO_2 catalysts derived from reduction/oxidation/reduction pre-treatments, which could also have happened during our

experiments. Consequently, quick scanning EXAFS studies are necessary to receive additional structural data of the Ni catalyst during dynamic reaction conditions.

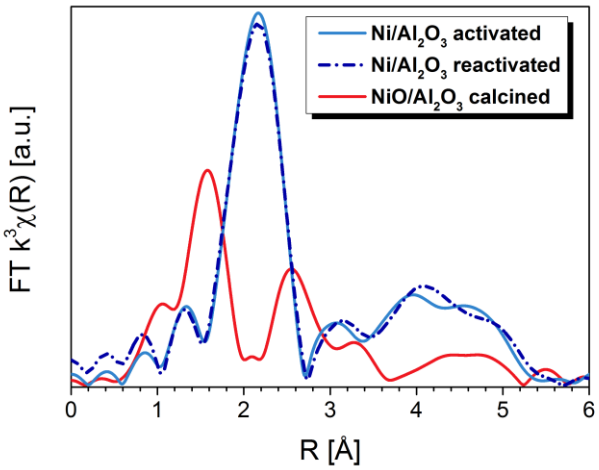

Figure 30: Magnitude of Fourier transformed k^3-weighted EXAFS spectra of the NiO reference (calcined catalyst), the 10 wt.% Ni/Al_2O_3 catalyst after reduction and reactivation recorded at room temperature. Reproduced from Mutz *et al.*[231] under the terms and conditions of CC BY 3.0 license (https://creativecommons.org/licenses/by/3.0/), Copyright © 2016.

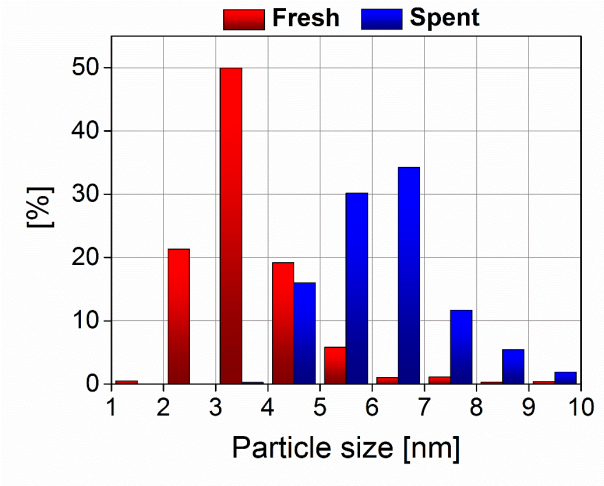

Figure 31: Results of the STEM images taken on the spent 10 wt.% Ni/Al_2O_3 catalyst sample compared to data of the fresh sample from Figure 24.

6.5 Conclusions

A 10 wt.% Ni/Al_2O_3 catalyst with an average Ni particle size of 4 nm and a narrow size distribution as well as a high metal dispersion of 21 % was prepared and applied for the methanation of CO_2. The catalyst shows high activity at 400 °C, converting 69 % of CO_2 to CH_4 with a selectivity of 95 %. Both uniform Ni particles and high catalytic performance represent optimal properties for structural investigations under dynamic reaction conditions.

Fast phase transformations between metallic Ni, NiO and $NiCO_3$ were observed under changing reaction atmospheres using *operando* X-ray absorption spectroscopy. Removing H_2 from the feed gas and, thus, simulating a H_2 dropout during the methanation reaction of technical CO_2 led to oxidation of the active sites to NiO and $NiCO_3$. After adding H_2 to restore methanation conditions ($H_2/CO_2 = 4$), $NiCO_3$ was first converted to NiO which was then reduced to metallic Ni. However, the initial fraction of reduced Ni could not be recovered. This was only possible with an effective reactivation step applying H_2 at increased temperatures (500 °C). Furthermore, a slight but steady deactivation of the catalyst was observed over several cycles. This experiment illustrates that *operando* XAS is a powerful tool to analyze catalysts under working conditions and to monitor changes of the active centers. This is crucial for a better understanding of the catalytic processes and the reasons for deactivation, especially in the methanation of CO_2 under dynamic reaction conditions.

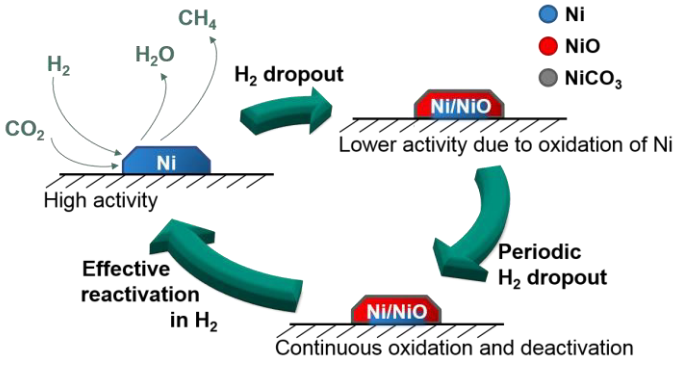

Scheme 2: Illustration of the phase transformations of the Ni particles during the methanation of CO_2 under dynamic reaction conditions.

7 High fluctuations in the supply of renewable hydrogen[1]

7.1 Introduction

The studies in the previous chapters have shown that during the dynamic methanation of technical CO_2 a fast partial oxidation of Ni-based catalysts occurred in a less reducing atmosphere after a H_2 dropout, which caused a deactivation in the following methanation sequence due to the presence of inactive NiO on the metallic catalyst (chapter 5).[219] Further deactivation occurred over cycles but the initial catalytic activity was recovered using reactivation in H_2 at elevated temperatures (chapter 6).[231] In general, interruptions in the H_2 feed must be prevented, since otherwise reactivation is required to retrieve high catalytic performance. Hence, methanation reactors have to be kept under reducing atmosphere during stand-by operation.[24] Based on these considerations, highly time-resolved *operando* XAS experiments were performed to gain a better insight into the kinetics and mechanisms of the redox processes and to evaluate the sensitivity of the catalyst towards deactivation. Furthermore, experiments including fast switches of the gas atmospheres have been performed to obtain insights into blocking of active sites under fast load changes.

7.2 Quick-EXAFS experiments

The *operando* QEXAFS experiments were executed in cooperation with Andreas Gänzler (ITCP, KIT) who was responsible for the recording of the QEXAFS spectra and their evaluation. These studies were performed to gather information on the oxidation

[1] The text and figures this chapter are taken from Mutz *et al.*:[223] B. Mutz, A. M. Gänzler, M. Nachtegaal, O. Müller, R. Frahm, W. Kleist, J.-D. Grunwaldt, "Surface Oxidation of Supported Ni Particles and Its Impact on the Catalytic Performance during Dynamically Operated Methanation of CO_2", *Catalysts* **2017**, *7*, 279. Available under the terms and conditions of the Creative Commons Attribution 4.0 license (CC BY 4.0, http://creativecommons.org/licenses/by/4.0/), Copyright © 2017.

state and the atomic structure of nickel during methanation conditions and, especially, during short periods of hydrogen dropouts. In previous studies, we observed a significant oxidation of nickel particles, when H_2 was withdrawn from the reaction feed, leading to lower catalytic activity during the subsequent methanation cycle.[219,231] In those studies, however, the hydrogen feed was interrupted for long periods of time (approx. 1 h) since conventional XAS methods were used, which require relatively long acquisition times per spectrum (approx. 5 min). Therefore, in the present study we applied the fast quick-scanning EXAFS technique[236,237] to obtain data even in the sub-second regime for studying the impact of short hydrogen dropouts (30 – 300 s).

The methanation of technical CO_2 containing traces of oxygen and the simulation of the H_2 dropouts were performed at 400 °C (highest conversion and selectivity, compare Figure 26 in section 6.3) and the same WHSV applied in the activity measurements. Before each experiment, the catalyst was reduced in 50 % H_2/He at 500 °C. To simulate a short dropout of H_2, caused for example by fluctuations in the hydrogen feed or by an unexpected change of the operation mode, hydrogen was switched on and off. The results of the experiment are presented in Figure 32.

First, the fully reduced catalyst was exposed to methanation conditions (H_2/ CO_2 = 4, 75 % He). After several minutes of operation and a stable MS signal of methane, the catalyst was subjected to a period of fluctuating H_2 feed for 15 min. During this modulation the feed was switched every 30 s between 5 % CO_2/He and methanation conditions (H_2/CO_2 = 4). Finally, the catalyst was again exposed to steady state methanation conditions. The applied feed composition expressed as the signal of the valve position is depicted in the upper part of Figure 32. The product gas was monitored during the entire experiment, all analyzed components are shown in the Appendix (Figure S 18). The methane production was monitored by mass spectrometry (m/z 15) and the resulting signal is presented in the middle part of Figure 32. Throughout the experiment, X-ray absorption spectra were recorded with an acquisition rate of 44 spectra s^{-1}. XANES spectra (exemplary sequence see Figure 33) were evaluated with LCA (details see Appendix) to monitor the Ni oxidation state during transient conditions. The results are plotted in the bottom part of Figure 32.

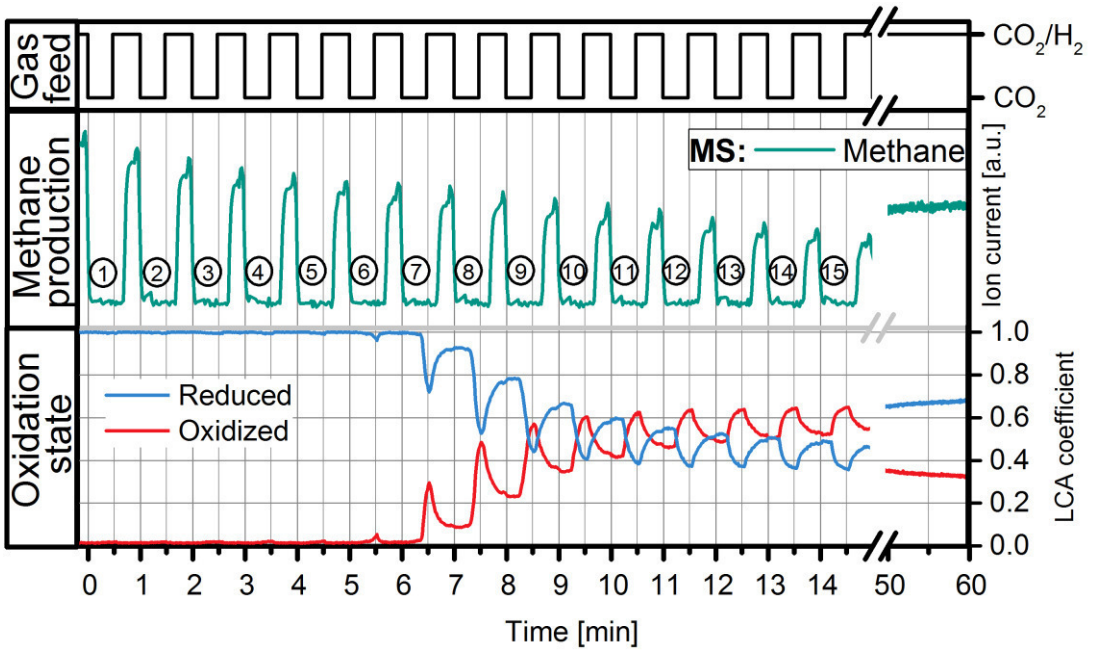

Figure 32: Methanation of CO_2 during dynamic operation switching every 30 s between methanation conditions ($H_2/CO_2 = 4$) and CO_2 at constant WHSV of 12000 $mL_{CO2}\ g_{cat}^{-1}\ h^{-1}$) and GHSV of 71700 h^{-1}. The figure shows the valve signal in the upper part (black), the CH_4 signal of the MS (m/z 15) in the middle part (green) and the fraction of reduced (blue) and oxidized (red) Ni from LCA of the XANES spectra. The numbers in circles count the H_2 dropouts. Reproduced from Mutz *et al.*[223] under the terms and conditions of CC BY 4.0 license (http://creativecommons.org/licenses/by/4.0/), Copyright © 2017.

The Ni particles were reduced during the methanation of CO_2 ($H_2/CO_2 = 4$) and an intense signal assigned to methane was observed in the mass spectrometer data. Short H_2 cut-offs, however, strongly affected the catalyst and its activity. As H_2 was switched back on the stream after a 30 s period of a less reducing atmosphere without H_2 (0 – 0.5 min), a slightly decreased methane signal was observed. The methane production decreased further with each H_2 dropout. However, no significant change of the Ni oxidation state was monitored during the first 5 min of the experiment. During the sixth H_2 free period (after 5.5 min) a first slight oxidation of Ni to a fraction of 6 % was observed, which was still accounted to be negligible. Fast and significant oxidation of Ni during the seventh H_2 dropout (at 6 - 6.5 min) was observed by XAS, indicated by the increasing intensity of the white line. As discussed later in this chapter, the oxidation of Ni in the absence of H_2 was caused by the traces of oxygen present in the technical CO_2. The oxidation stopped at 29 % oxidized Ni according to LCA when H_2 was switched back to the feed at 6.5 min.

Even though the catalyst was exposed to the H_2 containing atmosphere for 30 s (at 6.5 – 7 min), it did not regain its initial state and 9 % of the Ni atoms remained oxidized. The percentage of oxidized Ni species increased steadily during the subsequent modulation until the 12th H_2 dropout, during which approximately 65 % of the Ni atoms were oxidized. In the following oxidation and reduction events (between 11 and 15 min) a marginal but no significant increase in the percentage of oxidized Ni was observed and the fraction of oxidized Ni remained at a constant level altering between 65 % and 50 % over cycles. Nevertheless, the deactivation of the catalyst continued steadily as shown by the decreasing MS signal of methane.

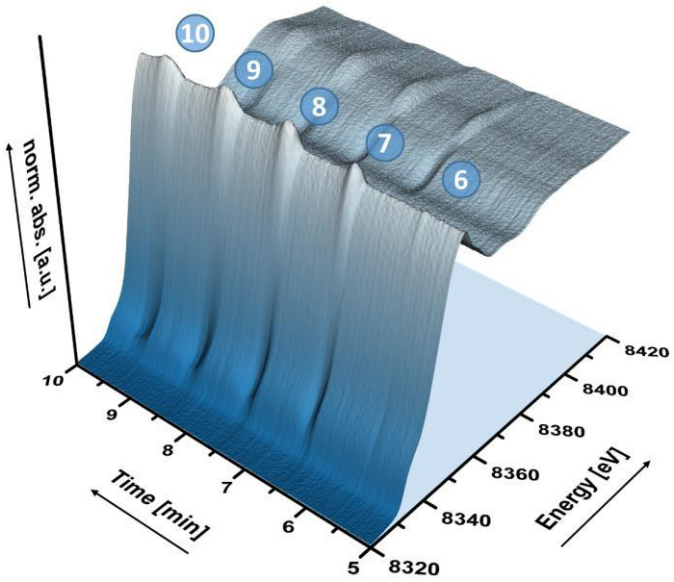

Figure 33: Section of the XANES spectra of the 10 wt.% Ni/Al_2O_3 catalyst during the 30 s H_2 dropout modulation (dropouts no. 6-10 according to Figure 32). Reproduced from Mutz *et al.*[223] under the terms and conditions of CC BY 4.0 license (http://creativecommons.org/licenses/by/4.0/), Copyright © 2017.

During the ensuing 10 min of modulation, the changes of the catalyst (altering oxidation/reduction and continuous deactivation) followed the same trend and are therefore not shown here (full range experiment see Figure S 9 in the Appendix). After the period of fluctuating operation (25 min in total), a sequence of steady state methanation was performed during which the oxidation state of the catalyst and structure was further monitored. During a 30 min measuring period significant reduction of Ni was

observed over time. This process, however, was very slow and even after 30 min (final 5 min of this sequence shown in Figure 32) the initial oxidation state was not regained and 30 % still remained oxidized. Consequently, the catalyst was less active and showed a similar methane production and oxidized fraction as observed after the ninth H_2 dropout. This supports a correlation between the oxidized fraction of Ni and the formation of methane.[219] Obviously, the temperature of 400 °C was too low to reduce Ni completely, which would have necessitated a reactivation of the catalyst at elevated temperatures.[231]

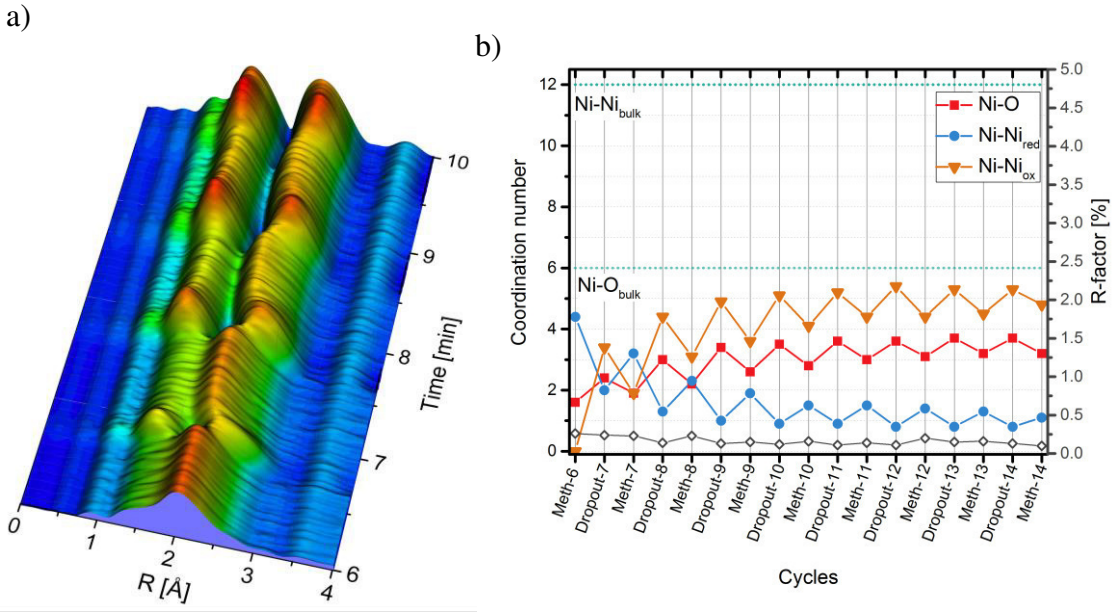

Figure 34: a) Fourier-transformed extended X-ray absorption fine structure (FT EXAFS) data (k: 3-11 Å-1; k2-weighted, not phase corrected) during 30 s H_2 dropouts (starting at the methanation sequence before the seventh H_2 dropout (Meth-6)); b) Results of the EXAFS fitting analysis during the 30 s modulation. The final spectra of each sequence (methanation sequences labeled as "Meth") were analyzed (details see Appendix). The coordination numbers (N) of neighboring atoms are presented: Ni-O and Ni-Ni$_{ox}$ correspond to O and Ni coordination numbers, respectively, in oxidized nickel and Ni-Ni$_{red}$ to the coordination number of the first nickel shell in reduced nickel. Reproduced from Mutz *et al.*[223] under the terms and conditions of CC BY 4.0 license (http://creativecommons.org/licenses/by/4.0/), Copyright © 2017.

The active catalyst state was obviously very sensitive towards oxidation, and already, a short exposure to a less reducing atmosphere was sufficient to initiate oxidation of Ni resulting in lower activity. Therefore, the full EXAFS spectra were further evaluated to extract information on the local structural changes of the Ni catalyst during fluctuating conditions. In Figure 34 a) Fourier-transformed (FT) EXAFS spectra are presented along

with best fitting parameters obtained by fitting the first two coordination shells (Figure 34 b). The EXAFS evaluation of the cycles 6-8 are shown in Figure 35, the structural parameters and the full analyzed datasets are listed in Table 8, more details are shown in the Appendix.

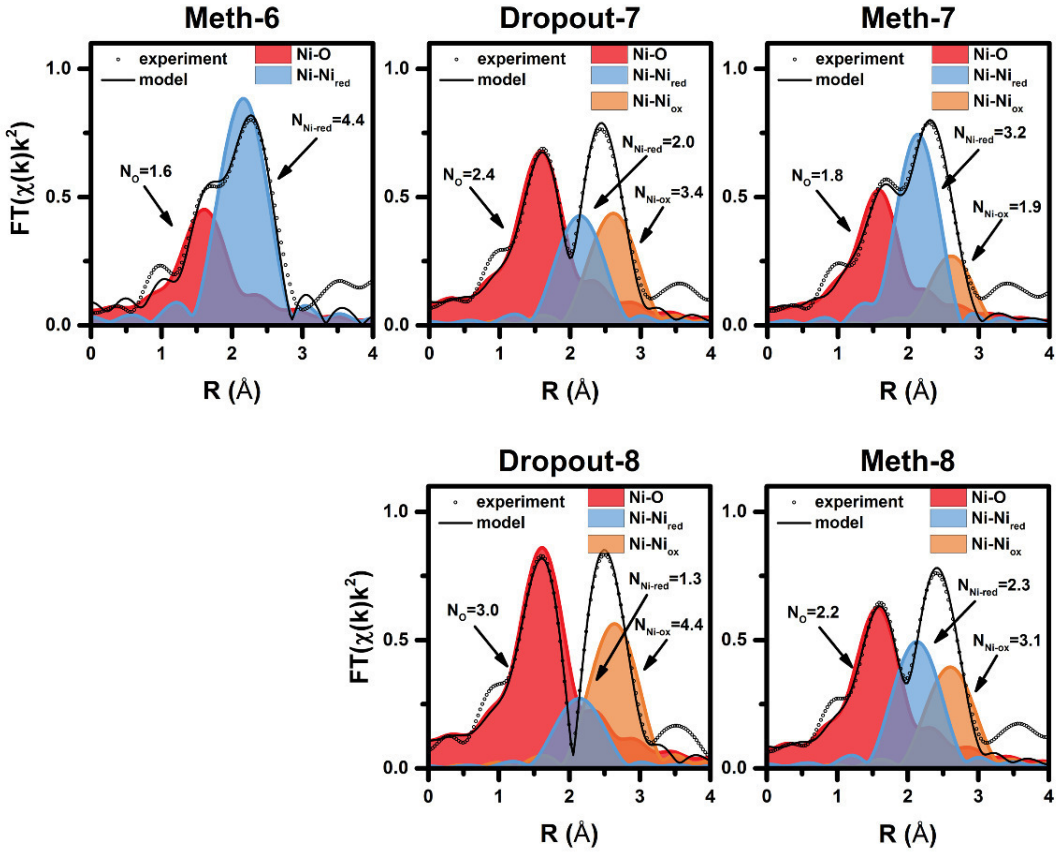

Figure 35: Experimental and simulated FT EXAFS data (magnitudes, not phase shift corrected) of the Ni catalyst during 30 s modulation, in addition, the estimated Ni coordination numbers (Cycles 6-8), k-range 3-9, k-weight = 2 (for details see Appendix). Reproduced from Mutz *et al.*[223] under the terms and conditions of CC BY 4.0 license (http://creativecommons.org/licenses/by/4.0/), Copyright © 2017.

For the first six cycles no significant changes in the EXAFS spectra were observed. The spectra were dominated by a feature at about 2 Å, predominantly originating from Ni neighbors in reduced Ni. The evaluated interatomic distance of 2.49 Å was similar to the one in metallic Ni. The O contribution determined in the reduced state may originate from the oxide support or incomplete reduction of the Ni particles. Including a Ni-Ni_{ox} (the Ni-

Ni backscattering contribution in nickel oxide) bond pair led to a worse fit and was therefore not considered in Meth-6. During the seventh H_2 dropout, when significant oxidation was observed for the first time (see LCA in Figure 32) changes in the FT EXAFS data were observed, indicating substantial changes in the structure of the Ni nanoparticles. During oxidation, the feature at 2 Å in the EXAFS spectra resulting from reduced Ni-Ni coordination disappeared quickly and was replaced by two peaks related to the O and Ni neighbors in a NiO-like structure. The evaluation of the final EXAFS spectra of each sequence (methanation atmosphere or less reducing atmosphere, respectively) facilitated monitoring the evolution of the respective coordination shells during fluctuating operation. The respective coordination numbers are therefore plotted in Figure 34 b) for this purpose. The data revealed the transformation from a reduced Ni particle to a partially-oxidized Ni particle. Even though the Ni particles were very small, they did not get fully oxidized due to the short duration of H_2 dropout indicating that a core of reduced Ni remained (coordination number $N_{Ni\text{-}Ni,red} > 1$). After the 12^{th} dropout predominantly a reversible oxidation and reduction was observed, in accordance with the LCA discussed earlier, and the core of the particles remained reduced.

The following steady state methanation operation (full range experiment see Figure S 9 in the Appendix) slowly transformed the catalyst back into its reduced state. However, even after 30 min in the methanation atmosphere, still, a significant fraction of nickel remained oxidized, also shown by the coordination numbers ($N_{Ni\text{-}O} = 2.2$, $N_{Ni\text{-}Ni,red} = 2.4$, $N_{Ni\text{-}Ni,ox} = 3.0$, see Table S 6). During this methanation experiment, only slight sintering was observed by an increase in the coordination number of reduced Ni by 0.2. This is within the accuracy of the evaluation; however, the Ni coordination number increased by 0.5 after repeating the whole experiment of 30 s modulation three times further (see Table S 5). Note that the evaluated Ni coordination was not adjusted to the fraction of the particles in the Ni/NiO mixture, and no conclusion on the correlation between coordination number and particle size was drawn. In this study, we focused on the progressive contribution of O in the catalyst during the modulation experiment to investigate oxidation and reduction effects.

Table 8: Structural parameters of the local Ni atomic environment extracted from best fitting the EXAFS spectra shown in Figure 35. k-range = 3-9 $Å^{-1}$, R-range = 1.2-3.2 Å, N^{ind} = 6, N^{var} = 5, a = fitted uncertainty 0.01 or lower, f = fixed during fit, N = number of neighboring atoms, R = distance, σ^2 = mean square deviation of interatomic distance, R factor = misfit between experimental data and theory. Reproduced from Mutz *et al.*[223] under the terms and conditions of CC BY 4.0 license (http://creativecommons.org/licenses/by/4.0/), Copyright © 2017.

Cycle	Atom	N	R [Å][a]	σ^2 10^{-3} [$Å^2$]	E_0 [eV]	R-factor [%]
Meth-6	O	1.6 ± 0.2	2.03 ± 0.2	8.3[f]	9.0 ± 1.5	0.27
	Ni	4.4 ± 0.3	2.49 ± 0.1	11.8[f]		
Dropout-7	O	2.4 ± 0.2	2.02 ± 0.03	8.3[f]	7.6 ± 2.9	0.25
	Ni	2.0 ± 0.6	2.48 ± 0.02	11.4[f]		
	Ni	3.4 ± 0.9	2.96 ± 0.03	11.8[f]		
Meth-7	O	1.8 ± 0.2	2.01 ± 0.2	8.3[f]	6.4 ± 2.2	0.23
	Ni	3.2 ± 0.4	2.48 ± 0.1	11.4[f]		
	Ni	1.9 ± 0.6	2.95 ± 0.3	11.8[f]		
Dropout-8	O	3.0 ± 0.2	2.04 ± 0.02	8.3[f]	8.9 ± 2.1	0.14
	Ni	1.3 ± 0.6	2.48 ± 0.03	11.4[f]		
	Ni	4.4 ± 0.7	2.97 ± 0.03	11.8[f]		
Meth-8	O	2.2 ± 0.2	2.02 ± 0.03	8.3[f]	6.8 ± 2.9	0.23
	Ni	2.3 ± 0.6	2.48 ± 0.01	11.4[f]		
	Ni	3.1 ± 0.9	2.96 ± 0.03	11.8[f]		

The delayed start of the Ni oxidation as observed in Figure 32 was rationalized when the spatial conditions of the experiment were considered.[190,191] XAS spectra were recorded in the middle of the catalyst bed with a 200 µm-sized X-ray beam and correlated to the integral activity data. Catalyst oxidation therefore probably started at the reactor inlet and propagated through the catalyst bed. We speculate that the oxidation was caused by the O_2 background present in the CO_2 feed (*cf.* the estimation in the later part of this chapter), which oxidized a small amount of Ni at the reactor inlet in the short 30 s period in a less reducing atmosphere and was thereby completely consumed. Significant oxidation by CO_2 was ruled out, as CO_2 was present in excess and should then also have oxidized Ni in the middle of the reactor already at the beginning of the experiment (*cf.*

Figure 32; oxidation started at the sixth switch). Furthermore, an additional experiment in the total absence of O_2 using short and thin stainless steel tubing and a CO_2 (99.998%) bottle directly placed next to the mass flow controllers showed that no catalyst deactivation occurred during 60 s H_2 dropouts (see Figure S 20). Catalyst deactivation occurred during 300 s cycles when 300 ppm and 500 ppm O_2 were added to the gas mixture, which was more pronounced with increasing O_2 content (Figure 41 in the following chapter). Finally, the oxidation of Ni by CO_2 is thermodynamically unfavorable ($\Delta G > 0$). Estimations of the amount of O_2 present in the spectroscopic experiment based on the formation of NiO showed that an amount of around 1000 ppm was sufficient for the oxidation (for details, *cf.* the discussion of Figure S 11in the Appendix). Reduction of the whole catalyst bed was not achieved within the following 30 s during methanation at 400 °C. Therefore, the overall fraction of oxidized Ni increased during fluctuating operation causing the steady decrease in catalytic activity. The methane production decreased continuously, even after Ni reached a stable oxidized fraction at the monitored position (after the 12th H_2 dropout), since Ni oxidation kept propagating towards the end of the catalyst bed.

To provoke a faster oxidation through the catalyst bed and to investigate the oxidation and its kinetics in a longer cycle duration, the catalyst was exposed to H_2 dropout events to an extended period of 300 s in a subsequent experiment using the same catalyst sample. In this experiment (Figure 36) oxidation was observed immediately during the first dropout event. However, there was a significant delay (approximately 80 s, details see Figure S 11) between the switch of the gas atmospheres and the oxidation observed in the XANES spectra, due to the gradual oxidation of the Ni along the catalyst bed. Again, oxidation was found to be fast, resulting in 91 % of NiO at the end of the 300 s cycle. Switching to methanation conditions after 300 s led to a re-reduction of the Ni particles and methane formation. About 38 % of oxidized nickel remained on the catalyst and changed the overall catalyst composition resulting in a decreased catalytic activity in the second methanation cycle. Reduction occurred approximately 20 s after the gas switch and, therefore, seemed to propagate faster than the oxidation due to the much higher concentration of the reducing agent in the feed. In the following H_2 dropout cycles the maximum oxidized fraction in the less reducing atmospheres remained at

approximately 95 %. Therefore, a 300 s H_2 dropout led to a (nearly) complete oxidation of the catalyst. A slowly-progressing reduction of the catalyst was observed during the 30 min period of steady state methanation at the end of the experiment, reaching a final value of a 48 % reduced fraction.

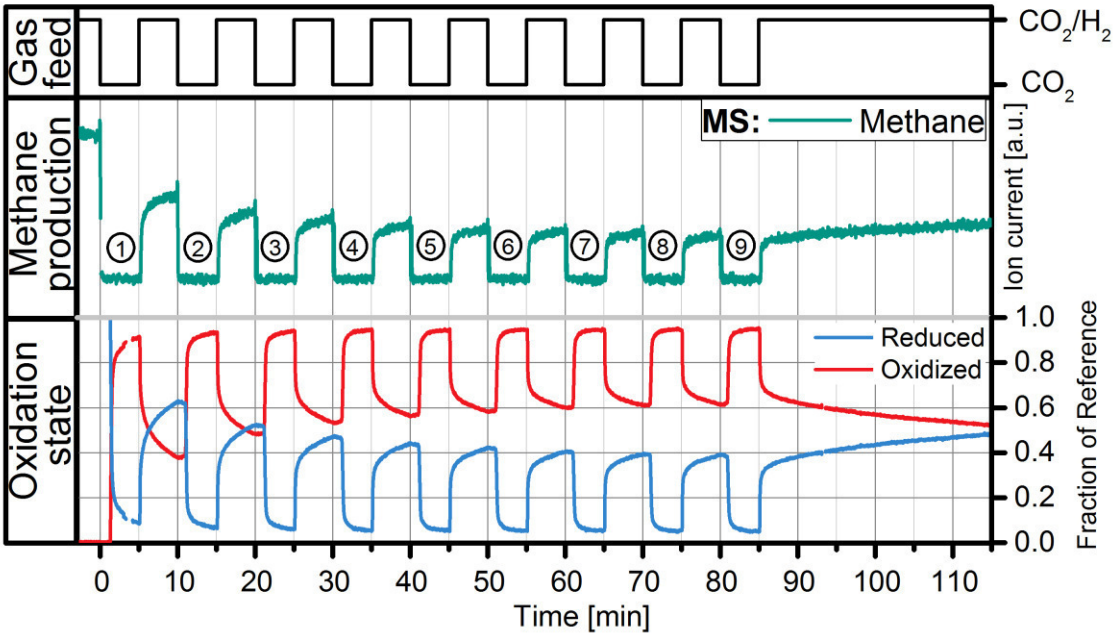

Figure 36: Methanation of CO_2 during dynamic operation switching every 300 s between methanation conditions ($H_2/CO_2 = 4$) and CO_2 at constant WHSV of 12000 $mL_{CO2}\ g_{cat}^{-1}\ h^{-1}$ and GHSV of 71700 h^{-1}. The figure shows the valve signal in the upper part (black), the CH_4 signal of the MS (m/z 15) in the middle part (green) and the fraction of reduced (blue) and oxidized (red) Ni from LCA of the XANES spectra. The numbers in cycles count the H_2 dropouts. Reproduced from Mutz *et al.*[223] under the terms and conditions of CC BY 4.0 license (http://creativecommons.org/licenses/by/4.0/), Copyright © 2017.

Similar to the 30 s modulation, the estimated amount of O_2 based on the formed NiO showed a value around 1000 ppm. Additional experiments with a quantified amount of O_2 (Figure 41) showed a full Ni oxidation after a few 300 s H_2 dropouts applying 500 ppm O_2. Consequently, we assumed an O_2 content between 500 and 1000 ppm present in the QEXAFS experiments. This small quantity is ideal to oxidize the most reactive sites and block in fact those Ni sites for methanation.

The FT EXAFS spectra collected during the 300 s modulation and the coordination numbers from the best fits of the EXAFS spectra are shown in Figure 37 a) and b),

respectively. As already observed during the 30 s modulation, the FT EXAFS spectra in the reduced state were dominated by one signal at 2 Å which is assigned to Ni-Ni coordination in reduced Ni. Note that the $N_{Ni\text{-}Ni,red}$ of 5.1 was slightly higher than the one determined from the EXAFS evaluation during the 30 s modulation ($N_{Ni\text{-}Ni,red}$ = 4.4). This can be explained by sintering of the Ni particles since the same sample was used for all experiments and three additional 30 s modulation experiments (not shown here) were performed before the 300 s modulation experiment (see Table S 4).

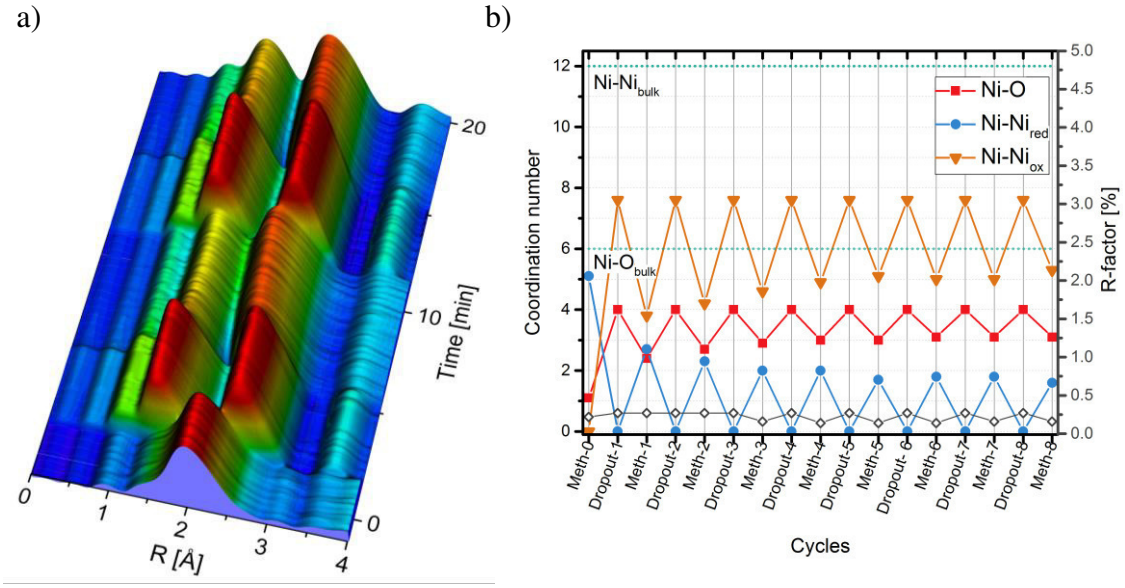

Figure 37: a) FT EXAFS data (k: 3-11 Å^{-1}; k^2-weighted) during repeated 300 s H_2 dropouts; b) Results of the EXAFS fitting analysis during the 300 s modulation. The final spectra of each sequence were analyzed. The coordination numbers of neighboring atoms are presented: Ni-O and Ni-O-Ni correspond to O and Ni coordination numbers, respectively, in oxidized nickel and Ni-Ni to the coordination number of the first nickel shell in reduced nickel. Reproduced from Mutz *et al.*[223] under the terms and conditions of CC BY 4.0 license (http://creativecommons.org/licenses/by/4.0/), Copyright © 2017.

Applying the 300 s modulation, the steady state of the maximum Ni-O path was already reached during the first H_2 dropout. A bulk oxidation of the Ni particles occurred during the absence of H_2 indicated by the $N_{Ni\text{-}Ni,red}$ which decreased to zero. The oxidation state reached its steady state after the first cycle, while the amount of receded Ni during the methanation periods decreased until the fourth cycle. Reduced Ni particles with a $N_{Ni\text{-}Ni,red}$ of 5.1 were transformed into oxidized Ni particles with a $N_{Ni\text{-}Ni,ox}$ of 7.6. This

can be either explained by incomplete reduction of the Ni particles contributing to the apparently lower coordination in reduced Ni and a higher coordination after oxidation. Another explanation for the difference in the coordination numbers can be a wetting effect of the flat reduced particles, increasing the contact with the oxidic support material, whereas the oxidized particles are more spherical with a higher average Ni-Ni coordination.[171]

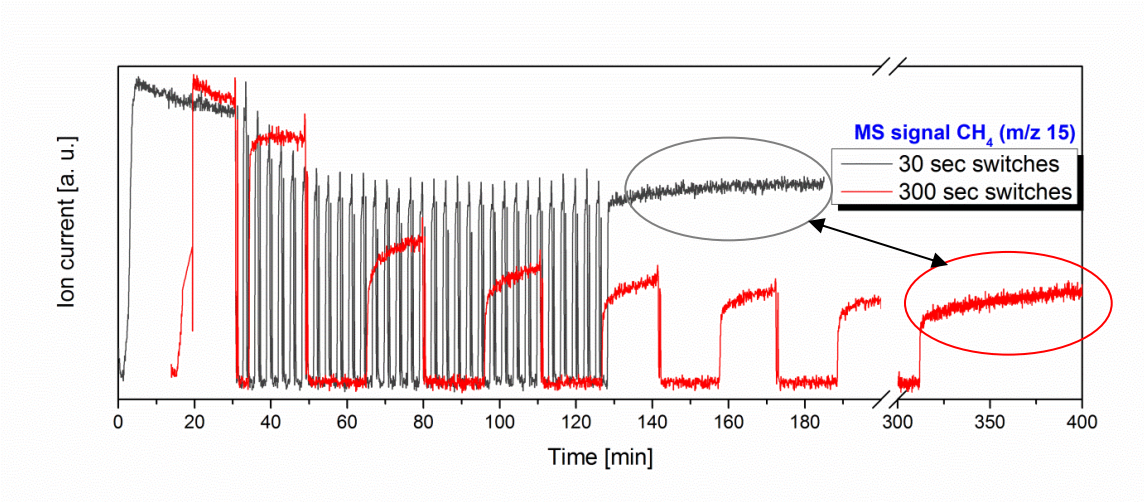

Figure 38: MS data of both the 30 s and 300 s H_2 dropout modulations put on top of each other for comparison. Reproduced from Mutz *et al.*[223] under the terms and conditions of CC BY 4.0 license (http://creativecommons.org/licenses/by/4.0/), Copyright © 2017.

The direct comparison of the MS signals of both modulation experiments (Figure 38) proved first, that the catalytic activity is fully restored after reactivation in H_2 and showed secondly that the deactivation was more distinctive during 300 s switches, where a significantly lower CH_4 signal was detected after the second cycle up until the end of the experiment. Furthermore, in the experiments with 30 s modulation, the catalyst was much more active during steady state methanation after the H_2 dropout sequence. This observation clearly emphasized the correlation of the Ni oxidation state and the methanation activity. Comparing the results of the LCAs from both experiments, full oxidation was interrupted during the 30 s cycles due to the fast switching. During the

300 s modulation, the oxidation state reached a plateau indicating the complete oxidation process. Thus, the impact of the short cycles on the catalyst deactivation was less severe.

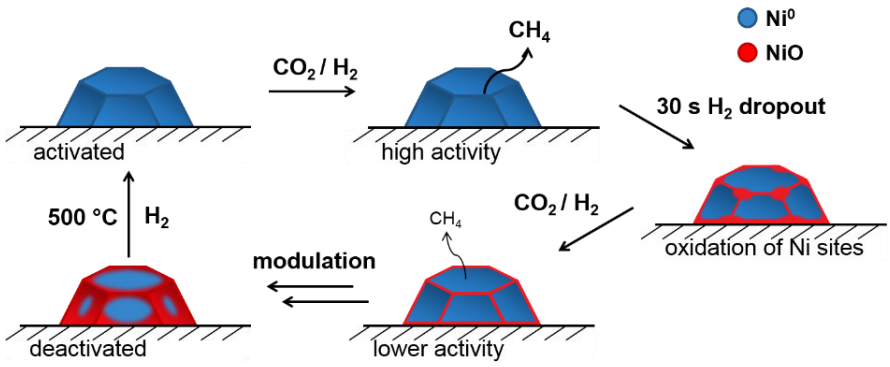

Figure 39: Scheme of the supported Ni particles during 30 s dropout modulations. Blue represents reduced Ni, whereas red describes oxidized Ni. Reproduced from Mutz *et al.*[223] under the terms and conditions of CC BY 4.0 license (http://creativecommons.org/licenses/by/4.0/), Copyright © 2017.

Figure 39 and 10 show schemes of the Ni particles during the dynamic methanation of CO_2. Short term H_2 dropout (Figure 39) first led to an oxidation of the most reactive sites such as low coordinated Ni atoms located at step sites, defect sites or at the interface to the support material.[238-242] Particularly, the interface sites appear important for the methanation of CO_2, since the key steps of the hydrogenation is speculated to take place at the interface of the metal particle and support.[96,114] Furthermore, step sites are more reactive in CO dissociation compared to plane facets.[241,243] NiO islands may form and grew to NiO structures to several layers.[244,245] Diffusion of oxygen into the bulk did not occur due to the short period of less reducing atmosphere. Full oxidation of the Ni particles was interrupted, and NiO planes were reduced partly in the methanation atmosphere. The highly active lower coordinated Ni sites remained oxidized under these reaction conditions due to their higher stability. Hence, the methanation of CO_2 could only take place at the reduced Ni plane sites resulting in lower activity. This supports earlier studies in the literature[238-240,246] that selective blockage of the low coordinated Ni edge or corner sites leads to differed or deteriorated catalytic properties. Similar structure sensitivity due to easier oxidation of low-coordinated sites was also observed during CO oxidation on Pt catalysts.[247,248] For example, oxidation of low-coordinated Pt atoms

located at edge and corner sites during CO oxidation was found by XAS resulting in an irreversible CO adsorption on PtO.[249] Cluster models show that metal particles of our size or dispersion contain 4 % edge sites.[250-253] This value correlated with the remaining oxidized fraction (10 %) in the methanation sequence after the first oxidation during the seventh H_2 dropout when additional sites at the interface, as well as corner and defect sites, would have been taken into account.

The schematic structural changes of Ni particles during 300 s modulations are illustrated in Figure 40. Compared to the short-time H_2 dropouts, the longer 300 s H_2 dropouts resulted in a less reducing atmosphere enabling a complete oxidation of the Ni particles, which then suffer from insufficient re-reduction during the reducing methanation atmosphere.

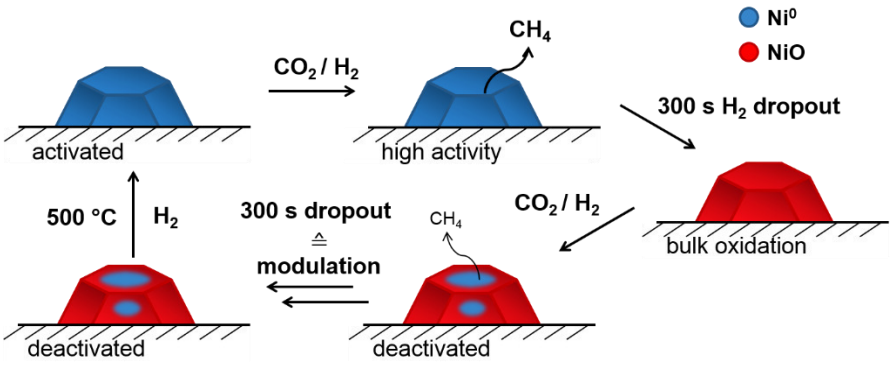

Figure 40: Scheme of the supported Ni particles exposed to H_2 dropout modulation with different cycle duration of 30 s and 300 s. Reproduced from Mutz *et al.*[223] under the terms and conditions of CC BY 4.0 license (http://creativecommons.org/licenses/by/4.0/), Copyright © 2017.

7.3 Operational adjustments in methanation applications

Since even short H_2 dropouts cause catalyst deactivation and necessitate a reactivation in H_2 at elevated temperatures to recover the initial activity, operational adjustments are essential in industrial methanation plants to prevent catalyst oxidation and the application of an unprofitable reactivation step.

Periods of 300 s of H_2 dropout were performed in the lab-scale reactor under similar reaction conditions (WHSV = 12000 mL_{CO2} g_{cat}^{-1} h^{-1}) as in the *operando* QEXAFS experiments. The 10 wt.% Ni/Al_2O_3 catalyst was exposed to a series of H_2 dropout periods intensified with 300 – 500 ppm O_2 to induce fast and deep oxidation and deactivation of the catalyst (Figure 41).

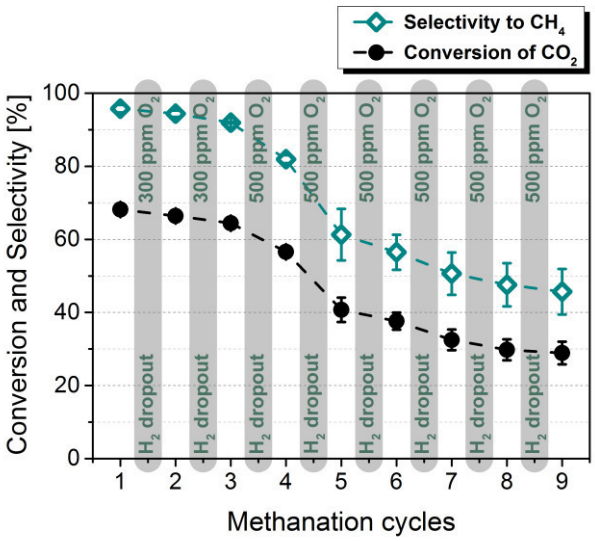

Figure 41: Series of 300 s H_2 dropout periods during the methanation of CO_2 containing 300 – 500 ppm O_2 using the 10 wt.% Ni/Al_2O_3 catalyst; conditions: stainless steel tubular fixed-bed reactor, 150 mg catalyst, H_2/CO_2 = 4 diluted in 75 % N_2 or 5 % CO_2 / N_2 + 300 – 500 ppm O_2, p = 1 atm, T = 400 °C, GHSV = 26700 h^{-1} and WHSV = 12000 mL_{CO2} g_{cat}^{-1} h^{-1}. Reproduced from Mutz *et al.*[223] under the terms and conditions of CC BY 4.0 license (http://creativecommons.org/licenses/by/4.0/), Copyright © 2017.

The initial activity of the catalyst (cycle 1) resulted in a conversion of CO_2 of 68 % with a selectivity of 96 % towards CH_4. The first two H_2 dropout periods containing 300 ppm O_2 caused only minor deactivation of the catalyst leading to a CO_2 conversion of 66 % (cycle 2) and 64 % (cycle 3) and a decline in selectivity to 94 % (cycle 2) and 92 % (cycle 3). A more pronounced deactivation was observed when 500 ppm O_2 were dosed during the H_2 dropout periods. The conversion of CO_2 declined to 57 % (cycle 4) and further to 41 % (cycle 5) and the selectivity towards CH_4 also decreased significantly to 82 % (cycle 4) and 61 % (cycle 5). Full oxidation of the catalyst was suspected during the fourth H_2 dropout indicated by a strong increase of the O_2 signal in the MS (Figure

42). This observation implies that Ni is fully transformed to NiO and O_2 is not consumed for oxidation anymore. Full Ni oxidation during H_2 dropouts is in line with the *operando* QEXAFS experiments (Figure 36). After a total of eight H_2 dropouts, the conversion of CO_2 declined to a final value of 29 % with a selectivity of 46 % towards CH_4.

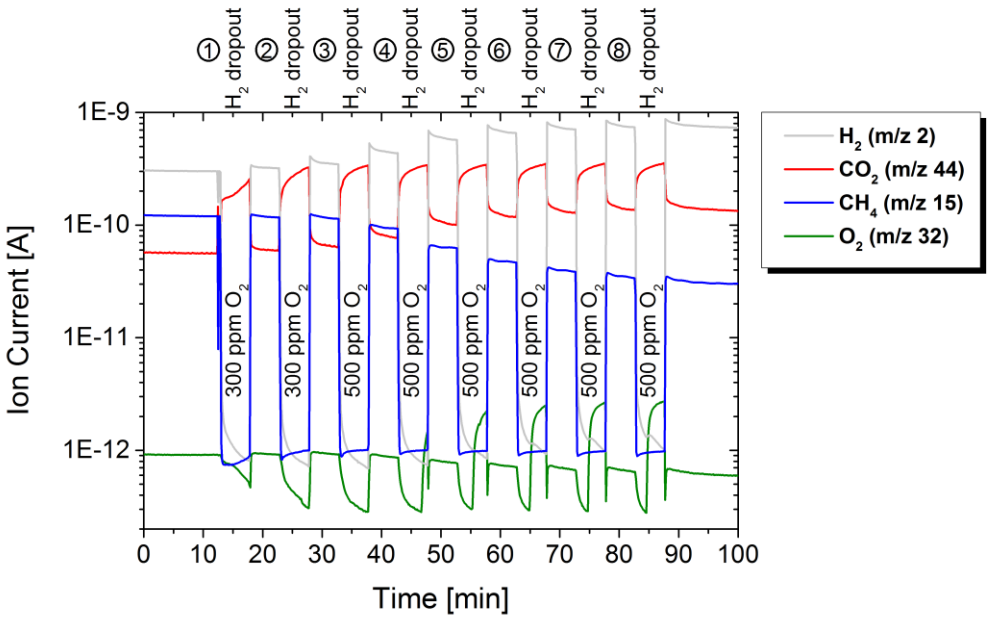

Figure 42: MS data corresponding to Figure 41 for a series of 300 s H_2 dropout periods during the methanation of CO_2 containing 300 – 500 ppm O_2. Reproduced from Mutz *et al.*[223] under the terms and conditions of CC BY 4.0 license (http://creativecommons.org/licenses/by/4.0/), Copyright © 2017.

One possibility to prevent catalyst oxidation during H_2 dropouts may be the integration of a small but permanent H_2 background flow through the methanation reactor. An experiment similar to that described in Figure 41 was performed but a constant flow of 1000 ppm H_2 was included in addition to the traces of O_2. The results (Figure 43) show that in the presence of H_2 no significant deactivation of the catalyst occurred. The conversion of CO_2 (initially 65 %, 63 % at the end) as well as the selectivity towards CH_4 (initially 94 %, 91 % at the end) remained nearly constant for eight H_2 dropout cycles with only a slight decrease over cycles.

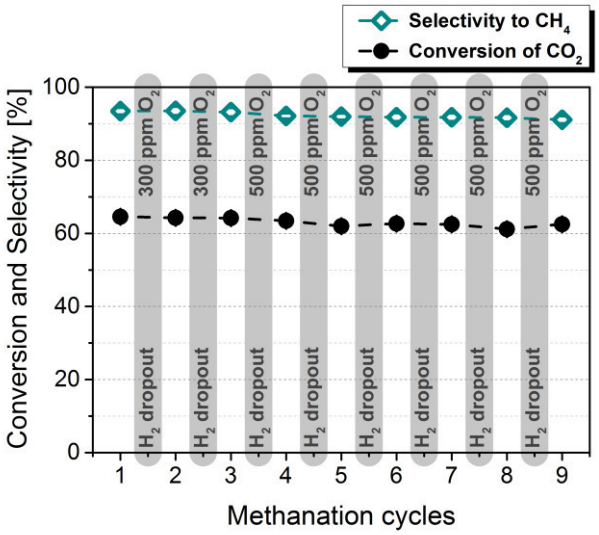

Figure 43: Integrated background flow of 1000 ppm H_2 for a series of 300 s H_2 dropout periods matching those in Figure 41 with the 10 wt.% Ni/Al_2O_3 catalyst; conditions: stainless steel tubular fixed-bed reactor, 150 mg catalyst, $H_2/CO_2 = 4$ diluted in 75 % N_2 or 5 % CO_2 / N_2 + 300 – 500 ppm O_2 + 1000 ppm H_2, p = 1 atm, T = 400 °C, GHSV = 26700 h^{-1} and WHSV = 12000 $mL_{CO2}\ g_{cat}^{-1}\ h^{-1}$.

Another possibility to avoid deactivation may be the methanation of a CO_2/CH_4 mixture, which can be obtained from biogas plants[8,24,124,138] or by product gas recycling within the methanation process.[84,125,149] The H_2 dropout experiment was performed analogue to the previous experiments but with a feed of CO_2/CH_4 = 5/4. The results (Figure 44) also show no significant deactivation of the catalyst during the methanation cycles. Constant conversion of CO_2 of 63 - 64 % and selectivities between 93 – 94 % were achieved during the entire experiment. Consequently, the reduction potential of CH_4 is sufficient to prevent catalyst oxidation and to retain its catalytic performance.

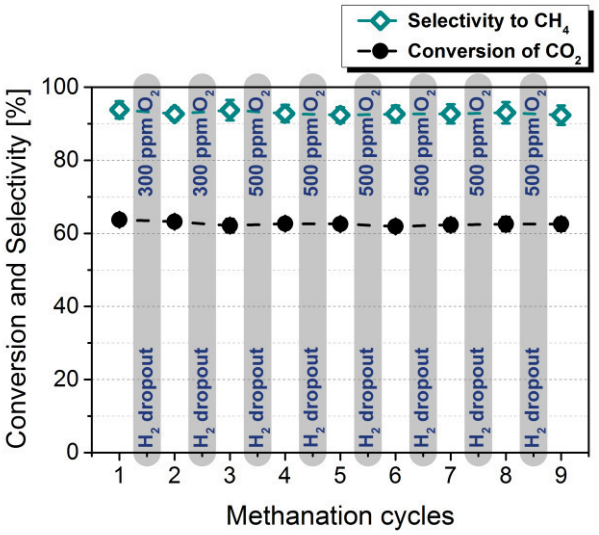

Figure 44: Series of 300 s H_2 dropout periods according to Figure 41 during the methanation of a CO_2/CH_4 mixture using the 10 wt.% Ni/Al_2O_3 catalyst; conditions: stainless steel tubular fixed-bed reactor, 150 mg catalyst, $H_2/CO_2/CH_4$ = 20/5/4 diluted in 71 % N_2 or 5 % CO_2 / N_2 + 300 – 500 ppm O_2 + 4 % CH_4, p = 1 atm, T = 400 °C, GHSV = 26700 h^{-1} and WHSV = 12000 mL_{CO2} g_{cat}^{-1} h^{-1}.

In conclusion, to prevent catalyst oxidation during H_2 dropouts CO_2/CH_4 mixtures could be used directly for the methanation of CO_2 or, if CH_4 is absent, the integration of a small background flow of H_2 *e.g.* from gas bottles or a small storage tank is a promising option. These first insights into operational adjustments to prevent catalyst oxidation during H_2 dropouts are crucial for industrial methanation applications operated in decentralized plants. Note that these are only first promising suggestions which need further optimization regarding the gas compositions.

7.4 Conclusions

Experiments with periodically changing atmospheres during the methanation of technical CO_2 simulated as H_2 dropouts were performed and resulted in detailed insights into the catalyst deactivation mechanism. During H_2 interruptions, catalyst deactivation occurred due to oxidation of the most active surface Ni sites in the presence of O_2 impurities (500 – 1000 ppm) in technical CO_2. Thirty-second short-term H_2 dropouts

show surface oxidation and reduction occurring after the seventh modulation cycle monitored in the center of the catalyst bed. The core of the Ni particles remained reduced, since full oxidation was interrupted. Nevertheless, catalyst deactivation occurred already after the first dropout since the oxidation of the active sites propagates stepwise through the catalyst bed starting from the reactor inlet. This gives important insight into the mechanism of the methanation reaction, and, obviously, even short interruptions in the H_2 feed, and thus, slight oxidation of the most active Ni sites cannot be tolerated by the catalyst. Therefore, it is important to prevent H_2 dropouts in industrial methanation applications, where traces of O_2 might be present. This can also be transferred to other power-to-chemicals processes using renewable H_2.

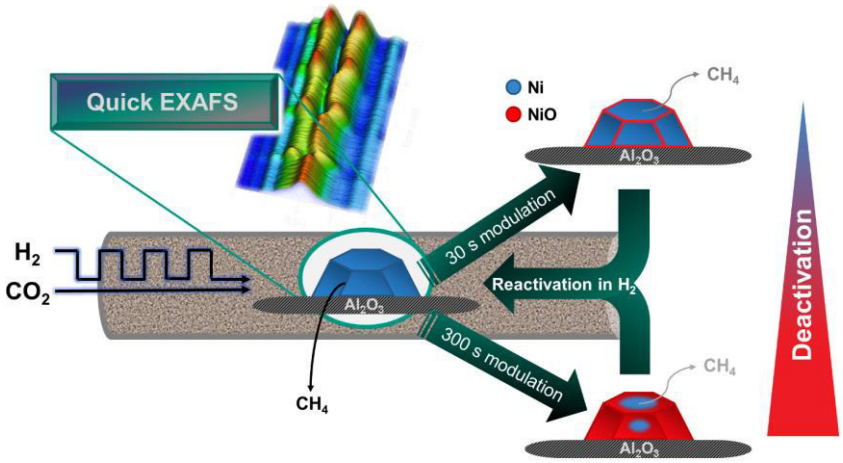

Scheme 3: Illustration of the QEXAFS experiment applying 30 s and 300 s modulations and the impact on the Ni particles of the model catalyst. Reproduced from Mutz *et al.*[223] under the terms and conditions of CC BY 4.0 license (http://creativecommons.org/licenses/by/4.0/), Copyright © 2017.

A higher impact on the deactivation was observed during 300 s modulation, where a bulk oxidation was observed even in the first H_2 dropout, which resulted in a higher fraction of oxidized Ni remaining on the catalyst during the methanation sequence and thus, an even lower CH_4 production. The presence of small amounts of oxygen in the CO_2 stream can already block a small fraction of most active Ni sites, which had a strong influence on the CO_2-methanation activity. This "titration" of active sites may be further used in future to understand the methanation of CO_2, but also other CO_2 hydrogenation

mechanisms in more detail. Variations in the Ni coordination numbers may indicate changes in the shape of the Ni particles such as flat reduced Ni particles with increased interacting area with the oxidic support and spherical particles of oxidized Ni. To investigate this mechanism of the oxidation propagating through the catalyst bed, spatially resolved *operando* EXAFS would provide important data to prove this theory.

In addition two possibilities to prevent the catalyst from oxidation in methanation applications *via* operational adjustments were presented. Constant catalytic performance over eight H_2 dropout cycles could be warranted using either a permanent H_2 background flow or utilizing the direct methanation of a CO_2/CH_4 mixture.

8 Formation of carbonaceous species during dynamic methanation[1]

8.1 Introduction

As discussed, the hydrogen feed produced *via* water electrolysis may underlie fluctuations depending on the availability of electricity generated from renewable resources. In the previous chapters 5 - 7 deactivation of a Ni-based catalyst was observed during H_2 dropouts, which was caused by oxidation of the active sites.[219,231] Usually, deactivation induced by carbon depositions does not occur during steady state CO_2 methanation under model gas compositions, since their formation is suppressed by the formed water during the reaction path.[53,93] However, the formation of carbonaceous deposits during dynamic reaction conditions is still under discussion. This might occur for example in CO_2 atmosphere caused by H_2 dropouts. Furthermore, such carbon depositions may be triggered by a CH_4 containing CO_2 feed, *e.g.* from biogas plants[8,24,124,138], from recycled gas streams[84,125,149] or from product formation along the fixed-bed reactor.

The methanation of CO and more recently CO_2 is well-known and thoroughly investigated process under steady state operation. The most commonly used catalysts for the methanation of CO_2 are Ni-based materials due to the low cost of the metal compared to *e.g.* Ru, which is especially more active at lower temperatures.[28,51,52] Ni-based catalysts have been improved specifically to enhance the catalytic performance and stability. As discussed in chapter 1.3.1 a bimetallic NiFe (Ni/Fe = 3) system was found to enhance conversion and selectivity in the methanation of CO_2.[87,91,104,106] Furthermore, the addition of a small amounts of Rh to a Ni/Al_2O_3 catalyst was reported to improve the

[1] The text and figures are taken from Mutz *et al.*:[211] B. Mutz, P. Sprenger, W. Wang, D. Wang, W. Kleist, J.-D. Grunwaldt, "*Operando* Raman spectroscopy on CO_2 methanation over alumina-supported Ni, Ni_3Fe and $NiRh_{0.1}$ catalysts: Role of carbon formation as possible deactivation pathway", *Appl. Catal. A* **2018**, *556*, 160-171.

activity and stability of the catalyst towards the methanation of CO_2 compared to the monometallic Ni catalyst due to enhanced Ni dispersion.[93]

Nevertheless, Ni catalysts are prone to form coke or carbon depositions in reactions containing CH_4 or CO (*e.g.* in reforming applications or syngas reactions).[139,144,153,154] A higher coking resistance in dry reforming application was once again reported for the NiFe catalyst, probably because of the oxidation of carbon deposits by lattice oxygen from FeO_x.[158,159] Furthermore, Ni catalysts promoted with small amounts of Rh exhibit a higher coke resistance in dry reforming applications.[160,161]

The nature, formation and removal of carbon deposits from CH_4 decomposition or in $CO/H_2/CH_4$ atmospheres have been investigated *ex situ, e.g.* by Takenaka *et al.*[163] or Bai *et al.*[162]. A particularly suited tool for the characterization of carbon depositions is Raman spectroscopy. Several Raman bands between 1000 and 2000 cm^{-1} are characteristic for certain carbonaceous species.[254-257] Since most of the investigations were performed *ex situ*, a more detailed insight into the formation and nature of the carbon deposits on a working catalyst requires spectroscopic studies under reaction conditions. *Operando* Raman spectroscopy was successfully applied in structural investigations of oxide catalysts by various groups.[258-261] Sattler *et al.*[200] recently investigated the nature of coke deposits during the dehydrogenation of propane, using *operando* Raman spectroscopy which was *e.g.* influenced by the H_2 concentration.

In this chapter, a monometallic 5 wt.% Ni/Al_2O_3 catalyst as well as state of the art bimetallic 5 wt.% Ni_3Fe/Al_2O_3 and 3.4 wt.% $NiRh_{0.1}/Al_2O_3$ systems with different catalytic properties were prepared, characterized using XRD, H_2-TPR, STEM-EDX as well as EELS, and tested for their catalytic performance in the methanation of CO_2. Then, these different catalyst systems were treated by various industrially relevant feed compositions related to the methanation of CO_2 while studying the formation of carbonaceous species in real time by *operando* Raman spectroscopy simultaneously. The main focus was on investigating the influence of CO_2 and CH_4 mixtures (in the absence of CO) on carbon formation. Thus, we elucidated the formation and nature of carbonaceous deposits in different and fluctuating reaction atmospheres, the effect on the catalytic activity and developed a reactivation strategy.

8.2 Characterization of the catalysts

Three Ni-based catalysts were synthesized and applied in this study to investigate the role of carbon deposition during methanation of CO_2 with various feed compositions. Apart from a monometallic 5 wt.% Ni/Al_2O_3 catalyst, a 5 wt.% Ni_3Fe/Al_2O_3 and a 3.4 wt.% $NiRh_{0.1}/Al_2O_3$ bimetallic catalyst were prepared by homogeneous deposition-precipitation. The elemental composition of the catalysts determined by ICP-OES is shown in Table 9. The molar Ni/Fe ratio was 3:1 and Ni/Rh ratio was 11:1, respectively. Note that the total metal loading of the $NiRh_{0.1}$ catalyst (3.6 wt.%) was lower compared to the Ni and Ni_3Fe catalysts (4.9 wt.% and 4.6 wt.%, respectively). In general, no significant decrease of the specific surface areas (Table 9) was observed for the different catalysts, which indicates that pore blockage or structural changes did not occur throughout precipitation and calcination.

Table 9: Elemental composition determined by ICP-OES and specific surface area from BET analysis of the three catalyst materials. Reproduced from Mutz *et al.*[211] Copyright © 2018 Published by Elsevier B.V.

Sample	Ni [wt.%]	Fe [wt.%]	Rh [wt.%]	S_{BET} [$m^2\ g^{-1}$]
γ-Al_2O_3 support	-	-	-	202
5 wt.% Ni/Al_2O_3	4.9	-	-	192
5 wt.% Ni_3Fe/Al_2O_3	3.5	1.1	-	187
3.4 wt.% $NiRh_{0.1}/Al_2O_3$	3.1	-	0.5	185

For the catalysts, XRD analysis showed only reflections of the γ-Al_2O_3 support (see Appendix, Figure S 21). No reflections of metal oxides or reduced metal species were observed, which indicates the presence of rather small crystallite sizes.

Scanning transmission electron microscopy was applied on the reduced catalyst samples to identify the morphology of the catalysts and to further estimate the size of the metal nanoparticles. The STEM images showed uniformly sized metal particles for the 5 wt.% Ni/Al_2O_3 (3.4 ± 0.7 nm, Figure 45 a)) and the 5 wt.% Ni_3Fe/Al_2O_3 catalyst (2.9 ± 0.8 nm, Figure 45 b)). The derived metal dispersion according to the method in Ref[210] was about 27 % and 32 %, respectively.

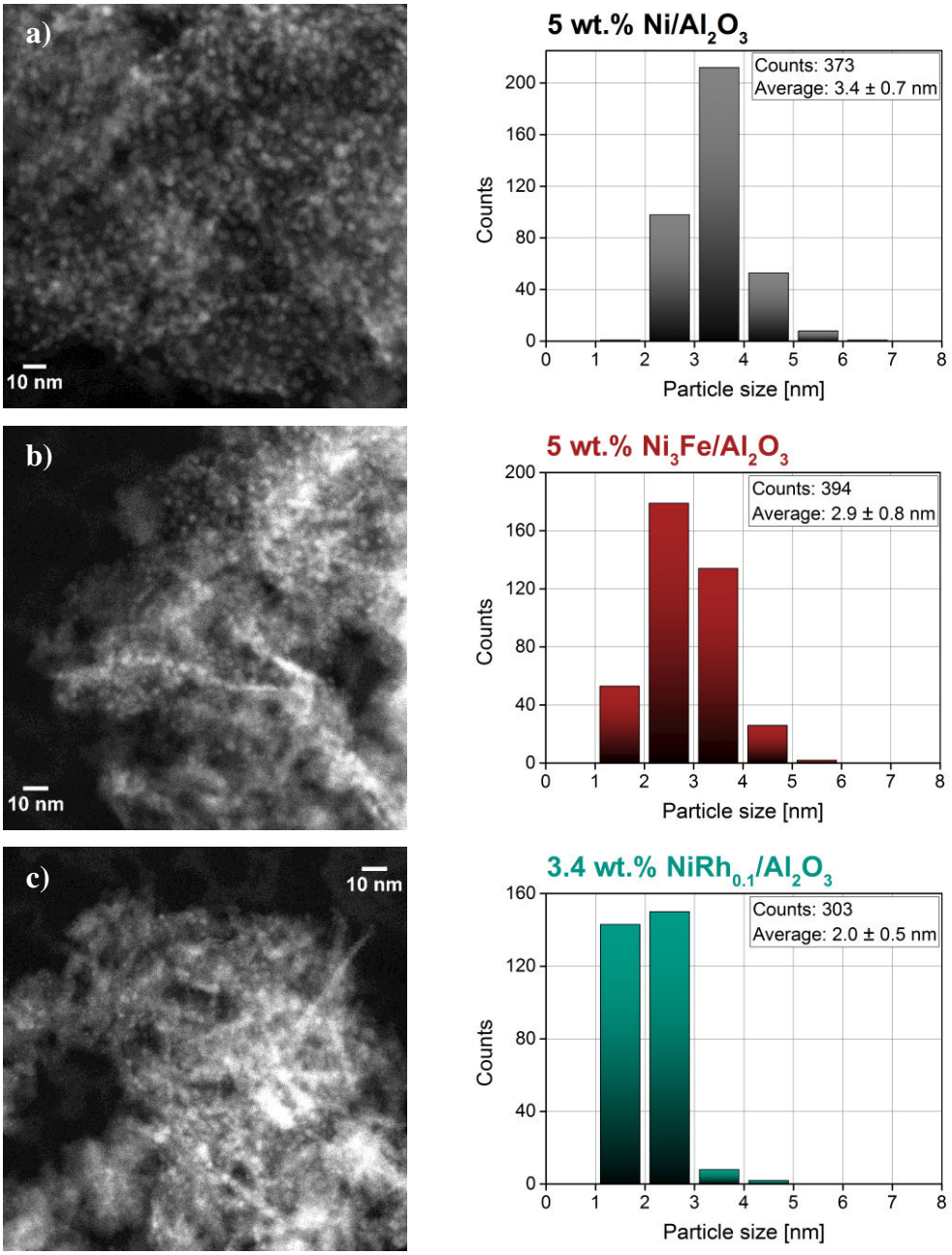

Figure 45: STEM-HAADF images (left) and metal particle size distribution (right) of a) 5 wt.% Ni/Al_2O_3, b) 5 wt.% Ni_3Fe/Al_2O_3 and c) 3.4 wt.% $NiRh_{0.1}/Al_2O_3$. The catalysts were reduced prior to the measurements at 500 °C (5 K min^{-1}) in 50 %H_2/N_2 for 2 h. Reproduced from Mutz *et al.*[211]

Further analysis of the composition using STEM-EDX in large regions (Table S 7 in the Appendix) revealed variations of the Ni/Fe ratios between 1.9:1 and 10.2:1. Smaller regions were investigated by STEM-EELS spectrum imaging (Figure S 22) and showed

that the metal nanoparticles can be monometallic Ni and bimetallic NiFe particles, which explains the variation of Ni/Fe ratio. The metal particles of the 3.4 wt.% $NiRh_{0.1}/Al_2O_3$ catalyst were slightly smaller (2.0 ± 0.5 nm, Figure 45 c)) than those of the Ni and Ni_3Fe catalysts. This may be explained by the lower metal loading of the $NiRh_{0.1}$ catalyst or by a milder reduction in the presence of Rh.[93,262] The dispersion of the metal particles was derived as 42 %. The elemental composition obtained from STEM-EDX analysis in large regions revealed a more pronounced deviation of the Ni/Rh ratio compared to the Ni_3Fe catalyst (Table S 8). An average Ni/Rh ratio gave a value of 19:1, which emphasizes the higher degree of segregation for the $NiRh_{0.1}$ catalyst. In conclusion, homogeneous deposition-precipitation resulted in similar particle sizes for all three catalysts which simplifies comparison. In general it appears to be a well-suited method to obtain small Ni, Ni-Fe and Ni-Rh particles with narrow size distribution, as proposed earlier for such Ni-based catalysts.[231-233] However, a higher metal loading of the catalysts and, thus, larger particles might have resulted in a more homogeneous dispersion of both metals on the bimetallic catalysts and a higher yield of the desired alloys (see chapter 9).

H_2-TPR was used to study the reducibility of the catalysts and thus to gain, in comparison with literature, complementary information on the phase composition of the catalysts. Note that the conditions during the TPR experiment (10 % H_2/Ar, 10 K min^{-1}), which allowed the identification of different species on the catalyst, were different compared to the activation procedure used for the *ex situ* characterization (50 % H_2/N_2, 500 °C, 2 h). The TPR profile (Figure 46) of the Ni catalyst showed a H_2 consumption in a small temperature range with a main peak at 580 °C attributed to reduction of NiO to Ni and a shoulder at 720 °C, which might originate from the reduction of smaller NiO particles with stronger interaction with the support. Mixed oxide formation such as $NiAl_2O_4$ would have resulted in TPR peaks at temperatures ≥ 800 °C.[86,263] Larger Ni particles would have shown reduction peaks at low temperatures. Both species were not observed here and, therefore, the TPR results supported the results obtained by STEM and also XRD, that the catalyst exhibited small particles, a narrow size distribution and the absence of large agglomerates.

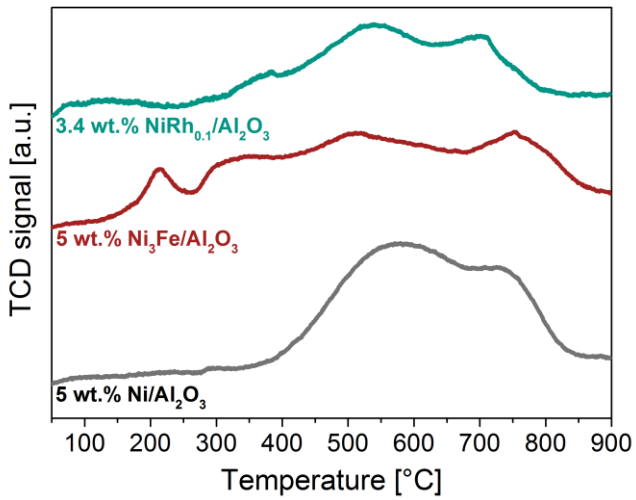

Figure 46: H_2-TPR measurements of the 5 wt.% Ni/Al_2O_3, 5 wt.% Ni_3Fe/Al_2O_3 and 3.4 wt.% $NiRh_{0.1}/Al_2O_3$ catalysts in 10 % H_2/Ar (10 K min^{-1}). Reproduced from Mutz *et al.*[211] Copyright © 2018 Published by Elsevier B.V.

Next to the main reduction peaks the TPR profile of the bimetallic Ni_3Fe catalyst featured a peak at 210 °C, which is assigned to the reduction of Fe_2O_3 to Fe_3O_4. The overlapping peaks between 350 - 650 °C can be attributed to the reduction of Fe_3O_4 to Fe and NiO to Ni.[105,264,265] Noble metal promotion of the Ni catalyst with Rh led to a shift of the reduction peaks by about 30 - 40 °C to lower temperatures compared to the monometallic catalyst (580 °C to 540 °C and 720 °C to 690 °C), probably due to hydrogen spillover.[93,160,161,266]

8.3 Catalytic performance and parameter screening

The 5 wt.% Ni/Al_2O_3, 5 wt.% Ni_3Fe/Al_2O_3 and 3.4 wt.% $NiRh_{0.1}/Al_2O_3$ catalysts were tested for the methanation of CO_2 in a temperature range of 200 – 450 °C (Figure 47) after *in situ* reduction (2 h, 50 % H_2/N_2, 500 °C *cf.* experimental details in section 3.3) in a lab-scale fixed-bed reactor.

In general, the conversion of CO_2 (Figure 47 a)) started between 200 and 250 °C and increased with temperature for all three catalysts. The catalytic performance of the catalyst systems diverged at around 300 °C. The highest activity was achieved using the Ni_3Fe catalyst (30 %), while Ni (19 %) and $NiRh_{0.1}$ (13 %) were less active. The promoting effect of Fe was most pronounced at 300 – 350 °C, where enhanced catalytic performance was achieved compared to the Ni and $NiRh_{0.1}$ systems. The highest conversion of CO_2 using Ni and Ni_3Fe catalysts was achieved at 400 °C (75 % and 70 %, respectively). The best results for the $NiRh_{0.1}$ catalyst were obtained at 450 °C (67 % conversion of CO_2). In comparison to the Ni and Ni_3Fe catalysts, the $NiRh_{0.1}$ system gave the lowest conversion of CO_2 over the full temperature range.

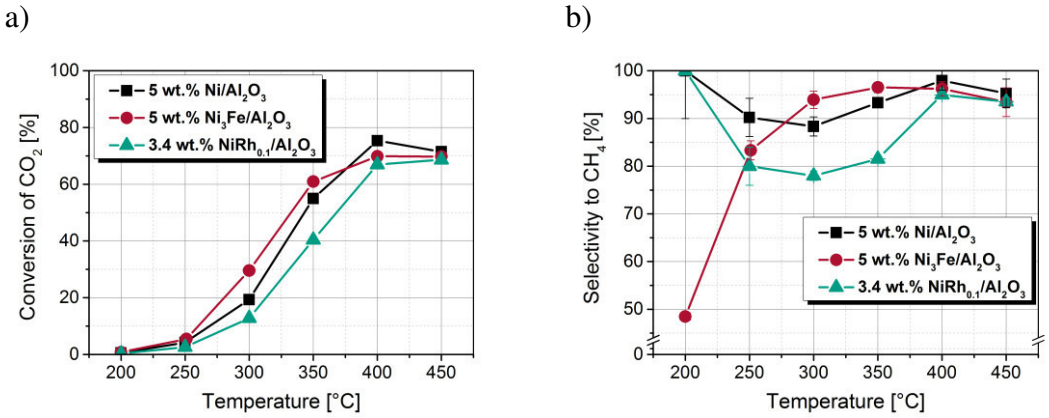

Figure 47: Catalytic performance of the 5 wt.% Ni/Al_2O_3 (squares, black), 5 wt.% Ni_3Fe/Al_2O_3 (circles, red) and 3.4 wt.% $NiRh_{0.1}/Al_2O_3$ (triangle, green) catalysts in the methanation of CO_2 (H_2/CO_2 = 4, 50 % N_2, 1 bar, 6000 $mL_{CO2}\ g_{cat}^{-1}\ h^{-1}$); a) conversion of CO_2 and b) selectivity to CH_4. Reproduced from Mutz *et al.*[211] Copyright © 2018 Published by Elsevier B.V.

CO was the main byproduct during the catalytic tests. Additionally, traces of C_2-hydrocarbons (< 1 %) were produced by the Ni and Ni_3Fe catalysts at 300 °C. At 200 °C, the selectivity for the Ni_3Fe catalyst was low, however, the conversion of CO_2 was < 1 % and, therefore, the produced amount of CO was negligible. At 250 °C, the selectivity towards CH_4 (Figure 47 b)) was highest for the Ni catalyst (90 %), whereas more CO was formed by the Ni_3Fe and $NiRh_{0.1}$ catalysts. The selectivity towards CH_4 achieved by the Ni_3Fe catalyst increased significantly with the temperature to 94 – 97 % at 300 – 350 °C, leading to the highest values in this temperature range. At 400 °C, all catalysts produced

CH_4 with a selectivity of 95 – 98 %. The selectivity decreased slightly to 93 – 95 % at higher temperatures due to the thermodynamic equilibrium and the endothermic reverse water-gas shift reaction.[53]

As the metal loading and the dispersion of the catalysts were slightly different, the TOFs were estimated at 250 °C and 300 °C (Table 10). At 250 °C, similar TOFs were achieved for the Ni and Ni_3Fe catalysts (0.012 s^{-1} and 0.013 s^{-1}, respectively). At 300 °C, a higher TOF was found for the Ni_3Fe catalyst (0.078 s^{-1}) compared to the monometallic Ni catalyst (0.055 s^{-1}), highlighting the synergetic effect of Ni and Fe. The $NiRh_{0.1}$ catalyst showed the lowest TOFs of 0.006 s^{-1} and 0.028 s^{-1} at 250 °C and 300 °C, respectively. Note that the TOF for the Ni_3Fe catalyst at 300 °C was calculated with a conversion (30 %), which is not fully differential. Therefore, the rate might be even higher in reality.

Table 10: Metal dispersion (estimated from STEM images) and turnover frequencies for the 5 wt.% Ni/Al_2O_3, 5 wt.% Ni_3Fe/Al_2O_3 and 3.4 wt.% $NiRh_{0.1}/Al_2O_3$ catalysts calculated at 250 °C and 300 °C considering the yield of CH_4. Reproduced from Mutz *et al.*[211] Copyright © 2018 Published by Elsevier B.V.

Catalyst	Dispersion [%]	TOF (250 °C) [s^{-1}]	TOF (300 °C) [s^{-1}]
5 wt.% Ni/Al_2O_3	27	0.012	0.055
5 wt.% Ni_3Fe/Al_2O_3	32	0.013	0.078
3.4 wt.% $NiRh_{0.1}/Al_2O_3$	42	0.006	0.028

A comparison of CO_2 conversion and reaction rates with literature values is difficult due to the different reaction conditions. Nevertheless, the TOFs obtained in this work are in a similar order of magnitude as reported for 15 - 20 wt.% Ni/Al_2O_3 systems in literature.[61,62,69] The high activity achieved by the Ni_3Fe system within this study is in agreement with CO methanation data, where Ni_3Fe has been reported to be more active than monometallic Ni catalysts.[102,103] This trend was further observed for the methanation of CO_2.[87,104,267] Thus, it can be expected that the reverse water-gas shift reaction occurred fast at the catalysts surface in the mid-temperature regime. The enhanced performance of the Ni_3Fe system in the methanation of CO_2 may be explained by its higher activity in the dissociation of CO.[87,100,101,103] In this study, the addition of

Rh did not offer the expected positive effect on the catalytic activity for the methanation of CO_2 as reported for a $NiRh_{0.1}$ catalyst supported on Ce/Zr mixed oxide.[93] This may explained by an insufficient intermixing of the metals or different support interactions. In general, the catalysts achieved high activity and selectivity at 400 °C and represent state of the art methanation catalysts, which are well-suited for *operando* Raman spectroscopic studies to investigate the formation of carbonaceous species during CO_2 methanation (in the absence of CO).

8.4 Methane initiated catalyst deactivation and reactivation in the lab-scale reactor

In a fist attempt, we investigated the impact of triggered carbon poisoning on the catalytic performance of the 5 wt.% Ni/Al_2O_3, 5 wt.% Ni_3Fe/Al_2O_3 and 3.4 wt.% $NiRh_{0.1}/Al_2O_3$ catalysts. For this purpose, CH_4/N_2 was fed to the catalysts to produce carbon deposits initiated by methane decomposition.[163,268] The experiments were conducted in the lab-scale reactor at 400 °C, *i.e.* the temperature at which the highest CO_2 conversion was observed during the catalytic performance tests (see section 8.3). The results are shown in Figure 48 and represent the basis for the *operando* Raman spectroscopy studies in section 8.5.

The test in standard CO_2 methanation reaction at 400 °C for 30 min ("Phase A") showed a similar trend in the catalytic activity for the three catalysts ($Ni > Ni_3Fe > NiRh_{0.1}$) as during the catalytic performance tests in section 8.3. The CO_2 conversion for all catalysts was slightly lower probably due to the higher inert gas flow and, thus, less hot spot formation. In the following "Phase B", the catalysts were exposed to 4 % CH_4 / N_2 for 30 min to induce carbon depositions. The decomposition of CH_4 over Ni/Al_2O_3 catalysts was reported to start around 250 °C and to accelerate above 400 °C.[257] Thus, a mild carbon formation was expected in the present experiments. In "Phase C", a second CO_2 methanation sequence was applied in order to unravel possible deactivation caused by the expected carbonaceous deposits compared to the results of the fresh catalysts in "Phase A". All three catalysts showed a remarkable decline in CO_2

conversion as well as an extensive shift of the selectivity towards CO. In case of the Ni catalyst, the CO_2 conversion dropped significantly to 30 % ("Phase A": 71 %). The selectivity towards CH_4 of the carbon-covered catalysts decreased in the order of $NiRh_{0.1}$ (39 %) > Ni (30 %) > Ni_3Fe (24 %). The deactivation seemed to be less pronounced (but still intensive) for the $NiRh_{0.1}$ catalyst, whereas the largest amount of CO was produced by Ni_3Fe. Obviously, the active sites of the catalysts were blocked, inhibiting the hydrogenation of CO_2 to CH_4. Instead, CO was formed by the Boudouard reaction or by an incomplete reduction since the poisoned metal particles could not provide a sufficient number of H atoms. Due to the short reaction periods of 30 min, significant sintering of the metal particles which might influence the catalytic performance are unlikely, especially as we did not see such an effect in a chapter 7.

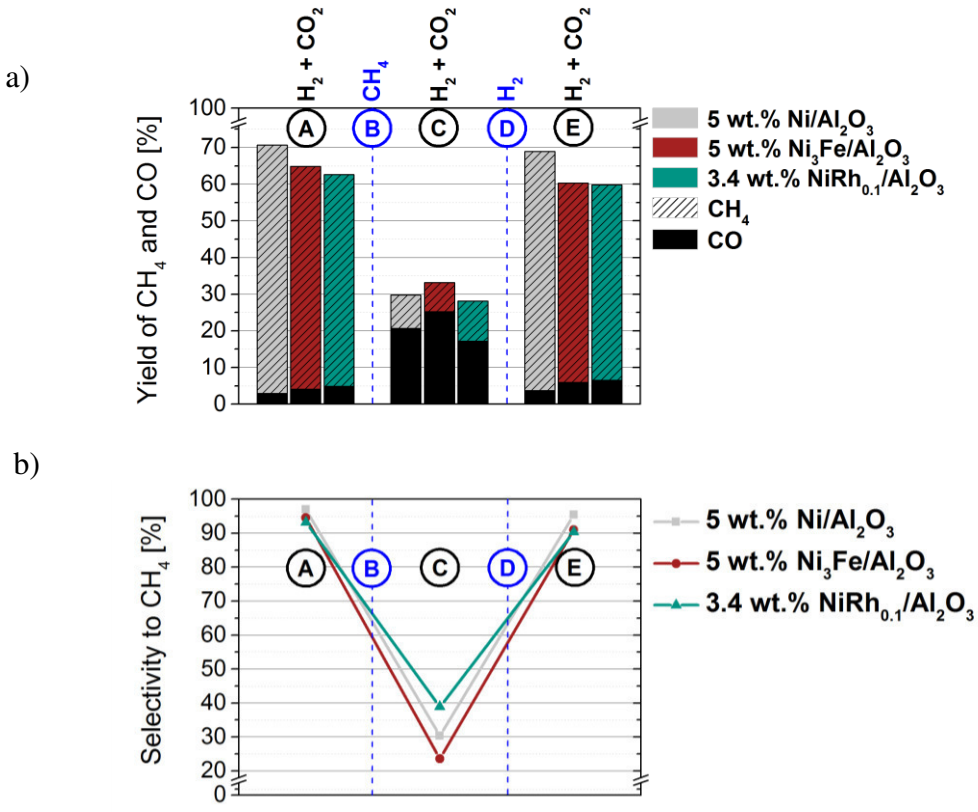

Figure 48: a) yields of CH_4 and CO during the methanation of CO_2 and b) selectivity towards CH_4 of the 5 wt.% Ni/Al_2O_3, 5 wt.% Ni_3Fe/Al_2O_3 and 3.4 wt.% $NiRh_{0.1}/Al_2O_3$ catalysts exposed to different phases at 400 °C. 1 bar, 6000 $mL_{CO2}\ g_{cat}^{-1}\ h^{-1}$, TOS 30 min): (A) 5 % CO_2 + 20 % H_2 / N_2, (B) 4 % CH_4 / N_2, (C) 5 % CO_2 + 20 % H_2 / N_2, (D) 50 % H_2 / N_2 at 500 °C, TOS 60 min and (E) 5 % CO_2 + 20 % H_2 / N_2 (see Table 3 in section 3.3.3). Reproduced from Mutz *et al.*[211] Copyright © 2018 Published by Elsevier B.V.

To reactivate the catalysts, a 1 h period of 50 %H_2/N_2 at 500 °C ("Phase D") was applied followed by another CO_2 methanation sequence at 400 °C ("Phase E"). High activity was restored for all catalysts after reactivation, matching nearly the results of the fresh samples in "Phase A". 69 % of CO_2 was converted by the Ni catalyst ("Phase A": 71 %) with a selectivity of 91 % towards CH_4 ("Phase A": 95 %). A similar behavior was observed for the Ni_3Fe and $NiRh_{0.1}$ catalysts (*cf.* Figure 48). Within this experiment, drastically inhibited catalyst activity in the methanation of CO_2 was observed induced by a period of CH_4 atmosphere.

The deactivation was expected to derive from carbon deposition. Thus, the formation and nature of such carbon deposits need to be investigated in more detail under reaction conditions. Furthermore, it is crucial to unravel whether such depositions may occur under non-steady state CO_2 methanation conditions using model gas compositions but rather during methanation of CO_2 containing CH_4 as discussed above. Additionally, fluctuations in the H_2 feed from renewable energies may result in a feed consisting of CO_2/CH_4 typical for dry reforming applications, which is known to lead to serious carbon formation on the catalyst.[154,155,269,270] A suitable tool to study the formation of carbonaceous species under reaction conditions is *operando* Raman spectroscopy.[185,200]

8.5 Monitoring the formation of carbon deposits *via operando* Raman spectroscopy

The quantitative results from the experiments in the lab-scale reactor (section 8.4) showed that carbon depositions might cause significant catalyst deactivation. Based on these findings the potential formation and the type of carbon deposits was investigated on the three different catalyst systems (5 wt.% Ni/Al_2O_3, 5 wt.% Ni_3Fe/Al_2O_3 and 3.4 wt.% $NiRh_{0.1}/Al_2O_3$) under various realistic feed gas compositions related to the methanation of CO_2 using *operando* Raman spectroscopy (Figure 49). Since the catalytic behavior of the three different catalysts was similar in section 8.4 as well as their structural changes during the *operando* Raman spectroscopy experiments, only the results of the Ni catalyst are discussed in this section as an example. If the results between the

catalyst systems differ, they will be discussed in the text. The full data sets of the Ni_3Fe and $NiRh_{0.1}$ catalyst are provided in the Appendix. The *operando* Raman spectroscopy experiments in this chapter were acquired in cooperation with Paul Sprenger (ITCP, KIT).

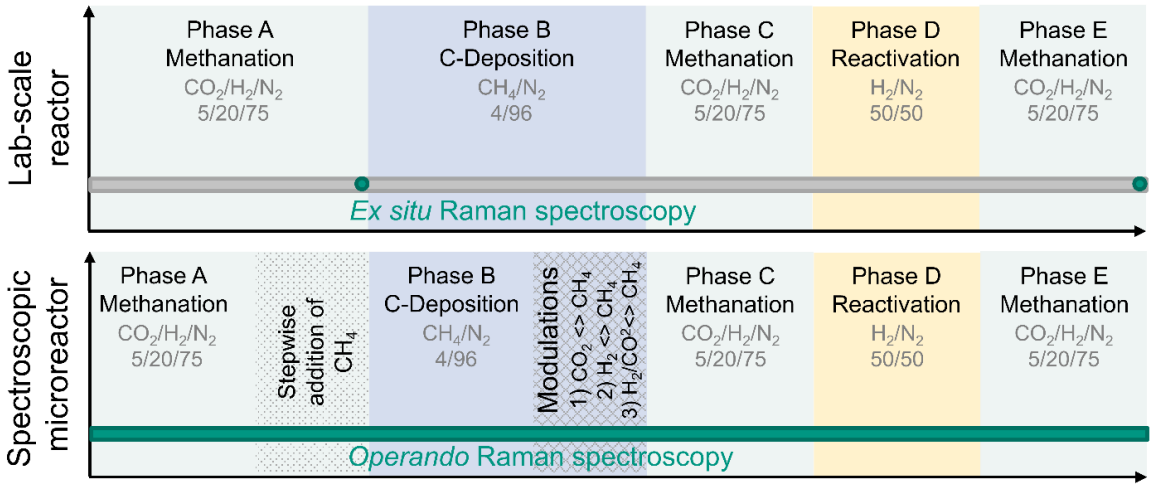

Figure 49: Summary of the applied gas mixtures in the lab-scale reactor and in the spectroscopic microreactor. Reproduced from Mutz *et al.*[211] Copyright © 2018 Published by Elsevier B.V.

8.5.1 Probing carbon formation under variegating feed concentrations ("Phase A")

Figure 50 shows the *operando* Raman spectra recorded on the 5 wt.% Ni/Al_2O_3 catalyst using the spectroscopic fixed-bed microreactor. The Raman spectra were recorded continuously while various gas mixtures were screened, which are relevant for methanation applications and may occur, if *e.g.* renewable energy sources cause fluctuations in the H_2 feed.[38] The full data sets of the *operando* Raman spectroscopy experiments with the corresponding MS data are given in the Appendix (Figure S 29 - Figure S 32). Note that the temperature in the spectroscopic microreactor was slightly lower (370 °C) during the *operando* Raman spectroscopy experiment compared to the experiment performed in the lab-scale reactor (400 °C) due to the different setup and heat sources.

First, CO_2 methanation was performed, which is comparable to "Phase A" applied in the lab-scale reactor experiments. During this 30 min sequence, no Raman bands from

carbonaceous species could be observed (Figure 50), which should appear between 1000 and 2000 cm^{-1}.[254-257] Subsequently, 4 % of CH_4 was added to the initial CO_2/H_2 gas mixture (GHSV was kept constant) to mimic *e.g.* a second reactor stage or biogas as feedstock. As shown by *operando* Raman spectroscopy on the Ni catalyst (Figure 50) and also for the other two catalysts (Figure S 29 b) and c)), no formation of carbonaceous species occurred during this period. Therefore, the utilization of a CO_2/CH_4 = 5/4 mixture for the methanation of CO_2 should be possible without major influences concerning catalyst deactivation or reduced CH_4 formation (*cf.* Figure S 36).

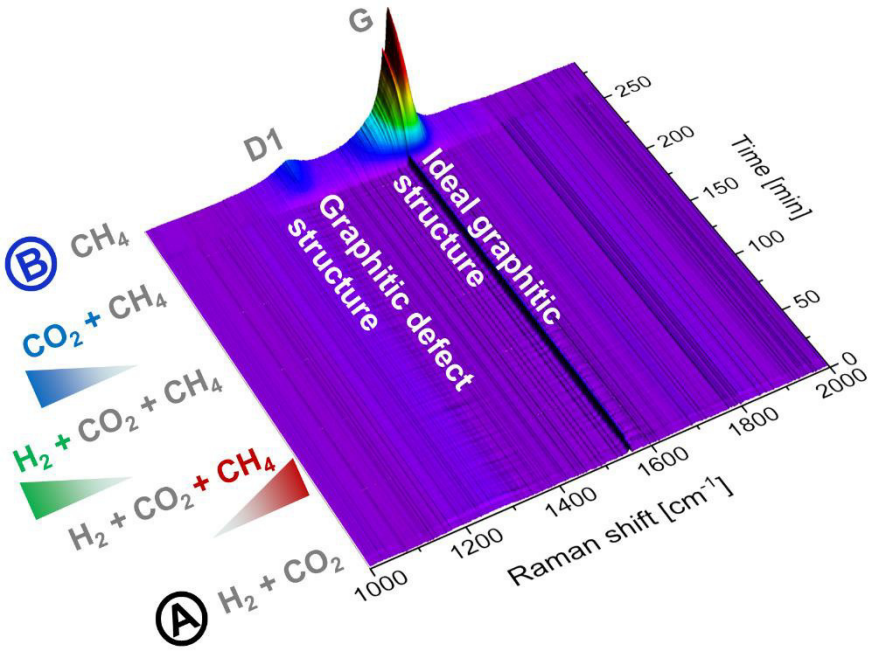

Figure 50: Raman spectra recorded continuously applying various gas mixtures during the methanation of CO_2 using the 5 wt.% Ni/Al_2O_3 catalyst and the spectroscopic fixed-bed microreactor (370 °C, 1 bar, 6000 mL_{CO2} g_{cat}^{-1} h^{-1}). Reproduced from Mutz *et al.*[211] Copyright © 2018 Published by Elsevier B.V.

Next, the H_2 flow was decreased, culminating in a complete H_2 dropout. In this period a CO_2/CH_4 = 5/4 mixture was fed to the catalyst. During this period also no carbon deposition was observed by Raman spectroscopy in contrast to dry reforming over Ni-based catalysts, where serious carbon disposition has been reported.[155,270,271] This might be due to the lower temperature applied in the methanation of CO_2 and, thus, milder conditions whereby carbon dioxide, for example, well adsorbs on the Ni-surface and

prevents methane dissociation. A complete H_2 dropout during the conventional methanation (CO_2/H_2) was also performed in a separate experiment similar to earlier *operando* XAS studies (chapters 5 - 7) considering fluctuations in the H_2 feed.[38,219,231] Also under these conditions no carbon bands were observed by Raman spectroscopy (Figure S 24). Thus, CO_2 dissociation did not take place on the catalyst surface in the absence of H_2[223] and, further, emphasizes, that the deactivation from H_2 interruptions as studied in the earlier chapters is caused by catalyst oxidation exclusively.

In summary, none of the applied feed compositions resulted in detectable carbon depositions on any of the Ni-based catalysts until this point (Figure 50, time = 260 min). Note that these experiments were performed in short-term periods (TOS of 30 – 60 min each gas atmosphere) at a reaction temperature where high selectivity was achieved by the catalysts. Further long-term studies (TOS > 2 days) under harsh reaction conditions should be applied to investigate further the reaction time and the influence of CO on the formation of carbon deposits. In this study we focused on the application of *operando* Raman spectroscopy for studying the influence of CH_4 and modulations of the gas atmospheres on carbon formation.

8.5.2 Forced carbon deposition by methane decomposition (“Phase B”)

Similar to the lab-scale experiment in “Phase B” (section 8.4) 4 % CH_4/He was fed to the reactor. Intensive Raman bands evolved as shown in Figure 50 and Figure 51 (as well as Figure S 29 b) and c) for Ni_3Fe and $NiRh_{0.1}$, respectively), which were referred to an ideal graphitic (G band, 1574 cm^{-1}) and a disordered graphitic lattice (D1 band, 1324 cm^{-1}).[254,272] The assignment of the Raman bands is further explained in the Appendix (Table S 9, Table S 10 as well as Figure S 25). The evolution of the G and D1 band intensities as a function of time is plotted in Figure 52. The intensities of the characteristic G and D1 Raman bands for the Ni catalyst increased steadily over time and no plateau was reached after 30 min, when treated with CH_4/He. A more distinctive rise in the band intensity was observed for the $NiRh_{0.1}$ catalyst, which reached a plateau after 20 min (Figure S 32).

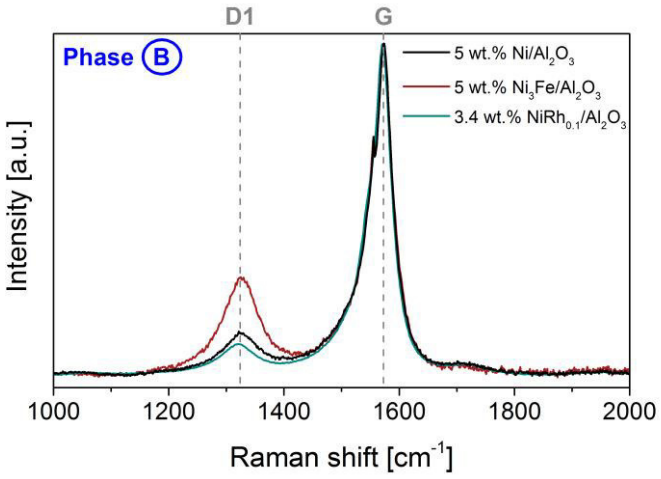

Figure 51: *Operando* Raman spectra recorded for the 5 wt.% Ni/Al_2O_3, 5 wt.% Ni_3Fe/Al_2O_3 and 3.4 wt.% $NiRh_{0.1}/Al_2O_3$ catalysts after exposure in a 4 % CH_4 / He atmosphere (370 °C, 1 bar, 6000 mL_{CO2} g_{cat}^{-1} h^{-1}, TOS = 30 min) corresponding to Phase B in the lab-scale reactor experiments. Reproduced from Mutz *et al.*[211] Copyright © 2018 Published by Elsevier B.V.

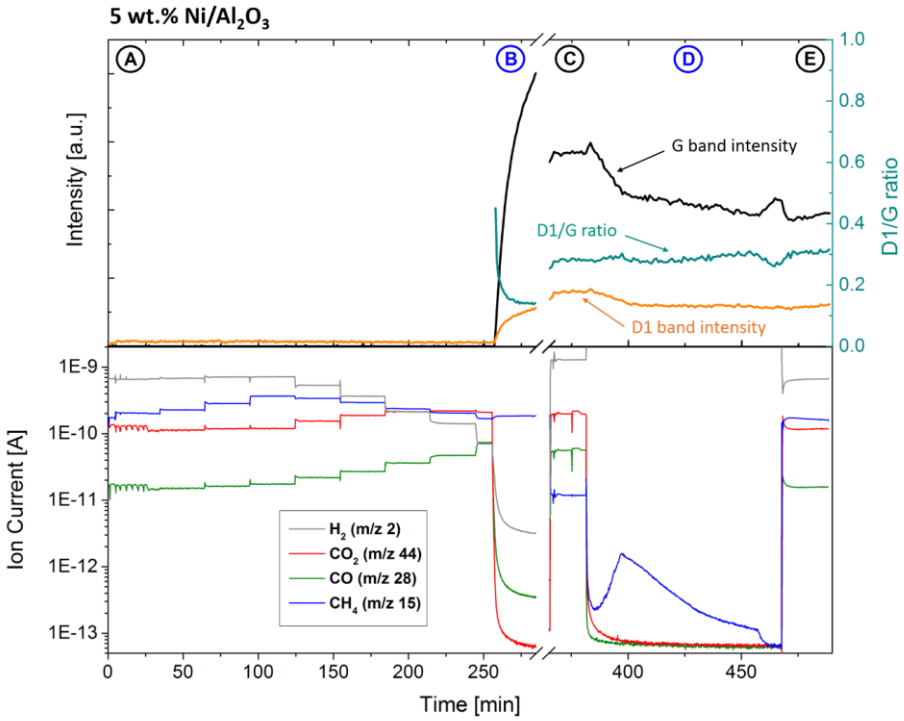

Figure 52: Intensities of the characteristic G and D1 Raman bands and the corresponding mass spectrometer data for the reaction cycle monitored *in situ* over the 5 wt.% Ni/Al_2O_3 catalyst in the spectroscopic fixed-bed microreactor (370 °C, 1 bar, 6000 mL_{CO2} g_{cat}^{-1} h^{-1}). The Phases A-E correspond to the experiments in the lab-scale reactor in section 3.3. The gas modulations were cut out and discussed in the following section, the full experiment is shown in the Appendix. Reproduced from Mutz *et al.*[211] Copyright © 2018 Published by Elsevier B.V.

Figure 51 shows the normalized Raman spectra of the Ni, Ni_3Fe and $NiRh_{0.1}$ catalysts after CH_4 exposure ("Phase B"). The D1/G ratio observed for the Ni (0.15), Ni_3Fe (0.37) and $NiRh_{0.1}$ (0.1) catalyst indicate a high crystallinity and an ordered structure of the graphitic carbon species. The narrow band widths of the intense D1 and G bands found for all catalysts and the absence of other intense D bands (*cf.* Table S 9), which are typical for amorphous carbon indicated the presence of graphitic carbon.[256,273]

The formation of carbon nanofibers can be ruled out since those species result in Raman spectra with a D1/G ratio of 1 - 2[268,274] and in an additional band at 100 – 300 cm^{-1} (radial breathing mode),[275,276] which was not observed in *ex situ* measurements. The low D1/G ratios of the Raman bands obtained in this study were in agreement with the Raman spectrum of graphite.[274] Other studies showed, that the carbon whiskers or nanotubes were formed in various CH_4 containing mixtures, but these studies were performed at higher temperatures (≥ 500 °C, *cf.* Refs[157,162,163]).

8.5.3 Nature of the carbon deposits under fluctuating conditions

The catalysts were rather resistant towards carbon deposition under various gas mixtures as shown in the previous section. However, dosing pure methane triggered the formation of carbonaceous species. In this section, the behavior and reactivity of the carbon deposits was investigated applying different modulations of the feed gas (between "Phase B" and "Phase C"). The modulation of $CH_4 \leftrightarrow CO_2$ (5 min each atmosphere, Figure 53) revealed that carbon is removed in the 5 % CO_2 periods either due to the Boudouard reaction or due to traces of O_2 (not detectable by mass spectrometry), which might have oxidized the carbon species. The removal of carbon in the presence of CO_2 was fast in the first minute and slowed down in the following minutes. This might indicate different kinds of carbon, the one easily removable and the other hardly removable carbon. Switching to CH_4 atmosphere led again to the formation of carbon deposits.

A similar behavior was observed during the $CH_4 \leftrightarrow H_2$ modulation (Figure S 34). Carbon deposits were removed in H_2, especially in the first cycle, but to a fewer extent than in CO_2 atmosphere. Also, this effect declined over cycles and was negligible at the

end of the modulation. The modulation of $CH_4 \leftrightarrow CO_2/H_2$ (methanation conditions) did not have a significant influence on the Raman bands referred to the carbon species (Figure S 35). Overall, the D1/G ratio increased during the modulations (Figure 52), indicating the formation of defects in the graphitic structure or decreasing graphite crystallite sizes over time.[200] The band positions did not change during the experiments. Modulations showed dynamic changes in the structure of the carbon species, which could be detected in real time by *operando* Raman spectroscopy. Those changes have to be investigated in more detail in future studies and might give a deeper insight in the nature and the reactivity of different carbonaceous species formed during the catalytic reactions.

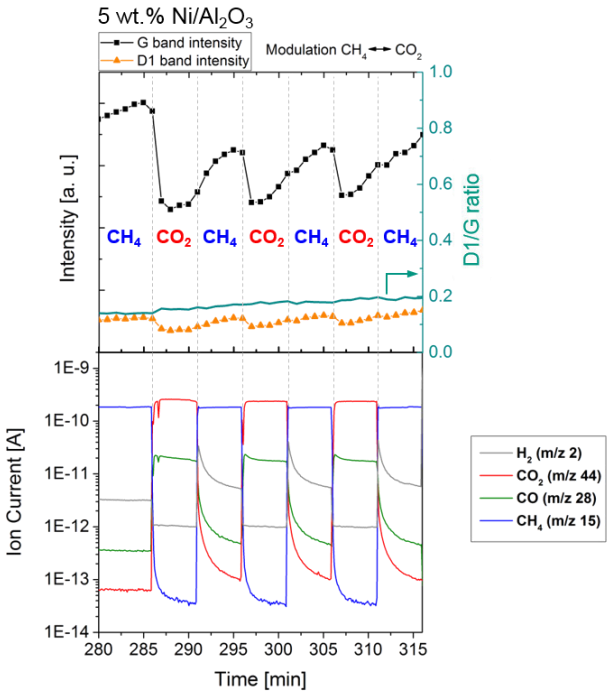

Figure 53: *Operando* Raman spectroscopy during the modulation between $CH_4 \leftrightarrow CO_2$ using the 5 wt.% Ni/Al_2O_3 catalyst. Conditions: 370 °C, 1 bar, 6000 $mL_{CO2}\ g_{cat}^{-1}\ h^{-1}$, gas composition *cf.* Table 6, 5 min each atmosphere. Reproduced from Mutz *et al.*[211] Copyright © 2018 Published by Elsevier B.V.

8.5.4 Reactivation of the catalyst

The carbon covered catalysts were then applied in a second CO_2 methanation sequence "Phase C". As expected, the MS data in Figure 52 showed a less intense MS

signal of CH_4 (m/z 15) compared to "Phase A" emphasizing the deactivation of the catalyst. This is in line with the deactivation, observed in lab-scale reactor tests in section 8.4. Within 15 - 20 min reaction time, no significant changes of the Raman bands were monitored indicating that the CO_2/H_2 mixture was not suited to remove the carbon deposits. Consequently, a reactivation step in 50 % H_2/He atmosphere at 500 °C was applied ("Phase D"). A decline of Raman D1 and G band intensities was observed, firstly, due to a temperature increase from 370 °C to 510 °C and, secondly, due to the successful reduction of carbon deposits to CH_4, which could be observed in the MS data. The amount of carbon species on the catalyst decreasing as indicated by a decreasing CH_4 formation. However, the CH_4 signal in the MS did not disappear fully after 60 min of reactivation and the Raman carbon bands were still present. This also indicated different kind or differently located carbon, which are rather easy to remove as already suggested in section 8.5.3. A reactivation under oxidizing conditions with CO_2 or O_2 at elevated temperatures might have been more efficient.[163,269] However, an additional reactivation step in H_2 would have been necessary afterwards due to a likely oxidation of the active sites, as discussed in the chapters 5-7.

After the H_2 treatment, a third CO_2 methanation sequence was performed ("Phase E"). As shown in Figure 52, the MS signals of CH_4, CO, H_2 and CO_2 (m/z 15, 28, 2 and 44) reached similar levels as the fresh catalyst during "Phase A". This is in agreement with the results from the quantitative experiments in the lab-scale reactor (section 8.4). Obviously, the active sites of the catalysts were again accessible reaching full catalytic performance. On the other hand, intensive Raman bands corresponding to graphitic carbon were still present. The Raman bands were less intense compared to those after methane decomposition in "Phase C", therefore the carbon species were partly removed during the reactivation in H_2.

In general, the *operando* Raman spectroscopy experiments can be correlated with the catalytic tests in the lab-scale reactor concerning both, the catalytic activity and carbon formation. Raman spectroscopy was performed *ex situ* on the catalyst taken from the lab-scale reactor after "Phase A" and "Phase E" (Figure 54). The *ex situ* (lab-scale reactor) as well as the *in situ* (spectroscopic microreactor) measurements confirm that no carbon deposition was formed during the methanation of CO_2 ("Phase A").

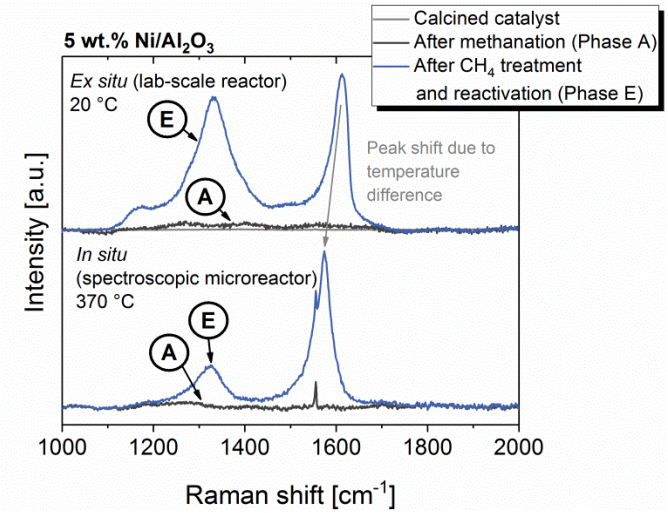

Figure 54: Raman spectra of 5 wt.% Ni/Al_2O_3 after "Phase A" and "Phase E" of both, lab-scale reactor (*ex situ*) and the spectroscopic microreactor (*in situ*). Reproduced from Mutz *et al.*[211] Copyright © 2018 Published by Elsevier B.V.

By comparing Raman spectra of "Phase E" it became obvious that carbon depositions remained after reactivation for both experiments. Only the obtained D1/G band ratio varied depending on the treatment in the lab-scale reactor or spectroscopic microreactor, which may be due to a higher temperature in the lab-scale reactor because of the different heating devices and due to the earlier discussed hot spot formation. The Raman laser may be another source of error for the type of carbon formed during the different experiments. However, by observing similar carbon formations by *ex situ* Raman spectroscopy in combination with a lab-scale reactor treatment and *in situ* Raman spectroscopy, we can rule out a strong influence of the Raman laser itself. Nonetheless, the residual carbon deposits require further investigation, since full catalytic performance was achieved despite of their presence.

8.6 Characterization of the residual carbon deposits

Since there were still carbon species present on the catalysts after reactivation in H_2 ("Phase D") but full catalytic performance was retrieved ("Phase E"), the location of such

residual carbon deposits was investigated by HRTEM at 80 kV to avoid knock-on damage by the electron beam as well as to enhance the contrast of C deposits.

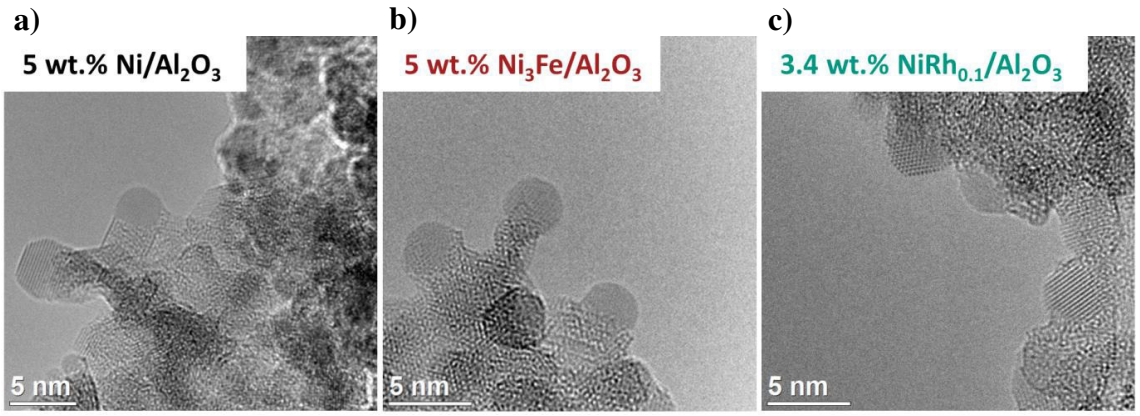

Figure 55: High resolution transmission electron microscopy images of the spent a) 5 wt.% Ni/Al_2O_3, b) 5 wt.% Ni_3Fe/Al_2O_3 and c) 3.4 wt.% $NiRh_{0.1}/Al_2O_3$ catalysts taken from the lab-scale reactor (section 8.4). Reproduced from Mutz *et al.*[211] Copyright © 2018 Published by Elsevier B.V.

HRTEM images of the spent samples (Figure 55) taken from the lab-scale reactor (section 8.4) revealed metal particles with defined structure and clean surfaces, without any indication of carbon coverage.[277] However, EELS verified the presence of carbon species (Figure S 23 in the Appendix), which is in line with the findings by Raman spectroscopy. The C K-edge is most prominent for the Ni catalyst and less intense for Ni_3Fe and $NiRh_{0.1}$. These results indicate that the residual carbon might be located on the support material, whereas the metal particles were free of carbon and fully accessible. According to the literature, the decomposition of CH_4 occurs on the reduced and low coordinated Ni or Fe sites on the surface followed by the migration of the formed carbonaceous compounds from the metal to the support.[156,157,278] These carbonaceous deposits on the support were also reported to be unreactive in H_2,[278] which is in line with the results in the present study. The methanation of CO_2 takes place at the interface of the support and the metal particles, as shown by mechanistic studies in the literature.[96,114] Under the described circumstances, graphite covered support as it was present in "Phase E" had only a minor influence on the methanation of CO_2, at least for the reaction conditions and the time-scale applied in this study.

Reactivation under reducing conditions led to a removal of carbon species located on the metal particles, which could be more easily removed. In order to remove the carbon species located on the Al_2O_3 support, an oxidative treatment may be necessary.[269] Therefore, the spent catalyst samples were treated in 10 % O_2 / He during a temperature-programmed oxidation (Figure 56) in combination with thermogravimetry and mass spectrometry to elucidate the removal of the residual carbon.

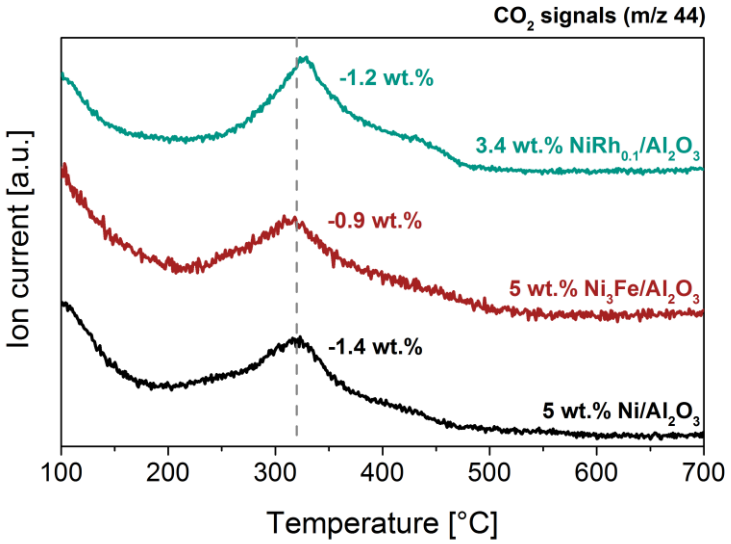

Figure 56: Temperature-programmed oxidation (10 % O_2 / He, 5 K min^{-1}) in combination with thermogravimetric analysis and mass spectrometry of the spent 5 wt.% Ni/Al_2O_3, 5 wt.% Ni_3Fe/Al_2O_3 and 3.4 wt.% $NiRh_{0.1}/Al_2O_3$ catalyst samples taken from the lab-reactor experiment in section 8.4. Reproduced from Mutz *et al.*[211] Copyright © 2018 Published by Elsevier B.V.

The MS signal of CO_2 (m/z 44) showed one peak around 100 °C, which could be assigned to physisorbed CO_2, and a second peak around 320 °C referred to carbon oxidation. The temperatures, at which the peaks occurred, vary slightly between 310 °C (Ni_3Fe) and 330 °C ($NiRh_{0.1}$). Additionally, the weight loss received from TG analysis showed that the lowest amount of carbon was found on the Ni_3Fe catalyst, which is reported to feature the highest coke resistance in dry reforming applications.[158,159] The highest concentration of carbon deposits after reactivation was found on the Ni catalyst, which is in agreement with the EELS data (Figure S 23). The carbon deposits have been oxidized and removed quantitatively from all three catalysts during TPO, which is

demonstrated by the absence of all carbon bands in *ex situ* Raman spectra (Appendix, Figure S 28).

8.7 Conclusions

Three different Ni-based catalyst systems (5 wt.% Ni/Al_2O_3, 5 wt.% Ni_3Fe/Al_2O_3 and 3.4 wt.% $NiRh_{0.1}$), which featured similar, rather uniform and small metal nanoparticles around 3 nm as well as a high catalytic activity in the methanation of CO_2, were presented. The best catalytic performance in the mid-temperature range at 300 – 350°C was found by the Ni_3Fe catalyst. At 400 °C the Ni catalyst reached the highest conversion and CH_4 yield. The $NiRh_{0.1}$ catalyst was less active compared to the Ni and Ni_3Fe systems in the whole temperature range.

Various gas mixtures related to the methanation of CO_2 were fed to the catalysts, while the formation and nature of carbon deposits was monitored by *operando* Raman spectroscopy. The experiments showed that gas atmospheres like CO_2/H_2 or $CO_2/H_2/CH_4$ for the methanation or in extreme scenarios CO_2 or CO_2/CH_4 were tolerated by the three Ni-based catalysts and no carbon depositions were observed. Only in pure CH_4 extensive carbon deposition occurred, which led to significant catalyst deactivation for all three systems blocking the catalytic surface. The conversion of CO_2 dropped and the selectivity shifted extensively to CO. The catalytic activity and selectivity could be restored after reactivation in H_2 at 500 °C, baring the metal particles from the carbon depositions. Residual carbon deposits remained on the support material, which did not affect the catalytic performance significantly and could be removed in O_2 at 310 – 330 °C.

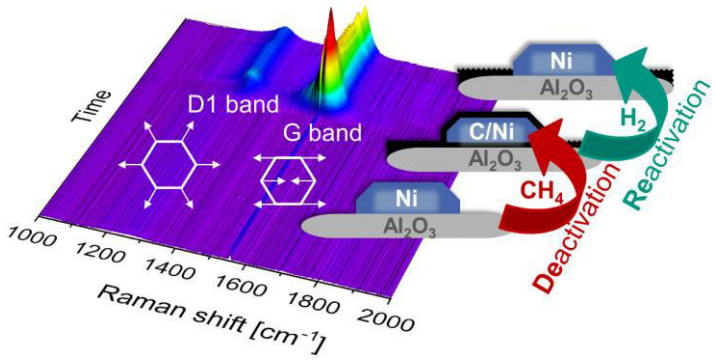

Scheme 4: Illustration of the results during the experiments applying *operando* Raman spectroscopy. Reproduced from Mutz *et al.*[211] Copyright © 2018 Published by Elsevier B.V.

The three Ni-based catalyst systems showed similar behavior in carbon formation and reactivation, with only minor deviations among each other. These findings are important for industrial methanation applications using CO_2/CH_4 mixtures from biogas plants or product gas recycling, since carbon deposition as potential deactivation pathway at temperatures ≤ 400 °C is rather unlikely even under fluctuating conditions and H_2 interruptions. The only feed composition, which needs to be avoided, is pure CH_4, which induced carbon deposition. In general, *operando* Raman spectroscopy was ideally suited to investigate the formation of carbon deposits and its nature on a working catalyst upon varying gas atmospheres. This makes it a powerful and valuable method for further and more detailed studies under reaction conditions and modulations of the reaction gas atmosphere as well as long-term experiments under harsh reaction conditions including CO.

9 Potential and limitations of a NiFe alloy catalyst[1]

9.1 Introduction

The synthesis of CH_4 from CO_2 and renewable H_2 within the power-to-gas concept is a well-known process utilizing Ni-based catalysts.[28,51,52,219] Doping these Ni catalyst with a second metal can improve both the catalytic performance and the stability of the catalyst.[51] Recently, NiFe alloy catalysts have been reported to claim a significantly better catalytic performance in the methanation of CO_2[87,91,104] (*cf.* section 1.3.1) which was also indicated by the results in section 8.3. The optimum Ni/Fe ratio in the desired alloy was found to be around 3 as reported by various studies.[103-106]

However, long-term stability and performance tests under harsh and industrially relevant reaction conditions combined with in-depth structural investigations are necessary to evaluate the potential of the Ni_3Fe system in methanation applications. Such structure-performance relationships require uniformly sized and well-dispersed Ni_3Fe alloy nanoparticles on the support material also allowing to monitor changes and modifications of the active material after the reaction.

In this chapter advances with respect to the preparation of the catalyst, new insights into its structural properties and the catalytic potential at elevated pressures are reported. The Ni_3Fe catalyst was prepared *via* a homogeneous deposition-precipitation method on an Al_2O_3 support that is suitable to obtain small and well-dispersed metal nanoparticles.[207,231-233] Compared to the 5 wt.%Ni_3Fe catalyst prepared in chapter 8, the total metal content was increased to form a higher fraction of the desired alloy. This catalyst and, for comparison, a monometallic Ni reference catalyst were well characterized using XRD, STEM combined with EDX, HRTEM imaging, H_2-TPR and

[1] The text and figures are taken from Mutz *et al.*:[212] B. Mutz, M. Belimov, W. Wang, P. Sprenger, M.-A. Serrer, D. Wang, P. Pfeifer, W. Kleist, J.-D. Grunwaldt, "Potential of an Alumina-Supported Ni_3Fe Catalyst in the Methanation of CO_2: Impact of Alloy Formation on Activity and Stability", *ACS Catal.* **2017**, *7*, 6802-6814. Reprinted with permission, Copyright © 2017, American Chemical Society.

Raman spectroscopy. A combination of these methods was important to prove the formation of the desired Ni_3Fe alloy. The catalytic performance in the methanation of CO_2 was screened in a custom made continuous flow laboratory setup equipped with a tubular packed bed reactor with diluted catalyst in the temperature range of 200 – 450 °C at 1 and 10 bar. Additionally, long-term stability tests under industrially relevant conditions were performed in a microchannel packed bed reactor setup (IMVT, KIT) for the Ni_3Fe catalyst in comparison to a commercial Ni-based methanation catalyst to compare the results and to draw conclusions concerning the potential and the limitations of the bimetallic Ni_3Fe system.

9.2 Catalyst characterization: particle size, alloy formation and crystal phases

The desired metal loading was chosen based on literature identifying an optimum of 15 – 20 wt.% of the active metal on the support for the methanation of CO_2 (*e.g.* Refs[63,86,279]) as well as for CO methanation.[103] Elemental analysis of the catalyst samples (Table 11) revealed a total metal loading of about 17 wt.% for both catalysts. Therefore, a slightly lower total metal content was obtained for the applied preparation procedure, which means that the metal ions in the solution were not precipitated entirely. The bimetallic catalyst exhibited the intended molar Ni/Fe ratio of 3, which was the most suitable composition for CO_2-methanation reported in literature.[100,104,106] The specific surface area of the catalysts was determined as 220 $m^2\ g^{-1}$.

Table 11: Elemental composition of the Ni/Al_2O_3 and Ni_3Fe/Al_2O_3 catalysts. Reproduced from Mutz *et al.*[212] Copyright © 2017, American Chemical Society.

Catalyst	Total metal loading [wt.%]	Ni [wt.%]	Fe [wt.%]
Ni/Al_2O_3	16.6	16.6	-
Ni_3Fe/Al_2O_3	17.0	12.9	4.1

The catalyst samples of the Ni and the bimetallic Ni_3Fe catalyst as well as the pure γ-Al_2O_3 support were analyzed by XRD to identify the crystalline phases (Figure 57). The XRD patterns of the catalysts are dominated by the reflections of Al_2O_3.

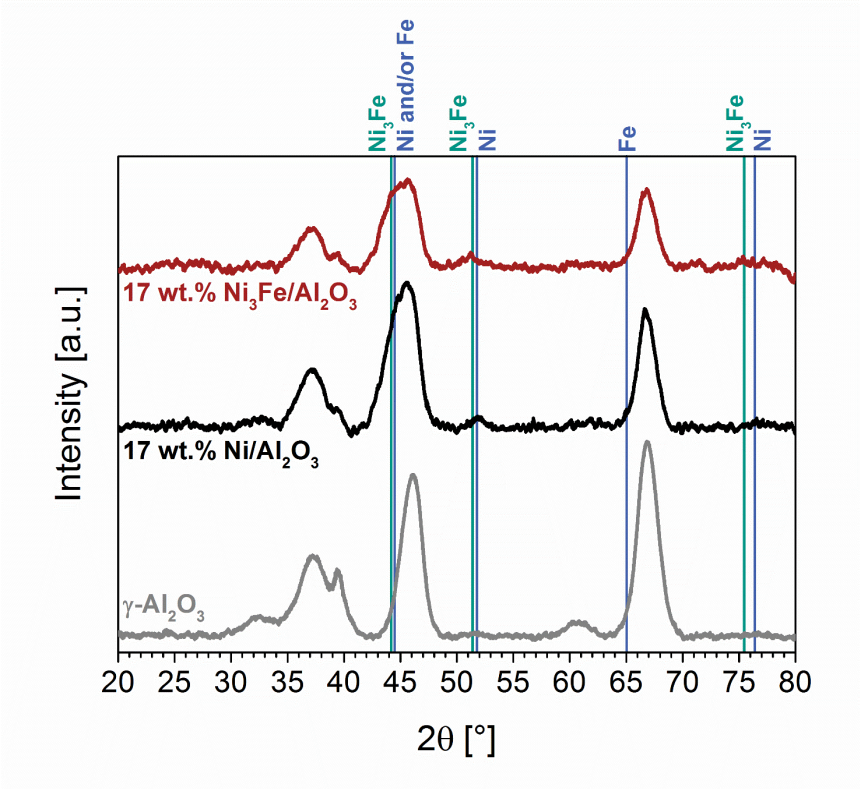

Figure 57: XRD patterns of the reduced 17 wt.% Ni/Al_2O_3 (black) and bimetallic 17 wt.% Ni_3Fe/Al_2O_3 (red) catalyst samples compared to the pure γ-Al_2O_3 support (grey). Reproduced from Mutz *et al.*[212] Copyright © 2017, American Chemical Society.

The Ni catalyst showed reflections of the Ni(111) plane at $2\Theta = 44.5°$ (ICSD 044767) represented as a shoulder of the reflection from Al_2O_3. At a similar 2Θ value a reflection of the Fe(110) plane (ICSD 064998) is expected for the iron containing catalyst. The reflections of Ni(111) and Fe(110) could not be resolved by XRD. The shoulder next to the Al_2O_3 reflection appeared to be slightly broader in the case of Ni_3Fe catalyst compared to the monometallic sample. This might be caused by an additional reflection occurring from the Ni_3Fe(111) plane at $2\Theta = 44.2°$ (ICSD 040334).

An isolated reflection was observed for the Ni(200) plane at 2Θ = 51.8°. Using this reflection with the Scherrer equation, a crystallite size of 5.4 nm was estimated. The pattern of the bimetallic catalyst revealed a reflection at slightly lower angles, which can be ascribed to the Ni_3Fe(200) plane at 2Θ = 51.5°. This angular shift based on the formation of a Ni_3Fe alloy and its change in the lattice parameters compared to metallic Ni has been reported in literature.[87,106,280-282] The crystallite size of the alloyed catalyst was calculated as 5.7 nm. No reflections from Fe at 2Θ = 65.0°, Ni_3Fe at 2Θ = 75.8° or Ni at 2Θ = 76.4° were observed.

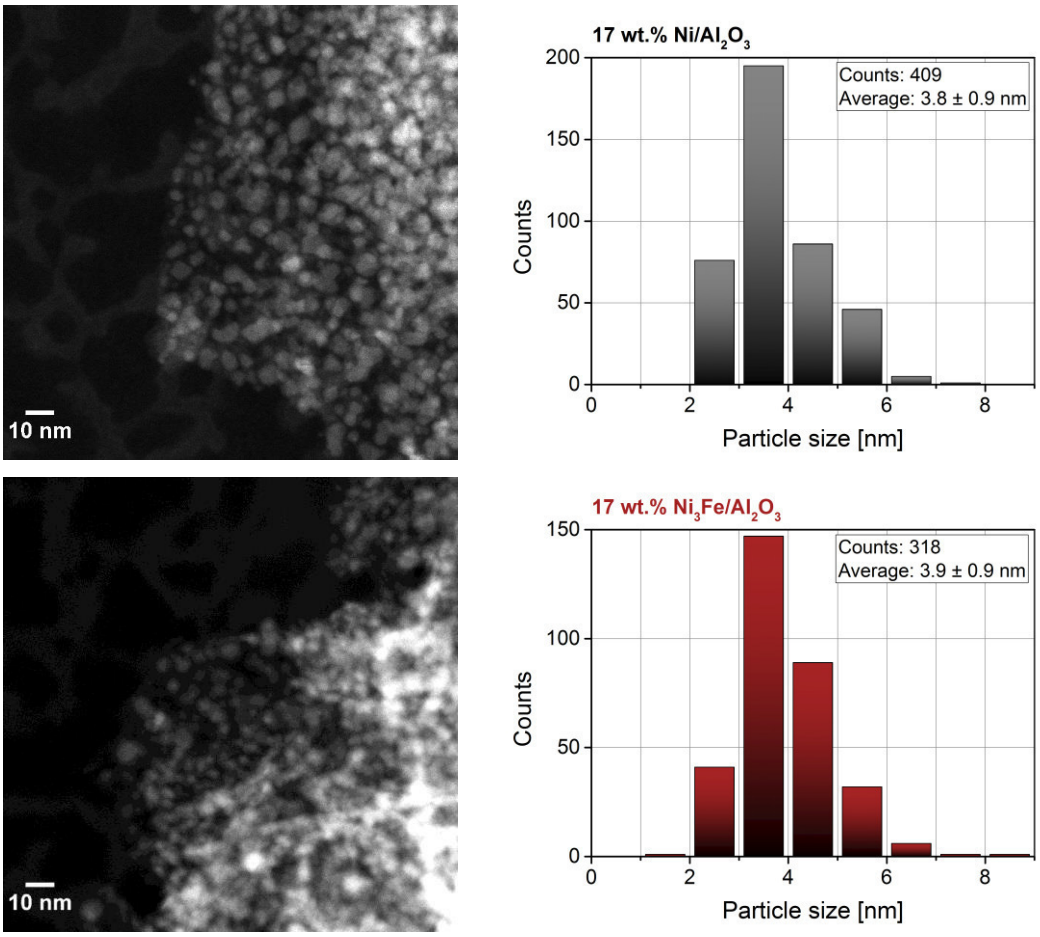

Figure 58: Representative STEM images and particle size distributions of the 17 wt.% Ni/Al_2O_3 (upper part) and 17 wt.% Ni_3Fe/Al_2O_3 (lower part) catalysts. Reproduced from Mutz *et al.*[212] Copyright © 2017, American Chemical Society.

The STEM image showed well-dispersed metal particles on the support (Figure 58) for the Ni_3Fe catalyst. Small metal nanoparticles with a narrow size distribution ($d_p = 3.9 \pm 0.9$ nm) were observed with a dispersion of 24 %. Similar results were obtained for the Ni catalyst regarding both, the metal particle size ($d_p = 3.8 \pm 0.9$ nm) and the dispersion (24 %). The size of the metal particles from the STEM images are in a similar range as the crystallite sizes estimated from XRD. The particle sizes determined by STEM also account for smaller particles that may be invisible for XRD.

Upon iron addition the particle size and, thus, the dispersion remained almost the same (Figure 58). 40 wt.% NiFe-alumina catalysts have been prepared by Hwang *et al.*[87] *via* a single step sol-gel method, which led to slightly larger particles of about 7.4 nm (but 2-fold metal loading) as determined by XRD. In contrast, larger metal particles of 10 - 12 or 13 - 15 nm depending on the support and loadings were reported in literature for NiFe catalysts that were prepared by impregnation methods.[103,281]

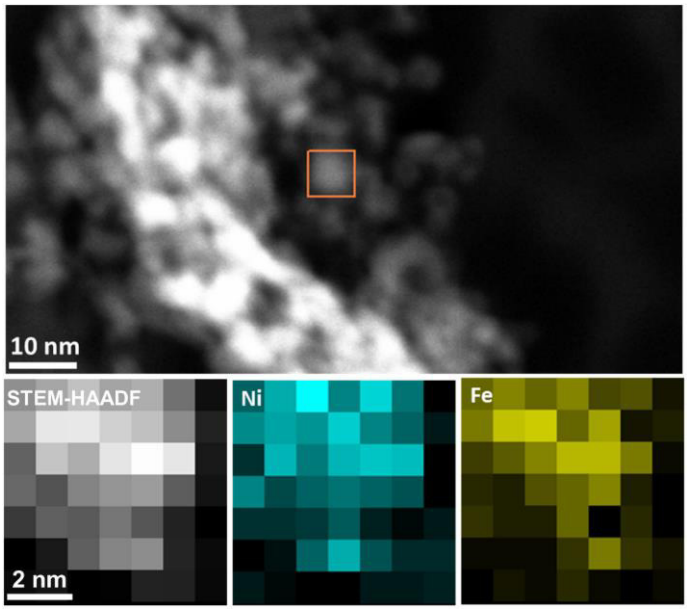

Figure 59: Overview STEM image of the 17 wt.% Ni_3Fe/Al_2O_3 catalyst and the corresponding elemental maps obtained from STEM-EDX spectrum imaging on an individual particle marked with the box. Reproduced from Mutz *et al.*[212] Copyright © 2017, American Chemical Society.

Composition maps of single Ni_3Fe nanoparticles obtained from a STEM-EDX spectrum image (Figure 59) revealed that Ni and Fe elements exhibit similar distribution, indicating the formation of alloy particles. The compositions of the Ni_3Fe nanoparticles quantified by STEM-EDX in different regions are shown in Table 12. The calculated Ni/Fe ratios are slightly higher than the overall desired Ni/Fe ratio of 3 and revealed slight local variations.

Table 12: Quantified elemental analysis of the 17 wt.% Ni_3Fe/Al_2O_3 nanoparticles measured at different regions by STEM-EDX. Reproduced from Mutz *et al.*[212] Copyright © 2017, American Chemical Society.

	Ni [at.%]	Fe [at.%]	Ni/Fe ratio
Region no. 1	75.5	24.5	3.1
Region no. 2	79.7	20.3	3.9
Region no. 3	80.6	19.4	4.2
Region no. 4	77.6	22.4	3.5
Region no. 5	79.6	20.4	3.9

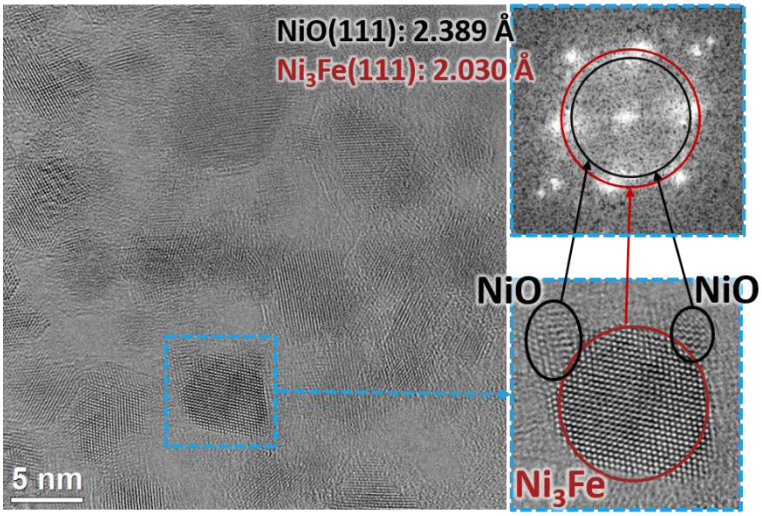

Figure 60: HRTEM image and structure analysis of the 17 wt.% Ni_3Fe/Al_2O_3 catalyst by FFT from one particle. Reproduced from Mutz *et al.*[212] Copyright © 2017, American Chemical Society.

The Ni_3Fe nanoparticles were further analyzed using HRTEM (Figure 60) and the crystal structure was identified by fast Fourier transformation (FFT) from an individual particle. The lower right part of Figure 60 shows the magnified image of the particle and the upper right part shows the corresponding FFT, indicating that the catalyst particles consist of the intended Ni_3Fe alloy and, thus, confirmed the observations from STEM-EDX spectrum imaging and XRD. Some of the Ni_3Fe particles were surrounded by very small NiO clusters that could not be detected using XRD. This also explains the local variations in the Ni/Fe ratio quantified by STEM-EDX. The oxidation of the small Ni particles might have occurred during the TEM sample preparation handled in air. Monometallic iron or iron oxide particles were not observed in the regions explored by electron microscopy.

Raman spectroscopy (Figure 61) was performed *ex situ* on the calcined samples before reduction to gather further structural information on the bimetallic Ni_3Fe alloy catalyst. In addition a 5 wt.% Fe/Al_2O_3 sample and bulk α-Fe_2O_3 were used as references to assign the Raman bands. α-Fe_2O_3 showed characteristic Raman bands at 222, 244, 290, 404, 492, 605, 617 and 1060 cm^{-1}.[283] These bands were present in the spectrum of the 5 wt.% Fe/Al_2O_3 sample. Additionally, two main features appeared at 699 and 750 cm^{-1}, which can both be assigned to $FeAl_2O_4$.[284,285] This does not necessarily imply the presence of bulk $FeAl_2O_4$ but Fe-oxide species in contact with Al_2O_3 as it is expected for supported nanoparticles.

The bimetallic 17 wt.% Ni_3Fe/Al_2O_3 alloy catalyst showed also these two features and a weak shoulder at 890 cm^{-1} in addition. However, the bimetallic catalyst did not show any bands characteristic for Fe_2O_3. [283,286] Since the presence of FeO gives a distinct band at 645 cm^{-1} [283,286] and supported Fe_3O_4 normally gives a main band around 665 cm^{-1},[287] these two iron species are hardly present. The band around 700 cm^{-1} may also originate from $NiFe_2O_4$ spinel in this catalyst. The band at 563 cm^{-1} is a Ni-O stretching mode, which has been shifted to higher wavenumbers due to a higher iron content, as it has been observed for oxides of bulk Ni_3Fe.[288,289] The Raman spectrum of 17 wt.% Ni/Al_2O_3, shows the band at 554 cm^{-1} with a shoulder around 481 cm^{-1} that can

be assigned to Ni-O vibrations, which is in agreement with earlier studies for supported NiO.[290,291]

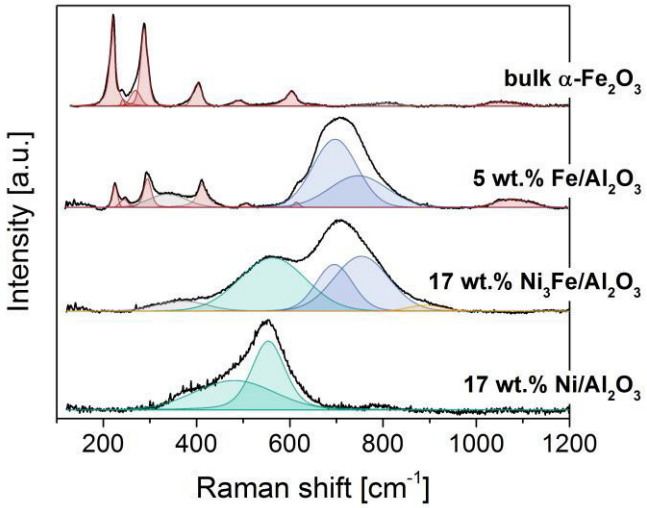

Figure 61: Raman spectra of the calcined 17 wt.% Ni_3Fe/Al_2O_3 catalyst and monometallic 17 wt.% Ni/Al_2O_3 compared to 5 wt.% Fe/Al_2O_3 and bulk α-Fe_2O_3. The deconvolution represents in green: Ni-O, blue: A_{1g} vibrations of $FeAl_2O_4$, red: α-Fe_2O_3 and orange: shoulder only present for the bimetallic catalyst. A list of the full deconvolution data is given in the Appendix (Table S 11). Reproduced from Mutz *et al.*[212] Copyright © 2017, American Chemical Society.

In general, it is difficult to conclude, whether broad Raman signals originate from a superposition of several bands or from a broadening effect due to the small crystallite size of iron oxide species. Raman spectroscopy cannot prove the formation of an alloy, since it is only sensitive to metal-oxygen-vibrations and spinels such as $NiFe_2O_4$ and $FeAl_2O_4$ give similar main bands. However, the slight change of the broad Fe-O-vibration band may indicate a different crystal structure compared to pure supported iron oxide and a strong interaction between Fe^{3+} and Ni^{2+}already in this "precursor" state.

The reducibility of the Ni_3Fe catalyst was investigated by temperature-programmed reduction with H_2 (H_2-TPR, Figure 62) and compared to the profile of the monometallic Ni catalyst. The H_2 consumption profile of the Ni catalyst revealed one main peak at 573 °C referring to the reduction of NiO to metallic Ni. The shoulder around 750 °C could

be ascribed to smaller NiO particles exhibiting stronger interactions with the support, which have also been observed in HRTEM images. Other possible species such as $NiAl_2O_4$ that would reduce at higher temperatures (> 800 °C, *e.g.* Refs[86,263]) have not been detected. The results from TPR confirm the presence of small Ni particles with a uniform size eliminating the possible formation of larger agglomerates on the catalyst, which would result in reduction peaks at lower temperatures.

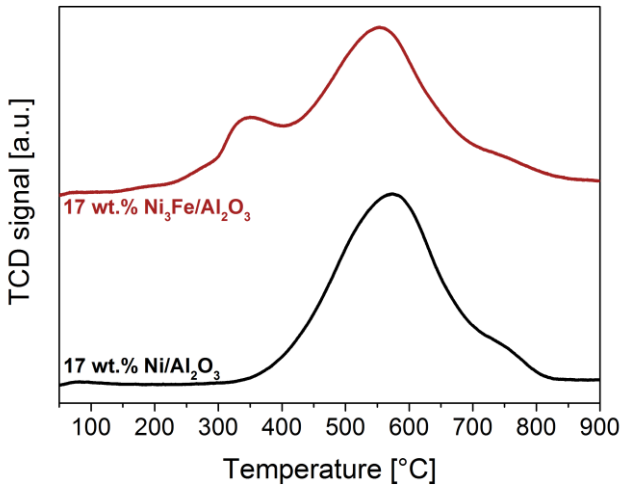

Figure 62: H_2-TPR profiles of the 17 wt.% Ni_3Fe/Al_2O_3 (top) and the 17 wt.% Ni/Al_2O_3 (bottom) catalyst, conditions: 100 mg of sample, 10 % H_2/Ar (50 mL min^{-1}) and a ramp rate of 10 K min^{-1}. Reproduced from Mutz *et al.*[212] Copyright © 2017, American Chemical Society.

The TPR profile of the Ni_3Fe catalyst showed the main peak at 555 °C and an additional peak at 350 °C. Two reduction peaks have also been reported in other studies and can be assigned to the reduction of Fe_2O_3 to Fe_3O_4 in the ternary NiFe oxide (350 °C) and to the reduction of Fe_3O_4 to Fe and NiO to Ni (555 °C).[87,105,264] Other studies involving bimetallic NiFe catalysts with higher metal loading and larger metal particles on a support with lower specific surface area showed TPR profiles with one single broad reduction peak. A second reduction peak appeared for catalysts with a higher amount of Fe.[102,292] In our case, the high temperature reduction peak may be sharper due to the small metal particles compared to literature and, therefore, separated into two peaks. The main reduction peak of the Ni_3Fe catalyst in Figure 62 shifted to slightly lower

temperatures (573 °C to 555 °C), as a consequence of a higher reducibility of the Ni_3Fe alloy compared to the monometallic Ni catalyst.[87,102]

The combined characterization results from XRD, STEM, Raman spectroscopy and H_2-TPR led to the conclusion that a high amount of the desired Ni_3Fe alloy was formed and small, rather uniformly sized particles are present. In addition, some very small Ni/NiO particles were identified but no Fe containing single metal particles were observed. Hence, the supported Ni and Ni_3Fe catalysts exhibit similar structural properties such as total metal content, metal particle size and dispersion, which is optimal to determine the potential of the Ni_3Fe alloy catalyst in the methanation of CO_2 and to gain insight into structure-performance relationships.

9.3 Catalytic performance: screening of temperature and pressure

Earlier pressure screenings during the methanation of CO_2 (Figure S 37 in the Appendix) between 1 – 20 bar (5 bar steps) revealed that under these conditions 10 bar seems to be the optimum pressure. Higher pressures did not lead to significant improvements of the catalytic performance. Based on these preliminary investigations the catalytic performance of the 17 wt.% Ni/Al_2O_3 and 17 wt.% Ni_3Fe/Al_2O_3 catalysts was investigated in the temperature range of 200 - 450 °C during the methanation of CO_2 at atmospheric pressure (1 bar) and at elevated pressure (10 bar) using a tubular packed bed reactor. Figure 63 shows the catalytic data for the Ni_3Fe alloy catalyst compared to the monometallic Ni catalyst. At 200 °C and 1 bar, the conversion of CO_2 (Figure 63 a)) was very low for both catalysts (2 – 3 %). The conversion started between 200 - 250 °C and increased with rising temperature. At 250 – 300 °C, a slightly higher conversion of CO_2 was achieved for the Ni_3Fe catalyst (21 – 76 %) compared to the monometallic Ni catalyst (15 – 73 %). The best results for both catalysts at atmospheric pressure were realized at 350 °C (Ni_3Fe: 82 %; Ni: 85 %). Further increase of the temperature resulted in a decline of the activity due to the thermodynamic equilibrium,[53] converting only 71 % (Ni_3Fe) and 72 % (Ni) of CO_2 at 450 °C.

Raising the pressure to 10 bar resulted in a significantly higher conversion of CO_2 in the temperature range of 250 – 450 °C. The superior activity of the alloyed catalyst emerged already at 250 °C, where an exceptional conversion of CO_2 of 87 % (21 % at 1 bar) was observed, whereas the Ni catalyst reached moderate activity with a conversion of only 28 % (15 % at 1 bar). For the Ni catalyst, a similar steep increase in activity occurred at 300 °C at the higher pressure, following the trend observed at atmospheric pressure. Both catalysts achieved excellent activity at 300 – 350 °C, converting 98 – 99 % (Ni) and 95 – 96 % (Ni_3Fe) of the CO_2 fed into the reactor.

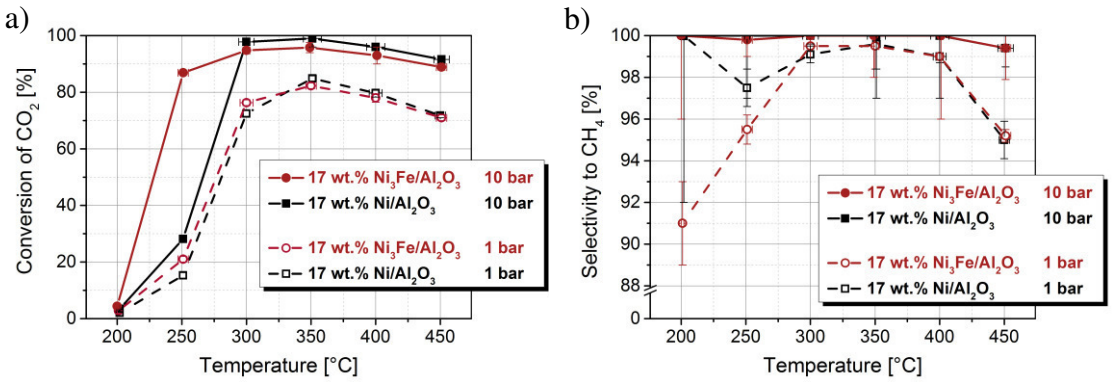

Figure 63: a) CO_2 conversion and b) CH_4 selectivity of the 17 wt.% Ni/Al_2O_3 (squares, black) and 17 wt.% Ni_3Fe/Al_2O_3 (circles, red) catalysts in the methanation of CO_2 at 1 bar (open symbols) and 10 bar (filled symbols) (WHSV = 6000 mL_{CO2} g_{cat}^{-1} h^{-1}). Reproduced from Mutz *et al.*[212] Copyright © 2017, American Chemical Society.

The selectivity towards CH_4 is plotted in Figure 63 b). As the reaction started at 250 °C under atmospheric pressure the Ni_3Fe catalyst showed moderate selectivity to CH_4 (ca. 96 %). The value reached by the monometallic Ni catalyst was slightly higher (98 %). CO was formed as the main by-product for both catalysts. The selectivity to CH_4 increased with temperature and reached values > 99 % at 300 – 350 °C for both catalysts. At higher temperatures, the selectivity decreased slightly, which was caused by the formation of CO due to the endothermic reverse water-gas shift reaction.[53] At 10 bar, both catalysts produced CH_4 with a selectivity of close to 100 % over the whole temperature range. Only at 450 °C the selectivity towards CH_4 declined slightly due to the detection of ca. 600 ppm CO in the µGC.

The significantly enhanced low temperature activity over the Ni_3Fe alloy catalyst compared to the monometallic Ni reference especially at elevated pressure (10 bar) supports results by Hwang *et al.*[87] or Ren *et al.*[91]. However, in those studies substantially different reaction conditions, catalyst loadings and support materials were used, which makes a direct comparison difficult. At higher temperatures, no significant promoting influence of Fe was observed.

9.4 Long-term performance

The catalytic results in section 9.3 showed that the Ni_3Fe alloy catalyst is an attractive alternative compared to a monometallic Ni catalyst. For a more realistic performance rating the Ni_3Fe catalyst was compared with a commercially available Ni-based methanation catalyst under industrially oriented reaction conditions with focus on catalyst stability and avoidance of mass and heat transport limitations using a microchannel packed bed reactor in cooperation with Michael Belimov (IMVT, KIT).

The extent of the external mass transport limitation was examined using the Carberry number.[214] The inequality was clearly fulfilled with $6 \cdot 10^{-3} < 0.1$ at given experimental conditions. The mass transfer coefficient was taken from Ref[293]. The reaction rate was approximated with the literature kinetics given by Koschany *et al.*[217] with the apparent reaction order of 0.5. This approximation was also applied for the evaluation of the internal mass transport limitation, *i.e.* the Weisz-Prater criterion.[215] On the average-sized catalyst particle of 250 µm, the Weisz-number was calculated to 0.07 and satisfied the suggested limit of 0.08 (360 °C, 6 bar, 9 % CO_2, $H_2/CO_2 = 4$). The effective diffusion coefficient for CO_2 was governed by Knudsen regime to be $1.1 \cdot 10^{-6}$ m^2 s^{-1} (particle porosity of 0.7 and tortuosity of 3). The extent of the external heat transfer limitation was evaluated according to Mears.[214] The heat transfer coefficient from particle to fluid in the packed bed was calculated to 1488 W m^{-2} K^{-1} from Ref[294] at 360 °C and a Reynolds particle number of 24 (Pr = 0.7) for the examined reaction mixture and conditions. The film overheating on the 250 µm particle was calculated to 2.7 K

which is slightly above the suggested limit of 2 K, however, was considered as negligible for the determination of the kinetic parameters.

The long-term stability of the commercial Ni-based methanation catalyst is shown in Figure 64 a) in terms of CO_2 conversion as a function of time on stream (TOS). The corresponding selectivity towards CH_4 is depicted in Figure 64 b). Starting at 358 °C, the commercial Ni-based catalyst achieved a CO_2 conversion of 52 % with selectivity towards CH_4 of 90 %. CO was detected as the only by-product. These conditions were kept for 47 h TOS steady state operation during which a linear decline in conversion of -0.12 % h^{-1} was observed. After 47 h the conversion of CO_2 decreased to 46 %, although the selectivity towards CH_4 remained constant (90 – 91 %).

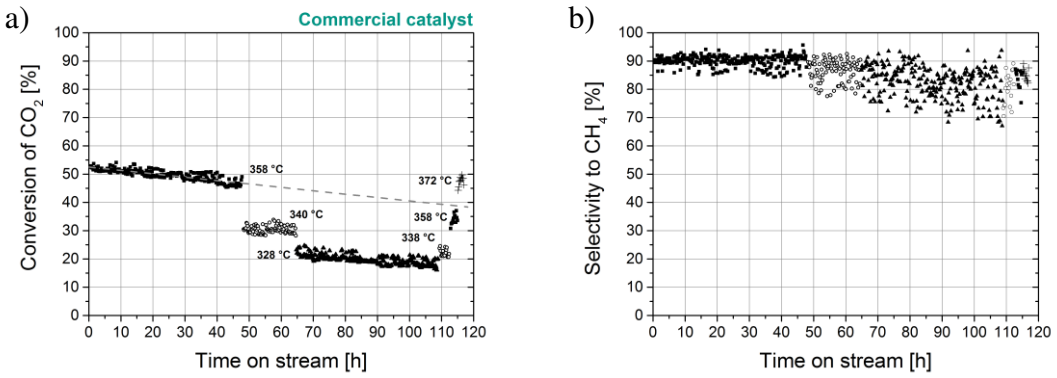

Figure 64: a) Conversion of CO_2 and b) selectivity towards CH_4 of the commercial Ni-based methanation catalyst during long-term performance testing at 80500 mL_{CO2} g_{cat}^{-1} h^{-1} and 6 bar. Reproduced from Mutz *et al.*[212] Copyright © 2017, American Chemical Society.

The effectiveness factor is used to describe the percentage of pore utilization of the catalysts and is estimated to around 90 % according to Ref[216]. Thus, the temperature was decreased to minimize mass transport limitations. At 328 °C 22 % of CO_2 was converted by the catalyst with a calculated effectiveness factor of > 95 % and, therefore, the catalyst particles in the bed operated near full utilization. The selectivity towards CH_4 decreased slightly to 85 % due to an increasing production of CO. As the formation of CO by the reverse water-gas shift reaction is generally assumed to happen at higher temperature, this increased CO production could indicate that the parallel reverse water-gas shift reaction

can improve in importance due to the competition on the same active sites. However, the selectivity calculation could also be falsified by the overall lower concentration of products at lower conversion. *i.e.* leading to a higher experimental error.

The temperature was kept constant at 328 °C for 44 h, in which a further slight decline of the CO_2 conversion of -0.09 % h^{-1} was observed following the trend monitored at 358 °C and resulting in 18 % CO_2 conversion in the end. Additionally, a declining selectivity toward CH_4 to 81 % was observed over 44 h TOS at 328 °C. Increasing the temperature to 358 °C again led to a conversion of 34 %, which is nearly the value that would have been expected for a linear decrease over time at this temperature.

The conversion of CO_2 achieved by the Ni_3Fe system is shown in Figure 65 a) as a function of TOS, the corresponding selectivity towards CH_4 is depicted in Figure 65 b). At 358 °C, the Ni_3Fe catalyst achieved a high CO_2 conversion of 71 %, which was superior to the conversion reached by the commercial catalyst at the same starting temperature. In addition, excellent stability was achieved over 45 h, which is of crucial importance for industrial applications. A linear decline in the conversion of -0.02 % h^{-1} was observed, which was 6 times slower than for the commercial catalyst. During this period, the selectivity towards CH_4 was high with a constant value of around 98 % making the bimetallic Ni_3Fe system superior to the commercial Ni catalyst ($S(CH_4)$ = 91 - 92 %). The effectiveness factor for this condition was estimated to 70 %. In accordance with the long-term performance test of the commercial methanation catalyst, the temperature was then decreased to obtain similar CO_2 conversions and an effectiveness factor of > 95 % at about 305 °C (compared to 328 °C for the commercial catalyst). At that temperature, 21 % of CO_2 was converted for the first 6 h TOS. The selectivity towards CH_4 slightly decreased to 91 % due to the lower temperature, which is also in alignment with the results from the commercial catalyst.

The initial TOF of the Ni_3Fe catalyst on the basis of the yield of CH_4 and the catalyst characterization data is calculated to be 0.26 s^{-1} (305 °C, 6 bar). The received TOF value locate in typical dimensions for alumina supported Ni catalysts reported in literature, ranging from 0.041 – 0.097 s^{-1} [61] and 0.1 s^{-1} [69] up to 0.69 s^{-1} [59]. However, the reaction rates are difficult to compare due to the unknown effectiveness factors and various

reaction conditions, which were applied in different studies. This is also the case, if comparing the results of long-term performance tests in the literature.

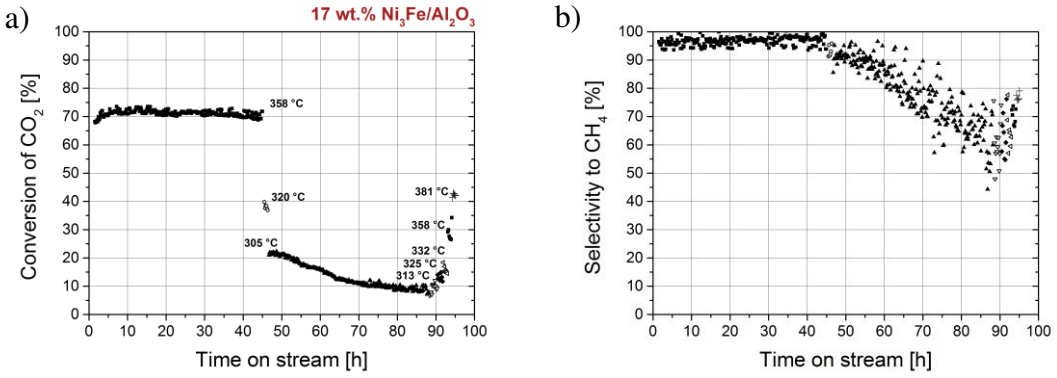

Figure 65: a) Conversion of CO_2 and b) selectivity towards CH_4 of the 17 wt.% Ni_3Fe/Al_2O_3 catalyst during long-term performance testing at 80500 mL_{CO2} g_{cat}^{-1} h^{-1} and 6 bar. Reproduced from Mutz *et al.*[212] Copyright © 2017, American Chemical Society.

After 6 h TOS with near constant conversion at 305 °C the conversion of Ni_3Fe dropped significantly during the total 40 h TOS period at 305 °C to only 9 % in the end. The degradation was ca. 17 times faster than at 358 °C. The deactivation behavior in this period is less predictable due to a non-linear conversion decline. At the same time, the selectivity towards CH_4 declined distinctly to only 63 % after 40 h TOS due to the rising production of CO. Both, catalyst deactivation and loss of selectivity were considerably less pronounced for the commercial system under full pore utilization and lower temperature conditions compared to the Ni_3Fe catalyst. Therefore, the low temperature leading to a higher CO production ability could probably accelerate the degradation process due to enhanced probability for soot formation from CO or segregation of the particles.

Slightly decreasing conversion of CO_2 over time has also been reported in literature and seems to be a common problem for Ni catalysts.[62,64,85,93,97] Such deactivation over time was attributed to both sintering of the metal particles and small degree of coke formation,[62,85,93] but also oxidation of Ni during long-term operation might play a role.[67,93,219,231] Studies on degradation under CO methanation conditions revealed that

asymptotic conversion decline is a common problem[151,295] and could be attributed to a strong deactivation mechanism, *e.g.*, pore mouth blockage by coke.[296] Indeed, in most cases carbon deposition due to CO decomposition to surface carbon was speculated as main deactivation route.[139,151,153,297,298]

After 40 h TOS at 305 °C the temperature was increased gradually resulting in an improved conversion and selectivity. However, even at the initial temperature of 358 °C only 29 % of CO_2 (compared to 71 % at the beginning) was converted with a selectivity of 70 % towards CH_4 (compared to 98 % in the beginning). Hence, a serious deactivation of the Ni_3Fe catalyst system occurred during the low temperature period.

Comparison of both catalyst systems revealed an enhanced conversion, selectivity and stability for the Ni_3Fe system at 358 °C pointing to a synergetic effect of the Ni and Fe. The enhanced activity may be explained by parallel contributions of an enhanced CO_2 adsorption and activation at the Fe species[91,106] and an optimal CO dissociation energy of the NiFe alloy that has been claimed in DFT studies[100] and confirmed experimentally.[87,103,104] However, the Ni_3Fe catalyst was not able to further convert CO to methane at 305 °C due to a combination of low temperature and consequently increased CO formation ability. Similar behavior was observed in the screening experiment (Figure 8) at 250 °C and 1 bar. Increased CO formation was also observed for iron rich NiFe catalysts.[106] Furthermore, Fe catalysts are active in the reverse water-gas shift reaction applied in Fischer-Tropsch processes.[299,300] Hence, *operando* spectroscopic investigations[38,164,165,171,187,199] should be conducted in future require to elucidate the structure of the Ni_3Fe catalyst at work and to evaluate, whether surface segregation of Fe might play a role in the enhanced CO production. However, this is beyond the scope of this study and such studies are currently performed on these well-characterized Ni-based catalysts.

Due to the deactivation that occurs at lower temperatures, the methanation of CO_2 with the Ni_3Fe catalyst needs to be operated at 358 °C to maintain optimal performance. Since internal mass transport limitations could only be prevented at different temperatures (305 °C for Ni_3Fe, 328 °C for the commercial catalyst), a more pronounced deactivation of the commercial catalyst at 305 °C in alignment with the deactivation observed on the

Ni_3Fe catalyst due to further increased CO formation also on the pure Ni catalyst could not be ruled out.

9.5 Characterization of the catalysts after long-term application

Since both catalyst systems suffered from deactivation in the long-term experiments they were characterized afterwards to gain information on the deactivation mechanism. Raman spectroscopy (Figure 66) revealed the deposition of carbon species on both catalysts.

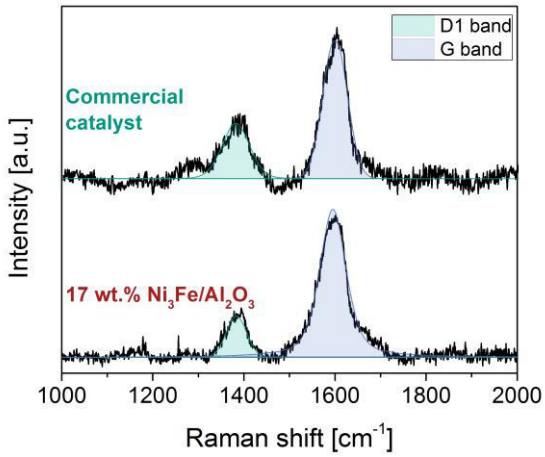

Figure 66: Raman spectroscopy performed *ex situ* on the 17 wt.% Ni_3Fe/Al_2O_3 and the commercial Ni-based catalyst after the long-term experiment under industrially-oriented conditions. Reproduced from Mutz *et al.*[212] Copyright © 2017, American Chemical Society.

The Raman bands around 1380 cm^{-1} and 1595 cm^{-1} could be assigned to the D1 and G bands representing a disordered graphitic structure and an ideal graphitic lattice, respectively.[254,272] The absence of further defect bands as well as the distinct and narrow shape of the D1 and G bands with full widths at half maximums of around 50 and 70 cm^{-1}, respectively, indicates that the carbon depositions are graphitic rather than amorphous. In

case of the Ni_3Fe system, the carbon formation might have occurred during the low temperature period where CO was formed that causes carbon deposits on Ni-based catalysts during CO methanation.[151,153,298] Even though, Raman microscopic measurements are barely quantitative, compared to similar measurements on carbon poisoned Ni-based catalysts in section 8.5 the intensity of the carbon signals is so low that the actual deposition may be very subtle.

Another reason for the deactivation of the catalysts might be sintering of the metal particles. Therefore, STEM images of the spent Ni_3Fe catalyst after re-reduction were recorded. The evaluation of the average particle size (Figure 67) showed a slight increase from 3.9 ± 0.9 nm to 4.6 ± 1.3 nm. Especially particles in the range of $5 - 7$ nm are observed to a higher extent on the spent catalyst. The dispersion decreased to 19 % for the spent catalyst (fresh: 24 %). HRTEM and STEM-EDX evaluation of the spent catalyst (*cf.* Appendix Figure S 38 - Figure S 40 and Table S 13) showed that still most of the Ni and Fe are alloyed with similar Ni/Fe ratios compared to the fresh catalyst. Moreover, the additional reduction step to recover a full reduction of the used catalyst might have contributed to re-dispersion effects.[168]

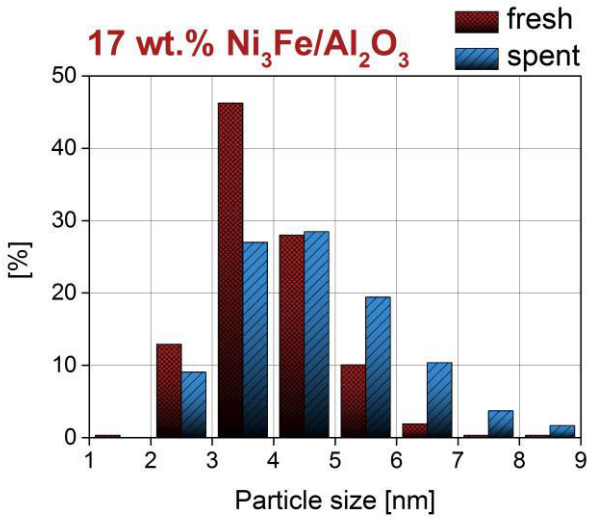

Figure 67: STEM evaluation of the 17 wt.% Ni_3Fe/Al_2O_3 catalyst in the fresh state (red) and after the long-term experiment (blue). Reproduced from Mutz *et al.*[212] Copyright © 2017, American Chemical Society.

The characterization results of the spent Ni_3Fe catalyst the loss of activity in the present case seemed to be caused by loss of metal particle dispersion combined with some carbon deposition (*cf.* discussion with respect to the long-term experiments). In addition, some oxidation of the active sites might also be at the origin of the deactivation. Carbon formation, particle sintering and loss of metal dispersion might have occurred at all temperatures on the commercial catalysts, explaining the slightly diminishing CO_2 conversion independent of the temperature. Because of the high performance stability of the Ni_3Fe catalyst, we suggest that carbon deposition for this catalyst occurred only during the low temperature sequence when more CO was formed and, therefore, the initial activity could not be retrieved after increasing the temperature again. Slight particle growth and loss of metal dispersion might be the reason for the minimal loss of activity during the first 45 h TOS.

9.6 Conclusions

A promising 17 wt.% Ni_3Fe alloy catalyst supported on γ-Al_2O_3 was prepared with high dispersion (24 %) by homogeneous deposition-precipitation method with urea. The combination of all results obtained from extensive characterization verified that a high fraction of Ni and Fe formed the intended Ni_3Fe alloy as 4 nm particles with narrow size distribution. Catalytic tests revealed enhanced low temperature activity of Ni_3Fe compared to a Ni monometallic reference catalyst, which was most prominent at elevated pressure. Long-term experiments of 45 h under industrially oriented conditions including much higher catalyst load revealed significantly enhanced activity (71 % conversion of CO_2)

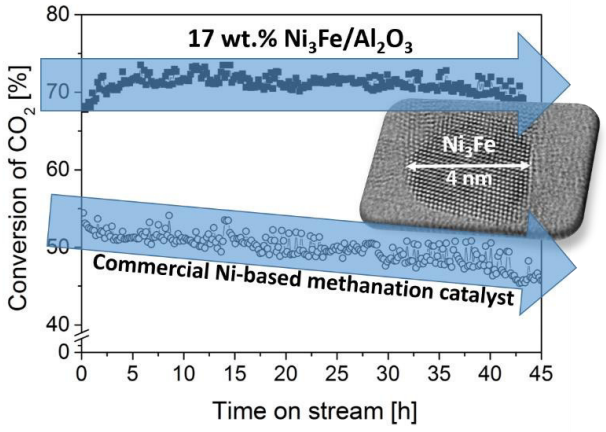

Scheme 5: Long-term performance of the bimetallic Ni_3Fe catalyst as compared to the commercial methanation catalyst. Reproduced from Mutz *et al.*[212] Copyright © 2017, American Chemical Society.

and selectivity (> 98 % selectivity towards CH_4) of the Ni_3Fe alloy compared to a commercially available Ni-based methanation catalyst at high temperature. Most remarkably the 17 wt.% Ni_3Fe/Al_2O_3 catalyst was highly stable above 350 °C whereas a decline of conversion was observed for the commercial catalyst. As the 17 wt.% Ni_3Fe/Al_2O_3 catalyst worked at high efficiency of > 95 %, a turnover frequency of 0.26 s^{-1} (305 °C, 6 bar) was achieved. Deactivation of the Ni_3Fe system occurred in the low temperature regime and the selectivity shifted significantly towards CO. Both catalysts showed some carbon deposition after the long-term treatment, which may contribute to the deactivation phenomena. In conclusion, an outstanding catalyst with high performance and stability is obtained when combining Ni and Fe in mid-temperature (358 °C) methanation of CO_2 for power-to-gas application.

10 Final conclusions and outlook

In this thesis, the methanation of CO_2 as exemplary reaction to produce a chemical energy carrier from CO_2 and green H_2 within the power-to-chemicals concept was studied under dynamic reaction conditions. Fluctuations in the H_2 feed is one of the scenarios when utilizing renewable energies from wind and sunlight. The thesis focused on the investigation of the structural behavior of a tailor-made Ni model catalyst and its deactivation mechanisms. For the catalytic tests, a continuous flow laboratory setup was planned and built-up, which was equipped with a stainless steel fixed-bed reactor and online gas analytics and was designed for catalyst screening and dynamic reaction conditions in the methanation of CO_2. The model Ni-based catalyst was further developed to a promising bimetallic system.

First insights into the structural behavior of a commercial Ni-based catalyst during a long-term H_2 dropout in the methanation of technical CO_2 as a worst case scenario revealed a fast bulk oxidation of the active metal and a deactivation in the subsequent methanation step due to residual NiO. Progressing deactivation was observed over cycles, but a reactivation protocol in H_2 at elevated temperatures was developed successfully.

A tailor-made 10 wt.% Ni/Al_2O_3 catalyst with small and uniformly sized 4 nm Ni particles was designed to study the structural changes during quickly fluctuating H_2 supply in more detail. Short-term H_2 dropouts of 30 s resulted in surface oxidation/reduction processes of the Ni particles propagating slowly through the catalyst bed as investigated by time-resolved *operando* QEXAFS experiments. Therefore, even short interruptions of the H_2 feed and, thus, a slight oxidation of Ni cannot be tolerated by the catalyst. The most reactive Ni sites were oxidized and could not be recovered under methanation conditions. Ni coordination numbers from EXAFS evaluation also suggested dynamic shape changes of the Ni particles. These first insights into the structural response of a model catalyst during dynamically operated methanation of CO_2 demonstrated the significance to study and evaluate power-to-chemicals processes on the catalyst scale, the influence of impurities such as O_2 and also in holistic approaches under such conditions.

Operational adjustments of the methanation process were developed successfully to prevent oxidation and, thus, deactivation of the catalyst caused by H_2 interruptions. The adjustments included either the integration of a small permanent background flow of H_2 through the reactor or the utilization of a CO_2/CH_4 mixture (*e.g.* from biogas plants or product gas recirculation) for the methanation, even if small impurities of O_2 are in the CO_2 feed.

In this context, furthermore the deactivation of Ni-based catalysts caused by carbon deposition was investigated in various reaction mixtures related to fluctuating reaction conditions as well as the methanation of CO_2/CH_4 mixtures. Within this study, *operando* Raman spectroscopy was successfully applied to investigate the formation and nature of carbon deposits on the catalyst during operation. Under the applied conditions no carbon deposition was observed, neither in CO_2 nor in dry reforming related CO_2/CH_4 atmosphere. Only in pure CH_4, significant deposits of graphitic carbon were formed leading to a blockage of the catalyst surface and a vast deactivation in the subsequent methanation step. However, the carbon deposits could be removed by CO_2 or H_2. The initial catalytic performance could be fully recovered by reactivation in H_2 at elevated temperatures, at which the carbon deposits were removed from the metal particles as revealed by electron microscopy. Combining these results, deactivation of Ni-based catalysts by oxidation or carbon deposition could be suppressed as long as a small permanent flow of H_2 or a CO_2/CH_4 mixture was present in the reactor

The Ni-based model catalyst was further developed to a promising bimetallic 17 wt.% Ni_3Fe/Al_2O_3 catalyst. The combined results of various characterization techniques such as XRD, STEM with EDX, HRTEM, H_2-TPR and Raman spectroscopy revealed 4 nm Ni_3Fe alloyed particles with a uniform size distribution and a high metal dispersion of 24 %. A high TOF of 0.26 s^{-1} was achieved in the methanation of CO_2 operating with an effectiveness factor of > 95 % (305 °C, 6 bar). The catalyst showed an impressive stability and outstanding catalytic performance compared to a commercial Ni-based methanation catalyst for 45 h time on stream at 358 °C. Thus, the 17 wt.% Ni_3Fe/Al_2O_3 catalyst represented a promising alternative system for methanation applications which was furthermore suitable for structural investigations using *operando* spectroscopy due to its defined alloy particles.

Future investigations of the bimetallic catalyst are necessary to study the nature of the Ni_3Fe particles under reaction conditions. The oxidation state of Fe, the structural behavior of the alloy and segregation effects need to be explored under steady state as well as under dynamic reaction conditions at atmospheric and elevated pressures. Combining *operando* XAS with XRD, IR or Raman spectroscopy should deliver valuable information, which could provide insights on the reaction mechanism, the interplay between the metals of the alloy catalyst and additional effects from surface segregation (as discussed in section 9.4). Further information about the structure of the Fe species could be gained by Mössbauer spectroscopy.

Additional research on the methanation of CO_2 under dynamic reaction conditions is required to resolve the influence of different parameters and reaction conditions on the catalyst. The effect of H_2 interruptions needs to be studied at lower temperatures and elevated pressures comparable to conditions realized in industrial applications. *Operando* XAS and DRIFTS should be combined for mechanistic studies on the oxidation/reduction of the catalyst under dynamic reaction conditions. Additionally, computational studies might help to understand, which Ni sites are oxidized and reduced under the applied reaction conditions. To investigate and to prove the proposed mechanism of the oxidation propagating through the catalyst bed, spatially resolved *operando* EXAFS would provide important data. Additional information about shape changes of the Ni particles in reducing and oxidizing atmosphere could be gained by *in situ* TEM studies.

Next to the spectroscopic studies under dynamic reaction conditions, the behavior of the reactor as well as product distribution and overheating effects requires detailed investigation. Additional feed components such as H_2O, CO, O_2 need to be included for *operando* spectroscopic studies to examine their effects on the catalyst as well as on the process itself. Finally, studies under dynamic reaction conditions need to be transferred to other processes within the power-to-chemicals concept, such as the Fischer-Tropsch reactions or methanol synthesis. Other reactions where fast changes in temperature, pressure or catalyst load are expected is *e.g.* exhaust gas catalysis.

The first insights into the carbon formation *via operando* Raman spectroscopy form the basis for further parameter variations or additional gases as discussed for further

operando XAS studies. CO and H_2O as well as harsh reaction conditions have influence on the formation of carbon deposits as shown during the long-term tests and should be studied within *operando* Raman experiments. Besides, the formation of Ni-carbides should be investigated under such reaction conditions. Alternatively, *in situ* X-ray photoelectron spectroscopy could be used to investigate surface carbon species.

Dopants, such as MgO or ZrO_2, could further improve the stability and performance of the Ni_3Fe/Al_2O_3 catalyst. Ni or Ni_3Fe catalysts doped with small amounts of Ru might also present promising catalyst systems exhibiting better reducibility and performance at lower temperatures. Ni-based catalysts with enhanced reducibility are also very interesting for studies under dynamic reaction conditions, where a full reduction in the methanation atmosphere would be possible. In the case of fully reversible dynamic changes of the catalysts, modulation excitation spectroscopy could be applied to gain information of active species in the methanation reaction. In contrast to complete H_2 dropouts, slight changes of the reduction potential of the reaction mixture might lead to small changes in context with strong metal-support interaction. Computational studies considering the direct hydrogenation of CO_2 (*cf* section 1.3.2) might result in a volcano plot different from the one obtained for the CO dissociation and, thus, might uncover new promising alloys with enhanced catalytic performance.

11 References

[1] R. Schlögl, "The Revolution Continues: Energiewende 2.0", *Angew. Chem. Int. Ed.* **2015**, *54*, 4436-4439.

[2] M. Pehnt, "Dynamic life cycle assessment (LCA) of renewable energy technologies", *Renew. Energy* **2006**, *31*, 55-71.

[3] R. Scholz, M. Beckmann, C. Pieper, M. Muster, R. Weber, "Considerations on providing the energy needs using exclusively renewable sources: Energiewende in Germany", *Renew. Sust. Energ. Rev.* **2014**, *35*, 109-125.

[4] A. Evans, V. Strezov, T. J. Evans, "Assessment of sustainability indicators for renewable energy technologies", *Renew. Sust. Energ. Rev.* **2009**, *13*, 1082-1088.

[5] P. McKendry, "Energy production from biomass (part 2): conversion technologies", *Bioresour. Technol.* **2002**, *83*, 47-54.

[6] "Fünfter Monitoring-Bericht zur Energiewende - Energie der Zukunft", Bundesministerium für Wirtschaft und Energie, Berlin, **2015**.

[7] "Energy Charts" www.energy-charts.de/price.htm, Fraunhofer Institute for Solar Energy Systems ISE - Fraunhofer Gesellschaft, (access date 28.02.2017).

[8] M. Sterner, "Erneuerbare Energien und Energieeffizienz - Renewable Energies and Energy Efficiency", *Vol. 14*, Kassel University Press GmbH, Kassel, Germany, **2009**.

[9] M. Specht, J. Brellochs, V. Frick, B. Stürmer, U. Zuberbühler, M. Sterner, G. Waldstein, "Speicherung von Bioenergie und erneuerbarem Strom im Erdgasnetz", *Erdöl, Erdgas, Kohle* **2010**, *126*, 342.

[10] T. Trost, S. Horn, M. Jentsch, M. Sterner, "Erneuerbares Methan: Analyse der CO_2-Potenziale für Power-to-Gas Anlagen in Deutschland", *Z Energiewirtsch* **2012**, *36*, 173-190.

[11] R. Schlögl, "Chemical Energy Storage", Walter de Gruyter GmbH, Berlin/Boston, Germany/USA, **2013**.

[12] F. Schüth, "Chemical Compounds for Energy Storage", *Chem. Ing. Tech.* **2011**, *83*, 1984-1993.

[13] H. Zhao, Q. Wu, S. Hu, H. Xu, C. N. Rasmussen, "Review of energy storage system for wind power integration support", *Appl. Energy* **2015**, *137*, 545-553.

[14] B. Dunn, H. Kamath, J.-M. Tarascon, "Electrical Energy Storage for the Grid: A Battery of Choices", *Science* **2011**, *334*, 928-935.

[15] F. Díaz-González, A. Sumper, O. Gomis-Bellmunt, R. Villafáfila-Robles, "A review of energy storage technologies for wind power applications", *Renew. Sust. Energ. Rev.* **2012**, *16*, 2154-2171.

[16] Z. Yang, J. Zhang, M. C. W. Kintner-Meyer, X. Lu, D. Choi, J. P. Lemmon, J. Liu, "Electrochemical Energy Storage for Green Grid", *Chem. Rev.* **2011**, *111*, 3577-3613.

[17] R. Schlögl, "The Role of Chemistry in the Energy Challenge", *ChemSusChem* **2010**, *3*, 209-222.

[18] A. Lanz, P. Eng, J. Heffel, C. Messer, "Module 1: Hydrogen properties" in *Hydrogen Fuel Cell Engines and Related Technologies: Rev 0*, College of the Desert - Energy Technology Training Center, Palm Desert, USA, **2001**.
[19] U. Eberle, M. Felderhoff, F. Schüth, "Chemical and Physical Solutions for Hydrogen Storage", *Angew. Chem. Int. Ed.* **2009**, *48*, 6608-6630.
[20] F. Schüth, "Challenges in hydrogen storage", *The European Physical Journal Special Topics* **2009**, *176*, 155-166.
[21] L. Zhou, "Progress and problems in hydrogen storage methods", *Renew. Sust. Energ. Rev.* **2005**, *9*, 395-408.
[22] J. L. Rowsell, O. M. Yaghi, "Strategies for hydrogen storage in metal–organic frameworks", *Angew. Chem. Int. Ed.* **2005**, *44*, 4670-4679.
[23] K. Hashimoto, M. Yamasaki, S. Meguro, T. Sasaki, H. Katagiri, K. Izumiya, N. Kumagai, H. Habazaki, E. Akiyama, K. Asami, "Materials for global carbon dioxide recycling", *Corros. Sci.* **2002**, *44*, 371-386.
[24] M. Götz, J. Lefebvre, F. Mörs, A. McDaniel Koch, F. Graf, S. Bajohr, R. Reimert, T. Kolb, "Renewable Power-to-Gas: A technological and economic review", *Renew. Energy* **2016**, *85*, 1371-1390.
[25] G. Centi, S. Perathoner, "Opportunities and prospects in the chemical recycling of carbon dioxide to fuels", *Catal. Today* **2009**, *148*, 191-205.
[26] G. Centi, S. Perathoner, "CO_2-based energy vectors for the storage of solar energy", *Greenhouse Gas. Sci. Technol.* **2011**, *1*, 21-35.
[27] X. Xiaoding, J. A. Moulijn, "Mitigation of CO_2 by Chemical Conversion: Plausible Chemical Reactions and Promising Products", *Energy Fuels* **1996**, *10*, 305-325.
[28] W. Wang, S. Wang, X. Ma, J. Gong, "Recent advances in catalytic hydrogenation of carbon dioxide", *Chem. Soc. Rev.* **2011**, *40*, 3703-3727.
[29] E. V. Kondratenko, G. Mul, J. Baltrusaitis, G. O. Larrazábal, J. Pérez-Ramírez, "Status and perspectives of CO_2 conversion into fuels and chemicals by catalytic, photocatalytic and electrocatalytic processes", *Energy Environ. Sci.* **2013**, *6*, 3112-3135.
[30] J. M. Thomas, "Heterogeneous Catalysis and the Challenges of Powering the Planet, Securing Chemicals for Civilised Life, and Clean Efficient Utilization of Renewable Feedstocks", *ChemSusChem* **2014**, *7*, 1801-1832.
[31] P. Kaiser, R. B. Unde, C. Kern, A. Jess, "Production of Liquid Hydrocarbons with CO_2 as Carbon Source based on Reverse Water-Gas Shift and Fischer-Tropsch Synthesis", *Chem. Ing. Tech.* **2013**, *85*, 489-499.
[32] M. Iglesias González, C. de Vries, M. Claeys, G. Schaub, "Chemical energy storage in gaseous hydrocarbons via iron Fischer–Tropsch synthesis from H_2/CO_2—Kinetics, selectivity and process considerations", *Catal. Today* **2015**, *242, Part A*, 184-192.
[33] L. K. Rihko-Struckmann, A. Peschel, R. Hanke-Rauschenbach, K. Sundmacher, "Assessment of Methanol Synthesis Utilizing Exhaust CO_2 for Chemical Storage of Electrical Energy", *Ind. Eng. Chem. Res.* **2010**, *49*, 11073-11078.
[34] F. Studt, F. Abild-pedersen, J. K. Nørskov, S. Dahl, I. Sharafutdinov, C. F. Elkjaer, US Patent 20,120,225,956, **2012**.

[35] F. Studt, I. Sharafutdinov, F. Abild-Pedersen, C. F. Elkjær, J. S. Hummelshøj, S. Dahl, I. Chorkendorff, J. K. Nørskov, "Discovery of a Ni-Ga catalyst for carbon dioxide reduction to methanol", *Nat. Chem.* **2014**, *6*, 320-324.
[36] K. Hashimoto, M. Yamasaki, K. Fujimura, T. Matsui, K. Izumiya, M. Komori, A. A. El-Moneim, E. Akiyama, H. Habazaki, N. Kumagai, A. Kawashima, K. Asami, "Global CO_2 recycling — novel materials and prospect for prevention of global warming and abundant energy supply", *Mater. Sci. Eng. A* **1999**, *267*, 200-206.
[37] K. Hashimoto, N. Kumagai, K. Izumiya, H. Takano, Z. Kato, "The production of renewable energy in the form of methane using electrolytic hydrogen generation", *Energy Sustain. Soc.* **2014**, *4*, 1-9.
[38] K. F. Kalz, R. Kraehnert, M. Dvoyashkin, R. Dittmeyer, R. Gläser, U. Krewer, K. Reuter, J.-D. Grunwaldt, "Future Challenges in Heterogeneous Catalysis: Understanding Catalysts under Dynamic Reaction Conditions", *ChemCatChem* **2017**, *9*, 17-29.
[39] M. E. Boot-Handford, J. C. Abanades, E. J. Anthony, M. J. Blunt, S. Brandani, N. Mac Dowell, J. R. Fernandez, M.-C. Ferrari, R. Gross, J. P. Hallett, R. S. Haszeldine, P. Heptonstall, A. Lyngfelt, Z. Makuch, E. Mangano, R. T. J. Porter, M. Pourkashanian, G. T. Rochelle, N. Shah, J. G. Yao, P. S. Fennell, "Carbon capture and storage update", *Energy Environ. Sci.* **2014**, *7*, 130-189.
[40] P. Markewitz, R. Bongartz, "Carbon Capture Technologies" in *Carbon Capture, Storage and Use: Technical, Economic, Environmental and Societal Perspectives* (Eds.: W. Kuckshinrichs, J.-F. Hake), Springer International Publishing, Cham, **2015**, pp. 13-45.
[41] W. Köppel, M. Götz, F. Graf, "Biogas upgrading for injection into the gas grid", *gwf-Gas / Erdgas* **2009**, *150*, 26-35.
[42] G. A. Olah, A. Goeppert, G. K. S. Prakash, "Chemical Recycling of Carbon Dioxide to Methanol and Dimethyl Ether: From Greenhouse Gas to Renewable, Environmentally Carbon Neutral Fuels and Synthetic Hydrocarbons", *J. Org. Chem.* **2008**, *74*, 487-498.
[43] T. Sakakura, J.-C. Choi, H. Yasuda, "Transformation of carbon dioxide", *Chem. Rev.* **2007**, *107*, 2365-2387.
[44] S. Rieke, "Erste industrielle Power-to-Gas-Anlage mit 6 Megawatt", *gwf–Gas / Erdgas* **2013**, 660-664.
[45] "Audi e-gas-project - Life Cycle Assessment", Audi CR-Report, Audi AG, Ingolstadt, **2014**.
[46] "Audi Technology Portal - Audi e-gas" www.audi-technology-portal.com, Audi AG, **2014**, (access date 25.04.2017).
[47] O. Deutschmann, J.-D. Grunwaldt, "Abgasnachbehandlung in mobilen Systemen: Stand der Technik, Herausforderungen und Perspektiven - Exhaust Gas Aftertreatment in Mobile Systems: Status, Challenges, and Perspectives", *Chem. Ing. Tech.* **2013**, *85*, 595-617.
[48] A. T. Gremminger, H. W. P. Carvalho, R. Popescu, J.-D. Grunwaldt, O. Deutschmann, "Influence of gas composition on activity and durability of bimetallic Pd-Pt/Al_2O_3 catalysts for total oxidation of methane", *Catal. Today* **2015**, *258, Part 2*, 470-480.

[49] M. Iglesias González, G. Schaub, "Fischer-Tropsch Synthesis with H_2/CO_2 – Catalyst Behavior under Transient Conditions", *Chem. Ing. Tech.* **2015**, *87*, 848-854.
[50] M. Iglesias González, H. Eilers, G. Schaub, "Flexible Operation of Fixed-Bed Reactors for a Catalytic Fuel Synthesis - CO_2 Hydrogenation as Example Reaction", *Energy Technol.* **2016**, *4*, 90-103.
[51] J. Gao, Q. Liu, F. Gu, B. Liu, Z. Zhong, F. Su, "Recent advances in methanation catalysts for the production of synthetic natural gas", *RSC Adv.* **2015**, *5*, 22759-22776.
[52] M. A. A. Aziz, A. A. Jalil, S. Triwahyono, A. Ahmad, "CO_2 methanation over heterogeneous catalysts: recent progress and future prospects", *Green Chem.* **2015**, *17*, 2647-2663.
[53] J. Gao, Y. Wang, Y. Ping, D. Hu, G. Xu, F. Gu, F. Su, "A thermodynamic analysis of methanation reactions of carbon oxides for the production of synthetic natural gas", *RSC Adv.* **2012**, *2*, 2358-2368.
[54] T. Abe, M. Tanizawa, K. Watanabe, A. Taguchi, "CO_2 methanation property of Ru nanoparticle-loaded TiO_2 prepared by a polygonal barrel-sputtering method", *Energy Environ. Sci.* **2009**, *2*, 315-321.
[55] S.-I. Fujita, N. Takezawa, "Difference in the selectivity of CO and CO_2 methanation reactions", *Chem. Eng. J.* **1997**, *68*, 63-68.
[56] G. A. Mills, F. W. Steffgen, "Catalytic Methanation", *Catal. Rev.* **1974**, *8*, 159-210.
[57] S. Fujita, H. Terunuma, M. Nakamura, N. Takezawa, "Mechanisms of methanation of carbon monoxide and carbon dioxide over nickel", *Ind. Eng. Chem. Res.* **1991**, *30*, 1146-1151.
[58] I. A. Fisher, A. T. Bell, "A Comparative Study of CO and CO_2 Hydrogenation over Rh/SiO_2", *J. Catal.* **1996**, *162*, 54-65.
[59] M. A. A. Aziz, A. A. Jalil, S. Triwahyono, R. R. Mukti, Y. H. Taufiq-Yap, M. R. Sazegar, "Highly active Ni-promoted mesostructured silica nanoparticles for CO_2 methanation", *Appl. Catal. B* **2014**, *147*, 359-368.
[60] G. Garbarino, P. Riani, L. Magistri, G. Busca, "A study of the methanation of carbon dioxide on Ni/Al_2O_3 catalysts at atmospheric pressure", *Int. J. Hydrogen Energy* **2014**, *39*, 11557-11565.
[61] L. Bian, L. Zhang, R. Xia, Z. Li, "Enhanced low-temperature CO_2 methanation activity on plasma-prepared Ni-based catalyst", *J. Nat. Gas Sci. Eng.* **2015**, *27, Part 2*, 1189-1194.
[62] S. He, C. Li, H. Chen, D. Su, B. Zhang, X. Cao, B. Wang, M. Wei, D. G. Evans, X. Duan, "A Surface Defect-Promoted Ni Nanocatalyst with Simultaneously Enhanced Activity and Stability", *Chem. Mater.* **2013**, *25*, 1040-1046.
[63] J. Liu, C. Li, F. Wang, S. He, H. Chen, Y. Zhao, M. Wei, D. G. Evans, X. Duan, "Enhanced low-temperature activity of CO_2 methanation over highly-dispersed Ni/TiO_2 catalyst", *Catal. Sci. Technol.* **2013**, *3*, 2627-2633.
[64] F. Ocampo, B. Louis, A.-C. Roger, "Methanation of carbon dioxide over nickel-based $Ce_{0.72}Zr_{0.28}O_2$ mixed oxide catalysts prepared by sol–gel method", *Appl. Catal. A* **2009**, *369*, 90-96.

[65] Q. Pan, J. Peng, T. Sun, D. Gao, S. Wang, S. Wang, "CO_2 methanation on $Ni/Ce_{0.5}Zr_{0.5}O_2$ catalysts for the production of synthetic natural gas", *Fuel Process. Technol.* **2014**, *123*, 166-171.
[66] S. Tada, T. Shimizu, H. Kameyama, T. Haneda, R. Kikuchi, "Ni/CeO_2 catalysts with high CO_2 methanation activity and high CH_4 selectivity at low temperatures", *Int. J. Hydrogen Energy* **2012**, *37*, 5527-5531.
[67] G. Du, S. Lim, Y. Yang, C. Wang, L. Pfefferle, G. L. Haller, "Methanation of carbon dioxide on Ni-incorporated MCM-41 catalysts: The influence of catalyst pretreatment and study of steady-state reaction", *J. Catal.* **2007**, *249*, 370-379.
[68] G. Garbarino, D. Bellotti, P. Riani, L. Magistri, G. Busca, "Methanation of carbon dioxide on Ru/Al_2O_3 and Ni/Al_2O_3 catalysts at atmospheric pressure: Catalysts activation, behaviour and stability", *Int. J. Hydrogen Energy* **2015**, *40*, 9171-9182.
[69] Y. Li, Q. Zhang, R. Chai, G. Zhao, Y. Liu, Y. Lu, F. Cao, "$Ni-Al_2O_3$/Ni-foam catalyst with enhanced heat transfer for hydrogenation of CO_2 to methane", *AlChE J.* **2015**, *61*, 4323-4331.
[70] H. Liu, X. Zou, X. Wang, X. Lu, W. Ding, "Effect of CeO_2 addition on Ni/Al_2O_3 catalysts for methanation of carbon dioxide with hydrogen", *J. Nat. Gas Chem.* **2012**, *21*, 703-707.
[71] N. Perkas, G. Amirian, Z. Zhong, J. Teo, Y. Gofer, A. Gedanken, "Methanation of Carbon Dioxide on Ni Catalysts on Mesoporous ZrO_2 Doped with Rare Earth Oxides", *Catal. Lett.* **2009**, *130*, 455-462.
[72] K. P. Brooks, J. Hu, H. Zhu, R. J. Kee, "Methanation of carbon dioxide by hydrogen reduction using the Sabatier process in microchannel reactors", *Chem. Eng. Sci.* **2007**, *62*, 1161-1170.
[73] C. Janke, M. S. Duyar, M. Hoskins, R. Farrauto, "Catalytic and adsorption studies for the hydrogenation of CO_2 to methane", *Appl. Catal. B* **2014**, *152–153*, 184-191.
[74] J. H. Kwak, L. Kovarik, J. Szanyi, "CO_2 Reduction on Supported Ru/Al_2O_3 Catalysts: Cluster Size Dependence of Product Selectivity", *ACS Catal.* **2013**, *3*, 2449-2455.
[75] K. Müller, M. Städter, F. Rachow, D. Hoffmannbeck, D. Schmeißer, "Sabatier-based CO_2-methanation by catalytic conversion", *Environ. Earth Sci.* **2013**, 1-8.
[76] S. Tada, O. J. Ochieng, R. Kikuchi, T. Haneda, H. Kameyama, "Promotion of CO_2 methanation activity and CH_4 selectivity at low temperatures over $Ru/CeO_2/Al_2O_3$ catalysts", *Int. J. Hydrogen Energy* **2014**, *39*, 10090-10100.
[77] D. C. Upham, A. R. Derk, S. Sharma, H. Metiu, E. W. McFarland, "CO_2 methanation by Ru-doped ceria: the role of the oxidation state of the surface", *Catal. Sci. Technol.* **2015**, *5*, 1783.
[78] A. Beuls, C. Swalus, M. Jacquemin, G. Heyen, A. Karelovic, P. Ruiz, "Methanation of CO_2: Further insight into the mechanism over $Rh/\gamma-Al_2O_3$ catalyst", *Appl. Catal. B* **2012**, *113–114*, 2-10.
[79] R. Büchel, A. Baiker, S. E. Pratsinis, "Effect of Ba and K addition and controlled spatial deposition of Rh in Rh/Al_2O_3 catalysts for CO_2 hydrogenation", *Appl. Catal. A* **2014**, *477*, 93-101.
[80] A. Karelovic, P. Ruiz, "Mechanistic study of low temperature CO_2 methanation over Rh/TiO_2 catalysts", *J. Catal.* **2013**, *301*, 141-153.

[81] G. Zhou, T. Wu, H. Xie, X. Zheng, "Effects of structure on the carbon dioxide methanation performance of Co-based catalysts", *Int. J. Hydrogen Energy* **2013**, *38*, 10012-10018.
[82] J.-N. Park, E. W. McFarland, "A highly dispersed Pd–Mg/SiO_2 catalyst active for methanation of CO_2", *J. Catal.* **2009**, *266*, 92-97.
[83] H. Y. Kim, H. M. Lee, J.-N. Park, "Bifunctional Mechanism of CO_2 Methanation on Pd-MgO/SiO_2 Catalyst: Independent Roles of MgO and Pd on CO_2 Methanation", *J. Phys. Chem. C* **2010**, *114*, 7128-7131.
[84] J. Kopyscinski, T. J. Schildhauer, S. M. A. Biollaz, "Production of synthetic natural gas (SNG) from coal and dry biomass – A technology review from 1950 to 2009", *Fuel* **2010**, *89*, 1763-1783.
[85] S. Abelló, C. Berrueco, D. Montané, "High-loaded nickel–alumina catalyst for direct CO_2 hydrogenation into synthetic natural gas (SNG)", *Fuel* **2013**, *113*, 598-609.
[86] S. Rahmani, M. Rezaei, F. Meshkani, "Preparation of highly active nickel catalysts supported on mesoporous nanocrystalline γ-Al_2O_3 for CO_2 methanation", *J. Ind. Eng. Chem.* **2014**, *20*, 1346-1352.
[87] S. Hwang, U. G. Hong, J. Lee, J. H. Baik, D. J. Koh, H. Lim, I. K. Song, "Methanation of Carbon Dioxide Over Mesoporous Nickel–M–Alumina (M= Fe, Zr, Ni, Y, and Mg) Xerogel Catalysts: Effect of Second Metal", *Catal. Lett.* **2012**, *142*, 860-868.
[88] M. Guo, G. Lu, "The effect of impregnation strategy on structural characters and CO_2 methanation properties over MgO modified Ni/SiO_2 catalysts", *Catal. Commun.* **2014**, *54*, 55-60.
[89] M. Yamasaki, M. Komori, E. Akiyama, H. Habazaki, A. Kawashima, K. Asami, K. Hashimoto, "CO_2 methanation catalysts prepared from amorphous Ni–Zr–Sm and Ni–Zr–misch metal alloy precursors", *Mater. Sci. Eng. A* **1999**, *267*, 220-226.
[90] M. Yamasaki, H. Habazaki, K. Asami, K. Izumiya, K. Hashimoto, "Effect of tetragonal ZrO_2 on the catalytic activity of Ni/ZrO_2 catalyst prepared from amorphous Ni–Zr alloys", *Catal. Commun.* **2006**, *7*, 24-28.
[91] J. Ren, X. Qin, J.-Z. Yang, Z.-F. Qin, H.-L. Guo, J.-Y. Lin, Z. Li, "Methanation of carbon dioxide over Ni–M/ZrO_2 (M = Fe, Co, Cu) catalysts: Effect of addition of a second metal", *Fuel Process. Technol.* **2015**, *137*, 204-211.
[92] C. de Leitenburg, A. Trovarelli, J. Kašpar, "A Temperature-Programmed and Transient Kinetic Study of CO_2 Activation and Methanation over CeO_2 Supported Noble Metals", *J. Catal.* **1997**, *166*, 98-107.
[93] F. Ocampo, B. Louis, L. Kiwi-Minsker, A.-C. Roger, "Effect of Ce/Zr composition and noble metal promotion on nickel based $Ce_XZr_{1-X}O_2$ catalysts for carbon dioxide methanation", *Appl. Catal. A* **2011**, *392*, 36-44.
[94] F. Ocampo, B. Louis, A. Kiennemann, A. Roger, in "IOP Conference Series: Materials Science and Engineering", *Vol. 19*, IOP Publishing, **2011**, p. 012007.
[95] P. A. U. Aldana, F. Ocampo, K. Kobl, B. Louis, F. Thibault-Starzyk, M. Daturi, P. Bazin, S. Thomas, A. C. Roger, "Catalytic CO_2 valorization into CH_4 on Ni-based ceria-zirconia. Reaction mechanism by *operando* IR spectroscopy", *Catal. Today* **2013**, *215*, 201-207.

[96] Q. Pan, J. Peng, T. Sun, S. Wang, S. Wang, "Insight into the reaction route of CO_2 methanation: Promotion effect of medium basic sites", *Catal. Commun.* **2014**, *45*, 74-78.
[97] M. Cai, J. Wen, W. Chu, X. Cheng, Z. Li, "Methanation of carbon dioxide on Ni/ZrO_2-Al_2O_3 catalysts: Effects of ZrO_2 promoter and preparation method of novel ZrO_2-Al_2O_3 carrier", *J. Nat. Gas Chem.* **2011**, *20*, 318-324.
[98] Y. Li, G. Lu, J. Ma, "Highly active and stable nano NiO-MgO catalyst encapsulated by silica with a core-shell structure for CO_2 methanation", *RSC Adv.* **2014**, *4*, 17420-17428.
[99] H. Takano, K. Izumiya, N. Kumagai, K. Hashimoto, "The effect of heat treatment on the performance of the Ni/(Zr-Sm oxide) catalysts for carbon dioxide methanation", *Appl. Surf. Sci.* **2011**, *257*, 8171-8176.
[100] M. P. Andersson, T. Bligaard, A. Kustov, K. E. Larsen, J. Greeley, T. Johannessen, C. H. Christensen, J. K. Nørskov, "Toward computational screening in heterogeneous catalysis: Pareto-optimal methanation catalysts", *J. Catal.* **2006**, *239*, 501-506.
[101] T. Bligaard, J. K. Nørskov, S. Dahl, J. Matthiesen, C. H. Christensen, J. Sehested, "The Brønsted–Evans–Polanyi relation and the volcano curve in heterogeneous catalysis", *J. Catal.* **2004**, *224*, 206-217.
[102] D. Tian, Z. Liu, D. Li, H. Shi, W. Pan, Y. Cheng, "Bimetallic Ni–Fe total-methanation catalyst for the production of substitute natural gas under high pressure", *Fuel* **2013**, *104*, 224-229.
[103] A. L. Kustov, A. M. Frey, K. E. Larsen, T. Johannessen, J. K. Nørskov, C. H. Christensen, "CO methanation over supported bimetallic Ni–Fe catalysts: From computational studies towards catalyst optimization", *Appl. Catal. A* **2007**, *320*, 98-104.
[104] J. Sehested, K. Larsen, A. Kustov, A. Frey, T. Johannessen, T. Bligaard, M. Andersson, J. Nørskov, C. Christensen, "Discovery of technical methanation catalysts based on computational screening", *Top. Catal.* **2007**, *45*, 9-13.
[105] S.-H. Kang, J.-H. Ryu, J.-H. Kim, S.-J. Seo, Y.-D. Yoo, P. S. Sai Prasad, H.-J. Lim, C.-D. Byun, "Co-methanation of CO and CO_2 on the Ni_X-Fe_{1-X}/Al_2O_3 catalysts; effect of Fe contents", *Korean J. Chem. Eng.* **2011**, *28*, 2282-2286.
[106] D. Pandey, G. Deo, "Promotional effects in alumina and silica supported bimetallic Ni–Fe catalysts during CO_2 hydrogenation", *J. Mol. Catal. A: Chem.* **2014**, *382*, 23-30.
[107] W. Zhen, B. Li, G. Lu, J. Ma, "Enhancing catalytic activity and stability for CO_2 methanation on Ni-Ru/γ-Al_2O_3 *via* modulating impregnation sequence and controlling surface active species", *RSC Adv.* **2014**, *4*, 16472-16479.
[108] C. Yuan, N. Yao, X. Wang, J. Wang, D. Lv, X. Li, "The SiO_2 supported bimetallic Ni–Ru particles: A good sulfur-tolerant catalyst for methanation reaction", *Chem. Eng. J.* **2015**, *260*, 1-10.
[109] F. Lange, U. Armbruster, A. Martin, "Heterogeneously-Catalyzed Hydrogenation of Carbon Dioxide to Methane using RuNi Bimetallic Catalysts", *Energy Technol.* **2015**, *3*, 55-62.
[110] S. Hwang, J. Lee, U. G. Hong, J. H. Baik, D. J. Koh, H. Lim, I. K. Song, "Methanation of carbon dioxide over mesoporous Ni–Fe–Ru–Al_2O_3 xerogel catalysts: Effect of ruthenium content", *J. Ind. Eng. Chem.* **2013**, *19*, 698-703.

[111] D. E. Peebles, D. W. Goodman, J. M. White, "Methanation of carbon dioxide on nickel(100) and the effects of surface modifiers", *J. Phys. Chem.* **1983**, *87*, 4378-4387.
[112] J. Ren, H. Guo, J. Yang, Z. Qin, J. Lin, Z. Li, "Insights into the mechanisms of CO_2 methanation on Ni(111) surfaces by density functional theory", *Appl. Surf. Sci.* **2015**, *351*, 504-516.
[113] S. J. Choe, H. J. Kang, S. Kim, S. Park, D. H. Park, D. S. Huh, "Adsorbed Carbon Formation and Carbon Hydrogenation for CO_2 Methanation on the Ni (111) Surface: ASED-MO Study", *Bull. Korean Chem. Soc* **2005**, *26*, 1682.
[114] M. Marwood, R. Doepper, A. Renken, "*In-situ* surface and gas phase analysis for kinetic studies under transient conditions The catalytic hydrogenation of CO_2", *Appl. Catal. A* **1997**, *151*, 223-246.
[115] C. Schild, A. Wokaun, R. A. Koeppel, A. Baiker, "Carbon dioxide hydrogenation over nickel/zirconia catalysts from amorphous precursors: on the mechanism of methane formation", *J. Phys. Chem.* **1991**, *95*, 6341-6346.
[116] A. Westermann, B. Azambre, M. C. Bacariza, I. Graça, M. F. Ribeiro, J. M. Lopes, C. Henriques, "Insight into CO_2 methanation mechanism over NiUSY zeolites: An *operando* IR study", *Appl. Catal. B* **2015**, *174–175*, 120-125.
[117] X. Wang, Y. Hong, H. Shi, J. Szanyi, "Kinetic modeling and transient DRIFTS–MS studies of CO_2 methanation over Ru/Al_2O_3 catalysts", *J. Catal.* **2016**, *343*, 185-195.
[118] Q. Pan, J. Peng, S. Wang, S. Wang, "*In situ* FTIR spectroscopic study of the CO_2 methanation mechanism on $Ni/Ce_{0.5}Zr_{0.5}O_2$", *Catal. Sci. Technol.* **2014**, *4*, 502-509.
[119] A. Westermann, B. Azambre, M. C. Bacariza, I. Graça, M. F. Ribeiro, J. M. Lopes, C. Henriques, "The promoting effect of Ce in the CO_2 methanation performances on NiUSY zeolite: A FTIR *In Situ/Operando* study", *Catal. Today* **2017**, *283*, 74-81.
[120] D. Türks, H. Mena, U. Armbruster, A. Martin, "Methanation of CO_2 on Ni/Al_2O_3 in a Structured Fixed-Bed Reactor—A Scale-Up Study", *Catalysts* **2017**, *7*, 152.
[121] S. Rönsch, J. Köchermann, J. Schneider, S. Matthischke, "Global Reaction Kinetics of CO and CO_2 Methanation for Dynamic Process Modeling", *Chem. Eng. Technol.* **2016**, *39*, 208-218.
[122] S. Rönsch, S. Matthischke, M. Müller, P. Eichler, "Dynamische Simulation von Reaktoren zur Festbettmethanisierung - Dynamic Simulation of Fixed-Bed Methanation Reactors", *Chem. Ing. Tech.* **2014**, *86*, 1198-1204.
[123] R. Güttel, "Study of Unsteady-State Operation of Methanation by Modeling and Simulation", *Chem. Eng. Technol.* **2013**, *36*, 1675-1682.
[124] T. Schaaf, J. Grünig, M. R. Schuster, T. Rothenfluh, A. Orth, "Methanation of CO_2-storage of renewable energy in a gas distribution system", *Energy Sustain. Soc.* **2014**, *4*, 2.
[125] S. Rönsch, J. Schneider, S. Matthischke, M. Schlüter, M. Götz, J. Lefebvre, P. Prabhakaran, S. Bajohr, "Review on methanation – From fundamentals to current projects", *Fuel* **2016**, *166*, 276-296.
[126] Z. Liu, B. Chu, X. Zhai, Y. Jin, Y. Cheng, "Total methanation of syngas to synthetic natural gas over Ni catalyst in a micro-channel reactor", *Fuel* **2012**, *95*, 599-605.

[127] M. Belimov, D. Metzger, P. Pfeifer, "On the temperature control in a microstructured packed bed reactor for methanation of CO/CO_2 mixtures", *AlChE J.* **2017**, *63*, 120-129.
[128] J. Kopyscinski, T. J. Schildhauer, S. M. A. Biollaz, "Employing Catalyst Fluidization to Enable Carbon Management in the Synthetic Natural Gas Production from Biomass", *Chem. Eng. Technol.* **2009**, *32*, 343-347.
[129] J. Li, L. Zhou, P. Li, Q. Zhu, J. Gao, F. Gu, F. Su, "Enhanced fluidized bed methanation over a Ni/Al_2O_3 catalyst for production of synthetic natural gas", *Chem. Eng. J.* **2013**, *219*, 183-189.
[130] J. Lefebvre, M. Götz, S. Bajohr, R. Reimert, T. Kolb, "Improvement of three-phase methanation reactor performance for steady-state and transient operation", *Fuel Process. Technol.* **2015**, *132*, 83-90.
[131] M. Götz, S. Bajohr, F. Graf, R. Reimert, T. Kolb, "Einsatz eines blasensäulenreaktors zur methansynthese", *Chem. Ing. Tech.* **2013**, *85*, 1146-1151.
[132] "Audi MediaCenter - Audi e-gas Anlage in Werlte" www.audi-mediacenter.com/de/fotos/detail/audi-e-gas-anlage-in-werlte-488, Audi AG, **2013**, (access date 12.05.2017).
[133] T. Bosa, C. Brusdeylins, A. Del Regno, G. Scherg, U. Zimmer, in "Anual Report", Zentrum für Sonnenenergie- und Wasserstoff-Forschung Baden-Württemberg (ZSW), Stuttgart, **2013**.
[134] "Erneuerbares Methan aus Ökostrom", ZSW, Fraunhofer IWES, ETOGAS, **2013**.
[135] K.-H. Busse, "Kommerzielle, dezentrale, emissionsfreie Power-to-Gas-Anlage und Konzepte im Bereich der Gebäude- und Kraftwerkstechnik", 4. Management Circle Fachkonferenz, Berlin, **2016**.
[136] M. Landgraf, "Power to Gas: Storing the Wind and Sun in Natural Gas", Press Release, Karlsruhe Institute of Technology, Karlsruhe, **2014**.
[137] M. Gruber, "Effizienzsteigerung der Power to Gas Technologie durch thermische Integration von Hochtemperatur Dampfelektrolyse und CO_2-Methanisierung - das HELMETH Projekt", Jahrestreffen der ProcessNet - Gasreinigung & Energieverfahrenstechnik, Frankfurt, **2017**.
[138] M. Bailera, P. Lisbona, L. M. Romeo, S. Espatolero, "Power to Gas projects review: Lab, pilot and demo plants for storing renewable energy and CO_2", *Renew. Sust. Energ. Rev.* **2017**, *69*, 292-312.
[139] C. H. Bartholomew, "Mechanisms of catalyst deactivation", *Appl. Catal. A* **2001**, *212*, 17-60.
[140] P. Munnik, M. E. Z. Velthoen, P. E. de Jongh, K. P. de Jong, C. J. Gommes, "Nanoparticle Growth in Supported Nickel Catalysts during Methanation Reaction—Larger is Better", *Angew. Chem. Int. Ed.* **2014**, *53*, 9493-9497.
[141] J. A. Moulijn, A. E. van Diepen, F. Kapteijn, "Catalyst deactivation: is it predictable?: What to do?", *Appl. Catal. A* **2001**, *212*, 3-16.
[142] P. Forzatti, L. Lietti, "Catalyst deactivation", *Catal. Today* **1999**, *52*, 165-181.
[143] J. Sehested, J. A. P. Gelten, S. Helveg, "Sintering of nickel catalysts: Effects of time, atmosphere, temperature, nickel-carrier interactions, and dopants", *Appl. Catal. A* **2006**, *309*, 237-246.
[144] J. Sehested, "Four challenges for nickel steam-reforming catalysts", *Catal. Today* **2006**, *111*, 103-110.

[145] L. Xu, F. Wang, M. Chen, J. Zhang, K. Yuan, L. Wang, K. Wu, G. Xu, W. Chen, "CO_2 methanation over a Ni based ordered mesoporous catalyst for the production of synthetic natural gas", *RSC Adv.* **2016**, *6*, 28489-28499.
[146] T. W. Hansen, A. T. DeLaRiva, S. R. Challa, A. K. Datye, "Sintering of Catalytic Nanoparticles: Particle Migration or Ostwald Ripening?", *Acc. Chem. Res* **2013**, *46*, 1720-1730.
[147] J. Sehested, J. A. P. Gelten, I. N. Remediakis, H. Bengaard, J. K. Nørskov, "Sintering of nickel steam-reforming catalysts: effects of temperature and steam and hydrogen pressures", *J. Catal.* **2004**, *223*, 432-443.
[148] X. Bai, S. Wang, T. Sun, S. Wang, "The sintering of Ni/Al_2O_3 methanation catalyst for substitute natural gas production", *Reac. Kinet. Mech. Cat.* **2014**, *112*, 437-451.
[149] J. R. Rostrup-Nielsen, K. Pedersen, J. Sehested, "High temperature methanation: Sintering and structure sensitivity", *Appl. Catal. A* **2007**, *330*, 134-138.
[150] T. T. M. Nguyen, L. Wissing, M. S. Skjøth-Rasmussen, "High temperature methanation: Catalyst considerations", *Catal. Today* **2013**, *215*, 233-238.
[151] J. Barrientos, M. Lualdi, R. Suárez París, V. Montes, M. Boutonnet, S. Järås, "CO methanation over TiO_2-supported nickel catalysts: A carbon formation study", *Appl. Catal. A* **2015**, *502*, 276-286.
[152] J. Sehested, S. Dahl, J. Jacobsen, J. R. Rostrup-Nielsen, "Methanation of CO over Nickel: Mechanism and Kinetics at High H_2/CO Ratios", *J. Phys. Chem. B* **2005**, *109*, 2432-2438.
[153] C. H. Bartholomew, "Carbon Deposition in Steam Reforming and Methanation", *Catal. Rev.* **1982**, *24*, 67-112.
[154] M. Bradford, M. Vannice, "CO_2 reforming of CH_4", *Catal. Rev.* **1999**, *41*, 1-42.
[155] Y. Li, Y. Wang, X. Zhang, Z. Mi, "Thermodynamic analysis of autothermal steam and CO_2 reforming of methane", *Int. J. Hydrogen Energy* **2008**, *33*, 2507-2514.
[156] I. Czekaj, F. Loviat, F. Raimondi, J. Wambach, S. Biollaz, A. Wokaun, "Characterization of surface processes at the Ni-based catalyst during the methanation of biomass-derived synthesis gas: X-ray photoelectron spectroscopy (XPS)", *Appl. Catal. A* **2007**, *329*, 68-78.
[157] S. Helveg, C. López-Cartes, J. Sehested, P. L. Hansen, B. S. Clausen, J. R. Rostrup-Nielsen, F. Abild-Pedersen, J. K. Nørskov, "Atomic-scale imaging of carbon nanofibre growth", *Nature* **2004**, *427*, 426-429.
[158] S. A. Theofanidis, V. V. Galvita, H. Poelman, G. B. Marin, "Enhanced Carbon-Resistant Dry Reforming Fe-Ni Catalyst: Role of Fe", *ACS Catal.* **2015**, *5*, 3028-3039.
[159] S. M. Kim, P. M. Abdala, T. Margossian, D. Hosseini, L. Foppa, A. Armutlulu, W. van Beek, A. Comas-Vives, C. Copéret, C. Müller, "Cooperativity and Dynamics Increase the Performance of NiFe Dry Reforming Catalysts", *JACS* **2017**, *139*, 1937-1949.
[160] Z. Hou, T. Yashima, "Small Amounts of Rh-Promoted Ni Catalysts for Methane Reforming with CO_2", *Catal. Lett.* **2003**, *89*, 193-197.
[161] Z. Hou, P. Chen, H. Fang, X. Zheng, T. Yashima, "Production of synthesis gas via methane reforming with CO on noble metals and small amount of noble-(Rh-) promoted Ni catalysts", *Int. J. Hydrogen Energy* **2006**, *31*, 555-561.

[162] X. Bai, S. Wang, T. Sun, S. Wang, "Influence of Operating Conditions on Carbon Deposition Over a Ni Catalyst for the Production of Synthetic Natural Gas (SNG) from Coal", *Catal. Lett.* **2014**, *144*, 2157-2166.
[163] S. Takenaka, E. Kato, Y. Tomikubo, K. Otsuka, "Structural change of Ni species during the methane decomposition and the subsequent gasification of deposited carbon with CO_2 over supported Ni catalysts", *J. Catal.* **2003**, *219*, 176-185.
[164] M. A. Newton, "Dynamic adsorbate/reaction induced structural change of supported metal nanoparticles: heterogeneous catalysis and beyond", *Chem. Soc. Rev.* **2008**, *37*, 2644-2657.
[165] J.-D. Grunwaldt, J. B. Wagner, R. E. Dunin-Borkowski, "Imaging Catalysts at Work: A Hierarchical Approach from the Macro- to the Meso- and Nano-scale", *ChemCatChem* **2013**, *5*, 62-80.
[166] R. Schlögl, "Heterogeneous Catalysis", *Angew. Chem. Int. Ed.* **2015**, *54*, 3465-3520.
[167] R. Schlögl, "Catalysis 4.0", *ChemCatChem* **2017**, *9*, 533-541.
[168] E. C. Lovell, A. Fuller, J. Scott, R. Amal, "Enhancing Ni-SiO_2 catalysts for the carbon dioxide reforming of methane: Reduction-oxidation-reduction pre-treatment", *Appl. Catal. B* **2016**, *199*, 155-165.
[169] W. S. Epling, L. E. Campbell, A. Yezerets, N. W. Currier, J. E. Parks, "Overview of the Fundamental Reactions and Degradation Mechanisms of NOx Storage/Reduction Catalysts", *Catal. Rev.* **2004**, *46*, 163-245.
[170] L. Lietti, P. Forzatti, I. Nova, E. Tronconi, "NOx Storage Reduction over Pt-Ba/γ-Al_2O_3 Catalyst", *J. Catal.* **2001**, *204*, 175-191.
[171] J.-D. Grunwaldt, A. M. Molenbroek, N. Y. Topsøe, H. Topsøe, B. S. Clausen, "*In Situ* Investigations of Structural Changes in Cu/ZnO Catalysts", *J. Catal.* **2000**, *194*, 452-460.
[172] P. L. Hansen, J. B. Wagner, S. Helveg, J. R. Rostrup-Nielsen, B. S. Clausen, H. Topsøe, "Atom-resolved imaging of dynamic shape changes in supported copper nanocrystals", *Science* **2002**, *295*, 2053-2055.
[173] T. Lunkenbein, J. Schumann, M. Behrens, R. Schlögl, M. G. Willinger, "Formation of a ZnO Overlayer in Industrial Cu/ZnO/Al_2O_3 Catalysts Induced by Strong Metal–Support Interactions", *Angew. Chem.* **2015**, *127*, 4627-4631.
[174] A. Ota, J. Kröhnert, G. Weinberg, I. Kasatkin, E. L. Kunkes, D. Ferri, F. Girgsdies, N. Hamilton, M. Armbrüster, R. Schlögl, M. Behrens, "Dynamic Surface Processes of Nanostructured Pd_2Ga Catalysts Derived from Hydrotalcite-Like Precursors", *ACS Catal.* **2014**, *4*, 2048-2059.
[175] H. Eilers, G. Schaub, "Fischer-Tropsch-Synthese unter instationären Bedingungen im Suspensionsreaktor: experimentelle und rechnerische Studien - Fischer-Tropsch Synthesis under Transient Conditions in a Slurry Reactor: Experimental and Mathematical Investigations", *Chem. Ing. Tech.* **2015**, *87*, 837-842.
[176] P. M. Haure, R. R. Hudgins, P. L. Silveston, "Periodic operation of a trickle-bed reactor", *AlChE J.* **1989**, *35*, 1437-1444.
[177] R. Lange, R. Gutsche, J. Hanika, "Forced periodic operation of a trickle-bed reactor", *Chem. Eng. Sci.* **1999**, *54*, 2569-2573.
[178] P. Silveston, R. R. Hudgins, A. Renken, "Periodic operation of catalytic reactors—introduction and overview", *Catal. Today* **1995**, *25*, 91-112.

[179] R. Möller, M. Votsmeier, C. Onder, L. Guzzella, J. Gieshoff, "Is oxygen storage in three-way catalysts an equilibrium controlled process?", *Appl. Catal. B* **2009**, *91*, 30-38.
[180] K. Robinson, S. Ye, Y. Yap, S. T. Kolaczkowski, "Application of a methodology to assess the performance of a full-scale diesel oxidation catalyst during cold and hot start NEDC drive cycles", *Chemical Engineering Research and Design* **2013**, *91*, 1292-1306.
[181] R. Lin, B. Li, Y. P. Hou, J. M. Ma, "Investigation of dynamic driving cycle effect on performance degradation and micro-structure change of PEM fuel cell", *Int. J. Hydrogen Energy* **2009**, *34*, 2369-2376.
[182] J. C. Meier, C. Galeano, I. Katsounaros, A. A. Topalov, A. Kostka, F. Schüth, K. J. J. Mayrhofer, "Degradation Mechanisms of Pt/C Fuel Cell Catalysts under Simulated Start–Stop Conditions", *ACS Catal.* **2012**, *2*, 832-843.
[183] B. M. Weckhuysen, "Determining the active site in a catalytic process: *Operando* spectroscopy is more than a buzzword", *Phys. Chem. Chem. Phys.* **2003**, *5*, 4351-4360.
[184] H. Topsøe, "Developments in *operando* studies and *in situ* characterization of heterogeneous catalysts", *J. Catal.* **2003**, *216*, 155-164.
[185] A. Iglesias-Juez, A. M. Beale, K. Maaijen, T. C. Weng, P. Glatzel, B. M. Weckhuysen, "A combined *in situ* time-resolved UV–Vis, Raman and high-energy resolution X-ray absorption spectroscopy study on the deactivation behavior of Pt and PtSn propane dehydrogenation catalysts under industrial reaction conditions", *J. Catal.* **2010**, *276*, 268-279.
[186] M. A. Bañares, "*Operando* methodology: combination of *in situ* spectroscopy and simultaneous activity measurements under catalytic reaction conditions", *Catal. Today* **2005**, *100*, 71-77.
[187] J.-D. Grunwaldt, C. G. Schroer, "Hard and soft X-ray microscopy and tomography in catalysis: bridging the different time and length scales", *Chem. Soc. Rev.* **2010**, *39*, 4741-4753.
[188] S. B. Simonsen, I. Chorkendorff, S. Dahl, M. Skoglundh, J. Sehested, S. Helveg, "Ostwald ripening in a Pt/SiO_2 model catalyst studied by *in situ* TEM", *J. Catal.* **2011**, *281*, 147-155.
[189] B. Clausen, L. Gråbæk, G. Steffensen, P. Hansen, H. Topsøe, "A combined QEXAFS/XRD method for on-line, *in situ* studies of catalysts: Examples of dynamic measurements of Cu-based methanol catalysts", *Catal. Lett.* **1993**, *20*, 23-36.
[190] D. E. Doronkin, M. Casapu, T. Günter, O. Müller, R. Frahm, J.-D. Grunwaldt, "*Operando* Spatially- and Time-Resolved XAS Study on Zeolite Catalysts for Selective Catalytic Reduction of NO_X by NH_3", *J. Phys. Chem. C* **2014**, *118*, 10204-10212.
[191] A. M. Gänzler, M. Casapu, A. Boubnov, O. Müller, S. Conrad, H. Lichtenberg, R. Frahm, J.-D. Grunwaldt, "*Operando* spatially and time-resolved X-ray absorption spectroscopy and infrared thermography during oscillatory CO oxidation", *J. Catal.* **2015**, *328*, 216-224.
[192] J.-D. Grunwaldt, N. van Vegten, A. Baiker, "Insight into the structure of supported palladium catalysts during the total oxidation of methane", *Chem. Commun.* **2007**, 4635-4637.

[193] B. Kimmerle, J.-D. Grunwaldt, A. Baiker, P. Glatzel, P. Boye, S. Stephan, C. G. Schroer, "Visualizing a Catalyst at Work during the Ignition of the Catalytic Partial Oxidation of Methane", *J. Phys. Chem. C* **2009**, *113*, 3037-3040.
[194] J. Stötzel, R. Frahm, B. Kimmerle, M. Nachtegaal, J.-D. Grunwaldt, "Oscillatory Behavior during the Catalytic Partial Oxidation of Methane: Following Dynamic Structural Changes of Palladium Using the QEXAFS Technique", *J. Phys. Chem. C* **2012**, *116*, 599-609.
[195] H. Wang, J. T. Miller, M. Shakouri, C. Xi, T. Wu, H. Zhao, M. C. Akatay, "XANES and EXAFS studies on metal nanoparticle growth and bimetallic interaction of Ni-based catalysts for CO_2 reforming of CH_4", *Catal. Today* **2013**, *207*, 3-12.
[196] F. Studt, M. Behrens, E. L. Kunkes, N. Thomas, S. Zander, A. Tarasov, J. Schumann, E. Frei, J. B. Varley, F. Abild-Pedersen, J. K. Nørskov, R. Schlögl, "The Mechanism of CO and CO_2 Hydrogenation to Methanol over Cu-Based Catalysts", *ChemCatChem* **2015**, *7*, 1105-1111.
[197] M. Behrens, F. Studt, I. Kasatkin, S. Kühl, M. Hävecker, F. Abild-Pedersen, S. Zander, F. Girgsdies, P. Kurr, B.-L. Kniep, M. Tovar, R. W. Fischer, J. K. Nørskov, R. Schlögl, "The Active Site of Methanol Synthesis over $Cu/ZnO/Al_2O_3$ Industrial Catalysts", *Science* **2012**, *336*, 893-897.
[198] S. Kuld, M. Thorhauge, H. Falsig, C. F. Elkjær, S. Helveg, I. Chorkendorff, J. Sehested, "Quantifying the promotion of Cu catalysts by ZnO for methanol synthesis", *Science* **2016**, *352*, 969-974.
[199] J. L. Eslava, A. Iglesias-Juez, G. Agostini, M. Fernández-García, A. Guerrero-Ruiz, I. Rodríguez-Ramos, "Time-Resolved XAS Investigation of the Local Environment and Evolution of Oxidation States of a Fischer–Tropsch Ru–Cs/C Catalyst", *ACS Catal.* **2016**, *6*, 1437-1445.
[200] J. J. Sattler, A. M. Beale, B. M. Weckhuysen, "*Operando* Raman spectroscopy study on the deactivation of Pt/Al_2O_3 and $Pt–Sn/Al_2O_3$ propane dehydrogenation catalysts", *Phys. Chem. Chem. Phys.* **2013**, *15*, 12095-12103.
[201] J. Zarfl, D. Ferri, T. J. Schildhauer, J. Wambach, A. Wokaun, "DRIFTS study of a commercial $Ni/\gamma\text{-}Al_2O_3$ CO methanation catalyst", *Appl. Catal. A* **2015**, *495*, 104-114.
[202] S. K. Beaumont, S. Alayoglu, C. Specht, W. D. Michalak, V. V. Pushkarev, J. Guo, N. Kruse, G. A. Somorjai, "Combining *in Situ* NEXAFS Spectroscopy and CO_2 Methanation Kinetics To Study Pt and Co Nanoparticle Catalysts Reveals Key Insights into the Role of Platinum in Promoted Cobalt Catalysis", *JACS* **2014**, *136*, 9898-9901.
[203] A. M. Abdel-Mageed, S. Eckle, H. G. Anfang, R. J. Behm, "Selective CO methanation in CO_2-rich H_2 atmospheres over a Ru/zeolite catalyst: The influence of catalyst calcination", *J. Catal.* **2013**, *298*, 148-160.
[204] D. Wierzbicki, R. Baran, R. Dębek, M. Motak, T. Grzybek, M. E. Gálvez, P. Da Costa, "The influence of nickel content on the performance of hydrotalcite-derived catalysts in CO_2 methanation reaction", *Int. J. Hydrogen Energy*.
[205] K. K. Bando, T. Saito, K. Sato, T. Tanaka, F. Dumeignil, M. Imamura, N. Matsubayashi, H. Shimada, "*In situ* XAFS analysis system for high-pressure catalytic reactions and its application to CO_2 hydrogenation over a Rh/Y-zeolite catalyst", *J. Synchrotron. Radiat.* **2001**, *8*, 581-583.

[206] K. K. Bando, N. Ichikuni, K. Soga, K. Kunimori, H. Arakawa, K. Asakura, "Characterization of Rh Particles and Li-Promoted Rh Particles in Y Zeolite during CO_2 Hydrogenation—A New Mechanism for Catalysis Controlled by the Dynamic Structure of Rh Particles and the Li Additive Effect", *J. Catal.* **2000**, *194*, 91-104.
[207] J. W. Geus, A. J. van Dillen, "Preparation of Supported Catalysts by Deposition–Precipitation" in *Handbook of Heterogeneous Catalysis* (Eds.: G. Ertl, H. Knözinger, F. Schüth, J. Weitkamp), Wiley-VCH, Weinheim, Germany, **2008**, pp. 428-467.
[208] K. P. de Jong, "Deposition Precipitation" in *Synthesis of Solid Catalysts* (Ed.: K. P. de Jong), Wiley-VCH, Weinheim, Germany, **2009**, pp. 111-134.
[209] M. K. van der Lee, J. van Dillen, J. H. Bitter, K. P. de Jong, "Deposition Precipitation for the Preparation of Carbon Nanofiber Supported Nickel Catalysts", *JACS* **2005**, *127*, 13573-13582.
[210] G. Bergeret, P. Gallezot, "Particle Size and Dispersion Measurements" in *Handbook of Heterogeneous Catalysis* (Eds.: G. Ertl, H. Knözinger, F. Schüth, J. Weitkamp), Wiley-VCH, Weinheim, Germany, **2008**, pp. 738-765.
[211] B. Mutz, P. Sprenger, W. Wang, D. Wang, W. Kleist, J.-D. Grunwaldt, "*Operando* Raman spectroscopy on CO_2 methanation over alumina-supported Ni, Ni_3Fe and $NiRh_{0.1}$ catalysts: Role of carbon formation as possible deactivation pathway", *Appl. Catal. A* **2018**, *556*, 160-171.
[212] B. Mutz, M. Belimov, W. Wang, P. Sprenger, M.-A. Serrer, D. Wang, P. Pfeifer, W. Kleist, J.-D. Grunwaldt, "Potential of an Alumina-Supported Ni_3Fe Catalyst in the Methanation of CO_2: Impact of Alloy Formation on Activity and Stability", *ACS Catal.* **2017**, *7*, 6802-6814.
[213] M. Belimov, "Methane production from co-electrolysis products applying a microchannel reactor", Dissertation in preparation, IMVT, Karlsruhe Institute of Technology, **2017**.
[214] D. E. Mears, "Diagnostic criteria for heat transport limitations in fixed bed reactors", *J. Catal.* **1971**, *20*, 127-131.
[215] G. F. Froment, K. B. Bischoff, J. De Wilde, "Transport Processes with Reactions Catalyzed by Solids" in *Chemical Reactor Analysis and Design*, 3rd ed., John Wiley & Sons, Inc., New York, USA, **2011**, pp. 154-239.
[216] R. Berger, "*EUROKIN_fixed-bed_html*, EUROKIN spreadsheet on requirements for measurement of intrinsic kinetics in the gas-solid fixed-bed reactor", **2012**. Available at the following: http://eurokin.org/wp-content/uploads/downloads/2012/08/EUROKIN_fixed-bed_html_guide.pdf.
[217] F. Koschany, D. Schlereth, O. Hinrichsen, "On the kinetics of the methanation of carbon dioxide on coprecipitated NiAl(O)x", *Appl. Catal. B* **2016**, *181*, 504-516.
[218] J.-D. Grunwaldt, M. Caravati, S. Hannemann, A. Baiker, "X-ray absorption spectroscopy under reaction conditions: suitability of different reaction cells for combined catalyst characterization and time-resolved studies", *Phys. Chem. Chem. Phys.* **2004**, *6*, 3037-3047.
[219] B. Mutz, H. W. P. Carvalho, S. Mangold, W. Kleist, J.-D. Grunwaldt, "Methanation of CO_2: Structural response of a Ni-based catalyst under fluctuating reaction conditions unraveled by *operando* spectroscopy", *J. Catal.* **2015**, *327*, 48-53.

[220] B. Ravel, M. Newville, "ATHENA, ARTEMIS, HEPHAESTUS: data analysis for X-ray absorption spectroscopy using IFEFFIT", *J. Synchrotron. Radiat.* **2005**, *12*, 537-541.
[221] J. J. Rehr, R. Albers, "Theoretical approaches to x-ray absorption fine structure", *Rev. Mod. Phys.* **2000**, *72*, 621.
[222] S. Calvin, E. Carpenter, B. Ravel, V. Harris, S. Morrison, "Multiedge refinement of extended x-ray-absorption fine structure of manganese zinc ferrite nanoparticles", *Phys. Rev. B: Condens. Matter* **2002**, *66*, 224405.
[223] B. Mutz, A. M. Gänzler, M. Nachtegaal, O. Müller, R. Frahm, W. Kleist, J.-D. Grunwaldt, "Surface Oxidation of Supported Ni Particles and Its Impact on the Catalytic Performance during Dynamically Operated Methanation of CO_2", *Catalysts* **2017**, *7*, 279.
[224] O. Müller, M. Nachtegaal, J. Just, D. Lutzenkirchen-Hecht, R. Frahm, "Quick-EXAFS setup at the SuperXAS beamline for *in situ* X-ray absorption spectroscopy with 10 ms time resolution", *J. Synchrotron. Radiat.* **2016**, *23*, 260-266.
[225] O. Müller, D. Lützenkirchen-Hecht, R. Frahm, "Quick scanning monochromator for millisecond *in situ* and *in operando* X-ray absorption spectroscopy", *Rev. Sci. Instrum.* **2015**, *86*, 093905.
[226] F. Kapteijn, J. A. Moulijn, "Laboratory Catalytic Reactors: Aspects of Catalyst Testing" in *Handbook of Heterogeneous Catalysis* (Eds.: G. Ertl, H. Knözinger, F. Schüth, J. Weitkamp), Wiley-VCH, Weinheim, **2008**, pp. 2019-2045.
[227] J. J. Carberry, "Chemical and Catalytic Reaction Engineering", Dover Publications, Mineola, New York, **2001**.
[228] C. Chu, K. Ng, "Flow in packed tubes with a small tube to particle diameter ratio", *AlChE J.* **1989**, *35*, 148-158.
[229] F.-W. Chang, M.-T. Tsay, S.-P. Liang, "Hydrogenation of CO_2 over nickel catalysts supported on rice husk ash prepared by ion exchange", *Appl. Catal. A* **2001**, *209*, 217-227.
[230] Y. Yang, S. Lim, G. Du, Y. Chen, D. Ciuparu, G. L. Haller, "Synthesis and Characterization of Highly Ordered Ni-MCM-41 Mesoporous Molecular Sieves", *J. Phys. Chem. B* **2005**, *109*, 13237-13246.
[231] B. Mutz, H. W. P. Carvalho, W. Kleist, J.-D. Grunwaldt, "Dynamic transformation of small Ni particles during methanation of CO_2 under fluctuating reaction conditions monitored by *operando* X-ray absorption spectroscopy", *J. Phys.: Conf. Ser.* **2016**, *712*, 012050.
[232] P. Burattin, M. Che, C. Louis, "Metal Particle Size in Ni/SiO_2 Materials Prepared by Deposition−Precipitation: Influence of the Nature of the Ni(II) Phase and of Its Interaction with the Support", *J. Phys. Chem. B* **1999**, *103*, 6171-6178.
[233] J. H. Bitter, M. K. van der Lee, A. G. T. Slotboom, A. J. van Dillen, K. P. de Jong, "Synthesis of Highly Loaded Highly Dispersed Nickel on Carbon Nanofibers by Homogeneous Deposition–Precipitation", *Catal. Lett.* **2003**, *89*, 139-142.
[234] Y.-S. Jung, W.-L. Yoon, T.-W. Lee, Y.-W. Rhee, Y.-S. Seo, "A highly active Ni-Al_2O_3 catalyst prepared by homogeneous precipitation using urea for internal reforming in a molten carbonate fuel cell (MCFC): Effect of the synthesis temperature", *Int. J. Hydrogen Energy* **2010**, *35*, 11237-11244.

[235] J. G. Seo, M. H. Youn, D. R. Park, I. Nam, I. K. Song, "Hydrogen production by steam reforming of liquefied natural gas (LNG) over Ni–Al_2O_3 catalysts prepared by a sequential precipitation method: Effect of precipitation agent", *Int. J. Hydrogen Energy* **2009**, *34*, 8053-8060.
[236] R. Frahm, "Quick scanning exafs: First experiments", *Nucl. Instrum. Methods Phys. Res., Sect. A* **1988**, *270*, 578-581.
[237] M. Nachtegaal, O. Müller, C. König, R. Frahm, "QEXAFS: Techniques and Scientific Applications for Time-Resolved XAS" in *X-Ray Absorption and X-Ray Emission Spectroscopy* (Eds.: J. A. van Bokhoven, C. Lamberti), Wiley-VCH, Weinheim, Germany, **2016**, pp. 155-183.
[238] F. Abild-Pedersen, O. Lytken, J. Engbæk, G. Nielsen, I. Chorkendorff, J. K. Nørskov, "Methane activation on Ni(111): Effects of poisons and step defects", *Surf. Sci.* **2005**, *590*, 127-137.
[239] A. M. Molenbroek, J. K. Nørskov, B. S. Clausen, "Structure and Reactivity of Ni−Au Nanoparticle Catalysts", *J. Phys. Chem. B* **2001**, *105*, 5450-5458.
[240] R. T. Vang, K. Honkala, S. Dahl, E. K. Vestergaard, J. Schnadt, E. Laegsgaard, B. S. Clausen, J. K. Nørskov, F. Besenbacher, "Controlling the catalytic bond-breaking selectivity of Ni surfaces by step blocking", *Nat. Mater.* **2005**, *4*, 160-162.
[241] H. S. Bengaard, J. K. Nørskov, J. Sehested, B. S. Clausen, L. P. Nielsen, A. M. Molenbroek, J. R. Rostrup-Nielsen, "Steam Reforming and Graphite Formation on Ni Catalysts", *J. Catal.* **2002**, *209*, 365-384.
[242] W. Kirstein, I. Petraki, F. Thieme, "A study on oxygen adsorption and coadsorption with carbonmonoxide on a stepped nickel surface", *Surf. Sci.* **1995**, *331*, 162-167.
[243] M. P. Andersson, F. Abild-Pedersen, I. N. Remediakis, T. Bligaard, G. Jones, J. Engbæk, O. Lytken, S. Horch, J. H. Nielsen, J. Sehested, J. R. Rostrup-Nielsen, J. K. Nørskov, I. Chorkendorff, "Structure sensitivity of the methanation reaction: H_2-induced CO dissociation on nickel surfaces", *J. Catal.* **2008**, *255*, 6-19.
[244] P. H. Holloway, "Chemisorption and oxide formation on metals: Oxygen–nickel reaction", *J. Vac. Sci. Technol.* **1981**, *18*, 653-659.
[245] F. Besenbacher, J. K. Nørskov, "Oxygen chemisorption on metal surfaces: General trends for Cu, Ni and Ag", *Prog. Surf. Sci.* **1993**, *44*, 5-66.
[246] S. Dahl, A. Logadottir, R. Egeberg, J. Larsen, I. Chorkendorff, E. Törnqvist, J. K. Nørskov, "Role of steps in N_2 activation on Ru(0001)", *Phys. Rev. Lett.* **1999**, *83*, 1814.
[247] F. J. Gracia, L. Bollmann, E. E. Wolf, J. T. Miller, A. J. Kropf, "*In situ* FTIR, EXAFS, and activity studies of the effect of crystallite size on silica-supported Pt oxidation catalysts", *J. Catal.* **2003**, *220*, 382-391.
[248] M. J. Kale, P. Christopher, "Utilizing Quantitative *in Situ* FTIR Spectroscopy To Identify Well-Coordinated Pt Atoms as the Active Site for CO Oxidation on Al_2O_3-Supported Pt Catalysts", *ACS Catal.* **2016**, *6*, 5599-5609.
[249] A. Boubnov, A. Gänzler, S. Conrad, M. Casapu, J.-D. Grunwaldt, "Oscillatory CO Oxidation Over Pt/Al_2O_3 Catalysts Studied by *In situ* XAS and DRIFTS", *Top. Catal.* **2013**, *56*, 333-338.

[250] C. J. H. Jacobsen, S. Dahl, P. L. Hansen, E. Törnqvist, L. Jensen, H. Topsøe, D. V. Prip, P. B. Møenshaug, I. Chorkendorff, "Structure sensitivity of supported ruthenium catalysts for ammonia synthesis", *J. Mol. Catal. A: Chem.* **2000**, *163*, 19-26.
[251] R. van Hardeveld, A. van Montfoort, "The influence of crystallite size on the adsorption of molecular nitrogen on nickel, palladium and platinum", *Surf. Sci.* **1966**, *4*, 396-430.
[252] P. M. Mortensen, J.-D. Grunwaldt, P. A. Jensen, A. D. Jensen, "Influence on nickel particle size on the hydrodeoxygenation of phenol over Ni/SiO_2", *Catal. Today* **2016**, *259, Part 2*, 277-284.
[253] R. E. Benfield, "Mean coordination numbers and the non-metal-metal transition in clusters", *J. Chem. Soc., Faraday Trans.* **1992**, *88*, 1107-1110.
[254] A. Sadezky, H. Muckenhuber, H. Grothe, R. Niessner, U. Pöschl, "Raman microspectroscopy of soot and related carbonaceous materials: Spectral analysis and structural information", *Carbon* **2005**, *43*, 1731-1742.
[255] B. M. Vogelaar, A. D. van Langeveld, S. Eijsbouts, J. A. Moulijn, "Analysis of coke deposition profiles in commercial spent hydroprocessing catalysts using Raman spectroscopy", *Fuel* **2007**, *86*, 1122-1129.
[256] T. Jawhari, A. Roid, J. Casado, "Raman spectroscopic characterization of some commercially available carbon black materials", *Carbon* **1995**, *33*, 1561-1565.
[257] J. Guo, H. Lou, X. Zheng, "The deposition of coke from methane on a $Ni/MgAl_2O_4$ catalyst", *Carbon* **2007**, *45*, 1314-1321.
[258] M. A. Bañares, M. O. Guerrero-Pérez, J. L. G. Fierro, G. G. Cortez, "Raman spectroscopy during catalytic operations with on-line activity measurement (*operando* spectroscopy): a method for understanding the active centres of cations supported on porous materials", *J. Mater. Chem.* **2002**, *12*, 3337-3342.
[259] M. O. Guerrero-Pérez, M. A. Bañares, "From conventional *in situ* to *operando* studies in Raman spectroscopy", *Catal. Today* **2006**, *113*, 48-57.
[260] C. Zhao, I. E. Wachs, "An *Operando* Raman, IR, and TPSR Spectroscopic Investigation of the Selective Oxidation of Propylene to Acrolein over a Model Supported Vanadium Oxide Monolayer Catalyst", *J. Phys. Chem. C* **2008**, *112*, 11363-11372.
[261] J. Engeldinger, J. Radnik, C. Kreyenschulte, F. Devred, E. M. Gaigneaux, A. Fischer, H.-W. Zanthoff, U. Bentrup, "Probing the Structural Changes and Redox Behavior of Mixed Molybdate Catalysts under Ammoxidation Conditions: An *Operando* Raman Spectroscopy Study", *ChemCatChem* **2016**, *8*, 976-983.
[262] W. Y. Teoh, D. E. Doronkin, G. K. Beh, J. A. H. Dreyer, J.-D. Grunwaldt, "Methanation of carbon monoxide over promoted flame-synthesized cobalt clusters stabilized in zirconia matrix", *J. Catal.* **2015**, *326*, 182-193.
[263] D. Hu, J. Gao, Y. Ping, L. Jia, P. Gunawan, Z. Zhong, G. Xu, F. Gu, F. Su, "Enhanced Investigation of CO Methanation over Ni/Al_2O_3 Catalysts for Synthetic Natural Gas Production", *Ind. Eng. Chem. Res.* **2012**, *51*, 4875-4886.
[264] D. Huang, M. Ke, X. Bao, H. Liu, "Fe-Promoted Ni/Al_2O_3 Thioetherification Catalysts with Enhanced Low-Temperature Activity for Removing Mercaptans from Liquefied Petroleum Gas", *Ind. Eng. Chem. Res.* **2016**, *55*, 1192-1201.

[265] T. Li, H. Wang, Y. Yang, H. Xiang, Y. Li, "Study on an iron–nickel bimetallic Fischer–Tropsch synthesis catalyst", *Fuel Process. Technol.* **2014**, *118*, 117-124.
[266] J. Kugai, S. Velu, C. Song, "Low-temperature reforming of ethanol over CeO_2-supported Ni-Rh bimetallic catalysts for hydrogen production", *Catal. Lett.* **2005**, *101*, 255-264.
[267] D. Pandey, G. Deo, "Effect of support on the catalytic activity of supported Ni–Fe catalysts for the CO_2 methanation reaction", *J. Ind. Eng. Chem.* **2016**, *33*, 99-107.
[268] I. Suelves, M. J. Lázaro, R. Moliner, B. M. Corbella, J. M. Palacios, "Hydrogen production by thermo catalytic decomposition of methane on Ni-based catalysts: influence of operating conditions on catalyst deactivation and carbon characteristics", *Int. J. Hydrogen Energy* **2005**, *30*, 1555-1567.
[269] K. Nagaoka, K. Seshan, K.-i. Aika, J. A. Lercher, "Carbon Deposition during Carbon Dioxide Reforming of Methane—Comparison between Pt/Al_2O_3 and Pt/ZrO_2", *J. Catal.* **2001**, *197*, 34-42.
[270] M. Usman, W. M. A. Wan Daud, H. F. Abbas, "Dry reforming of methane: Influence of process parameters—A review", *Renew. Sust. Energ. Rev.* **2015**, *45*, 710-744.
[271] Z. Hou, O. Yokota, T. Tanaka, T. Yashima, "Investigation of CH_4 Reforming with CO_2 on Meso-Porous Al_2O_3-Supported Ni Catalyst", *Catal. Lett.* **2003**, *89*, 121-127.
[272] A. C. Ferrari, J. Robertson, "Interpretation of Raman spectra of disordered and amorphous carbon", *Phys. Rev. B: Condens. Matter* **2000**, *61*, 14095.
[273] F. Tuinstra, J. L. Koenig, "Raman spectrum of graphite", *J. Chem. Phys.* **1970**, *53*, 1126-1130.
[274] S. Takenaka, Y. Tomikubo, E. Kato, K. Otsuka, "Sequential production of H_2 and CO over supported Ni catalysts", *Fuel* **2004**, *83*, 47-57.
[275] Q. Li, H. Yan, J. Zhang, Z. Liu, "Effect of hydrocarbons precursors on the formation of carbon nanotubes in chemical vapor deposition", *Carbon* **2004**, *42*, 829-835.
[276] M. S. Dresselhaus, A. Jorio, M. Hofmann, G. Dresselhaus, R. Saito, "Perspectives on Carbon Nanotubes and Graphene Raman Spectroscopy", *Nano Lett.* **2010**, *10*, 751-758.
[277] S. Campisi, C. E. Chan-Thaw, D. Wang, A. Villa, L. Prati, "Metal nanoparticles on carbon based supports: The effect of the protective agent removal", *Catal. Today* **2016**, *278*, 91-96.
[278] G. Boskovic, K. J. Smith, "Methane homologation and reactivity of carbon species on supported Co catalysts", *Catal. Today* **1997**, *37*, 25-32.
[279] R. Razzaq, H. Zhu, L. Jiang, U. Muhammad, C. Li, S. Zhang, "Catalytic Methanation of CO and CO_2 in Coke Oven Gas over $Ni–Co/ZrO_2–CeO_2$", *Ind. Eng. Chem. Res.* **2013**, *52*, 2247-2256.
[280] I. Chicinaş, V. Pop, O. Isnard, J. M. Le Breton, J. Juraszek, "Synthesis and magnetic properties of Ni_3Fe intermetallic compound obtained by mechanical alloying", *J. Alloys Compd.* **2003**, *352*, 34-40.
[281] S. Sitthisa, W. An, D. E. Resasco, "Selective conversion of furfural to methylfuran over silica-supported NiFe bimetallic catalysts", *J. Catal.* **2011**, *284*, 90-101.

[282] G. Wang, Y. Jin, G. Liu, Y. Li, "Production of Hydrogen and Nanocarbon from Catalytic Decomposition of Methane over a Ni–Fe/Al_2O_3 Catalyst", *Energy Fuels* **2013**, *27*, 4448-4456.
[283] D. L. A. de Faria, S. Venâncio Silva, M. T. de Oliveira, "Raman microspectroscopy of some iron oxides and oxyhydroxides", *J. Raman Spectrosc.* **1997**, *28*, 873-878.
[284] F. Ospitali, T. Sabetta, F. Tullini, M. C. Nannetti, G. Di Lonardo, "The role of Raman microspectroscopy in the study of black gloss coatings on Roman pottery", *J. Raman Spectrosc.* **2005**, *36*, 18-23.
[285] V. D'Ippolito, G. B. Andreozzi, D. Bersani, P. P. Lottici, "Raman fingerprint of chromate, aluminate and ferrite spinels", *J. Raman Spectrosc.* **2015**, *46*, 1255-1264.
[286] A. G. Nasibulin, S. Rackauskas, H. Jiang, Y. Tian, P. R. Mudimela, S. D. Shandakov, L. I. Nasibulina, S. Jani, E. I. Kauppinen, "Simple and rapid synthesis of α-Fe_2O_3 nanowires under ambient conditions", *Nano Res.* **2009**, *2*, 373-379.
[287] M. Baghaie Yazdi, K.-Y. Choi, D. Wulferding, P. Lemmens, L. Alff, "Raman study of the Verwey transition in magnetite thin films", *New J. Phys.* **2013**, *15*, 103032.
[288] S. Abelló, E. Bolshak, D. Montané, "Ni–Fe catalysts derived from hydrotalcite-like precursors for hydrogen production by ethanol steam reforming", *Appl. Catal. A* **2013**, *450*, 261-274.
[289] S. Abelló, E. Bolshak, F. Gispert-Guirado, X. Farriol, D. Montané, "Ternary Ni–Al–Fe catalysts for ethanol steam reforming", *Catal. Sci. Technol.* **2014**, *4*, 1111-1122.
[290] S. S. Chan, I. E. Wachs, "*In situ* laser Raman spectroscopy of nickel oxide supported on γ-Al_2O_3", *J. Catal.* **1987**, *103*, 224-227.
[291] M. A. Vuurman, D. J. Stufkens, A. Oskam, G. Deo, I. E. Wachs, "Combined Raman and IR study of MO_X-V_2O_5/Al_2O_3 (MO_X = MoO_3, WO_3, NiO, CoO) catalysts under dehydrated conditions", *J. Chem. Soc., Faraday Trans.* **1996**, *92*, 3259-3265.
[292] L. Wang, D. Li, M. Koike, S. Koso, Y. Nakagawa, Y. Xu, K. Tomishige, "Catalytic performance and characterization of Ni-Fe catalysts for the steam reforming of tar from biomass pyrolysis to synthesis gas", *Appl. Catal. A* **2011**, *392*, 248-255.
[293] N. Wakao, S. Kaguei, T. Funazkri, "Effect of fluid dispersion coefficients on particle-to-fluid heat transfer coefficients in packed beds", *Chem. Eng. Sci.* **1979**, *34*, 325-336.
[294] S. J. P. Romkes, F. M. Dautzenberg, C. M. van den Bleek, H. P. A. Calis, "CFD modelling and experimental validation of particle-to-fluid mass and heat transfer in a packed bed at very low channel to particle diameter ratio", *Chem. Eng. J.* **2003**, *96*, 3-13.
[295] J. Zhang, N. Fatah, S. Capela, Y. Kara, O. Guerrini, A. Y. Khodakov, "Kinetic investigation of carbon monoxide hydrogenation under realistic conditions of methanation of biomass derived syngas", *Fuel* **2013**, *111*, 845-854.

[296] J. B. Butt, E. E. Petersen, "Deactivation by Fouling" in *Activation, Deactivation, and Poisoning of Catalysts*, Academic Press Inc., San Diego, USA, **1988**, pp. 63-120.
[297] J. G. McCarty, H. Wise, "Hydrogenation of surface carbon on alumina-supported nickel", *J. Catal.* **1979**, *57*, 406-416.
[298] D. C. Gardner, C. H. Bartholomew, "Kinetics of carbon deposition during methanation of carbon monoxide", *Ind. Eng. Chem. Prod. Res. Dev.* **1981**, *20*, 80-87.
[299] M. K. Gnanamani, W. D. Shafer, D. E. Sparks, B. H. Davis, "Fischer–Tropsch synthesis: Effect of CO_2 containing syngas over Pt promoted Co/γ-Al_2O_3 and K-promoted Fe catalysts", *Catal. Commun.* **2011**, *12*, 936-939.
[300] M. Martinelli, C. G. Visconti, L. Lietti, P. Forzatti, C. Bassano, P. Deiana, "CO_2 reactivity on Fe–Zn–Cu–K Fischer–Tropsch synthesis catalysts with different K-loadings", *Catal. Today* **2014**, *228*, 77-88.
[301] S. Wasserman, "The analysis of mixtures: Application of principal component analysis to XAS spectra", *J. Phys. IV France* **1997**, *7*, C2-203-C202-205.
[302] W. H. Cassinelli, L. Martins, A. R. Passos, S. H. Pulcinelli, C. V. Santilli, A. Rochet, V. Briois, "Multivariate curve resolution analysis applied to time-resolved synchrotron X-ray Absorption Spectroscopy monitoring of the activation of copper alumina catalyst", *Catal. Today* **2014**, *229*, 114-122.
[303] R. P. W. J. Struis, D. Bachelin, C. Ludwig, A. Wokaun, "Studying the Formation of Ni_3C from CO and Metallic Ni at T = 265 °C *in Situ* Using Ni K-Edge X-ray Absorption Spectroscopy", *J. Phys. Chem. C* **2009**, *113*, 2443-2451.
[304] J. J. Rehr, J. J. Kas, F. D. Vila, M. P. Prange, K. Jorissen, "Parameter-free calculations of X-ray spectra with FEFF9", *Phys. Chem. Chem. Phys.* **2010**, *12*, 5503-5513.
[305] B. Ravel, "ATOMS: crystallography for the X-ray absorption spectroscopist", *J. Synchrotron. Radiat.* **2001**, *8*, 314-316.
[306] J. S. Gibson, J. Uddin, T. R. Cundari, N. K. Bodiford, A. K. Wilson, "First-principle study of structure and stability of nickel carbides", *J. Phys. Condens. Matter* **2010**, *22*, 445503.
[307] S. Nagakura, "Study of Metallic Carbides by Electron Diffraction Part II. Crystal Structure Analysis of Nickel Carbide", *J. Phys. Soc. Jpn* **1958**, *13*, 1005-1014.

12 Appendix

Supporting information for the *operando* XAS experiments

Methanation of CO_2 – blank test

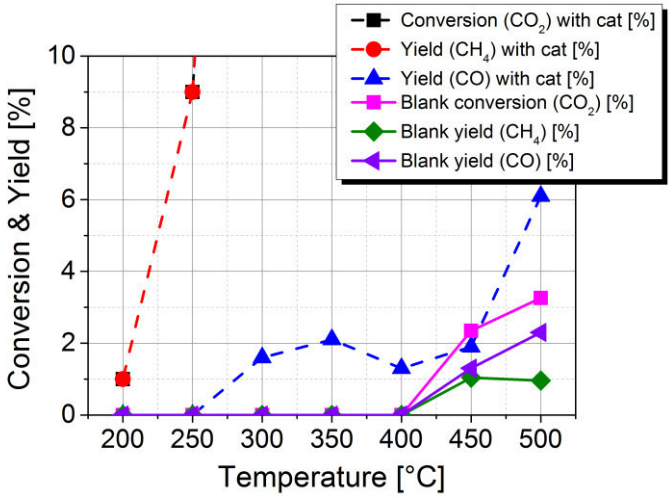

Figure S 1: Blank test for the methanation of CO_2 with Al_2O_3 (catalyst support, high surface area, 1/8" pellets, Alfa Aesar) at T = 200 – 500 °C performed in a stainless steel microreactor (H_2/CO_2 = 4, 40 % N_2, GHSV = 15000 h^{-1}). Dashed line is conversion and yield of the commercial catalyst shown in Figure 18 for comparison. The inert material was crushed and calcined at 600 °C (4 h, 5 K min^{-1}). Reproduced from Mutz *et al.*[219] Copyright © 2015, with permission from Elsevier.

The blank test in Figure S 1 showed CO formation above 450 °C to a maximum of 2 %; also 1 % CH_4 was formed. At 400 °C and below, no CO_2 conversion of the reactor wall or the inert material was observed.

MS data during hydrogen dropout

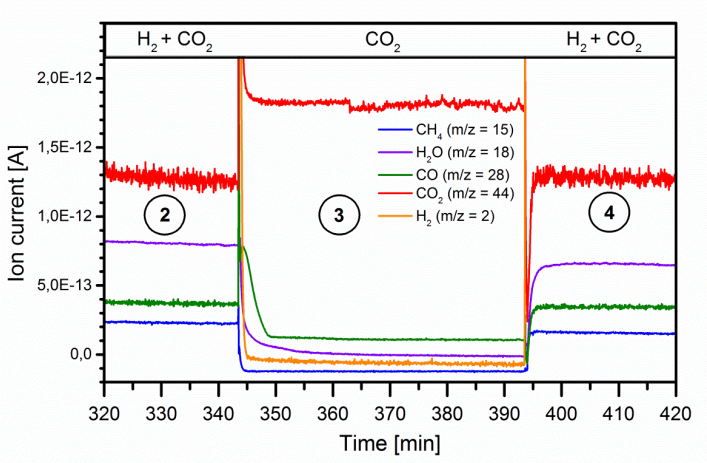

Figure S 2: MS data section monitoring the trend of the reaction gases while switching from $H_2 + CO_2$ to the less reducing atmosphere (step 2-4 according to Figure 21). Note that the mass spectrometer was not calibrated. Reproduced from Mutz *et al.*[219] Copyright © 2015, with permission from Elsevier.

XAS evaluation

Supplementary data on the evaluation of the XAS spectra discussed in chapter 5 is shown in Figure S 3, Figure S 4 and Table S 1.

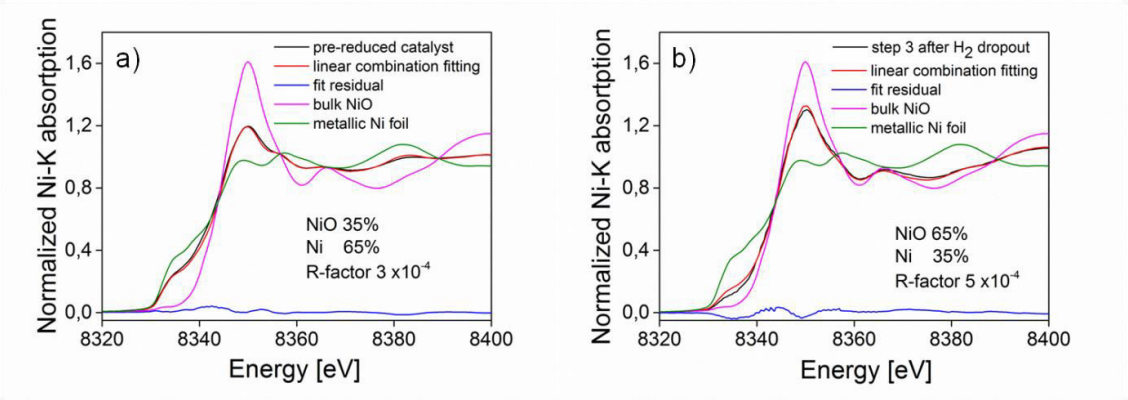

Figure S 3: XANES spectra of the pre-reduced catalyst (a) and the catalyst under less reducing atmosphere (b) (measured *in situ* according to Figure 21, step 3) each in black, metallic Ni (green) and NiO (purple) references. Additionally, the result of the linear combination fitting (red) and the fit residual (blue) is shown. The linear combination of the pre-reduced catalyst revealed 35 % of an oxidic Ni phase, the catalyst after H_2 dropout revealed 65 % NiO. Reproduced from Mutz *et al.*[219] Copyright © 2015, with permission from Elsevier.

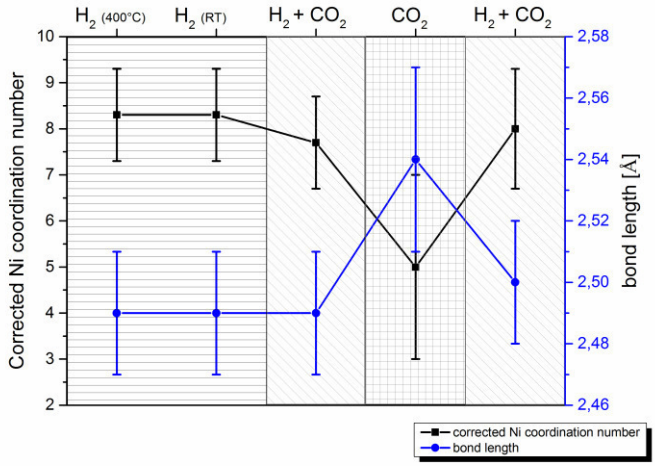

Figure S 4: Corrected coordination numbers and bond lengths from the EXAFS in Table S **1**. Reproduced from Mutz *et al.*[219] Copyright © 2015, with permission from Elsevier.

Table S 1: Local structural parameters of Ni extracted from the EXAFS spectra at the Ni K-edge of various samples presented in the study (with Ni $S_0^2 = 0.88$, NiO $S_0^2 = 0.91$). Reproduced from Mutz *et al.*[219] Copyright © 2015, with permission from Elsevier.

Sample	**Atom**	***N***	***r(Å)***	***σ² x10⁻³(Å²)***	***E0***	***ρ (%)***
Ni foil	N	12[f]	2.49[a§]	6.5 ± 0.7[a]	-2.9± 0.7[a]	2.5
	Ni	6[f]	3.52 [a§]	10.0 ± 2.9[a]		
	Ni	24[f]	4.31[a§]	8.1 ± 1.1[a]		
NiO	O	6[f]	2.07 [a§]	6.8 ± 0.9[a]	-2.6± 0.6[a]	1.3
	Ni	12[f]	2.96 ± 0.01[a]	7.8 ± 0.3[a]		
Pellet calcined	O	6[f]	2.07 [a§]	8.1 ± 0.3[a]		1.0
	Ni	12[f]	2.96[a§]	8.1 ± 0.3[a]		1.0
Pellet Pre-reduced	O	2.0±0.2[a]	2.08± 0.03[a]	7.6± 3.2[a]	6.1± 1.5[a]	2.0
	Ni	4.0±0.5[a] [6.2 ± 0.8]	2.48 [a§]	6.5± 1.3[a]		
	Ni	5.9±0.4[a]	2.96± 0.03[a]	10.0± 1.6[a]		
	Ni	3.5±1.2[a][5.4 ± 1.9]	3.51 [a§]	9.9± 5.0[a]		
	Ni	11.4±1.7[a][17.7 ± 2.6]	4.30 [a§]	8.3± 1.7[a]		
Reduced 500 °C	Ni	8.3±1.0[a‡]	2.49[a§]	12.5 ± 0.4[a]	7.2± 1.1[a]	1.9
	Ni	4.2±1.0[a‡]	3.49± 0.03[a]	17.9 ± 4.4[a]		
	Ni	19.3±6.5[a‡]	4.35± 0.02[a]	18.6 ± 1.9[a]		
Reduced RT	Ni	8.3±1.0[a]	2.49[a§]	6.5 ± 0.1[a]	6.9± 1.1[a]	2.3
	Ni	4.2±0.5[a†]	3.49± 0.03[a]	10.1 ± 3.4[a]		
	Ni	19.3±6.5[a]	4.34± 0.01[a]	9.6 ± 2.8[a]		
Methanation I	Ni	7.7±1.0[a]	2.49[a§]	11.9 ± 1.3[a]	6.7± 1.1[a]	1.8
	Ni	3.9±0.5[a†]	3.48± 0.03[a]	18.0 ± 4.5[a]		
	Ni	15.4±2.0[aℓ]	4.35± 0.02[a]	15.9 ± 2.1[a]		
CO_2	O	4.5±0.7[a]	2.06± 0.02[a§]	11.8 ± 3.1[a]	0.5±1.8[a]	0.4
	Ni	1.5±0.6[a][5.0 ± 2.0]	2.54± 0.03[a]	11.9 ± 1.3[fω]		
	Ni	8.9±2.0[a]	2.97± 0.02[a]	14.5 ± 2.2[a]		
Methanation II	Ni	7.0±1.1[a][8.0 ± 1.3]	2.50[a§]	11.5 ± 1.4[a]	7.6± 1.4[a]	2.1
	Ni	3.5±0.6[a†][4.2 ± 0.7]	3.49± 0.03[a]	17.3 ± 5.6[a]		
	Ni	9.5±5.5[a][11.4 ± 6.6]	4.35± 0.02[a]	11.6 ± 5.4[a]		

§ = fitted uncertainty lower 0.01 Å, a = fitted and f = fixed. † fitted with constraint Ni_2 = (Ni_1/2). ℓ fitted with constraint Ni_3 = (Ni_1*2). ‡ values fixed to be equal to the fitted at room temperature after cooling. ω fixed using the same value for Methanation I. Structural parameters: N = number of neighboring atoms, r = distance, σ^2 = mean square deviation of interatomic distances, ρ = misfiting between the experimental data and the theory.

Further information on linear combination and principal component analysis

The XANES spectra recorded during the experiment in chapter 5 were submitted to principal component analysis (PCA). The total number of components is equal to the number of spectra recorded. However to reproduce the experimental data one does not

need all spectra, but only the principal components. Thus PCA is a tool that uncovers how many different components exist during the chemical transformation.[301,302]

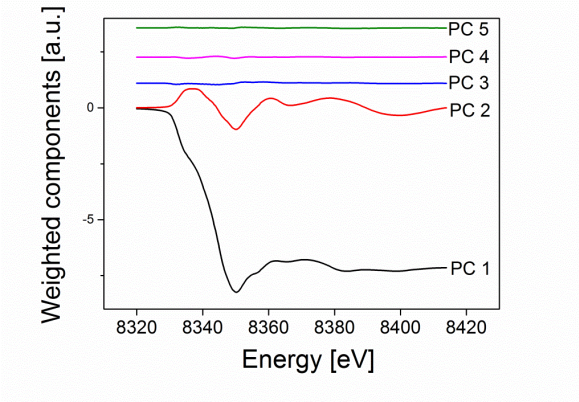

Figure S 5: Five principal components of the spectra recorded during the experiment weighted by their respective eigenvalues. Reproduced from Mutz *et al.*[219] Copyright © 2015, with permission from Elsevier.

Table S 2: Variance and cumulative variance of the five principal components of the spectra recorded during the experiment. Reproduced from Mutz *et al.*[219] Copyright © 2015, with permission from Elsevier.

Component	Variance	Cumulative Variance
PC 1	0.923	0.923
PC 2	0.056	0.979
PC 3	0.003	0.983
PC 4	0.002	0.985
PC 5	0.001	0.987

Figure S 5 and Table S 2 show the relative importance of each of the first five components. In total, 47 spectra were recorded during the experiment; the sum of the cumulative variance of these 47 spectra is equal to 1.0. Nevertheless to achieve cumulative variance of almost 0.99 one needs only the first five principal components. The remaining components do not contribute the spectral features but rather to the

experimental noise. The PCA shows that the first two components are most important and a cumulative variance of 0.98 is achieved. Further components showed no significant improvement.

The experimental data recorded during the experiment was reconstructed using two, three and four principal components. Although two components fairly reproduce the data, the addition of a third component may slightly improve the quality of the fit. On the other hand a detailed analysis using linear combinations was performed (Figure S2).

To check the suitability of $NiCO_3$ and Ni carbides as reference compounds, the target transformation analysis (conducted with SixPack software of the IFEFFIT package[220]) was used. The target transformation analysis is an operation that seeks whether a "candidate reference compound" is present in the mixture. Using a selected number of components (in the present case two, three and four) this procedure aims to reconstruct the candidate and therefore one can identify unknown components formed during the chemical reaction.

Considering the formation of carbonate species the target transformation was conducted on $NiCO_3$ reference compound recorded previously *ex situ* at the ANKA beamline (section 5.4). The results showed that not even four principal compounds can in any way reproduce the $NiCO_3$, and therefore one can state that $NiCO_3$ is not formed during the reaction.

Ni carbides are not stable under air and therefore they are hardly found as reference compounds for spectroscopic measurements. In order to verify the possible presence of Ni carbides in the sample, we have simulated the Ni-K XANES spectra for some NiC and Ni_3C species. Considering the present catalyst in which the Ni metallic were nanoparticles, one can assume that only a small amount of Ni carbide species could be formed. Afterwards again a target transformation was performed on the simulated spectra to check whether they could be considered as a component of the mixture or not. Note that this approach with calculated data has been for example successfully used in ref.[303].

The spectra were simulated using the Feff 9.0 code.[304] The first step consisted in preparing the atomic coordinates input files of clusters with different dimensions which was done using the atoms code.[305] The cell dimensions of the unit cell, the atomic positions and group symmetry of NiC and Ni_3C were taken from the ISCD database references,[304,306,307] respectively.

Figure S 6 presents the NiC a) simulated spectra for a molecular hexacoordinated NiC, a NiC 3 Å cluster (containing two coordination shells) and for NiC 8 Å larger clusters considering several outer shells. Figure S 6 b) shows the calculated spectra for Ni_3C 4 Å and 8 Å clusters which is similar to ref.[303]. Besides the chemical nature and coordinates of neighboring atoms, the XANES spectra shape is highly dependent on the cluster size since the photoelectron mean-free path is the range of tens of angstroms in low kinetic energy regime.

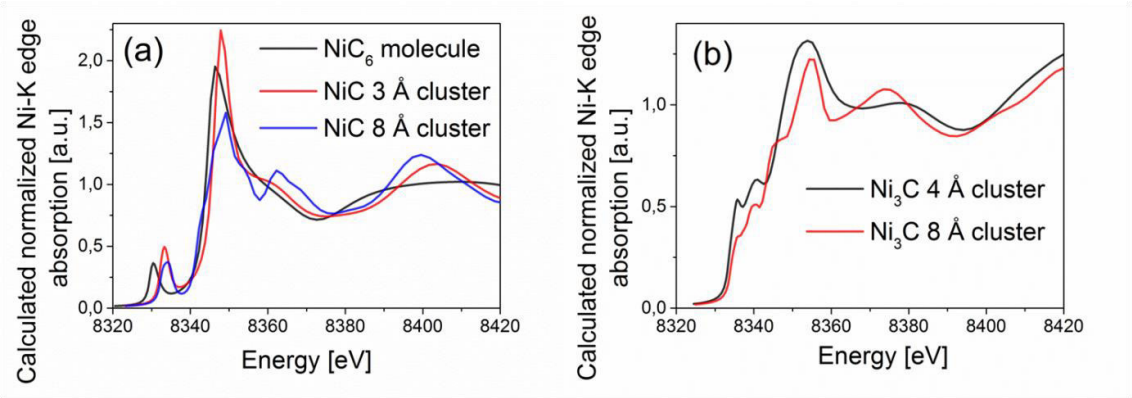

Figure S 6: a) Calculated XANES spectra for NiC6 and NiC clusters of 3 Å and 8 Å, b) calculated XANES spectra for Ni_3C clusters of 4 Å and 8 Å .The spectral features are highly dependent on the cluster size. Reproduced from Mutz *et al.*[219] Copyright © 2015, with permission from Elsevier.

Next again a target transformation based on the simulated spectra using two, three and four principal components was performed. The results revealed that the spectra recorded during the methanation experiment cannot be used to reconstruct neither the calculated NiC nor Ni_3C spectra, therefore these species are not suitable references for the linear combination analysis and they are probably not be present in the mixture as also suggested by earlier discussion in literature.

Details on QEXAFS data evaluation

To evaluate the Ni oxidation state during the experiment a linear combination of reference spectra was conducted to the respective sample spectra. In Figure S 7 XANES spectra of the catalyst are presented along data obtained on reference samples: Ni-Foil with an oxidation state of zero and NiO with nickel in the oxidation state of +2. The pronounced feature around 8350 eV is called white-line and its extent strongly depends on the Ni oxidation state. The depicted sample spectra show the catalyst with Ni in the highest and lowest oxidation state. Since the *operando* XAS experiment was performed at 400 °C, the catalyst sample oxidized *in situ* in 5 %O_2 and the corresponding XANES spectra at 400 °C was used as oxidized reference during the LCF analysis. As reduced reference the XANES spectrum acquired at 400 °C of the reduced catalyst was chosen. As shown in Figure S 7 and also the EXAFS fitting data (Table S 3 and Table S 4) the Ni component did not fully reduce due to the nature of the very small nanoparticles present in the catalyst and the intimate contact with the support (see also TPR-profile). Note furthermore, that the XAS spectrum is also dependent on the Ni particle size.

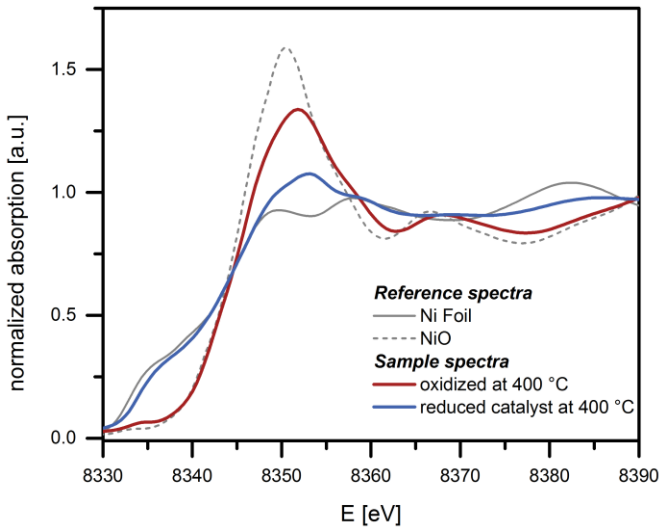

Figure S 7: Reference XANES spectra and selected spectra for linear combination analysis. Reproduced from Mutz *et al.*[223] under the terms and conditions of CC BY 4.0 license (http://creativecommons.org/licenses/by/4.0/), Copyright © 2017.

Reduced catalyst in He

Figure S 8 shows the XANES and the FT EXAFS spectra of the reduced catalyst (at 500 °C in 50 % H_2/He) in hydrogen atmosphere at room temperature and after heating again to 400 °C, and after the feed was switched to He. The Ni component was found stable in He atmosphere.

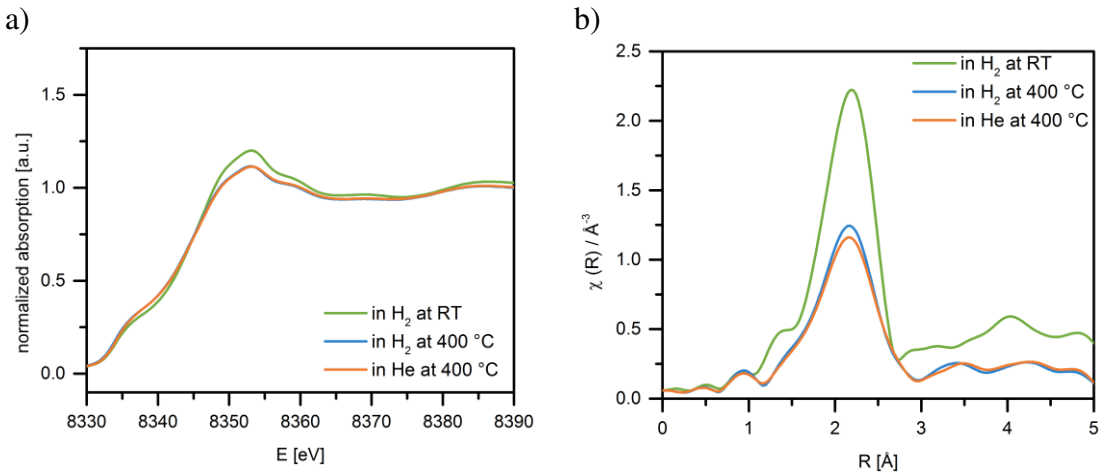

Figure S 8: XANES and FT EXAFS spectra of the reduced catalyst in H_2/He at room temperature (RT) and at 400 °C and in He atmosphere at 400 °C. Reproduced from Mutz *et al.*[223] under the terms and conditions of CC BY 4.0 license (http://creativecommons.org/licenses/by/4.0/), Copyright © 2017.

Results of EXAFS fitting analysis

Table S 3: Structural parameters of the local Ni atomic environment extracted from EXAFS spectra at the Ni K-edge of various samples measured at room temperature. Spectra of Ni foil and NiO references (measured as pellets) were used to obtain experimental amplitude reduction factors (Ni $S_0^2 = 0.91$, NiO $S_0^2 = 0.92$). Furthermore, the results for the calcined catalyst and after reduction at 500 °C are presented. The experimental and simulated EXAFS data are shown in Figure S 12 and Figure S 13 together with the fitting ranges. Reproduced from Mutz *et al.*[223] under the terms and conditions of CC BY 4.0 license (http://creativecommons.org/licenses/by/4.0/), Copyright © 2017.

Sample (Condition)	**Atom**	**N**	**R (Å)[a]**	**σ^2 *10^{-3} (Å^2)**	**ΔE_0 (eV)**	**ρ (%)**
Ni foil k-range: 3-13 R-range: 1-5 N^{ind}= 25; N^{var}=6	Ni	12[f]	2.49	6.5 ± 0.3	7.2 ± 0.5	0.14
	Ni	6[f]	3.52	8.8 ± 0.6		
	Ni	24[f]	4.31	8.8 ± 0.6		
	Ni	12[f]	4.97	8.8 ± 0.6		
NiO k-range: 3-13 R-range: 1-3 N^{ind}= 12; N^{var}=5	O	6[f]	2.08	7.2 ± 2.1	-2.9 ± 0.6	0.48
	Ni	12[f]	2.97	8.0 ± 0.9		
Sample at room temperature						
A: calcined pellet k-range: 3-12 R-range: 1-3.0 N^{ind}= 11; N^{var}=5	O	5.0 ± 0.2	2.04 ± 0.01	5.5 ± 2.1	-4.6 ± 0.7	0.19
	Ni	5.1 ± 0.4	2.97 ± 0.01	10.5 ± 4.3		
B: reduced k-range:3-11 R-range:1-2.8 N^{ind}= 9; N^{var}=7	O	2.5 ± 0.2	2.03 ± 0.01	5.5 ± 2.1	8.2 ± 1.6	0.15
	Ni	3.7 ± 0.3	2.49 ± 0.01	8.1 ± 0.1		
	Ni	1.9 ± 0.7	2.97 ± 0.03	10.5 ± 4.3		

f = value kept fixed during fitting procedure, a = fitted uncertainty 0.01 or lower, N = number of neighboring atoms, R = distance, σ^2 = mean square deviation of interatomic distance, ρ = misfit between experimental data and theory according to Ref[222].

Table S 4: Structural parameters of the local Ni atomic environment extracted from EXAFS spectra at the Ni K-edge of various samples measured at room temperature and at 500 °C before and after the presented experiments. They represent the most oxidizing and reducing states during the experiment. The experimental and simulated EXAFS data is shown in Figure S 14 together with the fitting ranges. Reproduced from Mutz *et al.*[223] under the terms and conditions of CC BY 4.0 license (http://creativecommons.org/licenses/by/4.0/), Copyright © 2017.

Sample (Condition)	Atom	N[a]	R (Å)[b]	σ^2 *10^{-3} (Å^2)[c]	E_0 (eV)	ρ (%)
Before 30 s H_2 dropouts						
RT	O	2.0 ± 0.2	2.05 ± 0.01	5.5 [f]	10.5 ± 1.0	0.21
k-range: 3-10 R-range: 1.3-2.8 N^{ind}= 6; N^{var}= 4	Ni	4.7 ± 0.6	2.51 ± 0.01	8.1 ± 0.1		
500 °C	O	2.0 ± 0.2	2.03 ± 0.01	15.0 ± 3.3	7.7 ± 1.0	0.27
k-range:3-8.5 R-range:1.2-2.8 N^{ind}= 5; N^{var}= 4	Ni	4.7 ± 0.6	2.48 ± 0.01	13.2 ± 1.5		
After 30 s H_2 dropouts						
500 °C	O	2.0 ± 0.3[l]	2.04 ± 0.02	15.0 ± 3.3	7.7 ± 1.9	0.12
k-range:3-8.5 R-range:1.2-2.8 N^{ind}= 5; N^{var}= 4	Ni	4.9 ± 0.3	2.49 ± 0.01	13.2 ± 1.5		
Before 300 s H_2 dropouts (after 4 total 30 s modulation experiments)						
500 °C	O	1.5 ± 0.2	2.03 ± 0.01	15.0 ± 3.3	7.8 ± 1.3	0.04
k-range:3-8.5 R-range:1.2-2.8 N^{ind}= 5; N^{var}= 4	Ni	5.4 ± 0.2	2.49 ± 0.01	13.2 ± 1.5 [b]		
After 300 s H_2 dropouts						
RT	O	1.5 ± 0.3	2.03 ± 0.02	5.5 [f]	8.5 ± 1.8	0.40
k-range: 3-10 R-range: 1.3-2.8 N^{ind}= 6; N^{var}= 4	Ni	5.7 ± 1.0	2.49 ± 0.01	8.1 ± 0.1		
500 °C	O	1.5 ± 0.3	2.03 ± 0.01	15.0 ± 3.3	7.8 ± 0.8	0.18
k-range:3-8.5 R-range:1.2-2.8 N^{ind}= 5; N^{var}= 4	Ni	5.7 ± 1.0	2.48 ± 0.01	13.2 ± 1.5		

N = number of neighboring atoms, R = distance, σ^2 = mean square deviation of interatomic distance, ρ = misfit between experimental data and theory, a = number of neighboring atoms constrained to be the same after each treatment at room temperature and 500 °C, f = value kept fixed during fitting procedure, b = fitted uncertainty 0.01 or lower, c = mean-square deviation constrained to be the same for respective temperature.

Table S 5: Structural parameters of the local Ni atomic environment extracted from EXAFS spectra at the Ni K-edge of various samples measured at 400 °C. They represent the most oxidizing and reducing states during the experiment. The experimental and simulated EXAFS data is shown in Figure S 15 together with the fitting ranges. Reproduced from Mutz *et al.*[223] under the terms and conditions of CC BY 4.0 license (http://creativecommons.org/licenses/by/4.0/), Copyright © 2017.

Sample (Condition)	Atom	N	R (Å)[a]	σ^2 *10^{-3} (Å^2)	E_0 (eV)	ρ (%)
Oxidized in O_2	O	4.1 ± 0.3	2.05 ± 0.02	8.3 [f]	9.8 ± 1.3	0.30
k-range: 3-8.5 R-range: 1.1-3.2 N^{ind}= 7; N^{var}=5	Ni	7.6 ± 0.8	2.97 ± 0.01	11.8[f]		
After reaction (30 s modulation) at 400 °C in CO_2/H_2	O	2.2 ± 0.2	2.02 ± 0.03	8.3 [f]	7.5 ± 2.7	0.16
	Ni	2.4 ± 0.6	2.48 ± 0.02	11.4 ± 1.2 [f]		
k-range: 3-9 R-range: 1.2-2.9 N^{ind}= 6; N^{var}=5	Ni	3.0 ± 0.8	2.94 ± 0.03	11.8 ± 2.1 [f]		
After reaction (300 s modulation) at 400 °C in CO_2/H_2	O	3.0 ± 0.2	2.04 ± 0.03	8.3 [f]	8.4 ± 2.5	0.18
	Ni	1.9 ± 0.8	2.48 ± 0.02	11.4 ± 1.2 [f]		
k-range: 3-9 R-range: 1.2-2.9 N^{ind}= 6; N^{var}=5	Ni	4.8 ± 0.9	2.97 ± 0.03	11.8 ± 2.1 [f]		

f = value kept fixed during fitting procedure, a = fitted uncertainty 0.01 or lower, N = number of neighboring atoms, R = distance, σ^2 = mean square deviation of interatomic distance, ρ = misfit between experimental data and theory.

Table S 6: Structural parameters of the local Ni atomic environment extracted from EXAFS spectra at the Ni K-edge of various samples measured at 400 °C during fluctuating methanation conditions during *30 s H_2 dropouts*. The EXAFS data is extracted from the data set presented in Figure 34 a). They represent the most oxidizing and reducing states during the experiment. The data was Fourier transformed in the k-range 3-9 Å^{-1} and fitted within the R-range 1-3.2 Å. This resulted in 9 independent variables while 7 variables were fitted. The evaluated Ni and O coordination numbers are plotted in Figure 34 b). The experimental and simulated EXAFS data is shown in Figure S 16. Reproduced from Mutz *et al.*[223] under the terms and conditions of CC BY 4.0 license (http://creativecommons.org/licenses/by/4.0/), Copyright © 2017.

Sample (Condition)	Atom	N	R (Å)[a]	σ^2 *10^{-3} (Å^2)	E_0 (eV)	ρ (%)
Meth-6	O	1.6 ± 0.2	2.03 ± 0.2	8.3[f]	9.0 ± 1.5	0.27
k-range: 3-9 R-range: 1.2-3.2 N^{ind}= 6; N^{var}=5	Ni	4.4 ± 0.3	2.49 ± 0.1	11.8[f]		
Dropout-7	O	2.4 ± 0.2	2.02 ± 0.03	8.3[f]	7.6 ± 2.9	0.25
k-range: 3-9 R-range: 1.2-3.2 N^{ind}= 6; N^{var}=5	Ni	2.0 ± 0.6	2.48 ± 0.02	11.4[f]		
	Ni	3.4 ± 0.9	2.96 ± 0.03	11.8[f]		
Meth-7	O	1.8 ± 0.2	2.01 ± 0.2	8.3[f]	6.4 ± 2.2	0.23
k-range: 3-9 R-range: 1.2-3.2 N^{ind}= 6; N^{var}=5	Ni	3.2 ± 0.4	2.48 ± 0.1	11.4[f]		
	Ni	1.9 ± 0.6	2.95 ± 0.3	11.8[f]		

Dropout -8	O	3.0 ± 0.2	2.04 ± 0.02	8.3[f]	8.9 ± 2.1	0.14
k-range: 3-9 R-range: 1.2-3.2 N^{ind}= 6; N^{var}=5	Ni	1.3 ± 0.6	2.48 ± 0.03	11.4[f]		
	Ni	4.4 ± 0.7	2.97 ± 0.03	11.8[f]		
Meth -8	O	2.2 ± 2.0	2.02 ± 0.03	8.3[f]	6.8 ± 2.9	0.23
k-range: 3-9 R-range: 1.2-3.2 N^{ind}= 6; N^{var}=5	Ni	2.3 ± 0.6	2.48 ± 0.01	11.4[f]		
	Ni	3.1 ± 0.9	2.96 ± 0.03	11.8[f]		
Dropout -9	O	3.4 ± 0.2	2.04 ± 0.02	8.3[f]	9.5 ± 2.0	0.13
k-range: 3-9 R-range: 1.2-3.2 N^{ind}= 6; N^{var}=5	Ni	1.0 ± 0.7	2.48 ± 0.03	11.4[f]		
	Ni	4.9 ± 0.8	2.97 ± 0.02	11.8[f]		
Meth -9	O	2.6 ± 0.2	2.03 ± 0.02	8.3[f]	8.1 ± 2.2	0.15
k-range: 3-9 R-range: 1.2-3.2 N^{ind}= 6; N^{var}=5	Ni	1.9 ± 0.5	2.48 ± 0.01	11.4[f]		
	Ni	3.6 ± 0.7	2.96 ± 0.03	11.8[f]		
Dropout -10	O	3.5 ± 0.2	2.05 ± 0.02	8.3[f]	9.8 ± 2.0	0.12
k-range: 3-9 R-range: 1.2-3.2 N^{ind}= 6; N^{var}=5	Ni	0.9 ± 0.7	2.46 ± 0.03	11.4[f]		
	Ni	5.1 ± 0.8	2.98 ± 0.02	11.8[f]		
Meth -10	O	2.8 ± 0.2	2.03 ± 0.03	8.3[f]	8.5 ± 2.2	0.16
k-range: 3-9 R-range: 1.2-3.2 N^{ind}= 6; N^{var}=5	Ni	1.5 ± 0.6	2.48 ± 0.02	11.4[f]		
	Ni	4.1 ± 0.8	2.97 ± 0.03	11.8[f]		
Dropout -11	O	3.6 ± 0.2	2.05 ± 0.02	8.3[f]	9.8 ± 1.9	0.11
k-range: 3-9 R-range: 1.2-3.2 N^{ind}= 6; N^{var}=5	Ni	0.9 ± 0.7	2.46 ± 0.03	11.4[f]		
	Ni	5.2 ± 0.8	2.98 ± 0.02	11.8[f]		
Meth -11	O	3.0 ± 0.2	2.04 ± 0.02	8.3[f]	8.8 ± 2.1	0.14
k-range: 3-9 R-range: 1.2-3.2 N^{ind}= 6; N^{var}=5	Ni	1.5 ± 0.6	2.48 ± 0.02	11.4[f]		
	Ni	4.4 ± 0.8	2.97 ± 0.02	11.8[f]		
Dropout -12	O	3.6 ± 0.2	2.05 ± 0.02	8.3[f]	9.8 ± 1.9	0.11
k-range: 3-9 R-range: 1.2-3.2 N^{ind}= 6; N^{var}=5	Ni	0.8 ± 0.7	2.46 ± 0.04	11.4[f]		
	Ni	5.4 ± 0.8	2.97 ± 0.02	11.8[f]		
Meth -12	O	3.1 ± 0.2	2.05 ± 0.03	8.3[f]	9.4 ± 2.4	0.20
k-range: 3-9 R-range: 1.2-3.2 N^{ind}= 6; N^{var}=5	Ni	1.4 ± 0.7	2.48 ± 0.02	11.4[f]		
	Ni	4.4 ± 0.9	2.97 ± 0.03	11.8[f]		
Dropout -13	O	3.7 ± 0.2	2.06 ± 0.03	8.3[f]	10.0 ± 2.1	0.15
k-range: 3-9 R-range: 1.2-3.2 N^{ind}= 6; N^{var}=5	Ni	0.8 ± 0.8	2.46 ± 0.04	11.4[f]		
	Ni	5.3 ± 0.9	2.98 ± 0.03	11.8[f]		
Meth -13	O	3.2 ± 0.2	2.05 ± 0.02	8.3[f]	9.5 ± 2.2	0.16
k-range: 3-9 R-range: 1.2-3.2 N^{ind}= 6; N^{var}=5	Ni	1.3 ± 0.7	2.48 ± 0.04	11.4[f]		
	Ni	4.5 ± 0.8	2.97 ± 0.02	11.8[f]		
Dropout -14	O	3.7 ± 0.2	2.06 ± 0.02	8.3[f]	10.0 ± 2.0	0.13
k-range: 3-9 R-range: 1.2-3.2 N^{ind}= 6; N^{var}=5	Ni	0.8 ± 0.7	2.46 ± 0.04	11.4[f]		
	Ni	5.3 ± 0.8	2.98 ± 0.02	11.8[f]		

Meth -14	O	3.2 ± 0.2	2.04 ± 0.02	8.3[f]	8.8 ± 1.8	0.10
k-range: 3-9 R-range: 1.2-3.2 N^{ind}= 6; N^{var}=5	Ni	1.1 ± 0.6	2.47 ± 0.02	11.4[f]		
	Ni	4.8 ± 0.7	2.97 ± 0.02	11.8[f]		

a = fitted uncertainty 0.01 or lower, f = fixed during fit, N = number of neighboring atoms, R = distance, σ^2 = mean square deviation of interatomic distance, ρ = misfit between experimental data and theory.

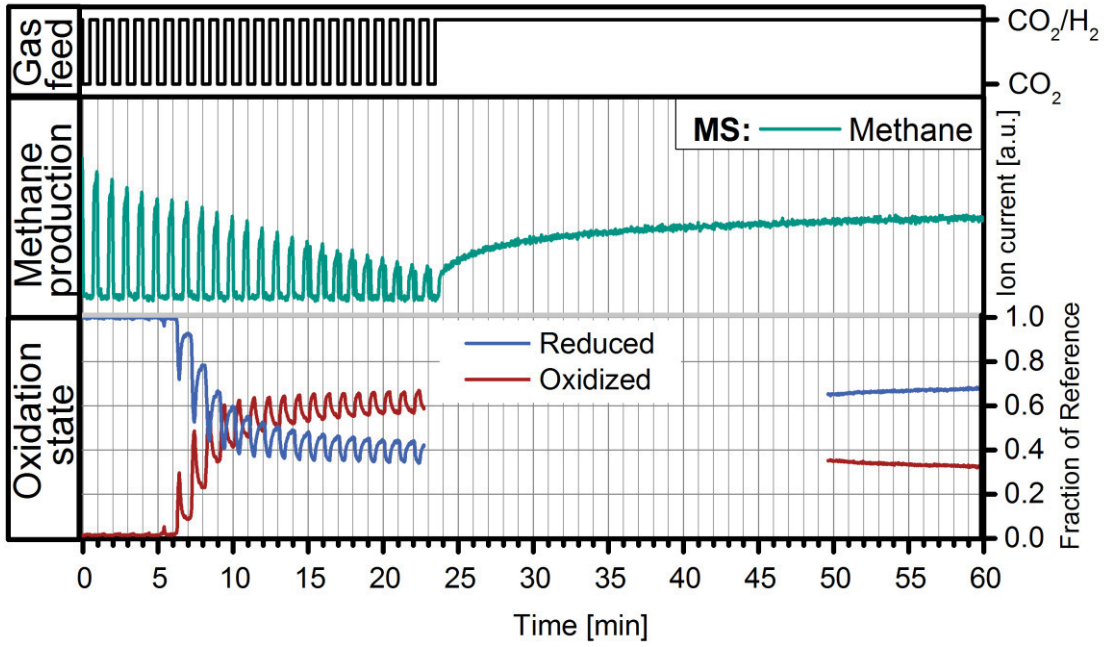

Figure S 9: Full length of the experiment including 30 s modulation of methanation of CO_2 (H_2/CO_2 = 4) and CO_2 at constant WHSV of 12000 mL_{CO2} g_{cat}^{-1} h^{-1} and GHSV of 71700 h^{-1}. The figure shows the valve signal in the upper part (black), the CH_4 signal of the MS (m/z 15) in the middle part (green) and the fraction of reduced (blue) and oxidized (red) Ni from LCF of the XANES spectra according to the references in Figure S 7. Reproduced from Mutz *et al.*[223] under the terms and conditions of CC BY 4.0 license (http://creativecommons.org/licenses/by/4.0/), Copyright © 2017.

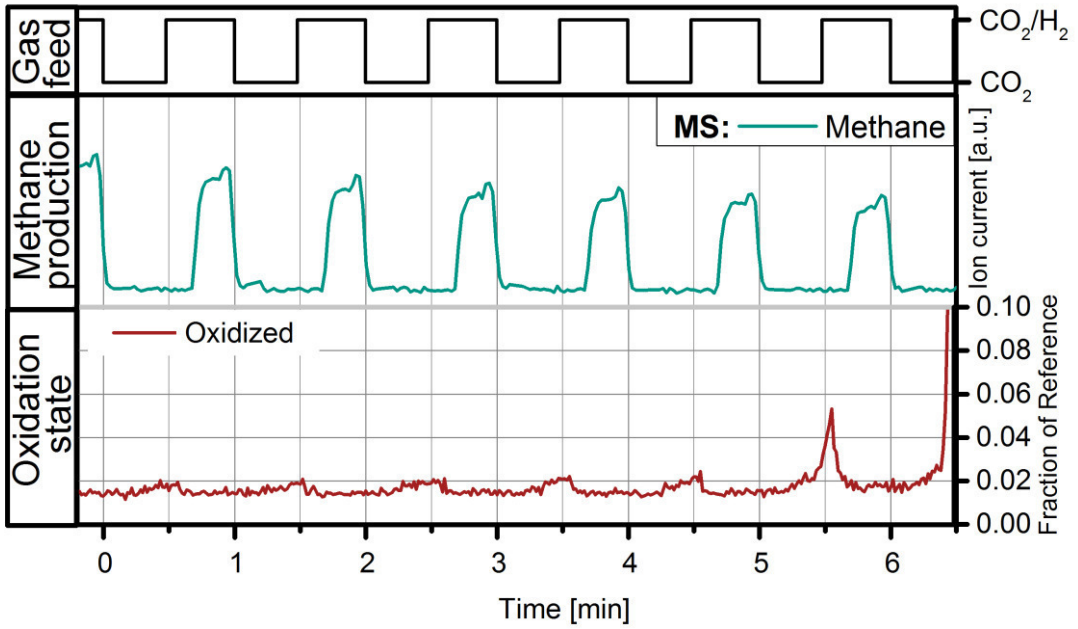

Figure S 10: Zoom of first 6 min of the 30 s modulation of Figure S 9. Reproduced from Mutz *et al.*[223] under the terms and conditions of CC BY 4.0 license (http://creativecommons.org/licenses/by/4.0/), Copyright © 2017.

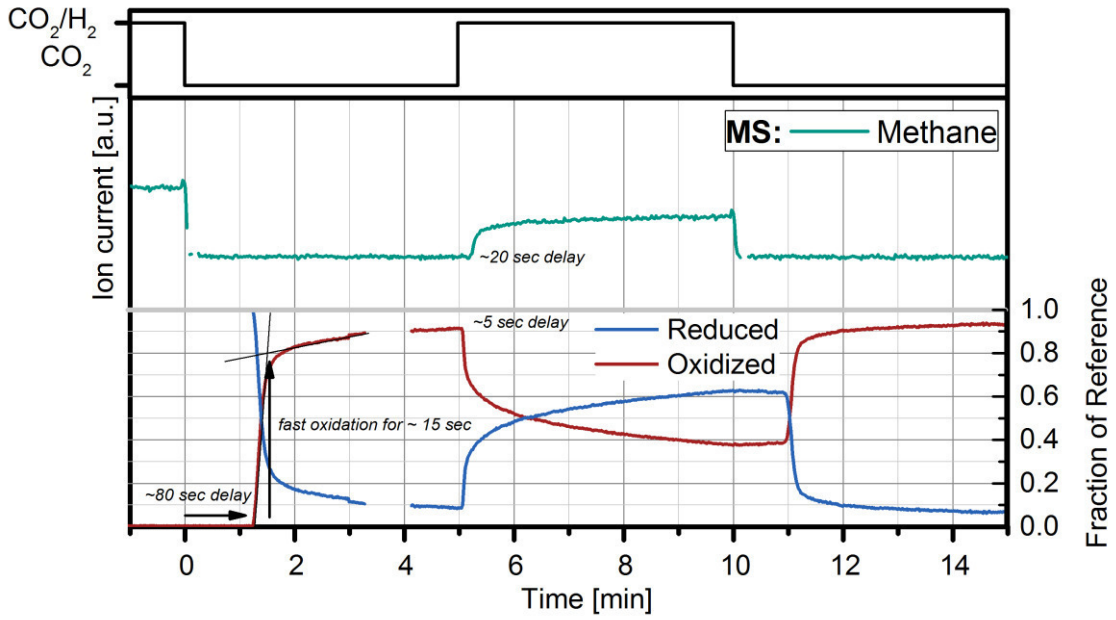

Figure S 11: Zoom of the first 14 min of the 300 s modulation of methanation of CO_2 (H_2/CO_2 = 4) and CO_2 at constant WHSV of 12000 mL_{CO2} g_{cat}^{-1} h^{-1} and GHSV of 71700 h^{-1}. The figure shows the valve signal in the upper part (black), the CH_4 signal of the MS (m/z 15) in the middle part (green) and the fraction of reduced (blue) and oxidized (red) Ni from LCF of the XANES spectra according to the references in Figure S 7. Reproduced from Mutz *et al.*[223] under the terms and conditions of CC BY 4.0 license (http://creativecommons.org/licenses/by/4.0/), Copyright © 2017.

Based on Figure S 11 the amount of O_2 present in the experiment was estimated. We assume that the oxidation of Ni starts at the reactor inlet and the oxidation front propagates through the catalyst bed. XAS spectra were recorded in the middle of the catalyst bed. Therefore, half of the catalyst was oxidized to approximately 75 % 95 s after the gas switch, as the fast increase in oxidation monitored by XAS declines. 3 µmol Ni was oxidized as the oxidation front reached the middle of the catalyst bed, necessitating an amount of 1.5 µmol O_2 which is approximately 1000 ppm O_2 of the 20 mL min^{-1} total gas flow.

Table S 5: Structural parameters of the local Ni atomic environment extracted from EXAFS spectra at the Ni K-edge of various samples measured at 400 °C during fluctuating methanation conditions during *300 s H_2 dropouts*. The EXAFS data is extracted from the data set presented in Figure 37 a). They represent the most oxidizing and reducing states during the experiment. The data was Fourier transformed in the k-range 3-9 $Å^{-1}$ and fitted within the R-range 1-3.2 Å. This resulted in 9 independent variables while 7 variables were fitted. The evaluated Ni and O coordination numbers are plotted in Figure 37 b). The experimental and simulated EXAFS data is shown in Figure S 17 together with the fitting ranges. Reproduced from Mutz *et al.*[223] under the terms and conditions of CC BY 4.0 license (http://creativecommons.org/licenses/by/4.0/), Copyright © 2017.

Sample (Condition)	**Atom**	**N**	**R(Å)**	**σ^2 *10^{-3} ($Å^2$)**	**E_0 (eV)**	**ρ (%)**
Meth -0	O	1.1 ± 0.2	2.03 ± 0.01	8.3 ± 1.5[b]	8.4 ± 2.0	0.22
k-range: 3-9 R-range: 1.2-3.2 N^{ind}= 6; N^{var}=5	Ni	5.1 ± 0.3	2.49 ± 0.03	11.4 ± 1.2 [b]		
Meth -1	O	2.4 ± 0.2	2.03 ± 0.03	8.3 ± 1.5 [b]	7.9 ± 2.5	0.27
k-range: 3-9 R-range: 1.2-3.2 N^{ind}= 6; N^{var}=5	Ni	2.7 ± 0.6	2.48 ± 0.02	11.4 ± 1.2 [b]		
	Ni	3.8 ± 0.8	2.96 ± 0.03	11.8 ± 2.1 [b]		
Meth -2	O	2.7 ± 0.2	2.03 ± 0.02	8.3 ± 1.5 [b]	8.5 ± 2.0	0.11
k-range: 3-9 R-range: 1.2-3.2 N^{ind}= 6; N^{var}=5	Ni	2.3 ± 0.6	2.48 ± 0.01	11.4 ± 1.2 [b]		
	Ni	4.2 ± 0.7	2.96 ± 0.02	11.8 ± 2.1 [b]		
Meth -3	O	2.9 ± 0.2	2.04 ± 0.03	8.3 ± 1.5 [b]	8.9 ± 2.3	0.16
k-range: 3-9 R-range: 1.2-3.2 N^{ind}= 6; N^{var}=5	Ni	2.0 ± 0.7	2.48 ± 0.02	11.4 ± 1.2 [b]		
	Ni	4.6 ± 0.9	2.96 ± 0.03	11.8 ± 2.1 [b]		
Meth -4	O	3.0 ± 0.2	2.04 ± 0.03	8.3 ± 1.5 [b]	9.0 ± 2.2	0.14
k-range: 3-9 R-range: 1.2-3.2 N^{ind}= 6; N^{var}=5	Ni	2.0 ± 0.7	2.48 ± 0.02	11.4 ± 1.2 [b]		
	Ni	4.9 ± 0.8	2.97 ± 0.02	11.8 ± 2.1 [b]		
Meth -5	O	3.0 ± 0.2	2.04 ± 0.01	8.3 ± 1.5 [b]	8.7 ± 2.3	0.14
k-range: 3-9 R-range: 1.2-3.2 N^{ind}= 6; N^{var}=5	Ni	1.7 ± 0.7	2.48 ± 0.01	11.4 ± 1.2 [b]		
	Ni	5.1 ± 0.9	2.97 ± 0.01	11.8 ± 2.1 [b]		

Meth -6	O	3.1 ± 0.2	2.04 ± 0.03	8.3 ± 1.5 [b]	9.0 ± 2.2	0.14
k-range: 3-9 R-range: 1.2-3.2 N^{ind}= 6; N^{var}=5	Ni	1.8 ± 0.7	2.48 ± 0.02	11.4 ± 1.2 [b]		
	Ni	5.0 ± 0.8	2.97 ± 0.02	11.8 ± 2.1 [b]		
Meth -7	O	3.1 ± 0.2	2.04 ± 0.03	8.3 ± 1.5 [b]	9.3 ± 2.3	0.16
k-range: 3-9 R-range: 1.2-3.2 N^{ind}= 6; N^{var}=5	Ni	1.8 ± 0.7	2.48 ± 0.02	11.4 ± 1.2 [b]		
	Ni	5.0 ± 0.9	2.97 ± 0.03	11.8 ± 2.1 [b]		
Meth -8	O	3.1 ± 0.2	2.05 ± 0.03	8.3 ± 1.5 [b]	9.0 ± 2.2	0.13
k-range: 3-9 R-range: 1.2-3.2 N^{ind}= 6; N^{var}=5	Ni	1.6 ± 0.7	2.48 ± 0.02	11.4 ± 1.2 [b]		
	Ni	5.3 ± 0.9	2.97 ± 0.02	11.8 ± 2.1 [b]		
Dropout -1-8	O	4.0 ± 0.2	2.05 ± 0.01	8.3 [f]	9.9 ± 0.9	0.27
k-range: 3-9 R-range: 1.2-3.2 N^{ind}= 6; N^{var}=5	Ni	7.6 ± 0.5	2.96 ± 0.01	11.8[f]		

[b] =mean-square deviation evaluated simultaneously spectra Red 0-8, f = fixed during fit, extracted from fit of Meth 0-8 during 300 s switches, N = number of neighboring atoms, R = distance, σ^2 = mean square deviation of interatomic distance, ρ = misfit between experimental data and theory according to Ref[222].

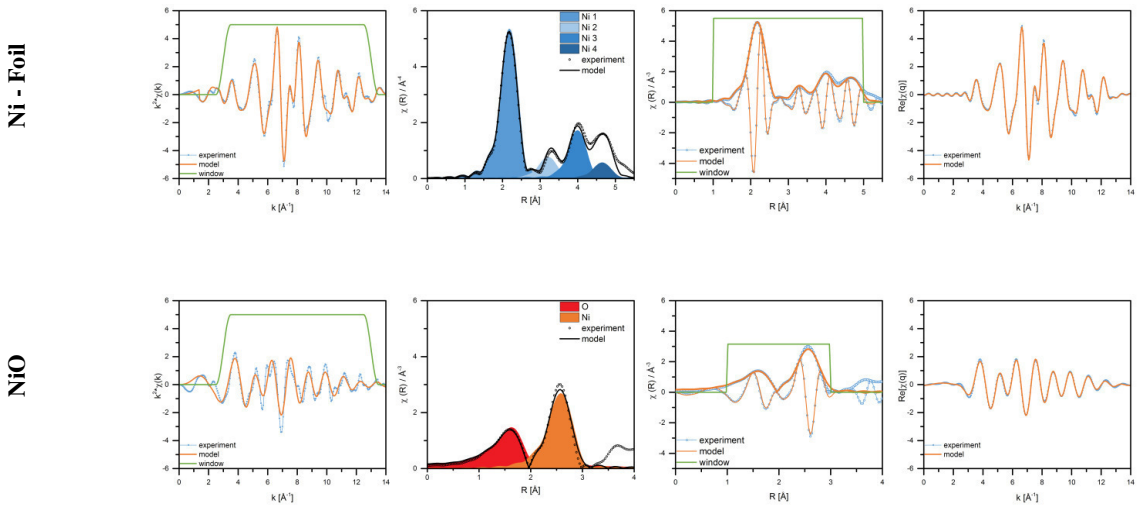

Figure S 12: Experimental and simulated EXAFS data of reference data (Ni-Foil and NiO). From left to right: extracted EXAFS data in k-space with k-range used for data fitting; FT EXAFS data and respective components of the simulated data (magnitude of FT); magnitude and imaginary part of FT EXAFS data with R-range used for data fitting, real part of back FT data (R-range: 1-3.2 Å). Reproduced from Mutz *et al.*[223] under the terms and conditions of CC BY 4.0 license (http://creativecommons.org/licenses/by/4.0/), Copyright © 2017.

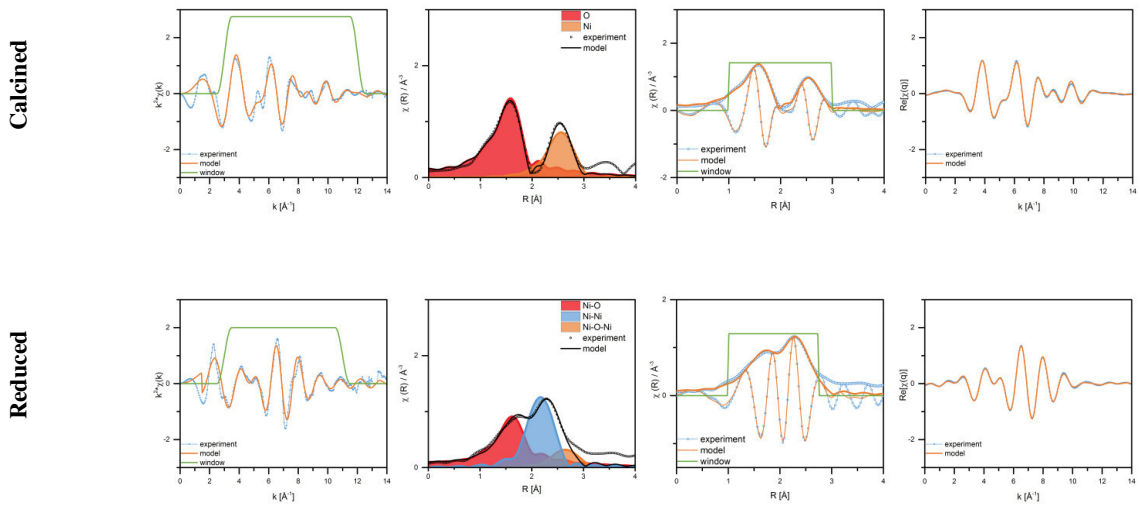

Figure S 13: Experimental and simulated EXAFS data of 10 wt.% Ni/Al_2O_3 catalyst at room temperature. From left to right: extracted EXAFS data in k-space with k-range used for data fitting; FT EXAFS data and respective components of the simulated data (magnitude of FT); magnitude and imaginary part of FT EXAFS data with R-range used for data fitting, real part of back FT data (R-range: 1-3.2 Å). Reproduced from Mutz *et al.*[223] under the terms and conditions of CC BY 4.0 license (http://creativecommons.org/licenses/by/4.0/), Copyright © 2017.

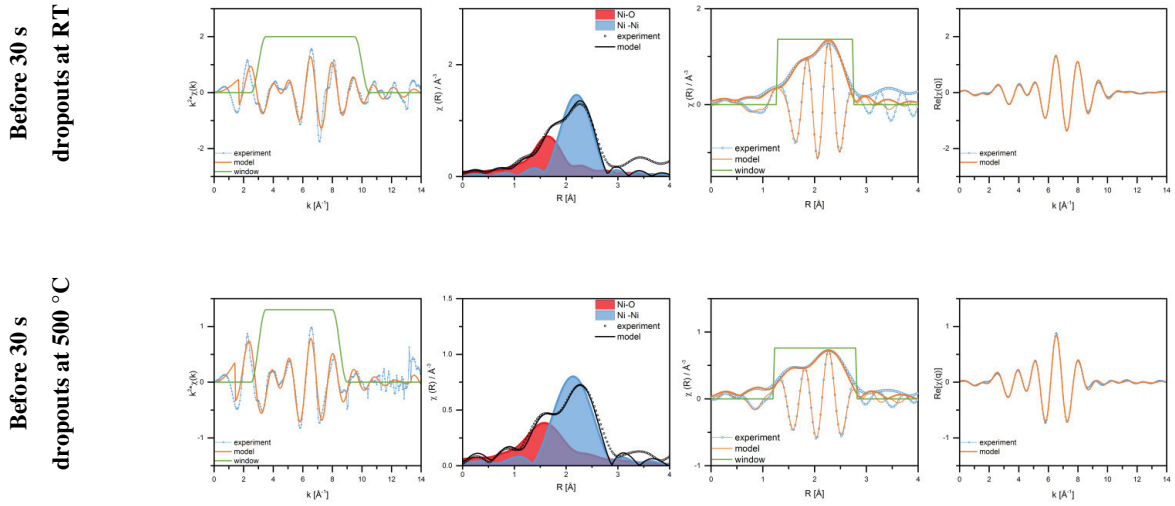

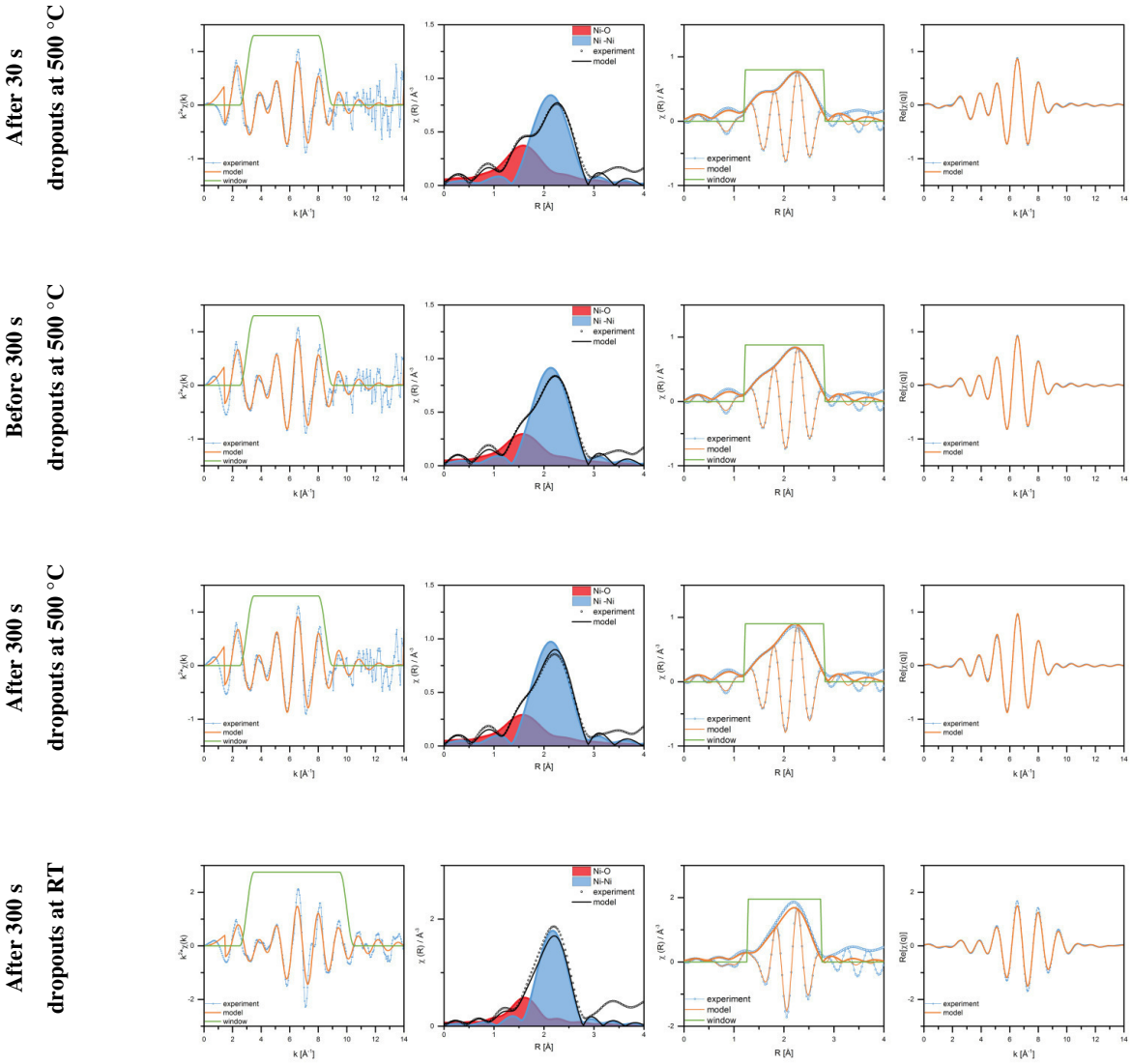

Figure S 14: Experimental and simulated EXAFS data of 10 wt.% Ni/Al_2O_3 catalyst at room temperature. From left to right: extracted EXAFS data in k-space with k-range (see Table S 4, k-weight=2) used for data fitting; FT EXAFS data and respective components of the simulated data (magnitude of FT); magnitude and imaginary part of FT EXAFS data with R-range used for data fitting, real part of back FT data (see Table S 4). Reproduced from Mutz *et al.*[223] under the terms and conditions of CC BY 4.0 license (http://creativecommons.org/licenses/by/4.0/), Copyright © 2017.

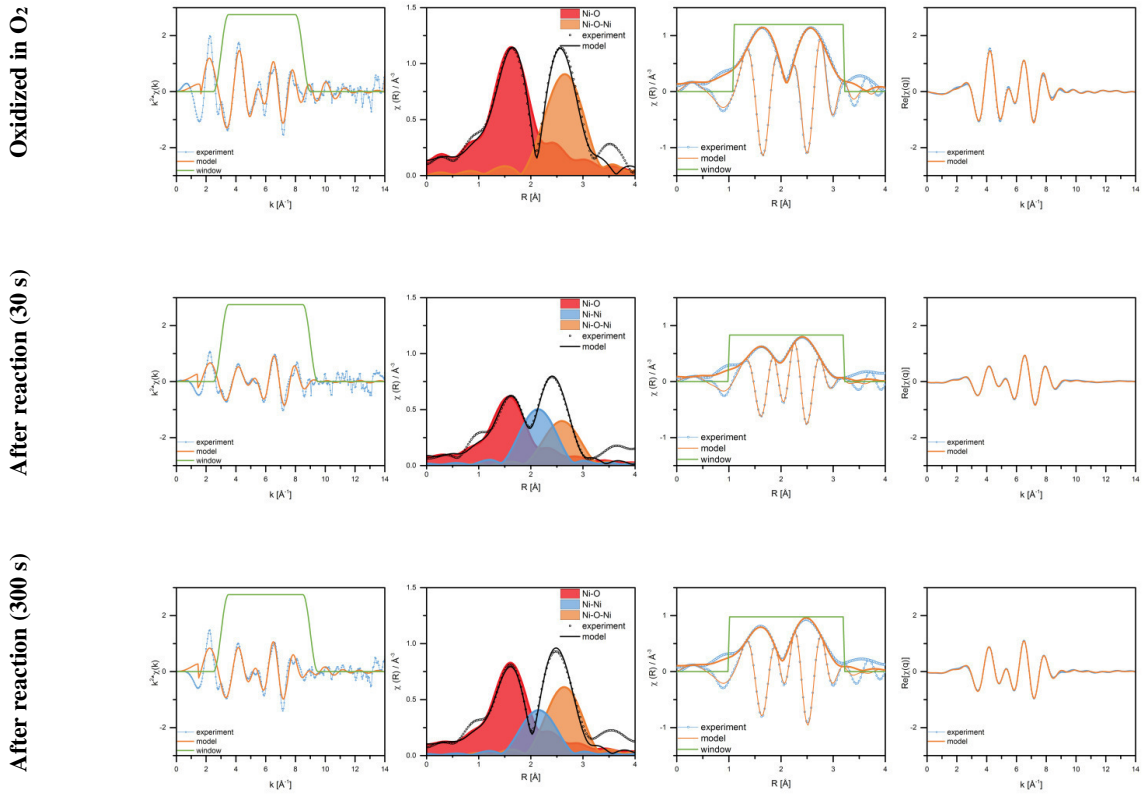

Figure S 15: Experimental and simulated EXAFS data of 10 wt.% Ni/Al_2O_3 catalyst at 400 °C. From left to right: extracted EXAFS data in k-space with k-range used for data fitting (see Table S 5, k-weight=2); FT EXAFS data and respective components of the simulated data (magnitude of FT); magnitude and imaginary part of FT EXAFS data with R-range used for data fitting, real part of back FT data (see Table S 5). Reproduced from Mutz *et al.*[223] under the terms and conditions of CC BY 4.0 license (http://creativecommons.org/licenses/by/4.0/), Copyright © 2017.

Meth -6

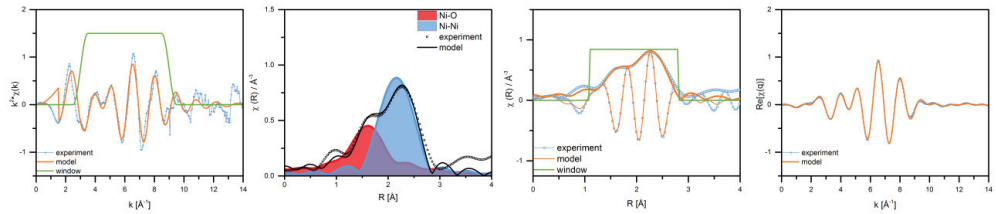

Dropout -7

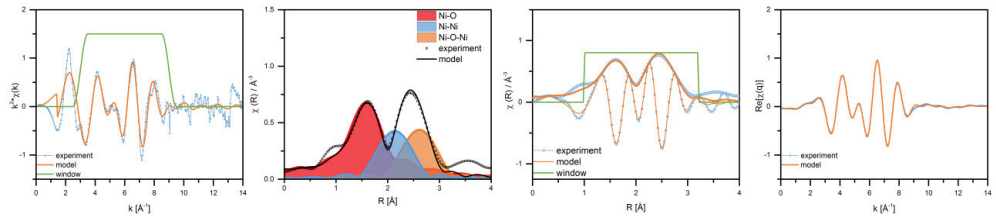

Meth -7

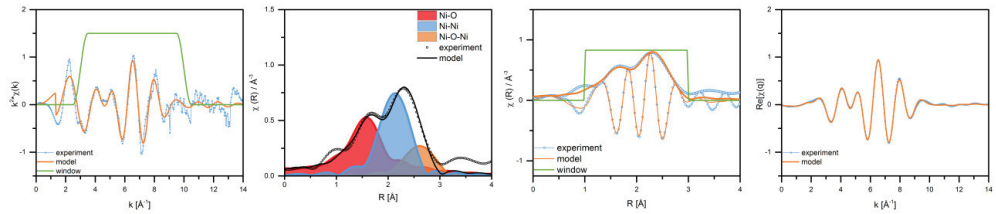

Dropout -8

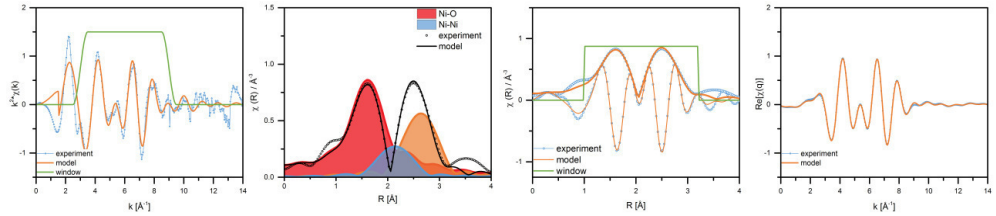

Meth -8

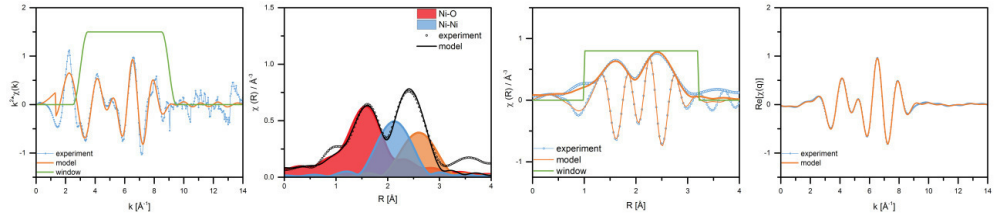

Dropout -9

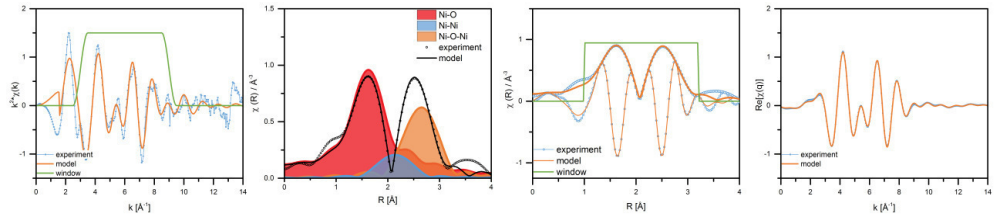

Meth -9

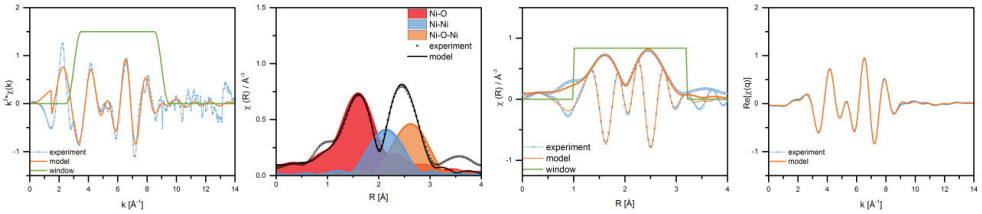

Dropout -10

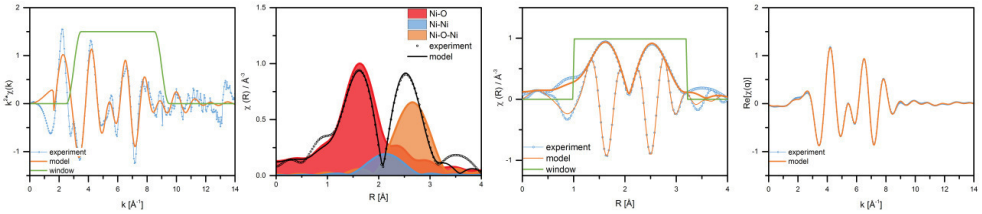

Meth -10

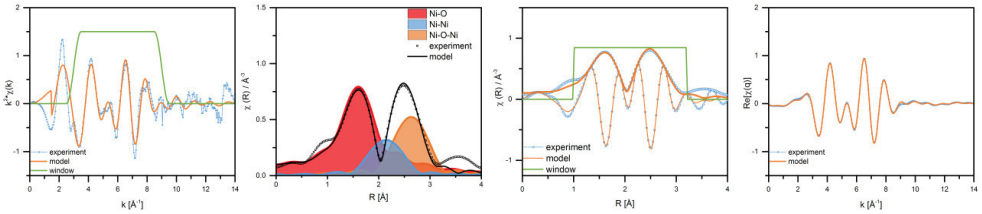

Dropout -11

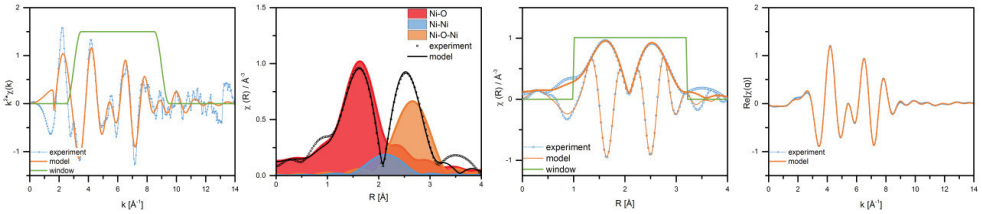

Meth -11

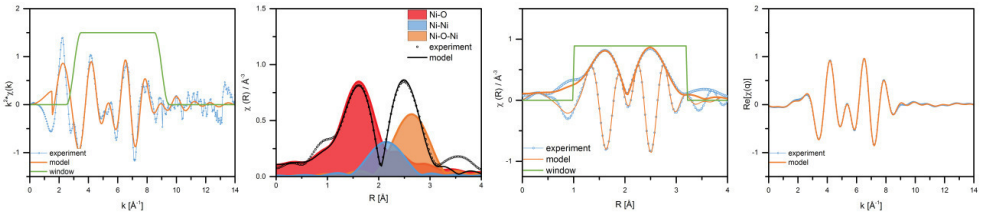

Dropout -12

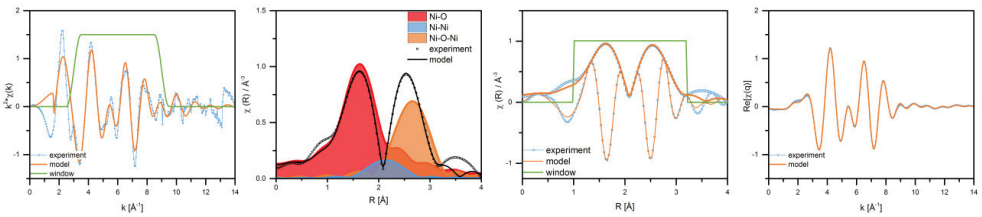

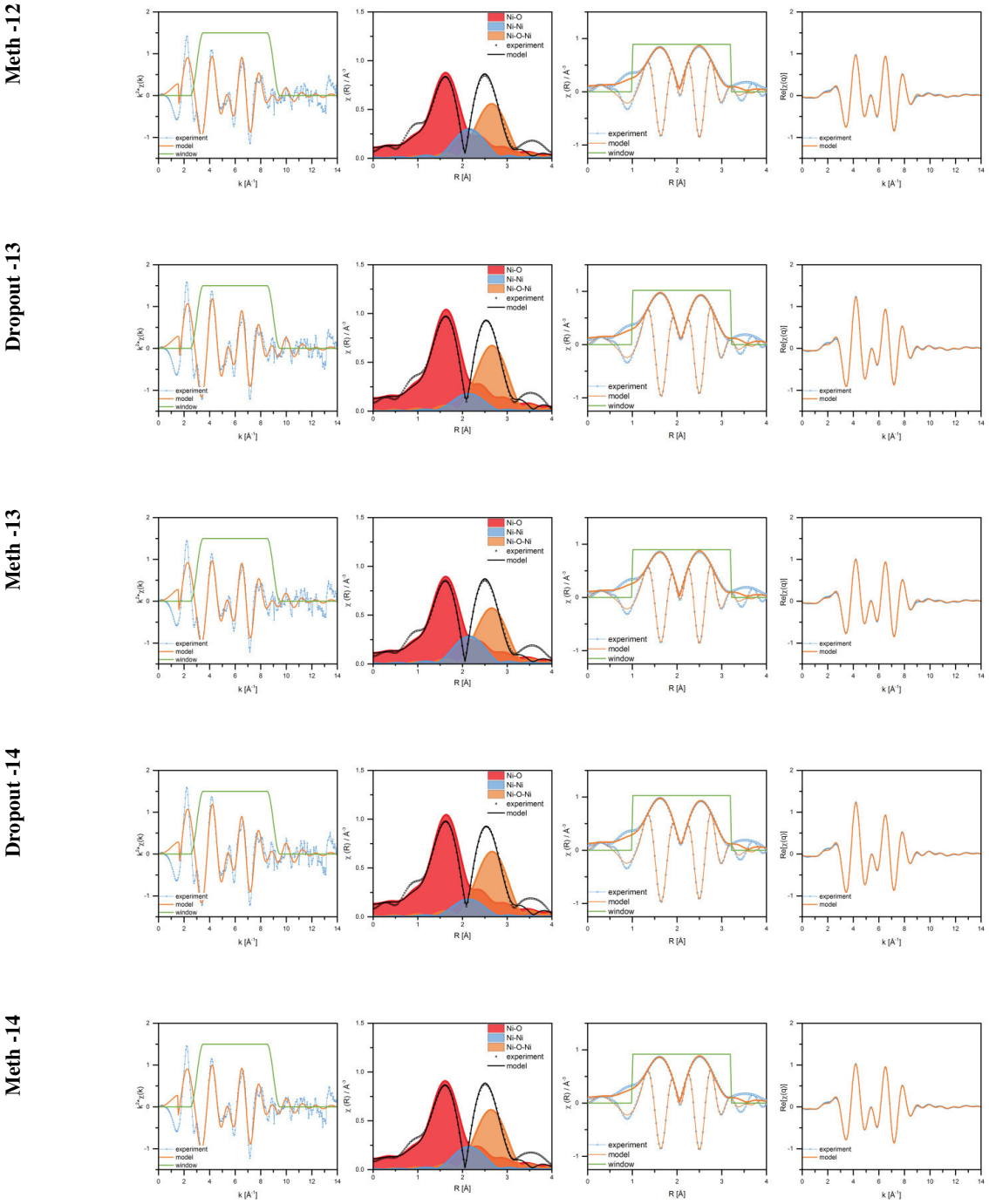

Figure S 16: Experimental and simulated EXAFS data of Ni/Al_2O_3 catalyst during methanation with *30 s H_2 dropouts*. From left to right: extracted EXAFS data in k-space with k-range used for data fitting (3-9 $Å^{-1}$, k-weight = 2); FT EXAFS data and respective components of the simulated data (magnitude of FT); magnitude and imaginary part of FT EXAFS data with R-range used for data fitting (see Table S 6), real part of back FT data (R-range: 1-3.2 Å). Reproduced from Mutz *et al.*[223] under the terms and conditions of CC BY 4.0 license (http://creativecommons.org/licenses/by/4.0/), Copyright © 2017.

300 s modul. oxidized

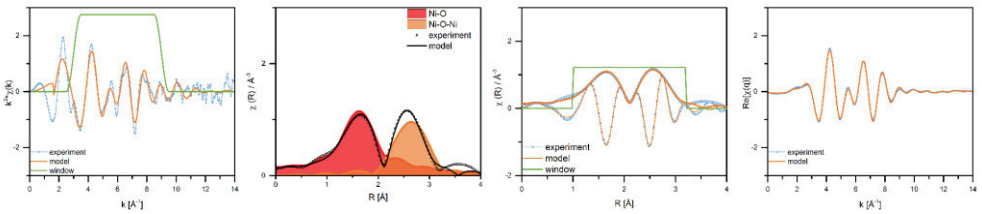

Meth -0

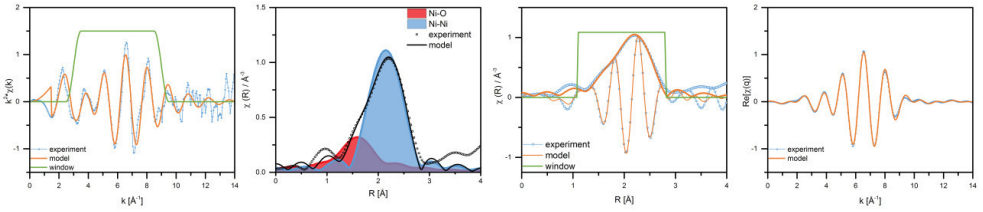

Meth -1

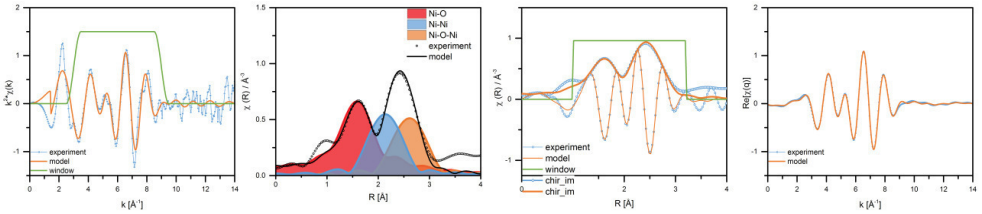

Meth -2

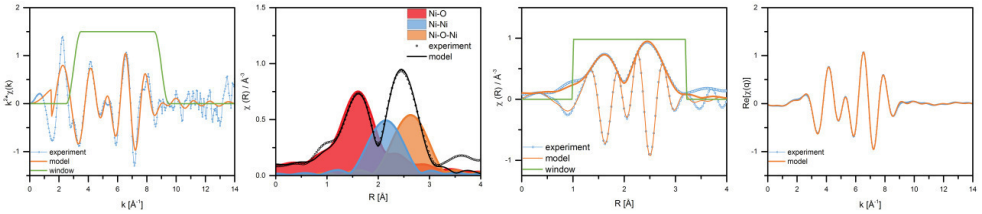

Meth -3

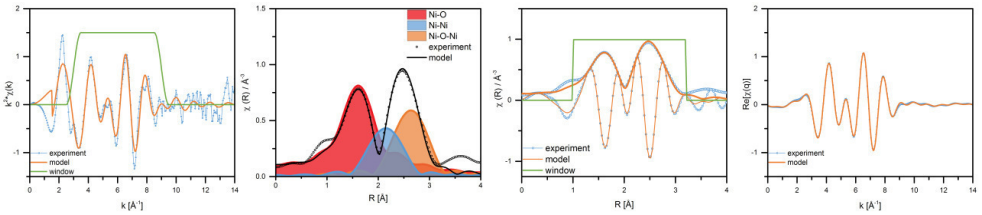

Meth -4

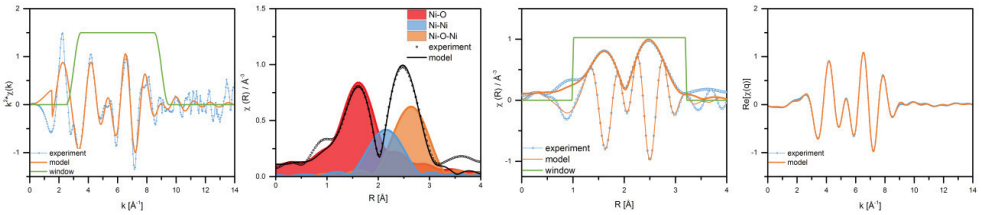

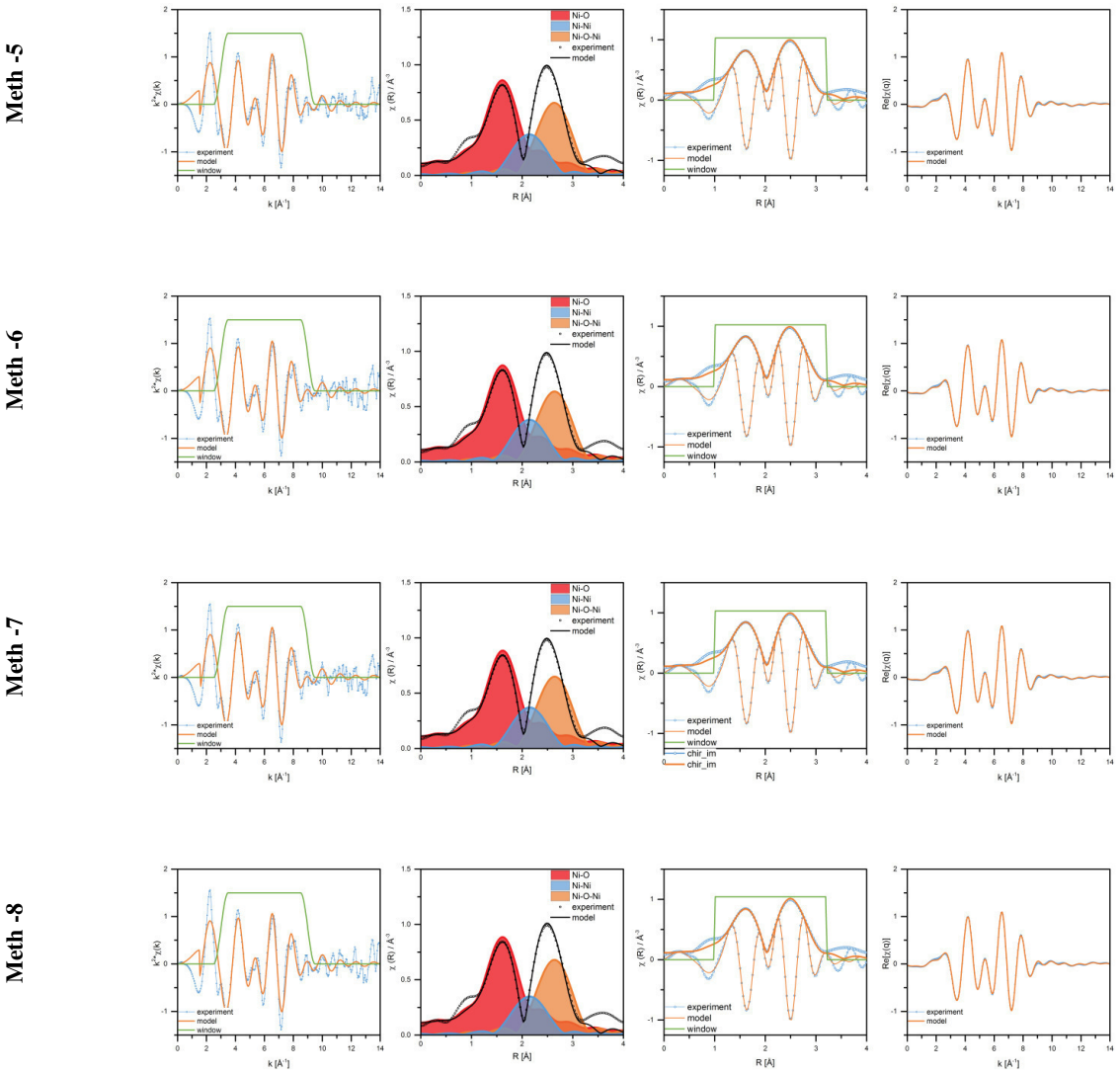

Figure S 17: Experimental and simulated EXAFS data of 10 wt.% Ni/Al_2O_3 catalyst during methanation with *300 s H_2 drop outs*. From left to right: extracted EXAFS data in k-space with k-range used for data fitting (2-9 $Å^{-1}$, k-weight =2); FT EXAFS data and respective components of the simulated data (magnitude of FT); magnitude and imaginary part of FT EXAFS data with R-range used for data fitting (see Table S 5) (1.2-2.9 Å), real part of back FT data (R-range: 1.2-3.2 Å). Reproduced from Mutz *et al.*[223] under the terms and conditions of CC BY 4.0 license (http://creativecommons.org/licenses/by/4.0/), Copyright © 2017.

Mass spectrometry data recorded during the QEXAFS experiments

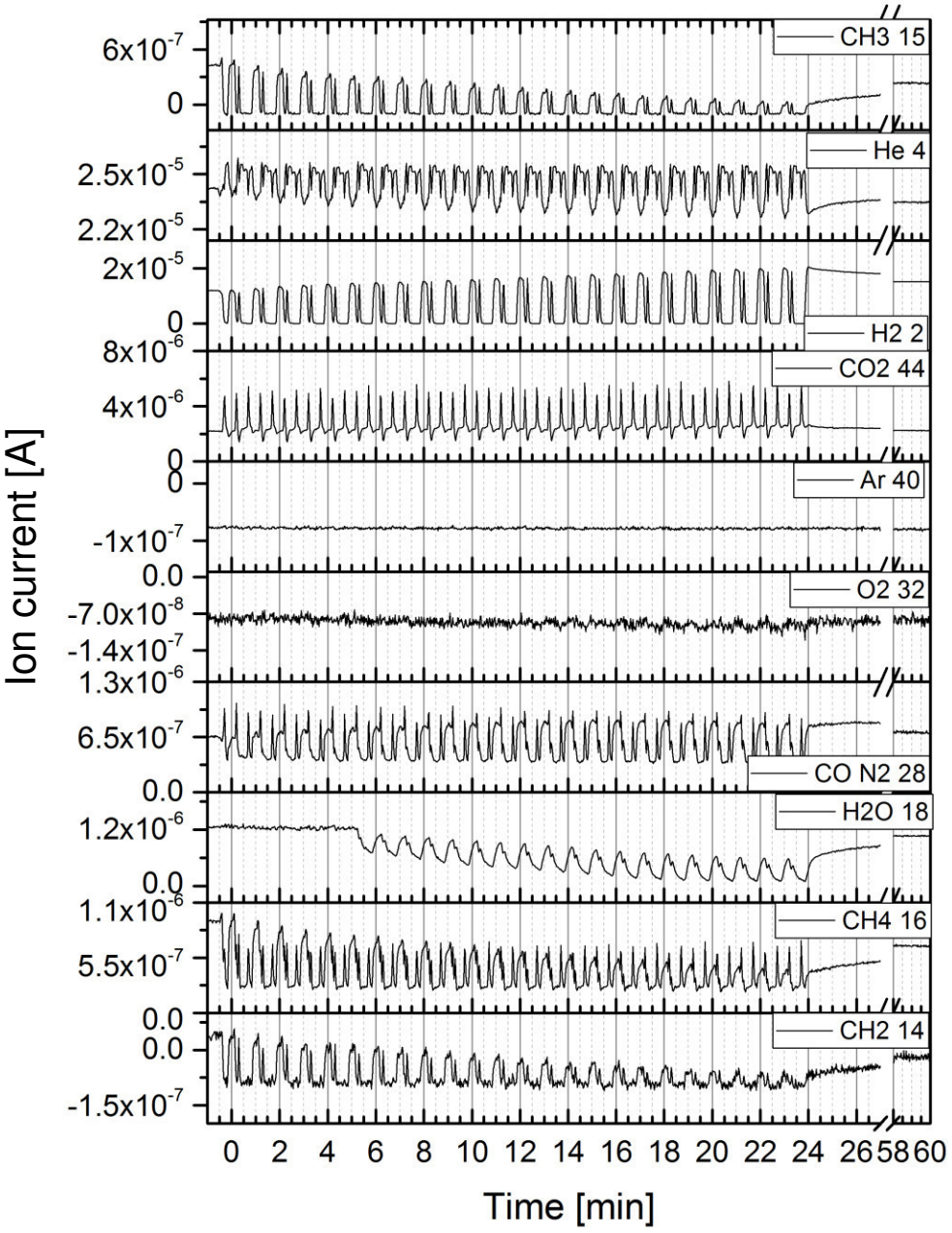

Figure S 18: MS data recorded during 30 s H_2 dropouts. Reproduced from Mutz *et al.*[223] under the terms and conditions of CC BY 4.0 license (http://creativecommons.org/licenses/by/4.0/), Copyright © 2017.

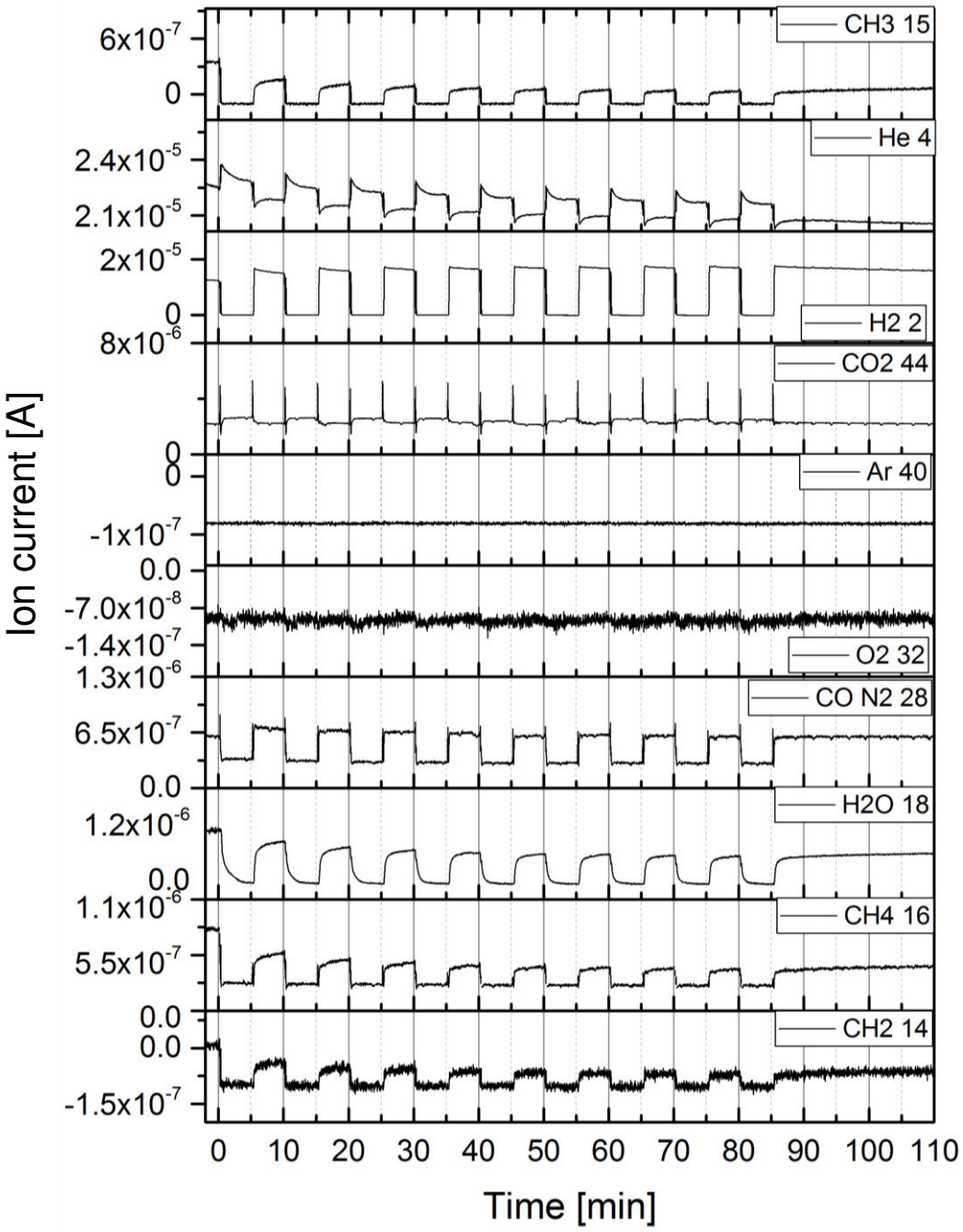

Figure S 19: MS data recorded during 300 s H_2 dropouts. Reproduced from Mutz *et al.*[223] under the terms and conditions of CC BY 4.0 license (http://creativecommons.org/licenses/by/4.0/), Copyright © 2017.

Additional H_2 modulation experiments

60 s H_2 dropout modulation experiment in the absence of O_2 using short and thin stainless steel tubing and a CO_2 (99.998 %) bottle directly placed next to the mass flow controllers (Figure S 20). The experiment showed a CH_4 signal in the MS on a stable level and no catalyst deactivation.

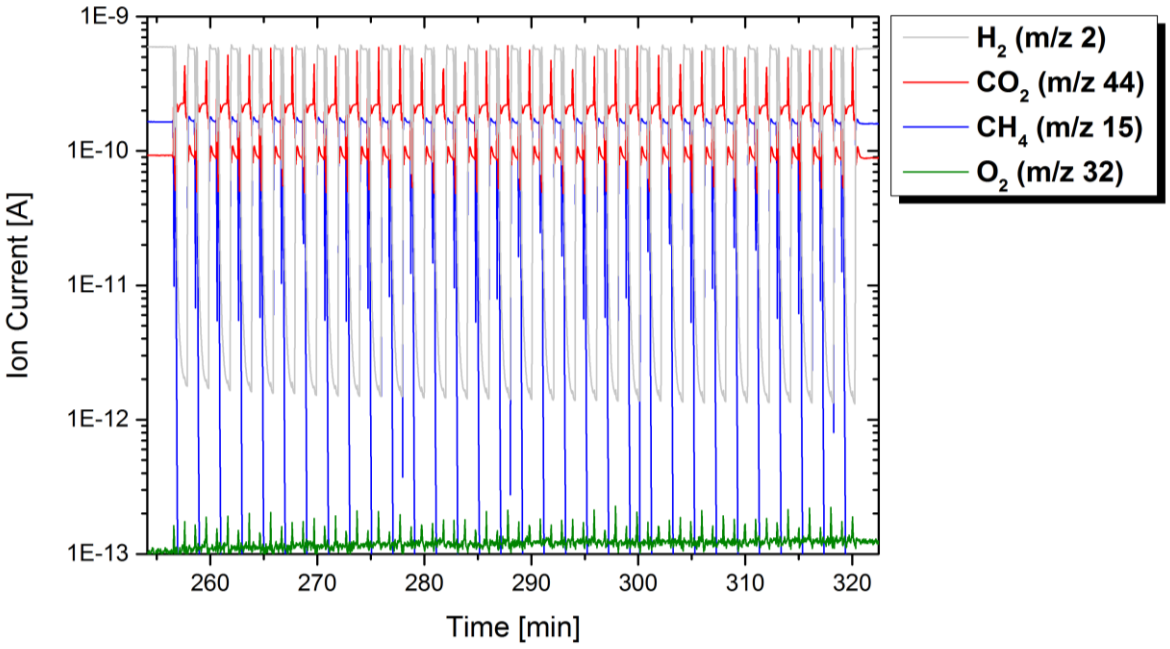

Figure S 20: Methanation of CO_2 during dynamic operation switching every 60 s between methanation conditions ($H_2/CO_2 = 4$) and CO_2 at constant WHSV of 12000 $mL_{CO2}\ g_{cat}^{-1}\ h^{-1}$ and GHSV of 71700 h^{-1} using the 10 wt.% Ni/Al_2O_3 catalyst in an O_2 free experiment (quartz glass capillary). The figure shows the MS signals of H_2, CO_2, CH_4 and O_2. Reproduced from Mutz *et al.*[223] under the terms and conditions of CC BY 4.0 license (http://creativecommons.org/licenses/by/4.0/), Copyright © 2017.

Supplementary data on *operando* Raman spectroscopy

Additional catalyst characterization - X-ray diffraction

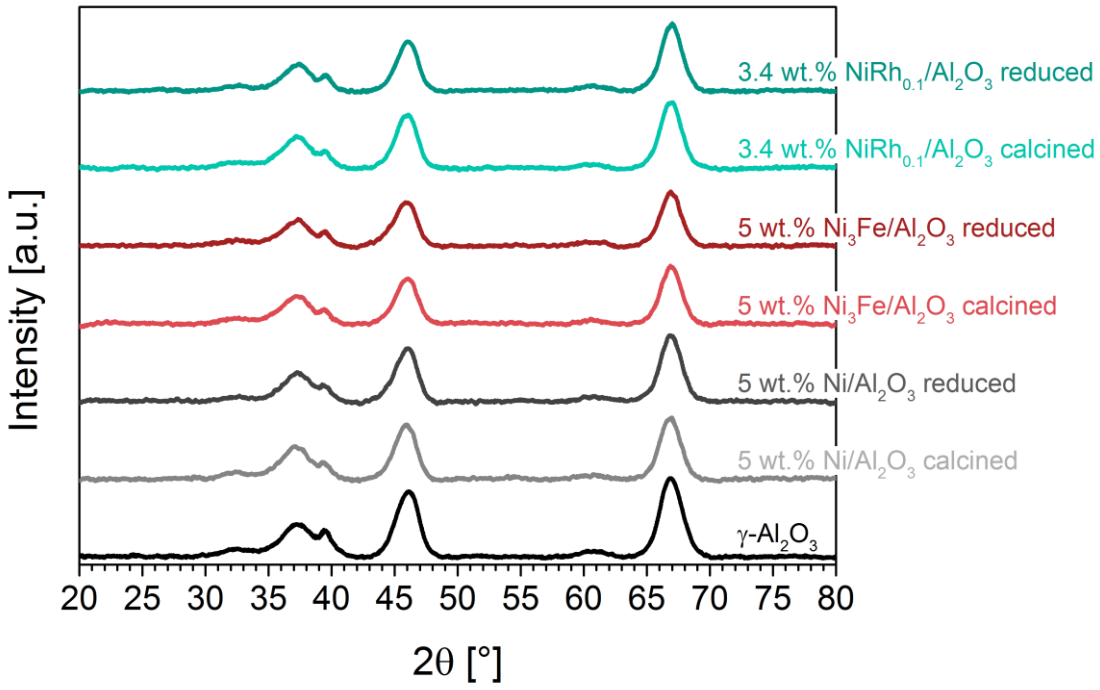

Figure S 21: XRD patterns of the Al_2O_3 support (calcined at 600 °C), and the 5 wt.% Ni/Al_2O_3, 5 wt.% Ni_3Fe/Al_2O_3 and $NiRh_{0.1}/Al_2O_3$ catalysts in the calcined (4 h at 500 °C, 5 K min^{-1}) and reduced (2 h, at 500 °C, 5 K min^{-1}) states. Reproduced from Mutz *et al.*[211] Copyright © 2018 Published by Elsevier B.V.

The X-ray diffraction (XRD) patterns of the 5 wt.% Ni/Al_2O_3, 5 wt.% Ni_3Fe/Al_2O_3 and 3.4 wt.% $NiRh_{0.1}/Al_2O_3$catalysts (Figure S 21) were all dominated by the reflections of the Al_2O_3 support at 32.0°, 37.2°, 39.4°, 46.1°, 60.9° and 66.8°. Reflections for NiO at 67.7°, 43.4° 63.0°, 75.6° and 79.6° (ICSD 024014) or metallic Ni at 44.5°, 51.8° and 76.4° (ICSD 044767) were not observed for any of the catalysts. For the Ni_3Fe catalyst we did not observe additional reflection, which would appear for Fe_2O_3 (ICSD: 201101) would appear at 24.3°, 33.5°, 35.9°, 41.2°, 49.9°, 54.6°, 62.9° and 64.5°, for Fe_3O_4 (ICSD:

027898) at 30.1°, 47.2° and 62.6°, for FeO (ICSD 082233) at 35.9°, 41.7°, 60.5°, 72.4° and 76.2°, for $NiFe_2O_4$ (ICSD: 076179) at 30.3°, 35.7°, 43.4°, 57.4°, 57.4°, 63.0°, for Fe (ICSD 064998) at 44.7° and 65.0° and for Ni_3Fe (ICSD 040334) at 44.2°, 51.5°, 75.9°.

The $NiRh_{0.1}$ catalyst where additional reflections would appear for Rh_2O_3 (ICDS 014264) at 23.4°, 32.8°, 35.0°, 39.0°, 48.7°, 53.4°, 61.3° and 62.7°, for $NiRh_2O_4$ (ICDS 023487) at 29.7°, 34.5°, 35.5°, 36.8°, 41.6°, 43.3°, 55.2°, 57.1°, 61.6° and 62.8° and for Rh (ICSD 064991) at 41.1°, 47.8°, 69.9° and 84.4° were not observed.

Most of the reflections were superimposed by the signals of the support material, others were not resolved by XRD due to the small crystallites of the metal particles or X-ray amorphous phases.

Additional catalyst characterization - Electron microscopy

Table S 7 and Table S 8 show the quantified composition information from STEM-EDX measurements acquired in 300 nm x 400 nm areas of Ni_3Fe and $NiRh_{0.1}$ catalysts. The results provide the distribution of both metals, Ni and Fe or Ni and Rh, respectively. The catalysts exhibit variations in both Ni/Fe and Ni/Rh ratios and indicate the segregation in both catalysts. The segregation effect is more pronounced for the $NiRh_{0.1}$ catalyst.

Table S 7: Analysis of the composition in selected regions of the 5 wt.% Ni_3Fe/Al_2O_3 catalyst using STEM-EDX. Reproduced from Mutz *et al.*[211] Copyright © 2018 Published by Elsevier B.V.

EDX	Ni [at.%]	Fe [at.%]	Ni/Fe
Region 1	66.6	33.4	2.0
Region 2	70.0	30.0	2.3
Region 3	65.5	34.5	1.9
Region 4	74.6	25.4	2.9
Region 5	81.7	18.3	4.5
Region 6	91.1	8.9	10.2

Table S 8: Analysis of the composition in selected regions of the 3.4 wt.% $NiRh_{0.1}/Al_2O_3$ catalyst measured using STEM-EDX. Reproduced from Mutz *et al.*[211] Copyright © 2018 Published by Elsevier B.V.

EDX scans	Ni [at.%]	Rh [at.%]	Ni/Rh
Region 1	97.2	2.8	34.7
Region 2	93.6	6.4	14.6
Region 3	92.9	7.1	13.1
Region 4	92.5	7.5	12.3
Region 5	87.0	13.0	7.5
Region 6	96.8	3.2	30.2

Figure S 22 shows typical STEM-EELS spectrum imaging of the Ni_3Fe catalyst. The results show that the metal nanoparticles are bimetallic NiFe particles but also monometallic Ni particles were found.

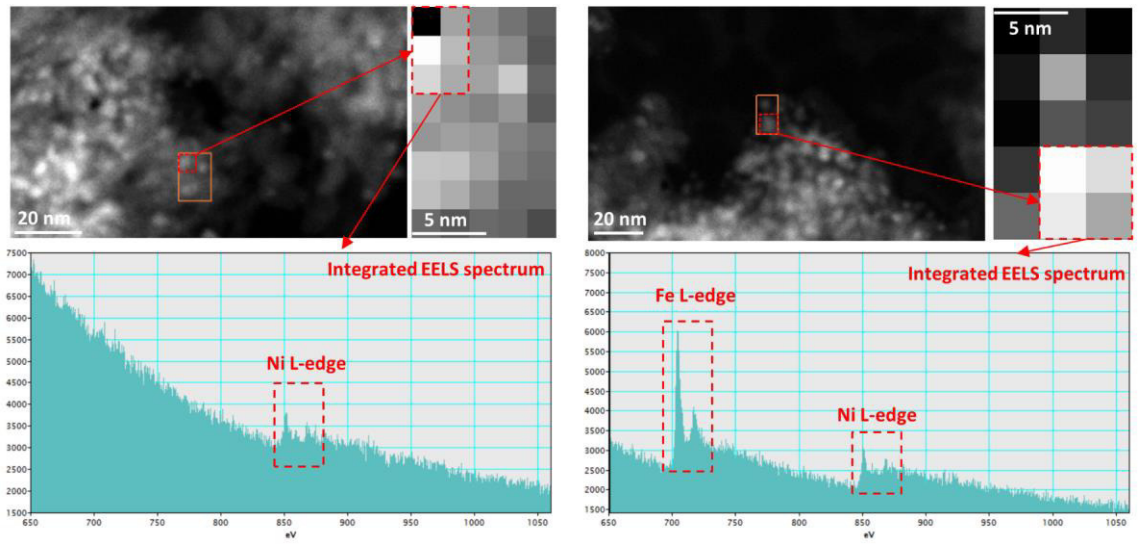

Figure S 22: Two typical STEM-EELS spectrum imaging in the area marked with box of the 5 wt.% Ni_3Fe/Al_2O_3 catalyst. Reproduced from Mutz *et al.*[211] Copyright © 2018 Published by Elsevier B.V.

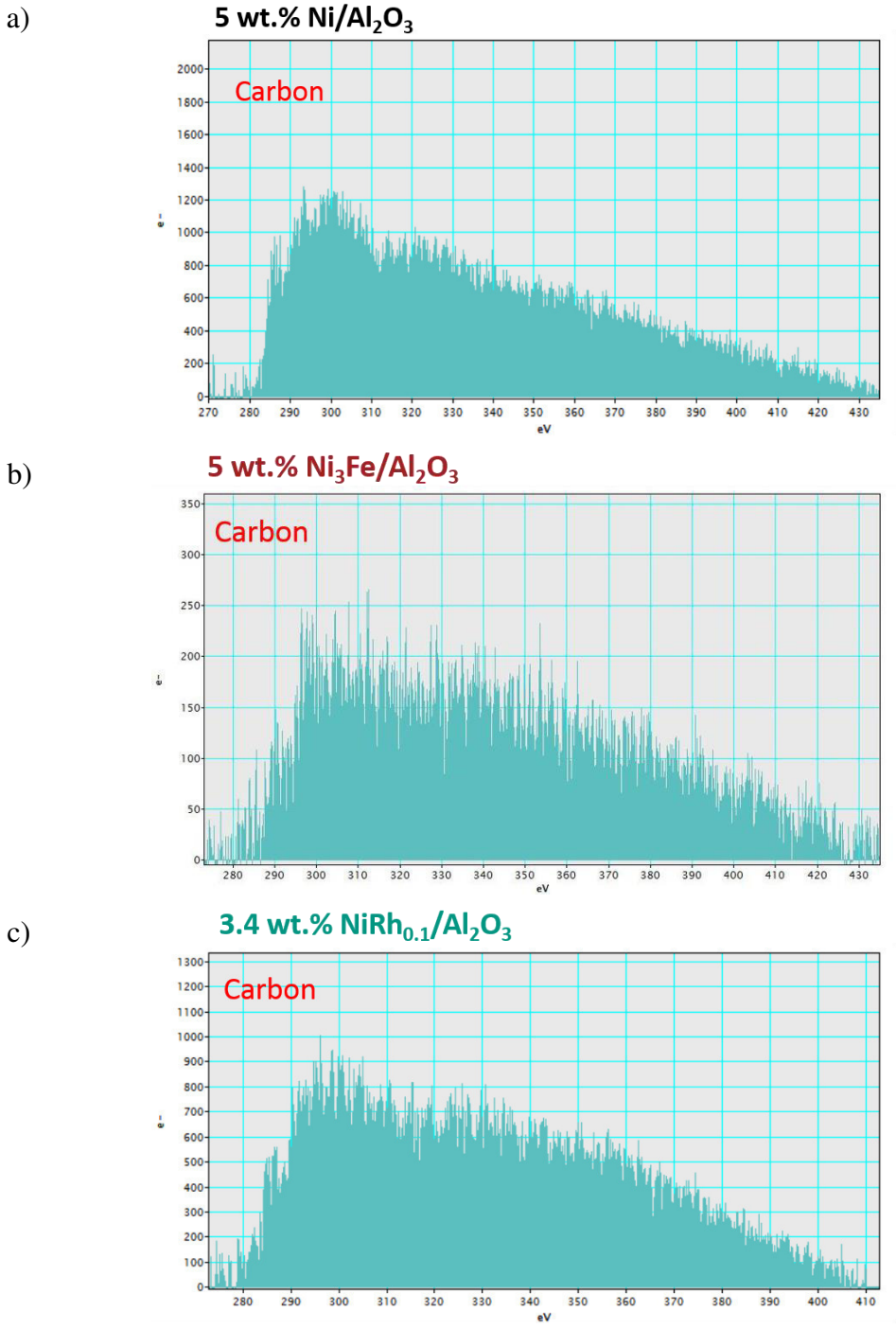

Figure S 23: Electron energy loss spectroscopy (EELS) of the spent catalysts a) 5 wt.% Ni/Al_2O_3, b)5 wt.% Ni_3Fe/Al_2O_3 and c) 3.4 wt.% $NiRh_{0.1}/Al_2O_3$ after Phase E taken from the lab-scale reactor. Reproduced from Mutz *et al.*[211] Copyright © 2018 Published by Elsevier B.V.

The results obtained from EELS (Figure S 23) show that carbon was present on the catalyst, which fits to the results from *operando* Raman spectroscopy. The C K-edge is

most prominent for the Ni catalyst and less for the Ni_3Fe and $NiRh_{0.1}$ catalysts. Figure S 23 c) is the most intense EELS signal found for the $NiRh_{0.1}$ catalyst, other areas show almost no carbon.

Raman spectroscopy

This section contains additional and supporting data from *ex situ* and *operando* Raman spectroscopy. Figure S 24 shows the Raman spectra of the catalysts in CO_2 atmosphere. No Raman bands related to carbon species (Table S 9) could be detected. The band at 1400 cm^{-1} in the Raman spectrum of the 5 wt.% Ni_3Fe/Al_2O_3 catalyst is ascribed to the overtone of the band referred to $FeAl_2O_4$ spinel at 700 cm^{-1}.[284,285]

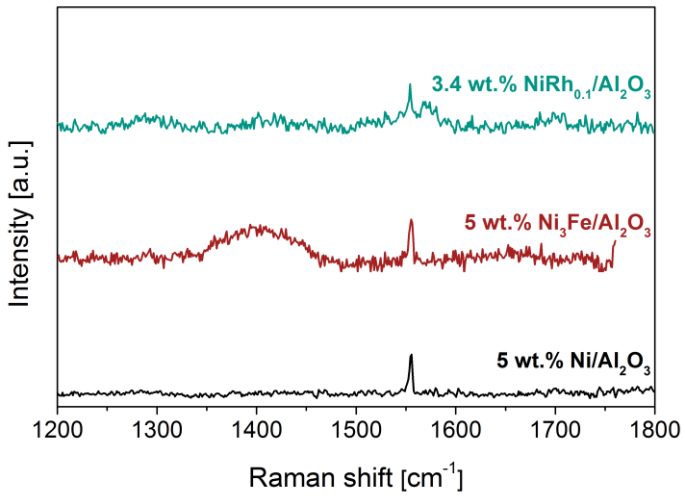

Figure S 24: Raman spectra of the 5 wt.% Ni/Al_2O_3, 5 wt.% Ni_3Fe/Al_2O_3 and 3.4 wt.% $NiRh_{0.1}/Al_2O_3$ catalysts in CO_2 atmosphere after H_2 dropout during the methanation of CO_2. Reproduced from Mutz *et al.*[211] Copyright © 2018 Published by Elsevier B.V.

Raman bands corresponding to carbonaceous species according to Sadezky *et al.*[254] are listed in Table S 9.

Table S 9: Summary of carbon related Raman bands and the corresponding interpretation. Reproduced from Mutz *et al.*[211] Copyright © 2018 Published by Elsevier B.V.

Band	Position (Ref[254]) [cm^{-1}]	Assignment
G	1571-1598	Ideal graphitic lattice
D1	1343-1358	Disordered graphitic lattice; graphitic lattice vibration mode with A_{1g} symmetry
D2	1599-1624	Graphitic lattice mode with E_{2g} symmetry
D3	1489-1530	Amorphous carbon fraction of soot (*e.g.* organic molecules, fragments or functional groups)
D4	1127-1208	Disordered graphitic lattice

D2 and D4 were excluded from fitting since preliminary tests suggested, that their contribution is just random and not a result of actual coke formation or their change is due to changes in neighboring curves. The curve parameters used for the evaluation of the Raman bands are listed in Table S 10:

Table S 10: Fitting parameters applied for the deconvolution of the Raman bands. Reproduced from Mutz *et al.*[211] Copyright © 2018 Published by Elsevier B.V.

Band	Position [cm^{-1}]	FWHM [cm^{-1}]	Shape
G	1565-1585	20-200	Lorentzian
D1	1310-1360	20-300	Lorentzian
D3	1480-1550	40-600	Gaussian
P1	1554-1557	1-8	Lorentzian
P2	1690-1730	10-200	Gaussian

P1 represents the band of molecular oxygen due to air between the fiber optic and the spectroscopic fixed-bed microreactor. The peak was also reported in the study of

Sattler *et al.*[200]. The band P2 cannot be assigned to any carbon band and may be an artefact due to baseline subtraction.

The curve fitting using the parameters in Table S 10 is visualized in Figure S 25, exemplary for the 5 wt.% Ni/Al_2O_3 catalyst after Phase B (CH_4 decomposition).

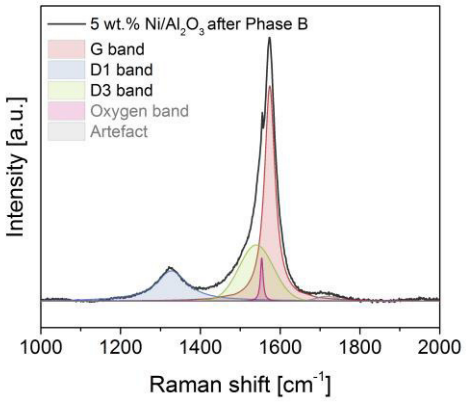

Figure S 25: Assignment of Raman bands exemplary for the Raman spectrum of the 5 wt.% Ni/Al_2O_3 catalyst (similar to Figure 51) in Phase B (CH_4 decomposition). Reproduced from Mutz *et al.*[211]

Figure S 26 shows further Raman data recorded during a) Phase C (coked catalysts in CO_2/H_2 atmosphere for the methanation reaction) and b) Phase E (catalysts after reactivation in H_2 in CO_2/H_2 atmosphere for the methanation reaction).

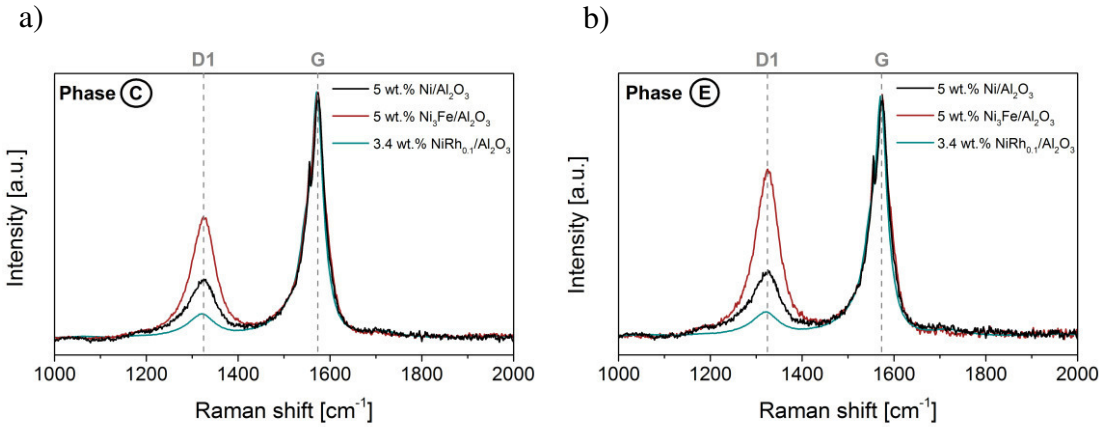

Figure S 26: *Operando* Raman spectra normalized on the G band intensity and the corresponding D1/G ratio; a) the coked catalysts during methanation in Phase C, and b) the reactivated catalysts during methanation in Phase E. Reproduced from Mutz *et al.*[211] Copyright © 2018 Published by Elsevier B.V.

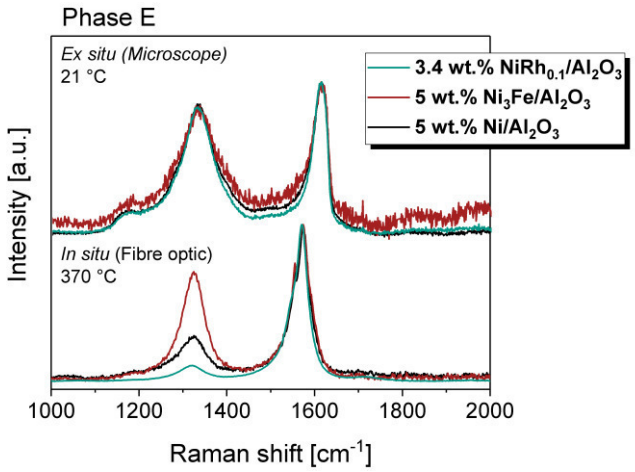

Figure S 27: Raman spectra of carbon deposits of the three catalysts 5 wt.% Ni/Al_2O_3, 5 wt.% Ni_3Fe/Al_2O_3 and 3.4 wt.% $NiRh_{0.1}/Al_2O_3$ after CH_4 treatment and H_2 reduction (Phase E). Reproduced from Mutz *et al.*[211] Copyright © 2018 Published by Elsevier B.V.

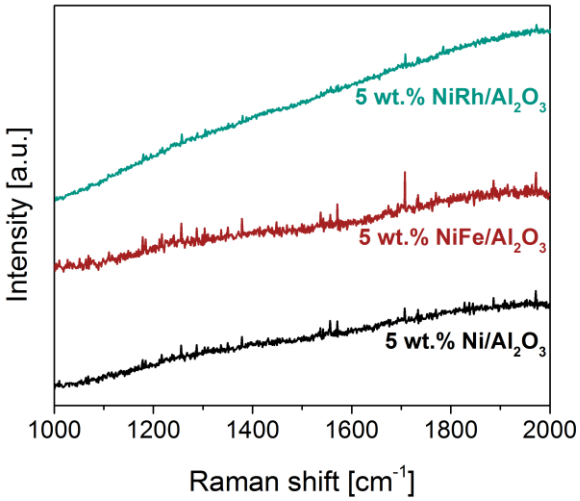

Figure S 28: Raman spectra of the 5 wt.% Ni/Al_2O_3, 5 wt.% Ni_3Fe/Al_2O_3 and 3.4 wt.% $NiRh_{0.1}/Al_2O_3$ after TPO-TG experiments recorded *ex situ*. The parameters were similar as for the other experiments (532 nm Laser with 100 mW, 0.1 % Laser power, 5 min acquisition time, 3 acquisitions per point and 7 different points per spectrum). Here, no baseline subtraction was performed. Reproduced from Mutz *et al.*[211] Copyright © 2018 Published by Elsevier B.V.

The absence of carbon bands in Figure S 28 supports the successful oxidation of all carbon deposits during TPO-TG.

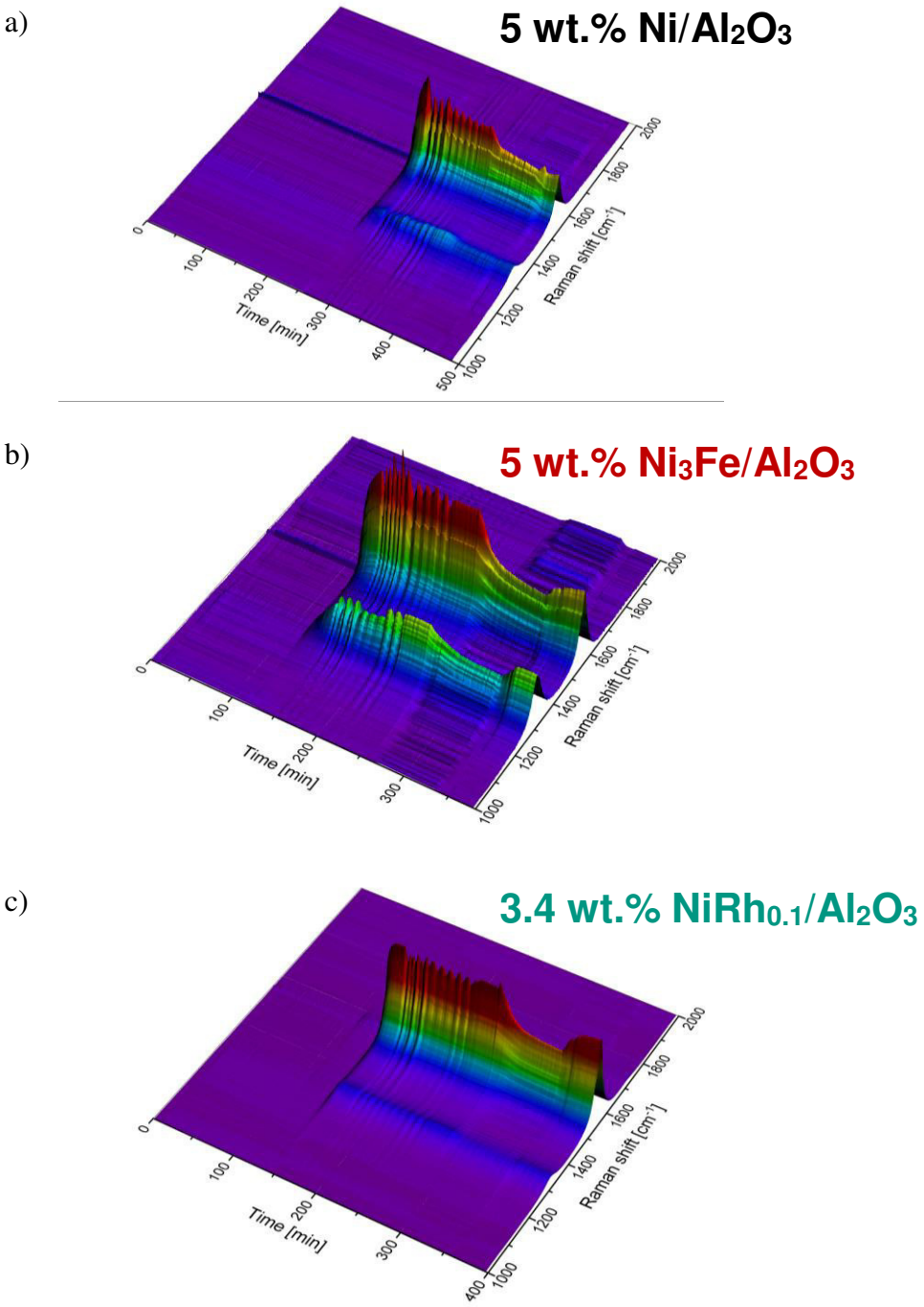

Figure S 29: 3D plots of the entire *operando* Raman spectroscopy experiments for a) 5 wt.% Ni/Al_2O_3, b) 5 wt.% Ni_3Fe/Al_2O_3 and c) 3.4 wt.% $NiRh_{0.1}/Al_2O_3$. Reproduced from Mutz *et al.*[211] Copyright © 2018 Published by Elsevier B.V.

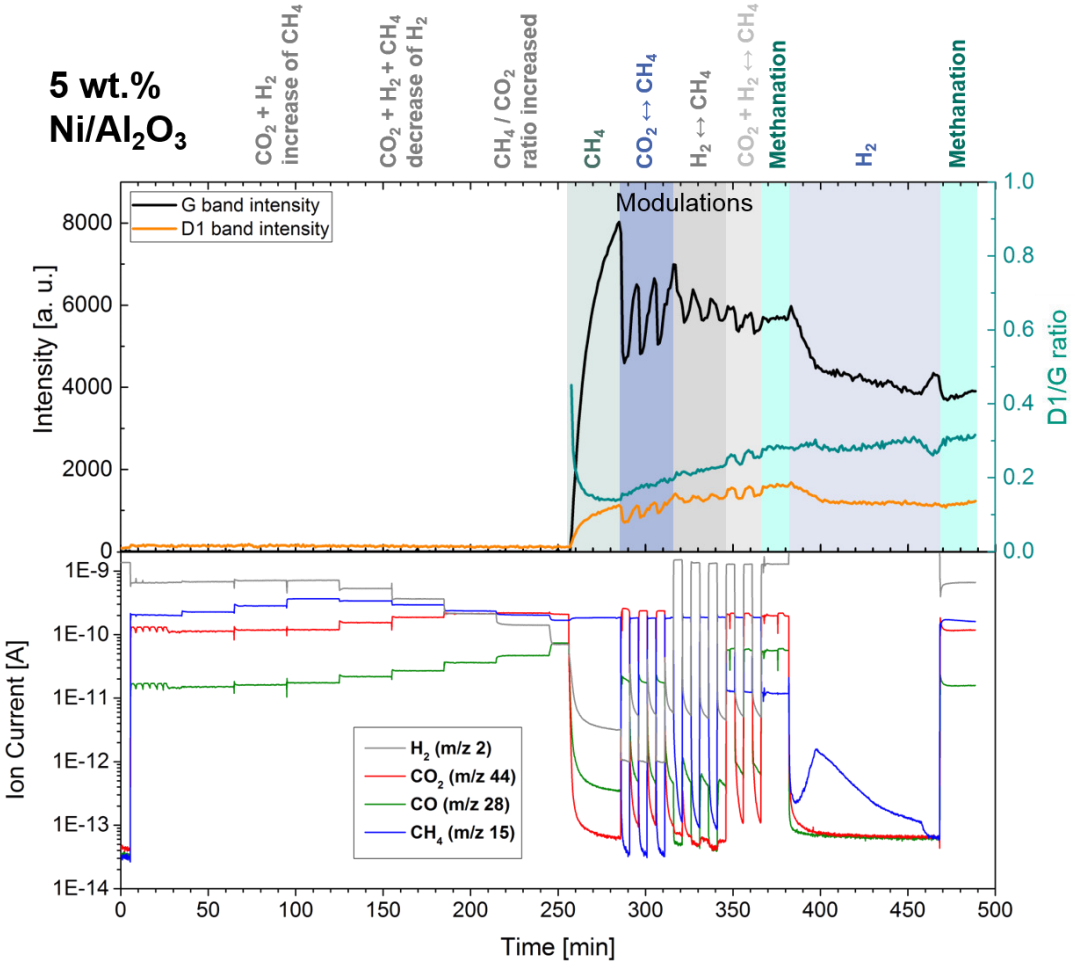

Figure S 30: Entire *operando* Raman spectroscopy experiment for the 5 wt.% Ni/Al_2O_3 catalyst (370 °C, 1 bar, 6000 mL_{CO2} g_{cat}^{-1} h^{-1}). The upper part of the figure shows the G (black) and D1 (orange) band intensities from Raman spectroscopy, as well as the D1/G ratio (green). The lower part of the figure shows the corresponding mass spectrometry data of H_2 (grey), CO_2 (red), CO (green) and CH_4 (blue). Reproduced from Mutz *et al.*[211] Copyright © 2018 Published by Elsevier B.V.

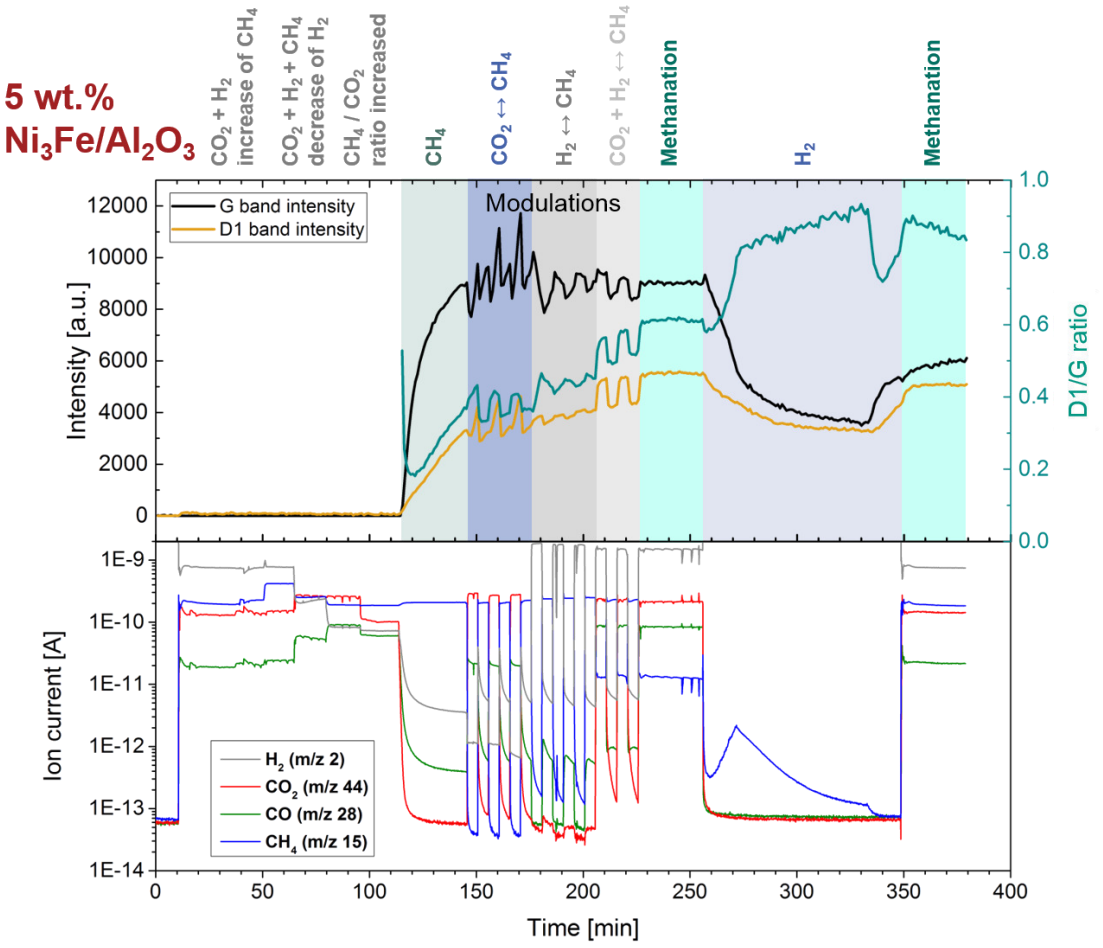

Figure S 31: Entire *operando* Raman spectroscopy experiment for the 5 wt.% Ni_3Fe/Al_2O_3 catalyst (370 °C, 1 bar, 6000 mL_{CO2} g_{cat}^{-1} h^{-1}). The upper part of the figure shows the G (black) and D1 (orange) band intensities from Raman spectroscopy, as well as the D1/G ratio (green). The lower part of the figure shows the corresponding mass spectrometry data of H_2 (grey), CO_2 (red), CO (green) and CH_4 (blue). Reproduced from Mutz *et al.*[211] Copyright © 2018 Published by Elsevier B.V.

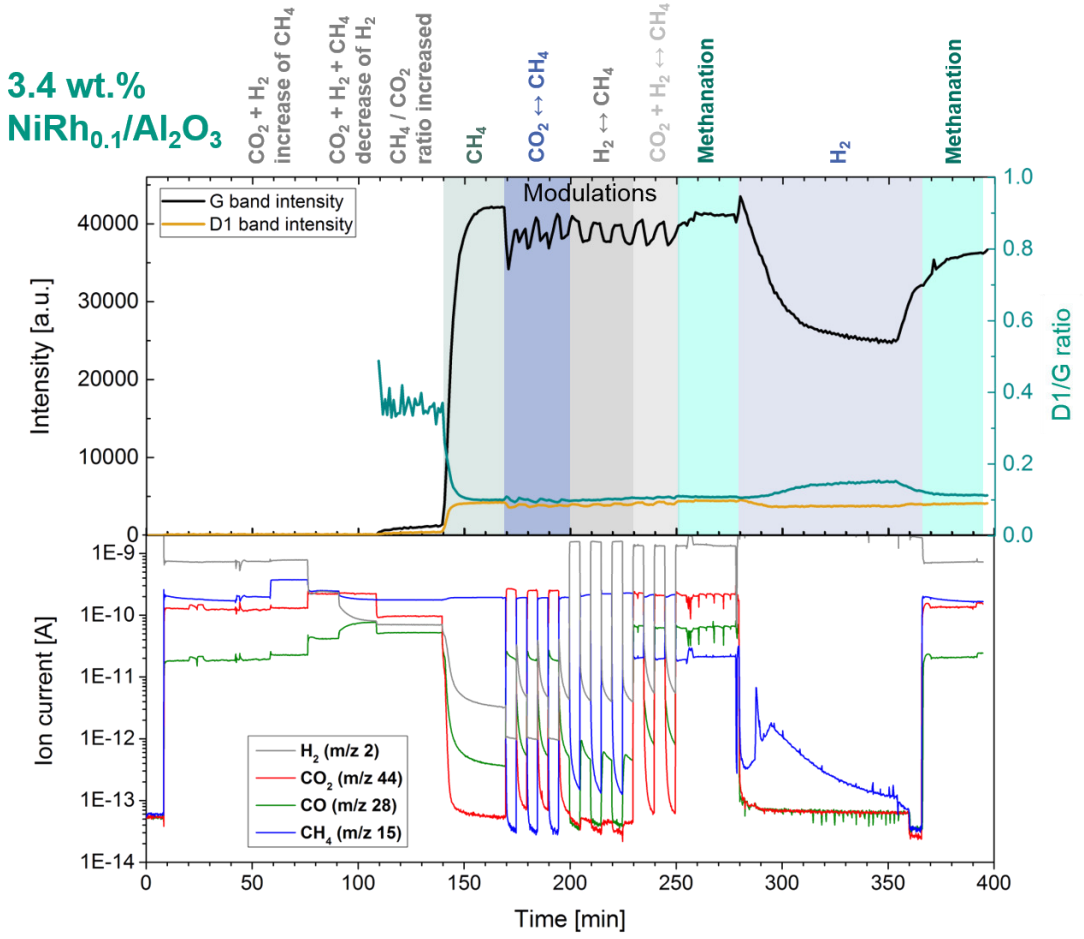

Figure S 32: Entire *operando* Raman spectroscopy experiment for the 3.4 wt.% $NiRh_{0.1}/Al_2O_3$ catalyst (370 °C, 1 bar, 6000 mL_{CO2} g_{cat}^{-1} h^{-1}). The upper part of the figure shows the G (black) and D1 (orange) band intensities from Raman spectroscopy, as well as the D1/G ratio (green). The lower part of the figure shows the corresponding mass spectrometry data of H_2 (grey), CO_2 (red), CO (green) and CH_4 (blue). Reproduced from Mutz *et al.*[211] Copyright © 2018 Published by Elsevier B.V.

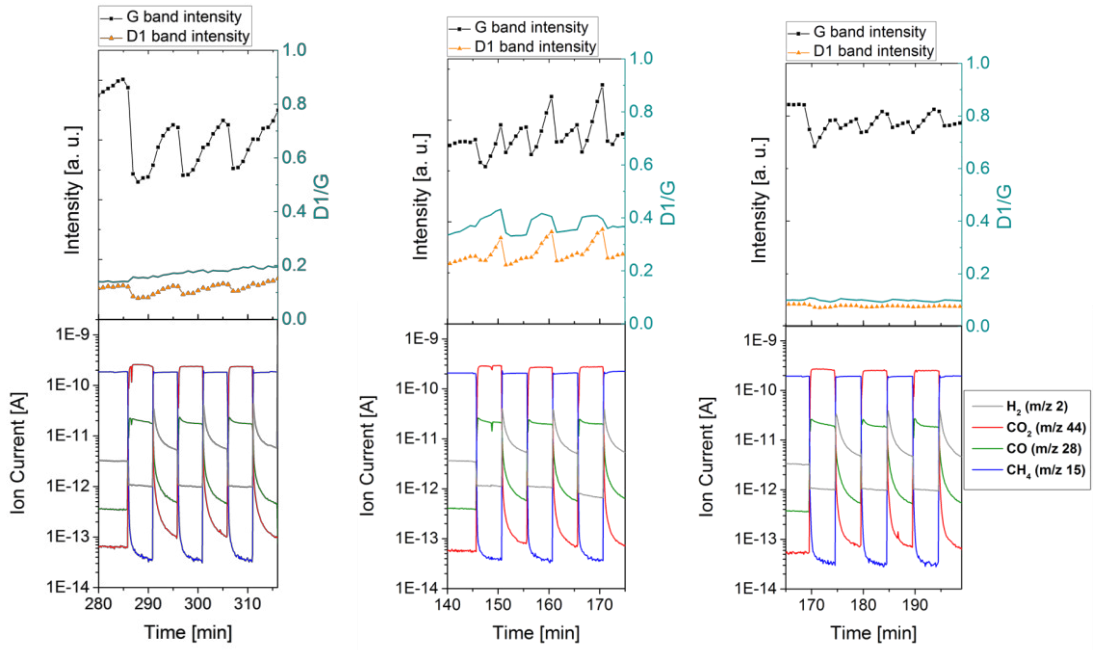

Figure S 33: Intensity of the G and D1 band in *operando* Raman spectroscopy correlated with the MS signals during 300 s modulation of 4 % CH_4 – 5 % CO_2. The upper part of the figures show the G (black) and D1 (orange) band intensities from Raman spectroscopy, as well as the D1/G ratio (green). The lower part of the figures show the corresponding mass spectrometry data of H_2 (grey), CO_2 (red), CO (green) and CH_4 (blue). Reproduced from Mutz *et al.*[211] Copyright © 2018 Published by Elsevier B.V.

Various gas modulations were conducted to study the behavior and reactivity of the carbon deposits on the catalyst systems. First, 300 s modulation of 5 % CO_2 ↔ 4 % CH_4 were performed on the carbon poisoned catalyst. A zoom of this period is shown in Figure S 33. The intensity of the Raman bands G and D1 decreased in CO_2 for all catalysts according to the Boudouard equilibrium (reaction (5) in section 1.3.4.4) indicated by the CO peak from MS in the beginning of the CO_2 period. Furthermore, oxidation of the carbon species by traces of O_2, not resolved by MS might be possible. Easily accessible carbon species were removed in CO_2 immediately after switching the gas atmosphere. This effect is most distinct on the monometallic Ni catalyst, where both Raman bands deceased significantly and simultaneously (no changes in the D1/G ratio as result of the

switching atmospheres). Carbon poisoned Ni_3Fe catalyst exposed to CO_2 first showed a reduction of the Raman band intensities immediately after the switch of the gas atmospheres, but after 3 min the band intensities increased again. The same behavior was observed then during the following CH_4 period: First, the Raman band intensities decreased and then increased again. An increase of the total band intensities during the CO_2 periods was observed over cycles. The amount of graphitic carbon with defects, indicated by the D1/G ratio, increased during the CO_2 period, and decreased again in CH_4. Based on these observations, different carbon species seemed to form on the Ni_3Fe catalyst. First, the common surface carbon was formed by the decomposition of CH_4, as observed for the Ni catalyst. During the CO_2 period, carbon species were oxidized, forming CO. After 3 min, most of the easily accessible carbon was removed, but still CO is formed from the oxidation of Fe to FeO_x by CO_2[158], which then interacted with carbon-free metal sites forming disordered carbon from CO disproportion. A further contribution to the carbon formation might stem from the higher ability of CO dissociation of Fe species compared to Ni.[100,101] Similar observations regarding the G1 band were made for the $NiRh_{0.1}$ catalyst but less pronounced.

The modulation between CH_4 and CO_2 atmospheres showed dynamic changes of the deposited carbon species on all catalysts. Regarding the $CO_2 \leftrightarrow CH_4$ modulation experiments entirely, the effect of carbon removal in CO_2 declined over cycles (or the carbon formation from CH_4 dominated the effect of carbon removal from CO_2) which was indicated by the net increase of the Raman bands for each cycle for all catalysts.

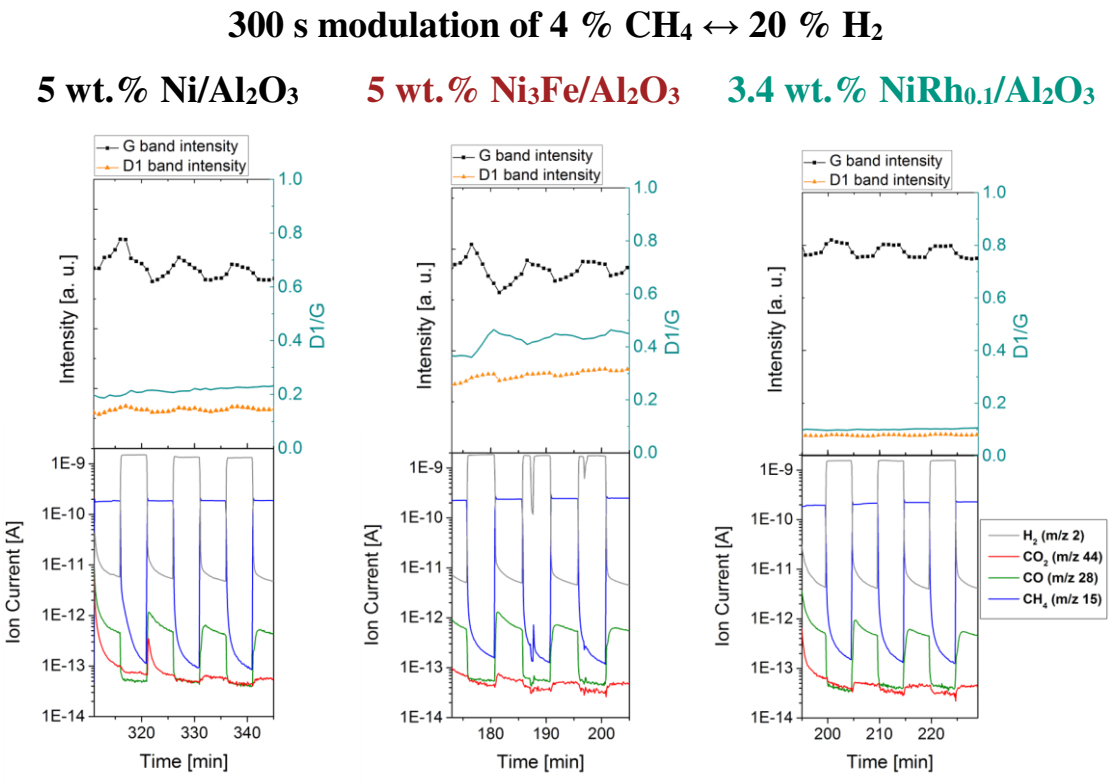

Figure S 34: Intensity of the G and D1 band in *operando* Raman spectroscopy correlated with the MS signals during the 300 s modulation of 4 % CH_4 ↔ 20 % H_2 (370 °C, 1 bar). The upper part of the figures show the G (black) and D1 (orange) band intensities from Raman spectroscopy, as well as the D1/G ratio (green). The lower part of the figures show the corresponding mass spectrometry data of H_2 (grey), CO_2 (red), CO (green) and CH_4 (blue). Reproduced from Mutz *et al.*[211] Copyright © 2018 Published by Elsevier B.V.

The influence of H_2 on the carbon species of the poisoned catalysts was studied during 300 s modulation of 20 % H_2 ↔ 4 % CH_4. The carbon species were reduced in H_2 on all catalysts forming CH_4, indicated by a higher and more slowly declining MS signal of CH_4 compared to the previous CO_2 periods (Figure S 34), where no CH_4 is formed. The intensity of the Raman bands decreased more slowly and to a lower extent during H_2 exposure of the poisoned catalysts compared to the periods with CO_2. Oxidation of the carbon species in CO_2 atmosphere was more efficient than the reduction in H_2. The metal surface was covered with carbon resulting in a low amount of free active sites to dissociate molecular H_2 to hydrogenate surface carbon stepwise to CH_4.

It has to be noted that the changes in the band intensities were small, especially during the 2nd and 3rd cycle. If also temperature effects are taken into account, these small changes in Raman band intensities cannot be ascribed to carbon reduction/formation exclusively.

Sattler *et al.*[200] observed an increased D1/G ratio on carbon poisoned Pt-based catalysts in H_2 atmosphere. This effect can be observed for the Ni_3Fe catalyst during the first H_2 atmosphere, indicating a higher amount of defects in the graphitic structure, which can be further interpreted as decreased graphite crystallites. H_2 did not influence the D1/G ratio of the Raman bands for the Ni and $NiRh_{0.1}$ catalysts.

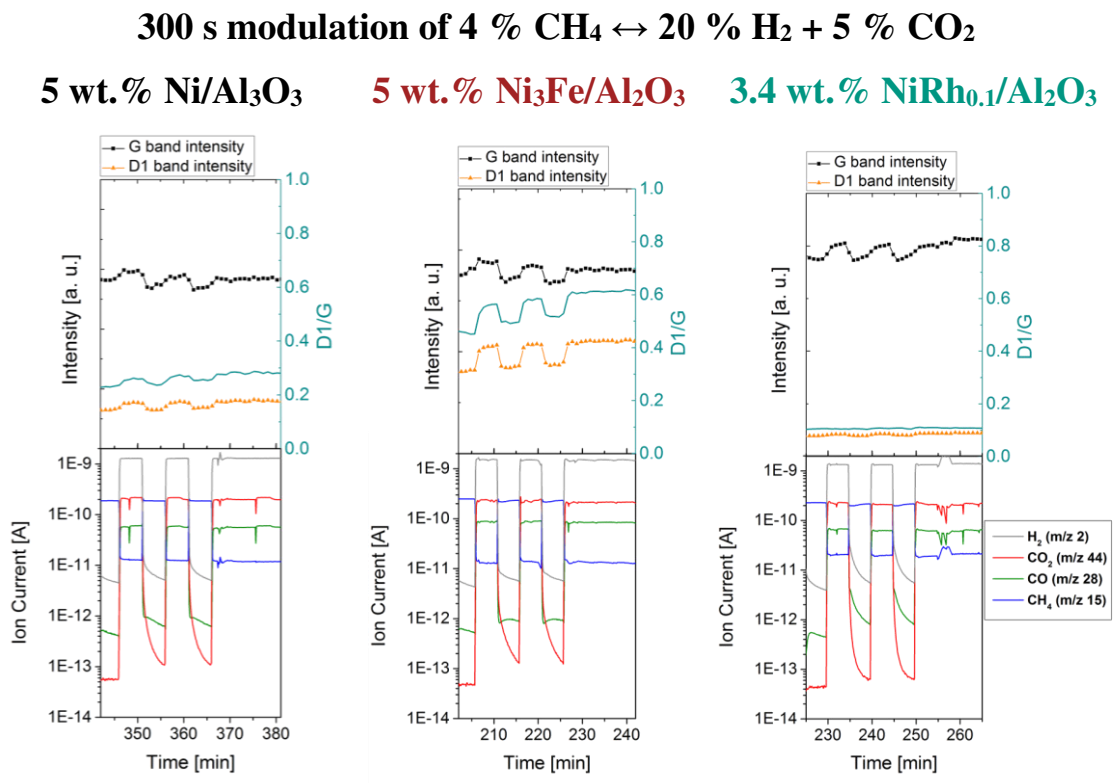

Figure S 35: Intensity of the G and D1 band in operando Raman spectroscopy correlated with the MS signals during the 300 s modulation of 4 % CH_4 ↔ 20 % H_2 + 5 % CO_2 (370 °C, 1 bar). The upper part of the figures show the G (black) and D1 (orange) band intensities from Raman spectroscopy, as well as the D1/G ratio (green). The lower part of the figures show the corresponding mass spectrometry data of H_2 (grey), CO_2 (red), CO (green) and CH_4 (blue). Reproduced from Mutz *et al.*[211] Copyright © 2018 Published by Elsevier B.V.

Methanation atmosphere (H_2/CO_2 = 4) showed marginal changes of the Raman band intensities of the carbon species. 15-20 min of steady state methanation showed no changes of the band intensities.

Overall, the D1/G ratio increased during the modulations for Ni and especially Ni_3Fe, which means that more and more defects in the ideal graphitic lattice are formed over time. The ratio remained constant for $NiRh_{0.1}$ due to the dominant G band.

Catalytic performance

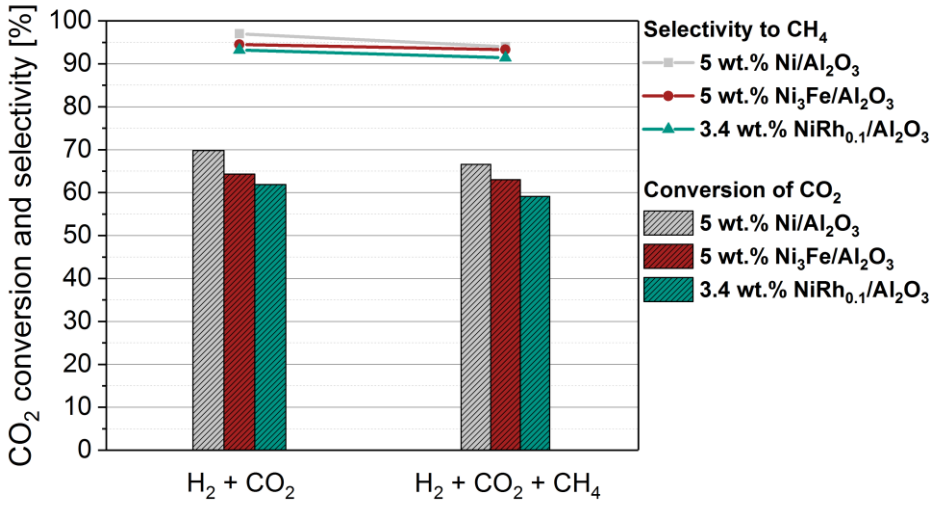

Figure S 36: Conversion of CO_2 and selectivity towards CH_4 of the Ni, Ni_3Fe and $NiRh_{0.1}$ catalysts during methanation of CO_2 using model gas composition ("Phase A") and methanation including 4 % CH_4 in the feed (400 °C. 1 bar, 6000 $mL_{CO2}\ g_{cat}^{-1}\ h^{-1}$). Reproduced from Mutz *et al.*[211] Copyright © 2018 Published by Elsevier B.V.

Figure S 36 shows the results for the conversion of CO_2 and the selectivity towards CH_4 for the Ni, Ni_3Fe and $NiRh_{0.1}$ catalysts during methanation of CO_2 using model gas composition (5% CO_2 + 20 % H_2 / N_2, (Phase A in Figure 4 of the manuscript)) and the methanation of CO_2 containing CH_4 in the feed (5 % CO_2 + 20 % H_2 + 4 % CH_4 / N_2). The catalysts showed similar activity. The decline might be negligible and within the error.

Additional data concerning the NiFe catalyst

Pressure screening

Pressure screenings during the methanation of CO_2 were performed using the 5 wt.% Ni/Al_2O_3 catalyst from section 8.3. The catalytic performance was monitored in the temperature range of 200- 450 °C at pressures between 1 – 20 bar in 5 bar steps (Figure S 37).

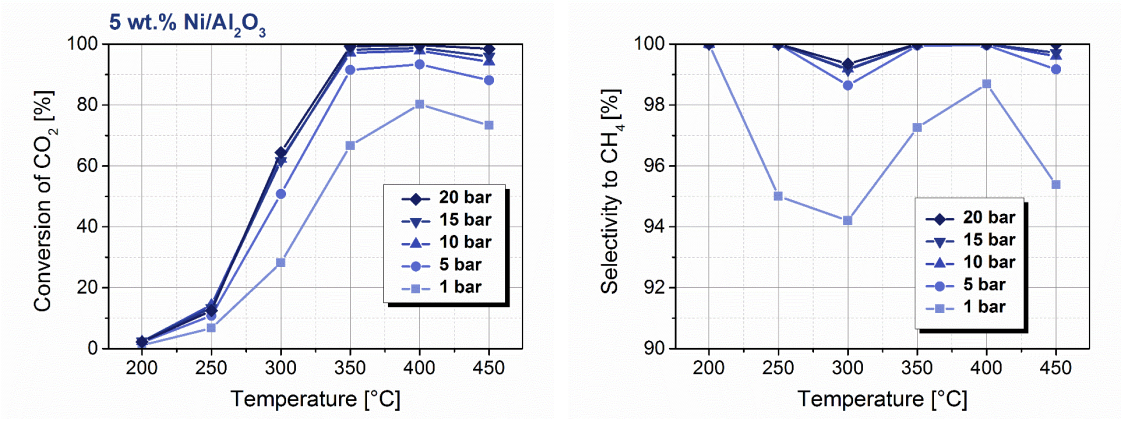

Figure S 37: a) Conversion of CO_2 and b) selectivity to CH_4 during the pressure screening between 1 – 20 bar using the 5 wt.% Ni/Al_2O_3 catalyst (WHSV = 3000 ml_{CO2} g_{cat}^{-1} h^{-1}, GHSV = 6700 h^{-1}).

Curve fitting parameters in Raman spectroscopy

Table S 11: List of curve fitting parameters for the Raman spectra in Figure 61. Reproduced from Mutz *et al.*[212]

Sample	Position [cm^{-1}]	Area	FWHM [cm^{-1}]	% Gaussian
Bulk α-Fe_2O_3	221.6	304436	13.2	0.0
	243.5	9471	7.7	100.0
	270.7	71817	25.6	100.0
	289.5	292891	18.1	57.2
	403.7	101240	23.7	78.3
	492.1	34402	28.6	48.4
	604.4	112998	29.5	0.0
	803.7	42637	71.6	89.9
	1059.1	67342	75.5	81.2
5 wt.% Fe/Al_2O_3	227.7	54253	13.0	100.0
	247.3	29992	19.8	100.0
	297.6	125780	19.5	48.1
	340.6	229803	93.0	100.0
	415.0	155124	23.9	0.0
	509.5	13460	19.3	100.0
	617.1	14364	14.8	100.0
	699.9	1427580	111.7	100.0
	750.2	855433	144.0	100.0
	1081.2	132707	83.5	100.0
17 wt.% Ni_3Fe/Al_2O_3	368.2	159898	126.4	100.0
	562.9	1124830	167.2	100.0
	695.5	562358	92.6	89.8
	753.6	953062	137.8	100.0
	890.6	60264	83.1	100.0
17 wt.% Ni/Al_2O_3	554.1	78797	84.5	55.8
	481.1	69010	201.5	100.0

Table S 12: List of curve fitting parameters for the Raman spectra of the spent catalysts after long-term performance tests. Reproduced from Mutz *et al.*[212] Copyright © 2017, American Chemical Society.

Spent sample	Position [cm^{-1}]	Area	FWHM [cm^{-1}]	Shape
Commercial catalyst	1380	39989	71	Lorentzian
	1598	85760	64	Lorentzian
17 wt.% Ni_3Fe/Al_2O_3	1384	29720	53	Lorentzian
	1596	168618	69	Lorentzian

Electron microscopy of the spent catalyst

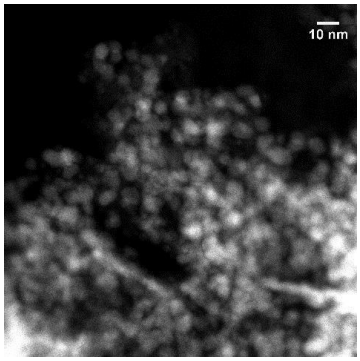

Figure S 38: STEM image of the 17 wt.% Ni_3Fe/Al_2O_3 catalyst after the long-term performance test and a reduction treatment (50 % H_2/N_2, 500 °C, 2 h). Reproduced from Mutz *et al.*[212] Copyright © 2017, American Chemical Society.

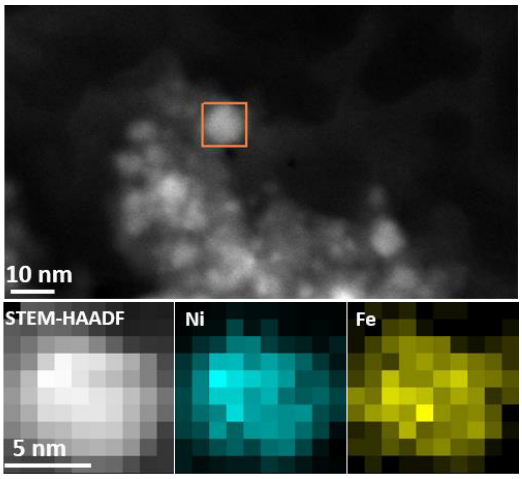

Figure S 39: STEM image and the corresponding elemental maps obtained from STEM-EDX spectrum imaging on an individual particle marked with the box taken on the 17 wt.% Ni_3Fe/Al_2O_3 catalyst after the long-term performance test and a reduction treatment (50 % H_2/N_2, 500 °C, 2 h). Reproduced from Mutz *et al.*[212] Copyright © 2017, American Chemical Society.

Table S 13: Quantified elemental analysis of the Ni_3Fe nanoparticles on the spent catalyst after the long-term performance experiment measured at different regions by STEM-EDX. Reproduced from Mutz *et al.*[212] Copyright © 2017, American Chemical Society.

	Ni [at.%]	Fe [at.%]	Ni/Fe ratio
Region no. 1	79.7	20.3	3.9
Region no. 2	79.3	20.7	3.8
Region no. 3	76.3	23.7	3.2
Region no. 4	80.3	19.7	4.1
Region no. 5	75.7	24.3	3.1

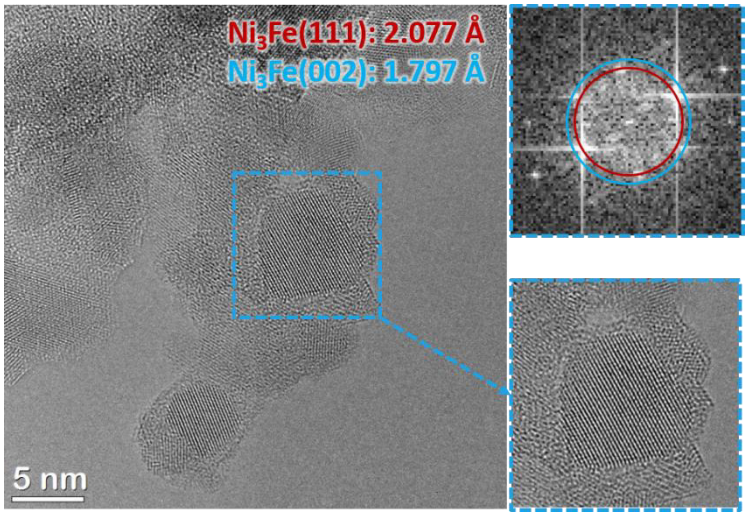

Figure S 40: HRTEM image and structure analysis by FFT of the spent 17 wt.% Ni_3Fe/Al_2O_3 catalyst after long-term performance test and reductive treatment (50 % H_2/N_2, 500 °C, 2 h). Reproduced from Mutz *et al.*[212] Copyright © 2017, American Chemical Society.

Acknowledgements

In the following I would like to thank the people who have supported me during my PhD work.

First of all, I am obliged to Prof. Dr. Jan-Dierk Grunwaldt who offered me the opportunity to conduct my PhD under his supervision. Thank you for providing the interesting topic, for the scientific discussions, the freedom of research and your confidence in me.

Furthermore, I would like to thank Priv.-Doz. Dr. Wolfgang Kleist for help in problem-solving, scientific discussions and support. I learned a lot about scientific writing and presenting results.

I also wish to thank Prof. Dr. Felix Studt for agreeing to be the co-referee of this thesis.

I am very grateful to the Helmholtz Association and the Research School "Energy-Related Catalysis" for the financial support, the training courses and the scholarship. Within this program Prof. Dr. Olaf Deutschmann, Prof. Dr.-Ing. Jörg Sauer, Dr. Steffen Tischer and Dr. Claudia Antinori as well as each member of the group are gratefully acknowledged.

I am much obliged to Michael Belimov (IMVT), Wu Wang (INT), Paul Sprenger, Andreas Gänzler and Ass. Prof. Hudson W.P. Carvalho for the huge effort they put into our cooperations. In this context, I also would like to thank Dr. Oliver Müller (former Uni Wuppertal), Dr. Henning Lichtenberg, Dr. Dmitry Doronkin, and all the others who joined the beamtimes for support. The ANKA synchrotron radiation source and Dr. Stefan Mangold, the Swiss lightsource (SLS) and Dr. Maarten Nachtegaal are acknowledged for providing beamtime and technical support.

I would like to thank Dr. Martin Schubert, Egbert Kehrwecker and Patrick Düppuis (Swagelok) for their help during the planning of the laboratory setup. Furthermore, I am grateful to Dr. Konstantin Hengst, Dr. Karin Walter and Jan Pesek for discussion and problem-solving during the construction process.

Thanks especially to Matthias Stehle, Marc-André Serrer and Kathrin Hackbarth who conducted their Bachelor, Master or other student research projects under my supervision. I am grateful for their input concerning research as well as leadership skills.

I would like to thank Dr. Di Wang (INT), Dr. Sina Baier and Dr. Sabrina Müller for TEM measurements and discussions, Dr. Thomas Bergfeld (IAM-AMP, chemical analytics) and Hermann Köhler for ICP-OES analysis, Angela Beilmann for N_2 physisorption, H_2-TPR and TPO-TG.

Furthermore, thanks go to Dr. Meike A. Gotthardt and Dr. Kai F. Kalz for revision of my thesis.

The BMBF projects “MatAkt” (05K10VKB) and “ZeitKatMat” (05K13VK13) are acknowledged for providing infrastructure for the *in situ* studies. I am also grateful to DFG and KIT for financing the Raman spectrometer (INST 121384/73-1) as well as the instrument for thermogravimetric analysis (INST 121384/70-1).

Last but not least, thanks to the all colleagues of AKG and AKD for the pleasant working atmosphere.

List of abbreviations

Abbreviation	Name
µGC	Micro gas chromatograph
a.u.	Arbitrary unit
ANKA	Angströmquelle Karlsruhe (synchrotron KIT)
BET	Brunauer-Emmet-Teller
BPR	Back pressure regulator
CCS	CO_2 capture and storage
CV	Check valve
DFT	Density functional theory
DRIFTS	Diffuse reflectance infrared Fourier transform spectroscopy
EDX	Energy dispersive X-ray spectroscopy
EXAFS	Extended X-ray absorption fine structure
FFT	Fast Fourier transformation
FT	Fourier transform
FWHM	Full width at half maximum
GHSV	Gas hourly space velocity
HAADF	High angle annular dark-field
HRTEM	High resolution transmission electron microscopy
ICP-OES	Optical emission spectroscopy with inductively coupled plasma
IKFT	Institute of Catalysis Research and Technology
IL-TEM	Identical location transmission electron microscopy
IMVT	Institute for Micro Process Engineering
INT	Institute of Nanotechnology
IR	Infrared
ITCP	Institute for Chemical Technology and Polymer Chemistry
IWES	Institute for Wind Energy and Energy System Technology

KIT	Karlsruhe Institute of Technology
LCA	Linear combination analysis
MFC	Mass flow controller
MS	Mass spectrometer
P&ID	Piping and instrumentation diagram
PCA	Principal component analysis
PR	Pressure reducer
PSI	Paul Scherrer Institute
PtG	Power-to-gas
QEXAFS	Quick extended X-ray absorption fine structure
RE	Renewable energy
RV	Relief valve
RWGS	Reverse water gas shift
SLS	Swiss Light Source (synchrotron Villigen, PSI)
SNG	Synthetic / substitute natural gas
STEM	Scanning transmission electron microscopy
TCD	Thermal conductivity detector
TEM	Transmission electron microscopy
TOF	Turnover frequency
TOS	Time on stream
TPD	Temperature-programmed desorption
TPO	Temperature-programmed oxidation
TPR	Temperature-programmed reduction
WHSV	Weight hourly space velocity
wt.%	Weight percent
XANES	X-ray absorption near edge structure
XAS	X-ray absorption spectroscopy
XRD	X-ray diffraction
ZSW	Centre for Solar Energy and Hydrogen Research Baden-Württemberg

List of publications

[1] B. Mutz, H.W.P. Carvalho, S. Mangold, W. Kleist, J.-D. Grunwaldt, "Methanation of CO_2: Structural response of a Ni-based catalyst under fluctuating reaction conditions unraveled by *operando* spectroscopy", *J. Catal.* **2015**, *327*, 48-53.

The results from this publication are presented in chapter 5.

[2] B. Mutz, H.W.P. Carvalho, W. Kleist, J.-D. Grunwaldt, "Dynamic transformation of small Ni particles during methanation of CO_2 under fluctuating reaction conditions monitored by *operando* X-ray absorption spectroscopy", *J. Phys.: Conf. Ser.* **2016**, *712*, 012050.

The results from this publication are presented in chapter 6.

[3] D. Chakraborty, C.D. Damsgaard, H. Silva, C. Conradsen, J.L Olsen, H.W.P. Carvalho, B. Mutz, T. Bligaard, M.J. Hoffmann, J.-D. Grunwaldt, F. Studt, I. Chorkendorff, "Bottom-Up Design of a Copper-Ruthenium Nanoparticulate Catalyst for Low-Temperature Ammonia Oxidation" *Angew. Chem. Int. Ed.* **2017**, *56*, 8711-8715.

[4] B. Mutz, M. Belimov, W. Wang, P. Sprenger, M.-A. Serrer, D. Wang, P. Pfeifer, W. Kleist, J.-D. Grunwaldt, "Potential of an alumina-supported Ni_3Fe catalyst in the methanation of CO_2: Impact of alloy formation on activity and stability", *ACS Catal.* **2017**, *7*, 6802-6814.

The results are presented in chapter 9.

[5] B. Mutz, A.M. Gänzler, M. Nachtegaal, O. Müller, R. Frahm, W. Kleist, J.-D. Grunwaldt, "Surface oxidation of Ni particles and its impact on the catalytic performance during dynamically operated methanation of CO_2", *Catalysts* **2017**, *7*, 279.

The results are presented in chapter 7.

B. Mutz, P. Sprenger, W. Wang, D. Wang, W. Kleist, J.-D. Grunwaldt, "*Operando* Raman spectroscopy on CO_2 methanation over alumina-supported Ni, Ni_3Fe and $NiRh_{0.1}$ catalysts: Role of carbon formation as possible deactivation pathway", *Appl. Catal. A* **2018**, *556*, 160-171.

The results are presented in chapter 8.

Oral presentations

B. Mutz, A.M. Gänzler, P. Sprenger, H.W. P. Carvalho, K. F. Kalz, W. Kleist, J.-D. Grunwaldt, "*Operando* spectroscopy as a tool to investigate the nature of Ni-based catalysts during dynamically operated methanation of CO_2", *50. Jahrestreffen Deutscher Katalytiker*, Weimar, Germany, March 15-17, 2017.

B. Mutz, H.W.P. Carvalho, W. Kleist, J.-D. Grunwaldt, "Methanation of CO_2: Structural response of Ni-based catalysts under fluctuating reaction conditions unraveled by *operando* XAS", *XAFS16 – 16th International Conference on X-ray Absorption Fine Structure*, Karlsruhe, Germany, August 23-28, 2015.

Poster presentations

B. Mutz, H.W.P. Carvalho, W. Kleist, J.-D. Grunwaldt, "Methanation of CO_2 under dynamic reaction atmospheres using supported Ni catalysts", *The 16th International Congress on Catalysis ICC16*, Beijing, China, July 3-8, 2016.

B. Mutz, H.W.P. Carvalho, W. Kleist, J.-D. Grunwaldt, "Methanation of CO_2: Structural response of Ni-based catalysts under dynamic reaction conditions unravelled by *operando* spectroscopy", *REGATEC2016: 3rd International Conference on Renewable Energy Gas Technology*, Malmö, Sweden, May 10-11, 2016.

B. Mutz, H.W.P. Carvalho, W. Kleist, J.-D. Grunwaldt, "Structural changes of Ni-based catalysts during dynamic methanation of CO_2 for power-to-gas applications", *49. Jahrestreffen Deutsche Katalytiker*, Weimar, Germany, March 16-18, 2016.

B. Mutz, H.W.P. Carvalho, W. Kleist, J.-D. Grunwaldt, "Methanation of CO_2: Structural response of Ni-based catalysts under fluctuating reaction conditions unraveled by *operando* X-ray absorption spectroscopy", *Operando V: 5th International Conference On Operando Spectroscopy*, Deauville, France, May 17-21, 2015.

B. Mutz, H.W.P. Carvalho, W. Kleist, J.-D. Grunwaldt, "Methanation of CO_2: *Operando* XAS study under dynamic reaction conditions", *ANKA User Meeting*, Karlsruhe, Germany, October 13-14, 2014.

B. Mutz, M. Schubert, W. Kleist, J.-D. Grunwaldt, „Methanation of CO_2: Parameter screening and catalyst stability under stationary and dynamic reaction conditions", *ProcessNet-Jahrestagung*, Aachen, Germany, September 30 – October 2, 2014.

Eidesstattliche Erklärung

Hiermit versichere ich eidesstattlich, dass ich die vorgelegte Dissertation selbständig angefertigt und keine anderen als die angegebenen Quellen und Hilfsmittel benutzt habe. Die wörtlichen oder inhaltlich übernommenen Stellen wurden als solche kenntlich gemacht. Weiterhin habe ich die Satzung des Karlsruher Instituts für Technologie (KIT) zur Sicherung guter wissenschaftlicher Praxis in der gültigen Fassung beachtet und die Primärdaten gemäß Abs. A (6) gesichert. Die elektronische Version der Arbeit stimmt mit der schriftlichen überein. Die Arbeit wurde in gleicher oder anderer Form keiner anderen Prüfungsbehörde zur Erlangung eines akademischen Grades vorgelegt.

Karlsruhe, den